GLOBAL INSTABILITIES OF ACCRETION DISKS

A Dissertation

Presented to the Faculty of the Graduate School

of Cornell University

in Partial Fulfillment of the Requirements for the Degree of

Doctor of Philosophy

by

David Chi-Wah Tsang

January 2009

GLOBAL INSTABILITIES OF ACCRETION DISKS

David Chi-Wah Tsang, Ph.D.

Cornell University 2009

Diskoseismological modes of accretion disks around compact objects are explored, in particular p-modes and their interaction with the corotation resonance. A WKB treatment of wave super-reflection due to corotation resonance and corotation absorption is developed, with super-reflection depending on the gradient of the so-called "vortensity" of the background flow. This result is applied to the context of black hole accretion disks where the background spacetime can modify the vortensity gradient so that p-modes trapped in the inner region of the disk may be amplified. The inner boundary condition for such disks is also explored in detail, in particular the effect of a transonic flow near the innermost stable circular orbit of a black hole is examined.

The effect of the corotation absorption is also briefly examined for other diskoseismic modes with vertical structure, in particular c-modes are shown to be damped by the absorption, and their damping rate is calculated. The inner boundary condition for a magnetosphere-disk model is calculated, as well as that of a star-disk interface. It is shown that interface modes, modes generated at the inner boundary of the disk, can be strongly unstable in the magnetosphere-disk model, due to the Rayleigh-Taylor and Kelvin-Helmholtz instabilities. However, due to the suppressing effect of the disk vorticity in differential rotation, the Rayleigh Taylor instability is suppressed (in models with no shear between the disk and magnetosphere) when sound speed is sufficiently small, while the Kelvin-Helmhotz instability may still be active for small sound

speed when there is shear between the magnetosphere and disk. Star-disk interface modes are found to be weakly unstable primarily due to wave absorption at the corotation. Lastly, a procedure for ray-tracing in the Kerr metric is described, and used to generate images and time-dependant observables from various disk models.

BIOGRAPHICAL SKETCH

David Tsang was born in Abbotsford, British Columbia, Canada, to a family of seven. He attended pre-school at Bumblebee pre-school where he excelled at blocks and block related studies. Indeed, these were the salad days.

Upon graduating pre-school he attended the block-renowned Ten-Broeck Elementary School, from which he was able to attend the Abbotsford Program for EXcellence (APEX) program, which has two programs, but he supposed they just weren't paying attention. These were the soup course days.

Graduation from Ten-Broeck was bittersweet, and not solely due to the bittersweet candy he received upon leaving. David's next stop in his educational life was Clearbrook Junior High School. His attendance that year was correlated with the school being shut down the following year, and all students transferred to the newly constructed Rick Hansen Secondary School. No causation has been definitively proven. This would probably have been the dinner-bun days.

At Rick Hansen Secondary, David excelled in both Science and English Literature and Composition. Taking advantage of excellent instruction by the school's plasma physicist he developed a strong affinity for both Math and Physics, and was able to attend the University College of the Fraser Valley part-time during his Junior and Senior years at Rick Hansen. These were the appetizer days, or maybe the vichyssoise days.

Upon graduation from high school in 1997, David began his studies at the University of British Columbia in Vancouver. After a wonderful freshman year in the multi-disciplinary Science One program, he started in UBC's Engineering Physics program, where he specialized in Mathematics and Electrical Engineering, while minoring in Commerce. During the course of these events many adventures occurred, which will not be relayed in this biographical sketch under

Figure 1: Table 1.

the advice of his attorney. During the penultimate year at UBC, David received a National Science and Engineering Research Council Undergraduate Student Research Award to study spin-foam quantum gravity with Professor Dan Christensen at the University of Western Ontario. His final senior project was completed under the supervision of Professor Matt Choptuik on the parallelization of the Rapid Numerical Prototyping Language. These were the meat course days.

In 2002, David was accepted into the Physics PhD program at Cornell, where he studied Theoretical Astrophysics under Professor Dong Lai, until 2009. These, apparently, were the dissertation days.

For my parents.

ACKNOWLEDGEMENTS

I would like to thank my family for their love and support, as well as the support of all my friends and colleagues at Cornell. In particular I would like to thank my advisor, Dong, for his amazing support and patience. Without his guidance and insightful advice I would certainly not have been able to have accomplish any of this work. I would also like to thank my collaborators on projects not related to this dissertation, Andy, Ruxandra and Mihai, for dragging me along on their adventures, as well as my group-members, Zach and Wen.

TABLE OF CONTENTS

LIST OF FIGURES

CHAPTER 1

INTRODUCTION

Accretion onto compact objects can occur in many systems, including X-ray binaries, cataclysmic variables, and active galactic nuclei. When the accreting matter has excess angular momentum, the flow takes the form of an accretion disk, where the matter undergoes differential rotation around the central object with near Keplerian frequency, while turbulent viscosity transports angular momentum outwards and allows the matter to be accreted.

Accretion disks are ubiquitous in astrophysics, and their study is important to understanding many phenomena, ranging from understanding variable emissions from binary systems to helping determine the extreme spacetime properties near black holes. Of particular interest are quasi-periodic oscillations (QPOs) detected in several X-ray binary systems. These are quasi-periodic variations in the luminosity of X-ray emissions from systems where matter is accreted onto a neutron star or black hole. There is considerable evidence, from timing arguments to comparison of spectral components, that the luminosity variations must arise from the inner regions of the accretion disks in these systems.

The study of oscillations of accretion disks, so-called "diskoseismology" is the main subject of this dissertation. The study of the instability of these modes can help to solve the riddle of QPOs, as unstable diskoseismic modes may be a source for the luminosity variation observed. In particular we discuss the diskoseismic instabilities involving density waves traversing their corotation point.

In Chapter 2 we describe the basic framework for treating the super reflection due to the presence of a corotation point in the disk. In differentially rotating disks with no self-gravity, density waves cannot propagate around the corotation, where the wave pattern rotation speed equals the fluid rotation rate. Waves incident upon the corotation barrier may be super-reflected (commonly referred to as the corotation amplifier), but the reflection can be strongly affected by wave absorptions at the corotation resonance/singularity. The sign of the absorption is related to the Rossby wave zone very near the corotation radius. We derive the explicit expressions for the complex reflection and transmission coefficients, taking into account wave absorption at the corotation resonance. We show that for generic disks this absorption plays a much more important role than wave transmission across the corotation barrier. Depending on the sign of the gradient of the vortensity of the disk, $\zeta = \kappa^2/(2\Omega\Sigma)$ (where Ω is the rotation rate, κ is the epicyclic frequency, and Σ is the surface density), the corotation resonance can either enhance or diminish the super-reflectivity, and this can be understood in terms of the location of the Rossby wave zone relative to the corotation radius. Our results provide the explicit conditions (in terms of disk thickness, rotation profile and vortensity gradient) for which super-reflection can be achieved. Global overstable disk modes may be possible for disks with super-reflection at the corotation barrier.

In Chapter 3 we study the global stability of non-axisymmetric p-modes (also called inertial-acoustic modes) trapped in the inner-most regions of accretion disks around black holes. We show that the lowest-order (highest-frequency) p-modes, with frequencies $\omega = (0.5-0.7)m\Omega_{\mathrm{ISCO}}$ (where $m = 1, 2, 3, \ldots$ is the azimuthal wave number, Ω_{ISCO} is the disk rotation frequency at the Inner-most Stable Circular Orbit, ISCO), can be overstable due to general relativistic

effects, according to which the radial epicyclic frequency κ is a non-monotonic function of radius near the black hole. The mode is trapped inside the corotation resonance radius r_c (where the wave pattern rotation speed ω/m equals the disk rotation rate Ω) and carries a negative energy. The mode growth arises primarily from wave absorption at the corotation resonance, and the sign of the wave absorption depends on the gradient of the disk vortensity. When the mode frequency ω is sufficiently high, such that $d\zeta/r > 0$ at r_c, positive wave energy is absorbed at the corotation, leading to the growth of mode amplitude. The mode growth is further enhanced by wave transmission beyond the corotation barrier. We also study how the rapid radial inflow at the inner edge of the disk affects the mode trapping and growth. Our analysis of the behavior of the fluid perturbations in the transonic flow near the ISCO indicates that, while the inflow tends to damp the mode, the damping effect is sufficiently small under some conditions (e.g., when the disk density decreases rapidly with decreasing radius at the sonic point) so that net mode growth can still be achieved. We further clarify the role of the Rossby wave instability and show that it does not operate for black hole accretion disks with smooth-varying vortensity profiles. Overstable non-axisymmetric p-modes driven by the corotational instability provide a plausible explanation for the high-frequency ($\gtrsim 100$ Hz) quasi-periodic oscillations (HFQPOs) observed from a number of black-hole X-ray binaries in the very high state. The absence of HFQPOs in the soft (thermal) state may result from mode damping due to the radial infall at the ISCO.

In Chapter 4 we discuss the effect of the corotation singularity on so-called corrugation waves, or c-modes. Diskoseismic c-modes in accretion disks have been invoked to explain low-frequency variabilities observed in black-hole X-ray binaries. These modes are trapped in the inner-most region of the disk

and have frequencies much lower than the rotation frequency at the disk inner radius. We show that because the trapped waves can tunnel through the evanescent barrier to the corotational wave zone, the c-modes are damped due to wave absorption at the corotation resonance. We calculate the corotational damping rates of various c-modes using the WKB approximation. The damping rate varies widely depending on the mode frequency, the black hole spin parameter and the disk sound speed, and is generally much less than 10% of the mode frequency. A sufficiently strong excitation mechanism is needed to overcome this corotational damping and make the mode observable.

Chapter 5 explores the effect of a magnetosphere or star surface as the inner boundary for an accretion disk on modes confined to the disk/magnetosphere or disc/star interface. Such boundaries may lead to the development of Rayleigh-Taylor or Kelvin-Helmholtz type instabilities. We find that the fluid vorticity due to differential rotation acts to suppress these modes, unless, for the disk/magnetosphere case, the disk is sufficiently hot. We find that in the disk/star case the effective gravity also helps to suppress instability, and only the corotation absorption can drive an instability, if the surface density index is sufficiently high.

Finally in Chapter 6, we describe a raytracing engine for use in the Kerr metric to calculate observables for disks located around rotating black holes. We present a user-interface for generating disk images and line profiles, as well as demonstrating the calculation of the observed polarization and of the time dependent changes in observed flux due to the types of perturbations discussed in earlier chapters.

CHAPTER 2

SUPER-REFLECTION IN FLUID DISKS: COROTATION AMPLIFIER, COROTATION RESONANCE, ROSSBY WAVES, AND OVERSTABLE MODES

2.1 Introduction

Differentially rotating fluid disks, ubiquitous in astrophysics, are known to exhibit rich dynamics and possible instabilities (e.g. Papaloizou & Lin 1995; Balbus & Hawley 1998). While local instabilities, such as Rayleigh's centrifugal instability (for disks with specific angular momentum decreasing outwards), gravitational instability (for self-gravitational disks with too large a surface density, or more precisely, Toomre $Q \lesssim 1$), and magnetorotational instability (for disks with a sub-thermal magnetic field), are well understood (at least in the linear regime), global effects and instabilities are more subtle, since they involve couplings and feedbacks of fluid at different locations (see Goldreich 1988 for an introduction/review). A well-known example is the corotation amplifier (e.g. Mark 1976; Narayan, Goldreich & Goodman 1987), which arises from the interaction across the corotation between waves carrying opposite signs of angular momentum. Much stronger corotation amplifications (WASER – wave amplification by the stimulated emission of radiation, and SWING amplifiers) can be achieved for self-gravitating disks (e.g., Goldreich & Lynden-Bell 1965; Julian & Toomre 1966; Lin & Lau 1975; see Shu 1992 for a review). Another well-known example is the Papaloizou-Pringle instability in finite accretion tori (confined between two free surfaces), in which coupling between waves inside the corotation with those outside, combined with reflecting inner and outer bound-

aries, leads to violent overstable modes (Papaloizou & Pringle 1984; Goldreich et al. 1986). Recent works on global disk instabilities include the Rossby wave instability (for disks with a strong enough density or vortensity bump; Lovelace et al. 1999; Li et al. 2000) and the accretion-ejection instability (for magnetized disks; Tagger & Pellat 1999, Tagger & Varniere 2006).

In this chapter we are interested in 2D fluid disks without self-gravity and magnetic field. For disturbances of the form $e^{im\phi - i\omega t}$, where $m > 0$ and ω is the wave (angular) frequency (and thus $\omega_p = \omega/m$ is the pattern frequency), the well-known WKB dispersion relation for density waves takes the form (e.g., Shu 1992)

$$(\omega - m\Omega)^2 = \tilde{\omega}^2 = \kappa^2 + k_r^2 c^2, \tag{2.1}$$

where Ω is the disk rotation frequency, $\tilde{\omega} = \omega - m\Omega$ is the Doppler-shifted wave frequency, κ is the radial epicyclic frequency, k_r is the radial wavenumber, and c is the sound speed. Thus waves can propagate either inside the inner Lindblad resonance radius $r_{\rm IL}$ (defined by $\tilde{\omega} = -\kappa$) or outside the outer Lindblad resonance radius $r_{\rm OL}$ (defined by $\tilde{\omega} = \kappa$), while the region around the corotation radius r_c (set by $\tilde{\omega} = 0$) between $r_{\rm IL}$ and $r_{\rm OL}$ is evanescent. Since the wave inside $r_{\rm IL}$ has pattern speed ω_p smaller than the fluid rotation rate Ω, it carries negative wave action (or angular momentum), while the wave outside $r_{\rm OL}$ carries positive wave action. As a result, a wave incident from small radii toward the corotation barrier will be super-reflected, (with the reflected wave having a larger amplitude than the incident wave amplitude) if it can excite a wave on the other side of the corotation barrier. If there exists a reflecting boundary at the inner disk radius $r_{\rm in}$, then a global overstable mode partially trapped between $r_{\rm in}$ and $r_{\rm IL}$ will result (see, e.g. Narayan et al. 1987 for specific examples in the shearing sheet model, and Goodman & Evans,1999 and Shu et al. 2000 for

global mode analysis of singular isothermal disks).

The simple dispersion relation (2.1), however, does not capture an important effect in the disk, i.e., corotation resonance or corotation singularity. Near corotation $|\tilde{\omega}| \ll \kappa$, the WKB dispersion relation for the wave is [see equation (2.17) below]

$$\tilde{\omega} = \frac{2\Omega k_\phi}{k_r^2 + k_\phi^2 + \kappa^2/c^2} \left(\frac{d}{dr} \ln \frac{\kappa^2}{2\Omega\Sigma} \right)_c, \tag{2.2}$$

where $k_\phi = m/r$ and Σ is the surface density, and the subscript "c" implies that the quantity is evaluated at $r = r_c$. The quantity

$$\zeta \equiv \frac{\kappa^2}{2\Omega\Sigma} = \frac{(\nabla \times \mathbf{u_0}) \cdot \hat{z}}{\Sigma} \tag{2.3}$$

is the vortensity of the (unperturbed) flow (where $\mathbf{u_0}$ is the flow velocity). The dispersion relation (2.2) describes Rossby waves, analogous to those studied in geophysics (e.g. Pedlosky 1987) [1]. For $k_r^2 \gg \kappa^2/c^2$ and $k_r^2 \gg k_\phi^2$, we see that Rossby waves can propagate either outside the rotation radius r_c (when $d\zeta/dr > 0$) or inside r_c (when $d\zeta/dr < 0$). In either case, we have $k_r \to \infty$ as $r \to r_c$. This infinite wavenumber signifies wave absorption (cf. Lynden-Bell & Kalnajs 1972 in stellar dynamical context; Goldreich & Tremaine 1979 in the context of wave excitation in disks by a external periodic force; see also Kato 2003, Li et. al. 2003, and Zhang & Lai 2006 for wave absorption at the corotation in 3D disks). At corotation, the wave pattern angular speed ω/m matches Ω, and there can be efficient energy transfer between the wave and the background flow, analogous to Landau damping in plasma physics. Narayan et al. (1987) treated this effect as a perturbation of the shearing sheet model, and showed that the corotational absorption can convert neutral modes in a finite shearing sheet into growing or

---

[1] A Rossby wave propagating in the Earth's atmosphere satisfies the dispersion relation $\tilde{\omega} = (2k_\phi/k^2 R)(\partial\Omega_3/\partial\theta)$, where $k^2 = k_\phi^2 + k_\theta^2$, $\Omega_3 = \Omega\cos\theta$ is the projection of the rotation rate on the local surface normal vector and θ is the polar angle (co-latitude).

decaying modes. Papaloizou & Pringle (1987) used a WKB method to examine the effect of wave absorption at corotation on the nonaxisymmetric modes in an unbound (with the outer boundary extending to infinity) cylindrical torus.

In this chapter, we derive explicit expressions for the complex reflection coefficient and transmission coefficient for waves incident upon the corotation barrier. We pay particular attention to the behavior of perturbations near the corotation resonance/singularity. Our general expressions include both the effects of corotation amplifier and wave absorption at corotation (which depends on $d\zeta/dr$). We show explicitly that depending on the sign of $d\zeta/dr$, the corotation resonance/singularity can either enhance or diminish the super-reflectivity, and this can be understood in terms of the location of the Rossby wave zone relative to the corotation radius.

Our chapter is organized as follows. After presenting the general perturbation equations (section 2), we discuss the the wave dispersion relation and propagation diagram, and derive the local solutions for the wave equation around the Lindblad resonances and corotation resonance (section 3). We then construct global WKB solution for the wave equation, and derive the wave reflection, transmission and corotaional damping coefficients in section 4. An alternative derivation of the wave damping coefficient is presented in section 5. Readers not interested in technical details can skip Sections 2-5 and concentrate on Section 6, where we illustrate our results and discuss their physical interpretations. Section 6.1 contains a numerical calculation of the wave reflectivity across corotation and discusses the limitation of the WKB analysis. We discuss how global overstable modes may arise when super-reflection at the corotation is present in section 7 and conclude in section 8.

2.2 Perturbation Equations

We consider a geometrically thin gas disk and adopt cylindrical coordinate system (r, ϕ, z). The unperturbed disk has an integrated surface density $\Sigma(r)$ and velocity $\mathbf{u_0} = (0, r\Omega, 0)$. The flow is assumed to be barotropic, so that the integrated pressure P depends only on Σ. Self gravity of the disk is neglected.

The linear perturbation equations for the flow read

$$\frac{\partial}{\partial t}\delta\mathbf{u} + (\mathbf{u}_0 \cdot \nabla)\delta\mathbf{u} + (\delta\mathbf{u} \cdot \nabla)\mathbf{u}_0 = -\nabla\delta h, \tag{2.4}$$

$$\frac{\partial}{\partial t}\delta\Sigma + \nabla \cdot (\Sigma\, \delta\mathbf{u} + \mathbf{u}_0\, \delta\Sigma) = 0, \tag{2.5}$$

where $\delta\Sigma$, $\delta\mathbf{u}$ and $\delta h = \delta P/\Sigma$ are the (Eulerian) perturbations of surface density, velocity and enthalpy, respectively. For barotropic flow, δh and $\delta\Sigma$ are related by

$$\delta h = c^2\frac{\delta\Sigma}{\Sigma}, \tag{2.6}$$

where c is the sound speed, with $c^2 = dP/d\Sigma$.

We assume that the ϕ and t dependence of the perturbation are of the form

$$\delta\mathbf{u},\ \delta\Sigma,\ \delta h \propto e^{im\phi - i\omega t}, \tag{2.7}$$

where m is a positive integer, and ω is the wave (angular) frequency. We presume $\omega > 0$ so that the pattern (angular) speed of the perturbation $\omega_p = \omega/m$ is positive (in the same direction as the flow rotation). Note that we usually assume ω is real, except in section 3.2 (dealing with the perturbation near corotation) where we include a small imaginary part ($\omega = \omega_r + i\omega_i$, with $\omega_i > 0$) to represent slowly growing disturbances. The perturbation equations (2.4)-(2.5)

become

$$-i\tilde{\omega}\frac{\Sigma}{c^2}\delta h + \frac{1}{r}\frac{\partial}{\partial r}(\Sigma r\delta u_r) + \frac{im}{r}\Sigma\delta u_\phi = 0, \tag{2.8}$$

$$-i\tilde{\omega}\delta u_r - 2\Omega\delta u_\phi = -\frac{\partial}{\partial r}\delta h, \tag{2.9}$$

$$-i\tilde{\omega}\delta u_\phi + \frac{\kappa^2}{2\Omega}\delta u_r = -\frac{im}{r}\delta h, \tag{2.10}$$

where the epicyclic frequency κ is given by

$$\kappa^2 = \frac{2\Omega}{r}\frac{d}{dr}(r^2\Omega). \tag{2.11}$$

Eliminating δu_r and δu_ϕ from equations (2.8)-(2.10), we obtain a standard second-order differential equation governing δh (e.g., Goldreich & Tremaine 1979):

$$\left[\frac{d^2}{dr^2} - \frac{d}{dr}\left(\ln\frac{D}{r\Sigma}\right)\frac{d}{dr} - \frac{2m\Omega}{r\tilde{\omega}}\left(\frac{d}{dr}\ln\frac{\Omega\Sigma}{D}\right) - \frac{m^2}{r^2} - \frac{D}{c^2}\right]\delta h = 0, \tag{2.12}$$

where

$$D \equiv \kappa^2 - \tilde{\omega}^2 = \kappa^2 - (\omega - m\Omega)^2. \tag{2.13}$$

Defining

$$S = D/(r\Sigma), \quad \eta = S^{-1/2}\delta h, \tag{2.14}$$

we can rewrite (2.12) as a wave equation

$$\left[\frac{d^2}{dr^2} - \frac{D}{c^2} - \frac{m^2}{r^2} - \frac{2m\Omega}{r\tilde{\omega}}\left(\frac{d}{dr}\ln\frac{\Omega\Sigma}{D}\right) - S^{1/2}\frac{d^2}{dr^2}S^{-1/2}\right]\eta = 0. \tag{2.15}$$

This is our basic working equation.

2.3 Propagation Diagram and Local Solutions Near Resonances

Consider local free wave solution of the form

$$\delta h \propto \exp\left[i\int^r k_r(s)ds\right]. \tag{2.16}$$

For $|k_r r| \gg m$ and away from the $D = 0$ region, we find from equation (2.15)

$$k_r^2 + \frac{D}{c^2} + \frac{2m\Omega}{r\tilde{\omega}} \left(\frac{d}{dr} \ln \frac{\Omega\Sigma}{D} \right) \simeq 0. \tag{2.17}$$

This is the general WKB dispersion relation. Away from the region where $\tilde{\omega} = 0$, this reduces to the well-known result $k_r^2 \simeq -D/c^2$ [equation (2.1)]; in the vicinity of $\tilde{\omega} = 0$ this describes local Rossby waves, with [see equations (2.2)-(2.3)]

$$\tilde{\omega} \simeq \frac{2m\Omega}{rk_r^2} \left(\frac{d\ln\zeta}{dr} \right)_c. \tag{2.18}$$

Before studying global solutions to the wave equation (2.12) or (2.15), it is useful to consider the special resonant locations in the disk. These can be recognized by investigating the singular points and turning points of the wave equation (2.12) or (2.15), or by examining the characteristics of the dispersion relation (2.17). The special radii are

(i) Lindblad resonances (LRs), where $D = 0$ or $\tilde{\omega}^2 = \kappa^2$, including the outer Lindblad resonance (OLR) at $\tilde{\omega} = \kappa$ and the inner Lindblad resonance (ILR) at $\tilde{\omega} = -\kappa$. The LRs are apparent singularities of equation (2.12) or (2.15) – all physical quantities are finite at $D = 0$. The LRs are turning points at which wave trains are reflected or transmitted. In the presence of an external force, waves are launched from LRs.

(ii) Corotation resonance (CR), where $\tilde{\omega} = 0$. In general, the CR is a singular point of the wave equation except in the special case of $d\zeta/dr = 0$ at corotation. Some physical quantities (e.g., azimuthal velocity perturbation) are divergent at corotation. Physically, this singularity signifies that a steady emission or absorption of wave action may occur there.

From equation (2.15), we define the effective potential for wave propagation

11

by

$$V_{\text{eff}}(r) = \frac{D}{c^2} + \frac{m^2}{r^2} + \frac{2m\Omega}{r\tilde{\omega}} \left(\frac{d}{dr} \ln \frac{\Omega\Sigma}{D} \right) + S^{1/2} \frac{d^2}{dr^2} S^{-1/2}$$

$$= V_{\text{eff},0}(r) + \Delta V_{\text{eff}}(r), \tag{2.19}$$

where

$$V_{\text{eff},0}(r) = \frac{D}{c^2} + \frac{m^2}{r^2} - \frac{2m\Omega}{r\tilde{\omega}} \left(\frac{d}{dr} \ln \zeta \right), \tag{2.20}$$

$$\Delta V_{\text{eff}}(r) = -\frac{2m\Omega}{r\tilde{\omega}} \frac{d}{dr} \ln \frac{D}{\kappa^2} + S^{1/2} \frac{d^2}{dr^2} S^{-1/2}. \tag{2.21}$$

Clearly, wave propagation is possible only in the region where $V_{\text{eff}}(r) < 0$. Figures 1-3 depict the wave propagation diagrams for the cases of $(d\zeta/dr)_c = 0, \ < 0$ and > 0, respectively. We are interested in the parameter regime $c/(r\Omega) \ll 1$ and m is of order unity. Note that the apparent singularity in $\Delta V_{\text{eff}}(r)$ at $D = 0$ can be eliminated by analysing the wave solution around the LRs (see section 3.1 below). Thus we also show $V_{\text{eff},0}(r)$ in Figs. 1-3.

We now consider the behaviors of the perturbations around the LRs and CR.

2.3.1 Solution Around Lindblad Resonances

Equation (2.15) has an apparent singularity at the LRs, where $D \rightarrow 0$. For concreteness we will explicitly examine the outer Lindblad resonance (OLR); a similar solution can be found for the inner Lindblad resonance (ILR).

In the vicinity of the OLR, equation (2.15) becomes

$$\frac{d^2}{dr^2}\eta + \left(k^2 - k\frac{d^2}{dr^2}\frac{1}{k} + \frac{4m\Omega}{r\tilde{\omega}k}\frac{dk}{dr} \right)\eta = 0, \tag{2.22}$$

12
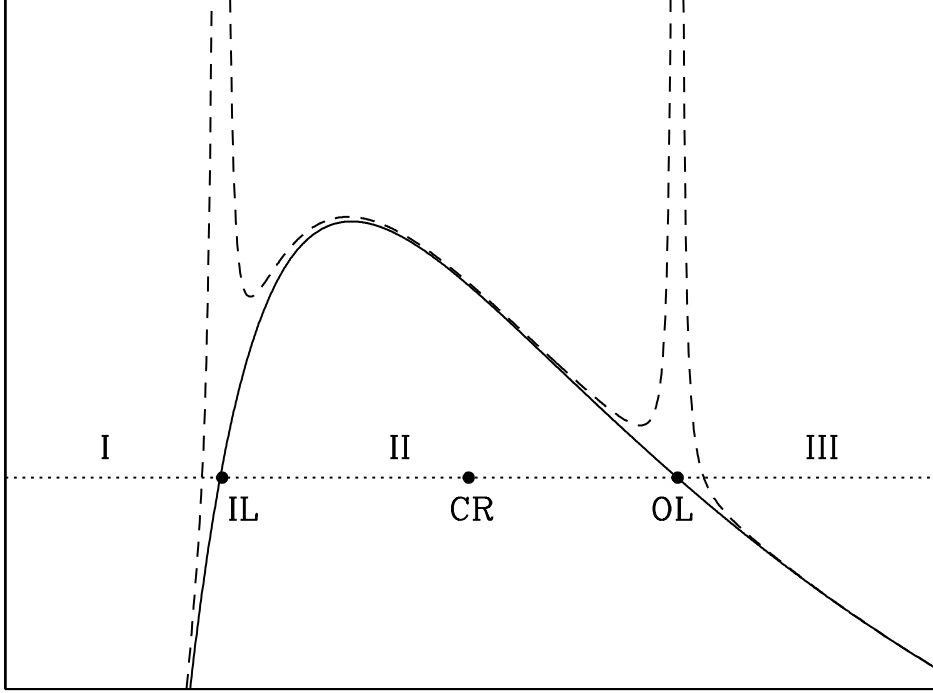
Figure 2.1: Wave propagation diagram in Keplerian disks: A sketch of the effective potential $V_{\mathrm{eff},0}(r)$ (solid line) and $V_{\mathrm{eff}}(r)$ (dashed line) as a function of r, for the case of $(d\zeta/dr)_c = 0$. Waves can propagate only in the region where $V_{\mathrm{eff}}(r) < 0$, i.e., where the curves are below the dotted line. The three special locations are denoted by IL (Inner Lindblad Resonance), OL (Outer Lindblad Resonance) and CR (Corotation Resonance). The divergence in the $V_{\mathrm{eff}}(r)$ curve around IL and OL represents an apparent singularity.
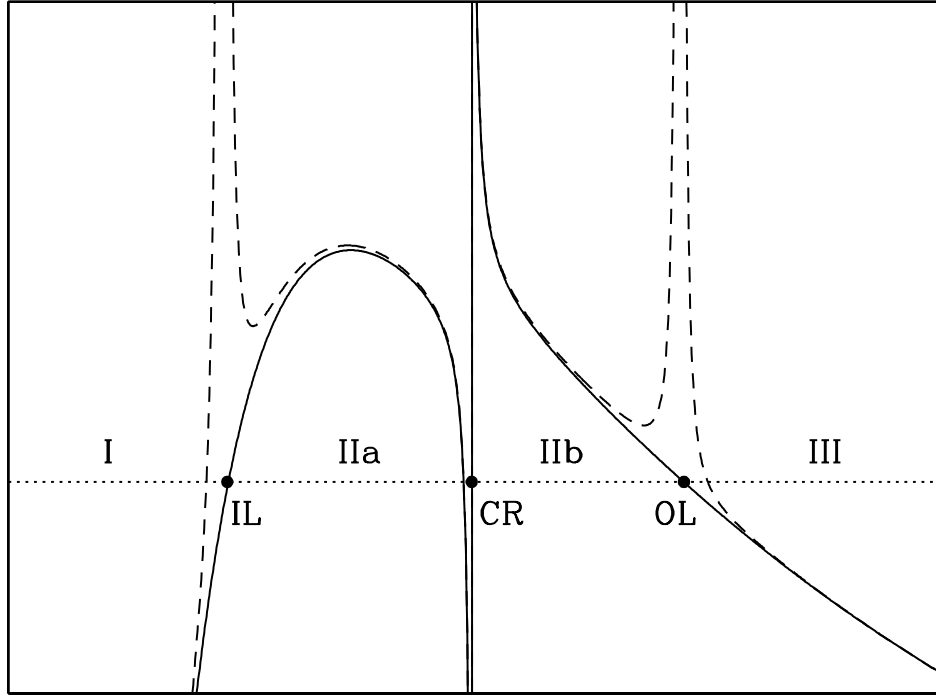
Figure 2.2: Same as Fig. 1, except for the case of negative vortensity gradient, $(d\zeta/dr)_c < 0$ (or $\nu < 0$). Note the CR represents a singularity, and the Rossby wave zone lies inside the corotation radius.
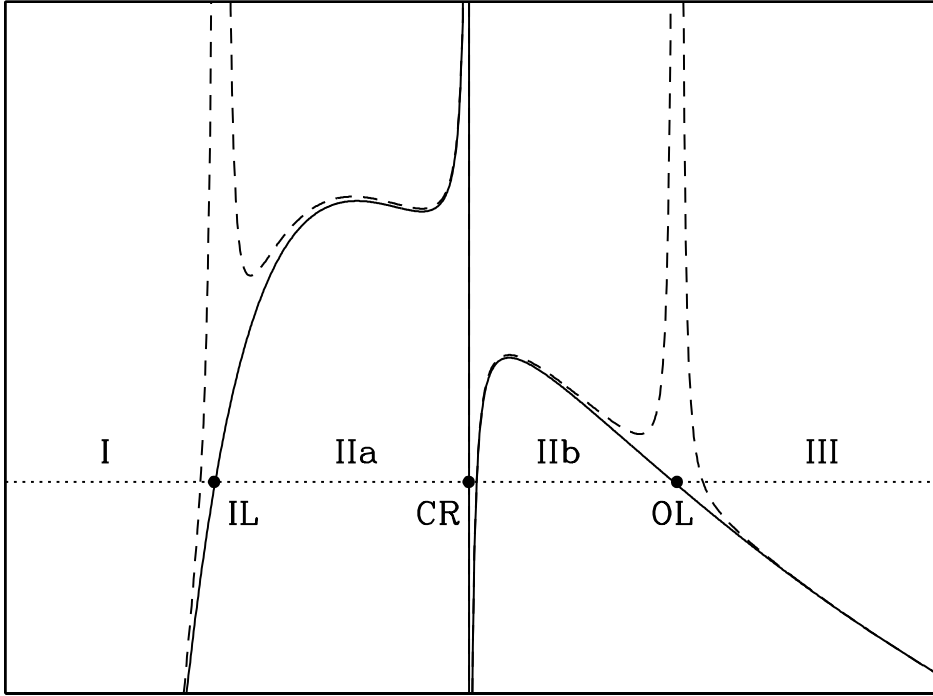
Figure 2.3: Same as Fig. 1, except for the case of positive vortensity gradient, $(d\zeta/dr)_c > 0$ (or $v > 0$), for which the Rossby wave zone lies outside the corotation radius.

where $k^2 \equiv -D/c^2$. The last term inside $(\cdots)$ is smaller than the second term and will be neglected. Changing the independent variable from r to the dimensionless integrated phase

$$z = \int_{r_{OL}}^{r} k \, dr, \tag{2.23}$$

we have

$$V'' + \left[\frac{k''}{2k} - \frac{3}{4}\left(\frac{k'}{k}\right)^2 + 1\right] V = 0, \tag{2.24}$$

where

$$V = \sqrt{k}\,\eta = \sqrt{\frac{k}{S}}\,\delta h, \tag{2.25}$$

and the prime denotes differentiation with respect to z. Note that near OLR, $k^2 \simeq C(r - r_{OL})$, with $C = (-c^{-2}dD/dr)_{OL} > 0$ a constant, we have

$$z = \begin{cases} \frac{2}{3}C^{1/2}(r - r_{OL})^{3/2} & \text{for } r > r_{OL} \\ \frac{2}{3}C^{1/2}(r_{OL} - r)^{3/2}e^{i3\pi/2} & \text{for } r < r_{OL} \end{cases} \tag{2.26}$$

We can then express k in terms of z as

$$k = \left(\frac{3}{2}C\right)^{1/3} z^{1/3}. \tag{2.27}$$

Using equation (2.27) in equation (2.24) we have

$$V'' + \left(1 - \frac{7}{36z^2}\right)V = 0. \tag{2.28}$$

Equation (2.28) has two independent solutions in terms of Bessel function (Abramowitz & Stegun 1964)

$$V = \sqrt{z}\,J_{\pm 2/3}(z) = \frac{1}{(12z)^{1/6}}\left[\pm\sqrt{3}\,\text{Ai}'(-Z) + \text{Bi}'(-Z)\right], \tag{2.29}$$

where $Z = (3z/2)^{2/3}$, and Ai$'$, Bi$'$ are the derivatives of the Airy functions. Instead of using $\sqrt{z}J_{\pm 2/3}(z)$, we we can construct two linearly independent solutions for

η in a form convenient for asymptotic matching:

$$\eta_1 = -\left(\frac{\pi}{k}\right)^{1/2}\left(\frac{2}{3z}\right)^{1/6} \text{Ai}'(-Z) \sim \begin{cases} \frac{1}{\sqrt{k}}\cos(z + \pi/4) & \text{for } |z| \gg 1 \text{ and } \arg(z) = 0 \\ \frac{1}{2\sqrt{k}}\exp(-|z|) & \text{for } |z| \gg 1 \text{ and } \arg(z) = 3\pi/2 \end{cases}$$
(2.30)

$$\eta_2 = \left(\frac{\pi}{k}\right)^{1/2}\left(\frac{2}{3z}\right)^{1/6} \text{Bi}'(-Z) \sim \begin{cases} \frac{1}{\sqrt{k}}\sin(z + \pi/4) & \text{for } |z| \gg 1 \text{ and } \arg(z) = 0 \\ \frac{1}{\sqrt{k}}\exp(|z|) & \text{for } |z| \gg 1 \text{ and } \arg(z) = 3\pi/2 \end{cases}$$
(2.31)

where $\sim$ indicates asymptotic expansions. This gives the connection formulae for the enthalpy perturbation at the OLR[2]:

$$\delta h_1 \sim \begin{cases} \frac{1}{2}\sqrt{S/k}\exp\left(-\int_r^{r_{\text{OL}}}|k|\,dr\right) & \text{for } r \ll r_{\text{OL}} \\ \sqrt{S/k}\cos\left(\int_{r_{\text{OL}}}^r k\,dr + \pi/4\right) & \text{for } r \gg r_{\text{OL}} \end{cases}$$
(2.32)

$$\delta h_2 \sim \begin{cases} \sqrt{S/k}\exp\left(\int_r^{r_{\text{OL}}}|k|\,dr\right) & \text{for } r \ll r_{OL} \\ \sqrt{S/k}\sin\left(\int_{r_{\text{OL}}}^r k\,dr + \pi/4\right) & \text{for } r \gg r_{\text{OL}} \end{cases}$$
(2.33)

The connection formulae for ILR can be similarly derived: [3]

$$\delta h_1 \sim \begin{cases} \frac{1}{2}\sqrt{S/k}\exp\left(-\int_{r_{\text{IL}}}^r|k|\,dr\right) & \text{for } r \gg r_{\text{IL}} \\ \sqrt{S/k}\cos\left(\int_r^{r_{\text{IL}}} k\,dr + \pi/4\right) & \text{for } r \ll r_{\text{IL}} \end{cases}$$
(2.34)

$$\delta h_2 \sim \begin{cases} \sqrt{S/k}\exp\left(\int_{r_{\text{IL}}}^r|k|\,dr\right) & \text{for } r \gg r_{IL} \\ \sqrt{S/k}\sin\left(\int_r^{r_{\text{IL}}} k\,dr + \pi/4\right) & \text{for } r \ll r_{\text{IL}} \end{cases}$$
(2.35)

---

[2]The usage here of $\gg$ is used as a shorthand for the range of validity for an asymptotic expansion of a local solution. The fitting formulae are to be used far enough away from the resonances so that the asymptotic expansion is valid, but close enough that the local approximation made in (22) holds.

[3]Note that for the ILR, k is real for $r < r_{\text{IL}}$ and imaginary for $r > r_{\text{IL}}$, while for the OLR, k is real for $r > r_{\text{OL}}$ and imaginary for $r < r_{\text{OL}}$.

2.3.2 Solution Around Corotation Radius

In the vicinity of the corotation radius r_c, we can rewrite (2.15) dropping the m^2/r^2 and S terms compared to the singular term proportional to $1/\tilde{\omega}$, giving

$$\left[\frac{d^2}{dr^2} - \tilde{k}^2 + \frac{2}{q}\left(\frac{d}{dr}\ln\frac{\kappa^2}{\Omega\Sigma}\right)_c\frac{1}{r - R_c}\right]\eta = 0, \qquad (2.36)$$

where

$$\tilde{k}^2 \equiv \frac{D}{c^2}, \quad q \equiv -\left(\frac{d\ln\Omega}{d\ln r}\right)_c, \quad R_c \equiv r_c - i\frac{r_c\omega_i}{q\omega_r}. \qquad (2.37)$$

Here we have introduced a small imaginary part to the wave frequency, so that $\omega = \omega_r + i\omega_i$. To study the response of the disk to a slowly increasing perturbation, we require $\omega_i > 0$. Defining

$$x = \int_{r_c}^{r} 2\tilde{k}\, dr, \quad \eta = \frac{1}{\sqrt{\tilde{k}}}\psi, \qquad (2.38)$$

and recognizing that $\tilde{k}$ can be treated as a constant around corotation, we have

$$\frac{d^2}{dx^2}\psi + \left(-\frac{1}{4} + \frac{\nu}{x + i\epsilon}\right)\psi = 0 \qquad (2.39)$$

where $\epsilon = 2\tilde{k}r_c\omega_i/(q\omega_r)$ and

$$\nu = \frac{1}{q\tilde{k}}\left(\frac{d}{dr}\ln\frac{\kappa^2}{\Omega\Sigma}\right)_c = \left(\frac{c}{q\kappa}\frac{d}{dr}\ln\zeta\right)_c. \qquad (2.40)$$

In equation (2.39) $\epsilon > 0$, consistent with the initial value problem in which the perturbation is gradually turned on starting from $t = -\infty$. The parameter ν determines the width of the Rossby wave region, $\Delta r_R = (2c/\kappa)|\nu|$. For $d\ln\zeta/dr \sim 1/r$, we have $|\nu| \sim (H/r)_c$ (H is the disk scale height). [4]

Equation (2.39) is the differential equation for the Whittaker function in complex variable $z = x + i\epsilon$ with index $1/2$ (Abramowitz & Stegun 1964). The two

---

[4]Note that the WKB wavenumber k_r in the Rossby region ranges from ∞ (at $r = r_c$) to H^{-1} (at $r \sim r_c \pm \Delta r_R$) [see equation (18)] while the width of the region is of order H^2/r for most Keplerian disks. Free Rossby waves tend to be sheared away by differential rotation (Tagger 2001).

linearly independent solutions convenient for the connection are

$$\psi_- = W_{\nu,1/2}(z), \qquad \psi_+ = e^{-i\pi\nu}W_{-\nu,1/2}(ze^{-i\pi}) + \frac{1}{2}T_0 W_{\nu,1/2}(z), \qquad (2.41)$$

where T_0 is the Stokes multiplier defined below, and z is defined in the complex plane so that $\arg(z)$ ranges from 0 to π. The particular linear combinations of Whittaker functions in (2.41) are chosen so that appropriate asymptotic expansions can be obtained. To obtain these asymptotic expansions and the connection formulae around the corotation, one must carefully consider the Stokes phenomenon, which alters the form of the asymptotic expansion of a function depending on the position of z in the complex plane. Since the appropriate asymptotic expansions (which connect the solution $W_{\pm\nu,1/2}$ analytically in different regions of the complex plane) are not readily available, we relegate the discussion of the Stokes phenomenon for the Whittaker function around the corotation to Appendix A[5]. The resulting connection formulae are

$$\delta h_- \sim \begin{cases} \sqrt{S/k}\,\exp\left(-\int_{r_c}^r \tilde{k}\,dr\right) & r \gg r_c \\ \sqrt{S/k}\,e^{i\pi\nu}\exp\left(+\int_r^{r_c} \tilde{k}\,dr\right) + \sqrt{S/k}\,\frac{T_1}{2}e^{-i\pi\nu}\exp\left(-\int_r^{r_c} \tilde{k}\,dr\right) & r \ll r_c\,. \end{cases} \qquad (2.42)$$

$$\delta h_+ \sim \begin{cases} \sqrt{S/k}\,\exp\left(+\int_{r_c}^r \tilde{k}\,dr\right) & r \gg r_c \\ \sqrt{S/k}\,\frac{T_0}{2}e^{i\pi\nu}\exp\left(+\int_r^{r_c} \tilde{k}\,dr\right) + \sqrt{S/k}\,\left(1 + \frac{T_1 T_0}{4}\right)e^{-i\pi\nu}\exp\left(-\int_r^{r_c} \tilde{k}\,dr\right) & r \ll r_c \end{cases} \qquad (2.43)$$

where T_0 and T_1 are the Stokes multipliers,

$$T_0 = \frac{2\pi i}{\Gamma(\nu)\Gamma(1+\nu)}, \qquad T_1 = \frac{2\pi i\,e^{i2\pi\nu}}{\Gamma(-\nu)\Gamma(1-\nu)}. \qquad (2.44)$$

Note that for $|\nu| \ll 1$, $[\Gamma(\pm\nu)]^{-1} = \pm\nu + \gamma\nu^2 + \cdots$, where $\gamma = 0.5772$ is the Euler constant.

---

[5]The Stokes phenomenon is present in our Lindblad resonance analysis as well, as we see, for example, the asymptotic expansion for $Bi'(-(3z/2)^{2/3})$ takes the form $e^{+|z|}$ for $\arg(z) = 3\pi/2$ but $\sin(z + \pi/4)$ (as opposed to e^{iz}) for $\arg(z) = 0$. The resulting connection formulae are well known for the Airy functions.

2.4 Global WKB Solutions and Calculation of Reflectivity

In this section we consider a wave train which approaches corotation from small radii ($r \ll r_{\mathrm{IL}}$). Its propagation is impeded by the potential barrier between r_{IL} and r_{OL}. The incident wave is partially transmitted beyond the OLR and a reflected wave propagates from the ILR toward small radii. We will derive the explicit expressions for the (complex) reflection coefficient $\mathcal{R}$ and transmission coefficient $\mathcal{T}$.

From the dispersion relation [equation (2.1), or equation (2.17) away from corotation], we find that the radial group velocity of the waves is

$$c_g = \frac{d\omega}{dk_r} = \frac{k_r c^2}{\tilde{\omega}(1 - \kappa^2/\tilde{\omega}^2)}. \tag{2.45}$$

Thus the sign of c_g/c_p (where $c_p = \omega/k_r$ is the phase velocity) is positive for $r > r_{\mathrm{OL}}$ and negative for $r < r_{\mathrm{IL}}$. This implies that in the $r > r_{\mathrm{OL}}$ region, the outgoing (transmitted) wave has the form $\exp(i \int^r k_r \, dr)$ (assuming $k_r > 0$). In the $r < r_{\mathrm{IL}}$ region, the incident wave (propagating from small radii toward corotation) has the form $\exp(-i \int^r k_r \, dr)$, while the reflected wave has the form $\exp(i \int^r k_r \, dr)$.

A well-known property of density waves is that for $r < r_{\mathrm{IL}}$ the wave carries negative energy (or angular momentum), while for $r > r_{\mathrm{OL}}$ the wave carries positive energy. An incident wave $\exp(-i \int^r k_r \, dr)$, carrying energy of the amount (-1), will give rise to a reflected wave $\mathcal{R} \exp(i \int^r k_r \, dr)$ and a transmitted wave $\mathcal{T} \exp(i \int^r k_r \, dr)$. Let $\mathcal{D}_c$ be the energy dissipated at the corotation. Then energy conservation gives $-1 = (-1)|\mathcal{R}|^2 + |\mathcal{T}|^2 + \mathcal{D}_c$, or

$$|\mathcal{R}|^2 = 1 + |\mathcal{T}|^2 + \mathcal{D}_c. \tag{2.46}$$

Because of the singularity at corotation and the associated energy absorption,

we first consider the simple case where the corotation singularity is neglected (section 4.1) before examining the general case (section 4.2).

2.4.1 Neglecting Corotation Singularity: Corotation Amplifier

Here we consider the case where the vortensity has zero slope at corotation, i.e., $(d\zeta/dr)_c = 0$. This would occur for disk models where the specific angular momentum $r^2\Omega$ is constant (as in the original Papaloizou & Pringle 1984 analysis), or for shearing sheet approximation (as in Narayan et al. 1987). In this case, there is no corotation singularity and no absorption of wave energy, and we always obtain super-reflection

$$|\mathcal{R}|^2 = 1 + |\mathcal{T}|^2 > 1. \tag{2.47}$$

This is the essence of the corotation amplifier.

To derive the complex $\mathcal{R}$ and $\mathcal{T}$, we assume that the outgoing wave in the $r > r_{\mathrm{OL}}$ region (region III in Fig.2.1) is given by [see eqs. (2.32)-(2.33)]

$$\delta h = \sqrt{S/k}\, \exp\left(i \int_{r_{\mathrm{OL}}}^{r} k\, dr + \frac{\pi}{4} \right), \tag{2.48}$$

where $k^2 \equiv -D/c^2$. The connection formulae (2.32)-(2.33) then give for the evanescent zone (region II in Fig. 1):

$$
\begin{aligned}
\delta h & \simeq \frac{\sqrt{S/k}}{2} \exp\left(- \int_{r}^{r_{\mathrm{OL}}} |k|\, dr \right) + i\sqrt{S/k} \exp\left(\int_{r}^{r_{\mathrm{OL}}} |k|\, dr \right) \\
& = \frac{\sqrt{S/k}}{2} \exp(-\Theta_{\mathrm{II}}) \exp\left(\int_{r_{\mathrm{IL}}}^{r} |k|\, dr \right) + i\sqrt{S/k} \exp(+\Theta_{\mathrm{II}}) \exp\left(- \int_{r_{\mathrm{IL}}}^{r} |k|\, dr \right) \tag{2.49}
\end{aligned}
$$

where

$$\Theta_{\mathrm{II}} = \int_{r_{\mathrm{IL}}}^{r_{\mathrm{OL}}} |k|\, dr = \int_{r_{\mathrm{IL}}}^{r_{\mathrm{OL}}} \frac{\sqrt{|D|}}{c}\, dr. \tag{2.50}$$

21

Using the connection formulae at ILR [eqs. (2.34)-(2.35)], we find that for $r < r_{IL}$ (region I in Fig. 1)

$$\delta h \simeq \frac{\sqrt{S/k}}{2} e^{-\Theta_{II}} \sin\left(\int_r^{r_{IL}} k\,dr + \frac{\pi}{4}\right) + i2\sqrt{S/k}e^{\Theta_{II}} \cos\left(\int_r^{r_{IL}} k\,dr + \frac{\pi}{4}\right). \tag{2.51}$$

Expressing this in terms of traveling waves, and defining $y = \int_{r_{IL}}^r k\,dr - \pi/4$ we have

$$\delta h \simeq i\sqrt{S/k}\left[e^{-iy}\left(e^{+\Theta_{II}} - \frac{1}{4}e^{-\Theta_{II}}\right) + e^{+iy}\left(e^{\Theta_{II}} + \frac{1}{4}e^{-\Theta_{II}}\right)\right]. \tag{2.52}$$

Thus the reflection coefficient is

$$\mathcal{R} = \frac{e^{\Theta_{II}} + \frac{1}{4}e^{-\Theta_{II}}}{e^{\Theta_{II}} - \frac{1}{4}e^{-\Theta_{II}}}. \tag{2.53}$$

Comparing equation (2.52) with equation (2.48), we obtain the transmission co-efficient

$$\mathcal{T} = \frac{-i}{e^{+\Theta_{II}} - \frac{1}{4}e^{-\Theta_{II}}}. \tag{2.54}$$

As expected, $|\mathcal{R}|^2 = 1 + |\mathcal{T}|^2 > 1$.

2.4.2 Including Corotation Singularity

As noted before, for disks with nonzero vortensity gradient ($d\zeta/dr \neq 0$), the singularity at corotation implies the absorption of wave energy (or angular momentum). Similar situations occur in geophysical wave systems (Dickenson 1968) and for waves in plasmas (Landau damping). In Appendix B, we discuss the toy problem of resonant tunneling which shares the similar energy absorption feature as the corotation singularity. Previous works on global modes in disk tori (e.g. Papaloizou & Pringle 1987; Goldreich et al. 1986; Narayan et al. 1987) suggest that the sign of $d\zeta/dr$ determines whether the singularity acts

22

to stabilize or destabilize a global mode. Here we derive the explicit expression for the reflectivity and the related source term $\mathcal{D}_c$.

As in section 4.1, we assume an outgoing wave in Region III, and the connection formulae at the OLR then give for Region IIb of Fig. 2.2 or Fig. 2.3

$$\delta h \simeq \frac{\sqrt{S/k}}{2} \exp(-\Theta_{\mathrm{IIb}}) \exp\left(\int_{r_c}^{r} |k|\, dr\right) + i\,\sqrt{S/k}\exp(+\Theta_{\mathrm{IIb}}) \exp\left(-\int_{r_c}^{r} |k|\, dr\right), \quad (2.55)$$

where

$$\Theta_{\mathrm{IIb}} = \int_{r_c}^{r_{\mathrm{OL}}} |k|\, dr. \quad (2.56)$$

Equation (2.55) is the asymptotic solution away from the r_c in region IIb. The corresponding general solution around r_c is

$$\delta h = \frac{\sqrt{S/k}}{2}\exp(-\Theta_{\mathrm{IIb}})\psi_+(r) + i\,\sqrt{S/k}\exp(\Theta_{\mathrm{IIb}})\psi_-(r), \quad (2.57)$$

where ψ_+ and ψ_- are given by (2.41). Using equations (2.42) and (2.43) to match asymptotes over the corotation singularity, we obtain in Region IIa

$$\delta h \quad \simeq \quad \left[\frac{1}{2}\exp(-\Theta_{\mathrm{IIb}})(1 + \frac{1}{4}T_0 T_1) + \frac{i}{2}T_1\exp(+\Theta_{\mathrm{IIb}})\right]\sqrt{S/k}\,e^{-i\pi\nu}\exp\left(-\int_{r}^{r_c} |k|\, dr\right)$$

$$+i\left[\exp(+\Theta_{\mathrm{IIb}}) - \frac{i}{4}T_0\exp(-\Theta_{\mathrm{IIb}})\right]\sqrt{S/k}\,e^{i\pi\nu}\exp\left(\int_{r}^{r_c} |k|\, dr\right). \quad (2.58)$$

Using the connection formulae at the ILR, we have for Region I:

$$
\begin{aligned}
\delta h \quad &\simeq \quad \left[\frac{1}{2}\exp(-\Theta_{\mathrm{II}})\left(1\frac{1}{4}T_0T_1\right)+\frac{i}{2}T_1\exp(\Theta_{\mathrm{IIb}}-\Theta_{\mathrm{IIa}})\right]\sqrt{S/k}\,e^{-i\pi\nu}\sin\left(\int_r^{r_{\mathrm{IL}}}k\,dr+\frac{\pi}{4}\right) \\
&\quad +2i\left[\exp(+\Theta_{\mathrm{II}})-\frac{i}{4}T_0\exp(\Theta_{\mathrm{IIa}}-\Theta_{\mathrm{IIb}})\right]\sqrt{S/k}\,e^{i\pi\nu}\cos\left(\int_r^{r_{\mathrm{IL}}}k\,dr+\frac{\pi}{4}\right) \\
&= \quad \left[1+\frac{1}{4}e^{-i2\pi\nu}e^{-2\Theta_{\mathrm{II}}}\left(1+\frac{1}{4}T_0T_1\right)\right. \\
&\qquad\qquad \left.+\frac{i}{4}T_1\,e^{-i2\pi\nu}e^{-2\Theta_{\mathrm{IIa}}}-\frac{i}{4}T_0e^{-2\Theta_{\mathrm{IIb}}}\right]i\,\sqrt{S/k}\,e^{\Theta_{\mathrm{II}}}e^{i\pi\nu}e^{iy} \\
&\quad +\left[1-\frac{1}{4}e^{-i2\pi\nu}e^{-2\Theta_{\mathrm{II}}}\left(1+\frac{1}{4}T_0T_1\right)\right. \\
&\qquad\qquad \left.-\frac{i}{4}T_1e^{-i2\pi\nu}e^{-2\Theta_{\mathrm{IIa}}}-\frac{i}{4}T_0e^{-2\Theta_{\mathrm{IIb}}}\right]i\,\sqrt{S/k}\,e^{\Theta_{\mathrm{II}}}e^{i\pi\nu}e^{-iy},
\end{aligned}
\tag{2.59}
$$

where $y=\int_{r_{\mathrm{IL}}}^{r}k\,dr-\pi/4$ and

$$
\Theta_{\mathrm{IIa}}=\int_{r_{\mathrm{IL}}}^{r_c}|k|\,dr,\qquad \Theta_{\mathrm{II}}=\Theta_{\mathrm{IIa}}+\Theta_{\mathrm{IIb}}=\int_{r_{\mathrm{IL}}}^{r_{\mathrm{OL}}}|k|\,dr.
\tag{2.60}
$$

The reflection coefficient and transmission coefficient are then

$$
\begin{aligned}
\mathcal{R} &= \frac{1+\frac{1}{4}e^{-i2\pi\nu}e^{-2\Theta_{\mathrm{II}}}\left(1+\frac{1}{4}T_0T_1\right)+\frac{i}{4}T_1e^{-i2\pi\nu}e^{-2\Theta_{\mathrm{IIa}}}-\frac{i}{4}T_0e^{-2\Theta_{\mathrm{IIb}}}}{1-\frac{1}{4}e^{-i2\pi\nu}e^{-2\Theta_{\mathrm{II}}}\left(1+\frac{1}{4}T_0T_1\right)-\frac{i}{4}T_1e^{-i2\pi\nu}e^{-2\Theta_{\mathrm{IIa}}}-\frac{i}{4}T_0e^{-2\Theta_{\mathrm{IIb}}}}, \\
&= \frac{1+\frac{1}{4}\left(e^{-i2\pi\nu}+\sin^2\pi\nu\right)e^{-2\Theta_{\mathrm{II}}}+\frac{\pi\nu}{2}\frac{e^{-2\Theta_{\mathrm{IIa}}}}{(\Gamma(1-\nu))^2}-\frac{\pi\nu}{2}\frac{e^{-2\Theta_{\mathrm{IIb}}}}{(\Gamma(1+\nu))^2}}{1-\frac{1}{4}\left(e^{-i2\pi\nu}+\sin^2\pi\nu\right)e^{-2\Theta_{\mathrm{II}}}-\frac{\pi\nu}{2}\frac{e^{-2\Theta_{\mathrm{IIa}}}}{(\Gamma(1-\nu))^2}-\frac{\pi\nu}{2}\frac{e^{-2\Theta_{\mathrm{IIb}}}}{(\Gamma(1+\nu))^2}}
\end{aligned}
\tag{2.61}
$$

$$
\begin{aligned}
\mathcal{T} &= \frac{-i\,e^{-\Theta_{\mathrm{II}}}e^{i\pi\nu}}{1-\frac{1}{4}e^{-i2\pi\nu}e^{-2\Theta_{\mathrm{II}}}\left(1+\frac{1}{4}T_0T_1\right)-\frac{i}{4}T_1e^{-i2\pi\nu}e^{-2\Theta_{\mathrm{IIa}}}-\frac{i}{4}T_0e^{-2\Theta_{\mathrm{IIb}}}} \\
&= \frac{-ie^{-\Theta_{\mathrm{II}}}e^{i\pi\nu}}{1-\frac{1}{4}\left(e^{-i2\pi\nu}+\sin^2\pi\nu\right)e^{-2\Theta_{\mathrm{II}}}-\frac{\pi\nu}{2}\frac{e^{-2\Theta_{\mathrm{IIa}}}}{(\Gamma(1-\nu))^2}-\frac{\pi\nu}{2}\frac{e^{-2\Theta_{\mathrm{IIb}}}}{(\Gamma(1+\nu))^2}}
\end{aligned}
\tag{2.62}
$$

The dissipation term due to the corotation singularity obtained from $\mathcal{D}_c=|\mathcal{R}|^2-1-|\mathcal{T}|^2$ is

$$
\mathcal{D}_c = \frac{\frac{\pi\nu}{2}\frac{\cos^2\pi\nu}{(\Gamma(1+\nu))^2}e^{-2\Theta_{\mathrm{II}}-2\Theta_{\mathrm{IIb}}}+\frac{2\pi\nu}{(\Gamma(1-\nu))^2}e^{-2\Theta_{\mathrm{IIa}}}}{|1-\frac{1}{4}\left(e^{-i2\pi\nu}+\sin^2\pi\nu\right)e^{-2\Theta_{\mathrm{II}}}-\frac{\pi\nu}{2}\frac{e^{-2\Theta_{\mathrm{IIa}}}}{(\Gamma(1-\nu))^2}-\frac{\pi\nu}{2}\frac{e^{-2\Theta_{\mathrm{IIb}}}}{(\Gamma(1+\nu))^2}|^2}.
\tag{2.63}
$$

For $|v| \ll 1$ equations (2.61) and (2.62) can be simplified, and we have

$$\mathcal{R} \to \frac{e^{\Theta_{\mathrm{II}}} + \frac{1}{4}e^{-\Theta_{\mathrm{II}}}}{e^{\Theta_{\mathrm{II}}} - \frac{1}{4}e^{-\Theta_{\mathrm{II}}}} + \frac{e^{+2\Theta_{\mathrm{IIb}}} - \frac{1}{4}e^{-2\Theta_{\mathrm{IIb}}}}{\left(e^{\Theta_{\mathrm{II}}} - \frac{1}{4}e^{-\Theta_{\mathrm{II}}}\right)^2}\pi v + O[v^2], \tag{2.64}$$

$$\mathcal{T} \to \frac{-i}{e^{\Theta_{\mathrm{II}}} - \frac{1}{4}e^{-\Theta_{\mathrm{II}}}} - \frac{i}{2}\frac{e^{\Theta_{\mathrm{IIb}}-\Theta_{\mathrm{IIa}}} - e^{\Theta_{\mathrm{IIa}}-\Theta_{\mathrm{IIb}}}}{\left(e^{\Theta_{\mathrm{II}}} - \frac{1}{4}e^{-\Theta_{\mathrm{II}}}\right)^2}\pi v + O[v^2], \tag{2.65}$$

$$\mathcal{D}_c \to \frac{2\left(e^{\Theta_{\mathrm{II}}} + \frac{1}{4}e^{-\Theta_{\mathrm{II}}}\right)\left(e^{2\Theta_{\mathrm{IIb}}} - \frac{1}{4}e^{-2\Theta_{\mathrm{IIb}}}\right) + \left(e^{\Theta_{\mathrm{IIb}}-\Theta_{\mathrm{IIa}}} - e^{\Theta_{\mathrm{IIa}}-\Theta_{\mathrm{IIb}}}\right)}{\left(e^{\Theta_{\mathrm{II}}} - \frac{1}{4}e^{-\Theta_{\mathrm{II}}}\right)^3}\pi v + O[v^2].\tag{2.66}$$

Clearly, for $v = 0$, equations (2.64)-(2.65) reduce to (2.53) and (2.54).

2.5 Wave Damping at Corotation: Alternative Calculation

In the previous section we obtained the expression for the dissipation term $\mathcal{D}_c$ at the corotation resonance using the reflection and transmission coefficients. Here we provide a more direct derivation of $\mathcal{D}_c$ using the change of angular momentum flux across the corotation radius.

In the absence of self-gravity, the angular momentum flux carried by the the waves in the disk is entirely due to advection. The time-averaged transfer rate of the z-component of angular momentum across a cylinder of radius r (in the outward direction) is given by (e.g. Goldreich & Tremaine 1979)

$$F(r) = r^2 \Sigma(r) \int_0^{2\pi} d\phi \, \mathrm{Re}[\delta u_r(r, \phi, t)]\mathrm{Re}[\delta u_\phi(r, \phi, t)]. \tag{2.67}$$

Using equations (2.9)-(2.10) to express δu_r and δu_ϕ in terms of δh, this reduces to (see Tanaka et al. 2002; Zhang & Lai 2006)

$$F(r) = \frac{\pi m r \Sigma}{D}\mathrm{Im}\left(\delta h \frac{d\delta h^*}{dr}\right). \tag{2.68}$$

In Region III (see Figs. 1-3) the outgoing wave has the enthalpy perturbation given by (up to a proportional constant)

$$\delta h = \sqrt{S/k}\, \mathcal{T} \exp\left[i \int_{r_{\mathrm{OL}}}^{r} k\, dr + \frac{\pi}{4}\right]$$

(2.69)

Calculating the angular momentum flux (setting the incoming wave flux to 1),

$$F(r \gg r_{\mathrm{OL}}) \simeq \pi m |\mathcal{T}|^2,$$

(2.70)

we see that angular momentum is transferred outwards (positive flux) since waves in $r > r_{\mathrm{OL}}$ carries positive angular momentum. For Region I we have [up to the same proportional constant as in (2.69)]

$$\delta h = \sqrt{S/k}\left[\exp\left(-i \int_{r_{\mathrm{IL}}}^{r} k\, dr + \frac{\pi}{4}\right) + \mathcal{R} \exp\left(i \int_{r_{\mathrm{IL}}}^{r} k\, dr - \frac{\pi}{4}\right)\right],$$

(2.71)

which gives the angular momentum flux:

$$F(r \ll r_{\mathrm{IL}}) \simeq \pi m (|\mathcal{R}|^2 - 1).$$

(2.72)

We see that the incident wave carries negative angular momentum outward, and the reflected wave transfers positive angular momentum. The net angular momentum transfer is positive (in the outward direction) for $|\mathcal{R}| > 1$.

Now consider the angular flux near the corotation radius, at $r = r_c^-$ (just inside corotation) and at $r = r_c^+$ (just outside corotation). Integrating equation (2.36) across the singularity, we find the discontinuity in the enthalpy perturbation derivatives:

$$\left.\frac{d\,\delta h}{dr}\right|_{r_c^+} - \left.\frac{d\,\delta h}{dr}\right|_{r_c^-} = \frac{2\pi i}{q}\left(\frac{d}{dr}\ln \zeta\right)\delta h\bigg|_{r_c} = 2\pi \nu i \frac{\kappa}{c}\delta h\bigg|_{r_c}.$$

(2.73)

Here we have chosen to integrate from r_c^- to r_c^+ by going through the upper complex plane, to be consistent with the physical requirement of a gradually

26

growing perturbation, turned on at $t = -\infty$. Thus the change in the angular momentum flux across the corotation is

$$\Delta F_c = F(r_c^+) - F(r_c^-) = -\frac{2\pi^2 mr\Sigma\nu\kappa}{cD}|\delta h|^2\bigg|_{r_c}. \tag{2.74}$$

The wavefunction around r_c is given by equation (2.57) multiplied by $\mathcal{T}$. Noting that

$$\psi_-(r_c) = W_{\nu,1/2}(0) = \frac{1}{\Gamma(1-\nu)}, \tag{2.75}$$

$$\psi_+(r_c) = e^{-i\pi\nu}W_{-\nu,1/2}(0) + \frac{1}{2}T_0 W_{\nu,1/2}(0) = \frac{\cos\pi\nu}{\Gamma(1+\nu)}, \tag{2.76}$$

where we have used the convenient identity $\Gamma(\nu)\Gamma(1-\nu) = \pi/\sin\pi\nu$. We can evaluate the enthalpy perturbation at the corotation, giving

$$\delta h(r_c) = \sqrt{S/k}\,\mathcal{T}\left[\frac{1}{2}e^{-\Theta_{\mathrm{IIb}}}\frac{\cos\pi\nu}{\Gamma(1+\nu)} + ie^{\Theta_{\mathrm{IIb}}}\frac{1}{\Gamma(1-\nu)}\right]. \tag{2.77}$$

The change in angular momentum flux across the corotation is then

$$\Delta F_c = -\pi m|\mathcal{T}|^2\nu\left[\frac{\pi}{2}\frac{\cos^2\pi\nu}{(\Gamma(1+\nu))^2}e^{-2\Theta_{\mathrm{IIb}}} + \frac{2\pi}{(\Gamma(1-\nu))^2}e^{2\Theta_{\mathrm{IIb}}}\right]. \tag{2.78}$$

With $F(r \ll r_{\mathrm{IL}}) = F(r_c^-)$, $F(r \gg r_{\mathrm{OL}}) = F(r_c^+)$, and thus $F(r \ll r_{\mathrm{IL}}) = F(r \gg r_{\mathrm{OL}}) - \Delta F_c$, we find

$$\mathcal{D}_c = |\mathcal{T}|^2\nu\left[\frac{\pi}{2}\frac{\cos^2\pi\nu}{(\Gamma(1+\nu))^2}e^{-2\Theta_{\mathrm{IIb}}} + \frac{2\pi}{(\Gamma(1-\nu))^2}e^{2\Theta_{\mathrm{IIb}}}\right]. \tag{2.79}$$

This expression exactly agrees with $\mathcal{D}_c$ given in section 4.2.

2.6   Results and Discussion

The key new results of this chapter consist of the analytical expressions for the reflection coefficient $\mathcal{R}$, transmission coefficient $\mathcal{T}$ and the dissipation term $\mathcal{D}_c$

when a wave impinges upon the corotation barrier from small radii. These expressions, (2.61)-(2.66) and (2.79), can be applied to disks with generic rotation and surface density profiles.

For definiteness, here we illustrate our results using a (Newtonian) Keplerian disk model with

$$\Omega = \kappa \propto r^{-3/2}, \quad \Sigma \propto r^{-p}, \quad \frac{c}{r\Omega} = \beta, \tag{2.80}$$

where p and β are constants. The important parameter that determines the behavior of the corotation singularity is [see eq. (2.40)]

$$\nu = \left(\frac{2c}{3\kappa} \frac{d}{dr} \ln \zeta \right)_c = \frac{2}{3}\beta \left(p - \frac{3}{2} \right). \tag{2.81}$$

Clearly the models are scale-free, and $\mathcal{R}$, $\mathcal{T}$ and $\mathcal{D}_c$ depend only on the two parameters p and β (or ν). Figure 4 depicts $|\mathcal{R}|$ as a function of β for different values of p, while Figure 5 shows $|\mathcal{R}|$, $\mathcal{D}_c$ and $|\mathcal{T}|$ as a function of ν for $\beta = 0.05$ and $\beta = 0.1$.

A key result of chapter is that wave absorption at the corotation resonance plays an important role in determining the reflection and transmission of waves across the corotation barrier. Without corotation resonance (as for disks with zero vortensity gradient, or $\nu = 0$), super-reflection is always achieved, but $|\mathcal{R}|^2 - 1 \simeq \exp(-2\Theta_{\mathrm{II}})$ (assuming $\Theta_{\mathrm{II}} \gg 1$, where $\Theta_{\mathrm{II}} = \Theta_{\mathrm{IIa}} + \Theta_{\mathrm{IIb}} = \int_{r_{\mathrm{IL}}}^{r_{\mathrm{OL}}} |k| \, dr$, with $|k| = |D|^{1/2}/c$) is rather small. In the presence of wave absorption at the corotation resonance (when $\nu \neq 0$), we find (assuming $\Theta_{\mathrm{IIa}} \gg 1$ and $|\nu| \ll 1$),

$$|\mathcal{R}|^2 - 1 \simeq \exp(-2\Theta_{\mathrm{II}}) + 2\pi\nu \exp(-2\Theta_{\mathrm{IIa}}), \tag{2.82}$$

and super-reflection can be much more prominent. From Fig. 5 we see that the transmission coefficient is generally much smaller than $\mathcal{D}_c$. Thus the reflectivity depends mainly on the wave damping at corotation.
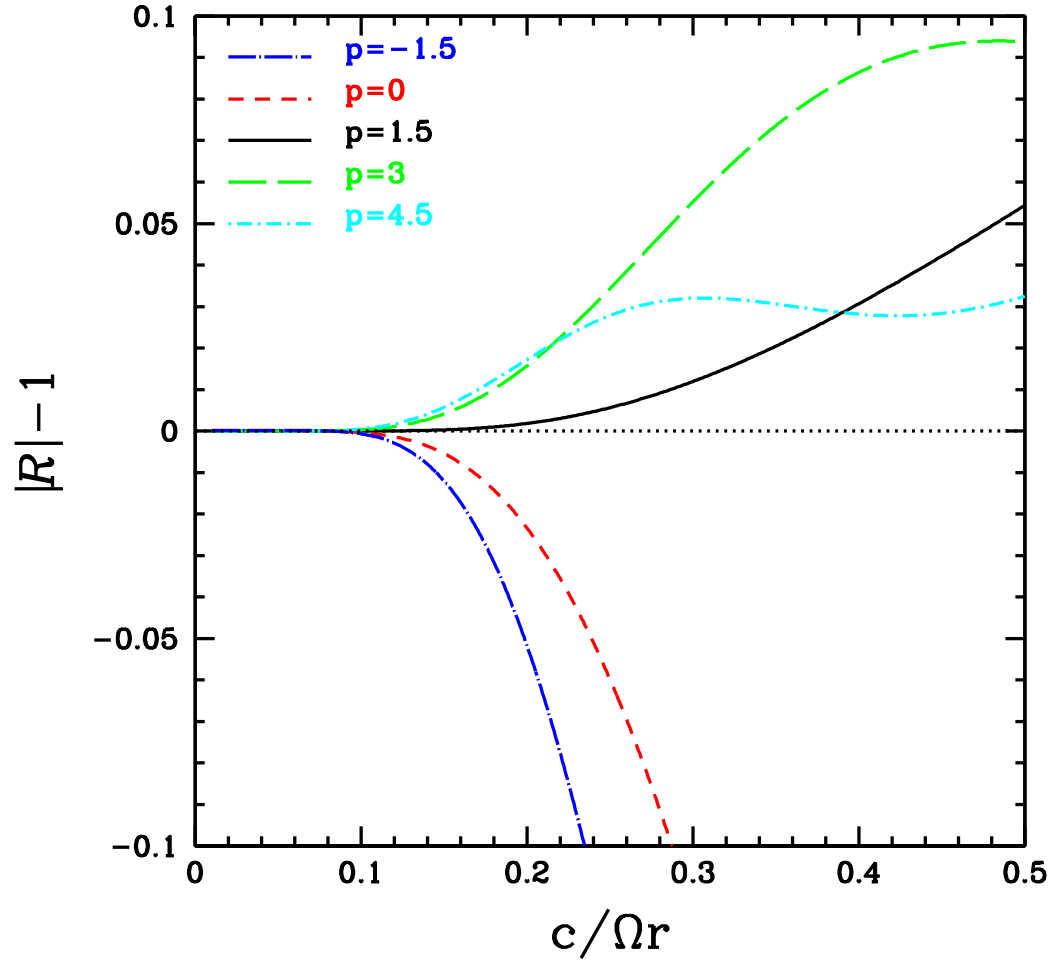
Figure 2.4: The reflection coefficient as a function of $\beta = c/(r\Omega)$ for Keplerian disks with surface density profile $\Sigma \propto r^{-p}$. Note that for $p = 1.5$, wave absorption at the corotation resonance is absent.
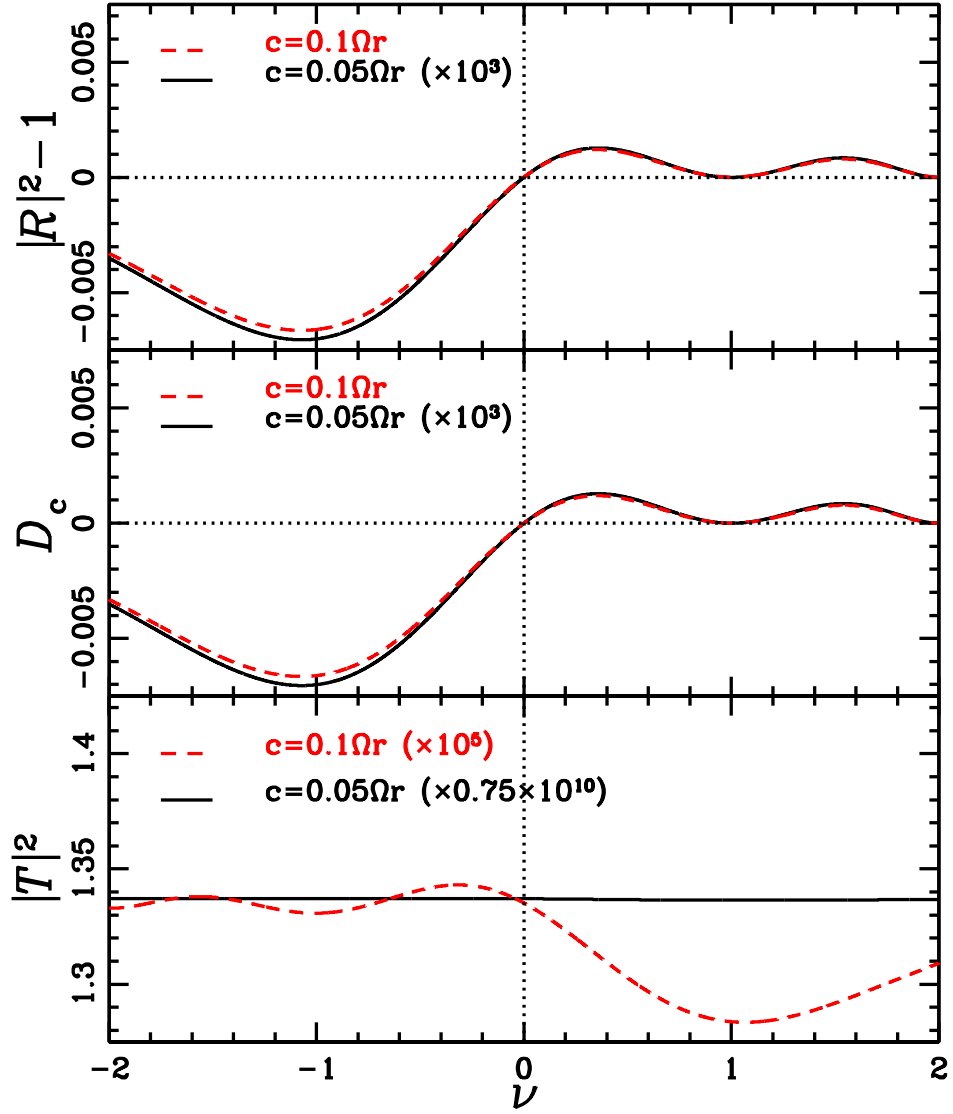
Figure 2.5: The reflection coefficient, wave damping coefficient and transmission coefficient as a function of ν for two different values of $\beta = c/(r\Omega)$. Note that for $\nu = 0$ (no corotation resonance), wave damping is zero ($\mathcal{D}_c = 0$) and $|\mathcal{R}|^2 - 1$ is positive.

Equation (2.79) or (2.66) clearly shows that for $v > 0$, the wave damping term due to corotation resonance is positive, $\mathcal{D}_c > 0$. This can be understood from the fact that for $v > 0$ the Rossby wave region lies outside r_c (see Fig. 2.3), and the dissipation at the corotation singularity carries away positive energy (just like the transmitted wave) so that energy conservation [see eq. (2.46)] requires $-1 = -|\mathcal{R}|^2 + |\mathcal{T}|^2 + |\mathcal{D}_c|$. In this case the corotation singularity enhances super-reflection, as seen in Figs. 4-5. On the other hand, for $v < 0$, the Rossby wave zone lies inside r_c (Fig. 2.2) and the dissipation carries away negative energy (like the reflected wave) so that $-1 = -|\mathcal{R}|^2 + |\mathcal{T}|^2 - |\mathcal{D}_c|$. In this case the corotation singularity tends to reduce super-reflection, and there is a competition between the effect of the corotation amplifier [the first term in eq. (2.64)] and the effect of the corotational absorption [the second term]. To obtain $|\mathcal{R}| > 1$ we require

$$v > -\frac{1}{2\pi} \frac{1 - \frac{1}{4}e^{-2\Theta_{\mathrm{II}}}}{e^{2\Theta_{\mathrm{IIb}}} - \frac{1}{4}e^{-2\Theta_{\mathrm{IIb}}}} \simeq -\frac{1}{2\pi}e^{-2\Theta_{\mathrm{IIb}}}, \tag{2.83}$$

where the second inequality applies in the limit of $\Theta_{\mathrm{IIb}} \gg 1$. This puts a constraint on the disk thickness and the specific vorticity slope (note that the sound speed c enters into both v and Θ_{IIb}) in order to achieve super-reflection. For example, for a given c, the inequality (2.83) determines the critical value of p for which $|\mathcal{R}| = 1$.

Figures 4-5 also reveal an intriguing oscillatory behavior of the reflection, transmission and damping coefficients. This non-monotonic behavior may be qualitatively understood from the Rossby wave zone around r_c (see Figs. 2-3). The WKB wavenumber k_r in the near vicinity of r_c is given by

$$k_r^2 \simeq -\frac{\kappa^2}{c^2} + \frac{2m\Omega}{r\tilde{\omega}}\frac{d}{dr}\ln\zeta = \frac{\kappa^2}{c^2}\left(-1 + \frac{2\beta vr}{r - r_c}\right). \tag{2.84}$$

For $v > 0$, the Rossby wave zone lies between r_c and $r_c + \Delta r_R$, where $\Delta r_R = 2\beta vr_c$. For quasi-normal modes to be "trapped in" the Rossby wave zone they must

obey the the Sommerfeld "quantization" condition[6] $\int_{r_c}^{r_c+\Delta r_R} dr \, k_r = \pi \nu \sim n\pi + \pi/2$, where $n = 0, 1, 2, \cdots$. Thus when $\nu \simeq n+1/2$, the wave propagating in the Rossby zone (Fig. 3) is maximally reflected back to the singularity, leading to maximum negative damping and enhanced net reflection, as seen in Fig. 2.5. For $\nu < 0$ the Rossby wave zone lies between $r_c - |\Delta r_R|$ and r_c (Fig. 2), the wave in the Rossby zone is mostly absorbed at the corotation singularity. The asymmetry in the $\nu > 0$ case and the $\nu < 0$ case can also be seen in the toy problem of resonant tunneling (Appendix B). Note that for thin Keplerian disks, $|\nu|$ is much less than unity for reasonable density profiles ($|p| \sim 1$), so this non-monotonic behavior is of no practical interest.

2.6.1 Numerical Calculation of Reflectivity and Improved WKB Treatment

Our analytical expressions derived in section 4-5 are based on global WKB analysis and involves several approximations. In particular, in our treatment of the corotation resonance (section 3.2), we assumed $c \ll r\Omega$ — if this is not satisfied, some of the neglected terms must be included in equation (2.36) and the numerical values of our solution may be modified. Thus our results for $\beta \gtrsim 0.1 - 0.2$ should be treated with caution.

To assess the validity of our WKB analysis, we also carry out computation of the reflectivity by numerical integration of equations (8)-(10). The outgoing wave boundary condition, equation (2.48), is imposed at some radius $r_{\text{out}} \gg r_{\text{OL}}$,

---

[6]The phase factor $\pi/2$ arises from a detailed analysis of the wave behavior at $r = r_c$ and at $r = r_c + \Delta r_R$: The former gives a phase of $-3\pi/4$ and the latter gives $\pi/4$.
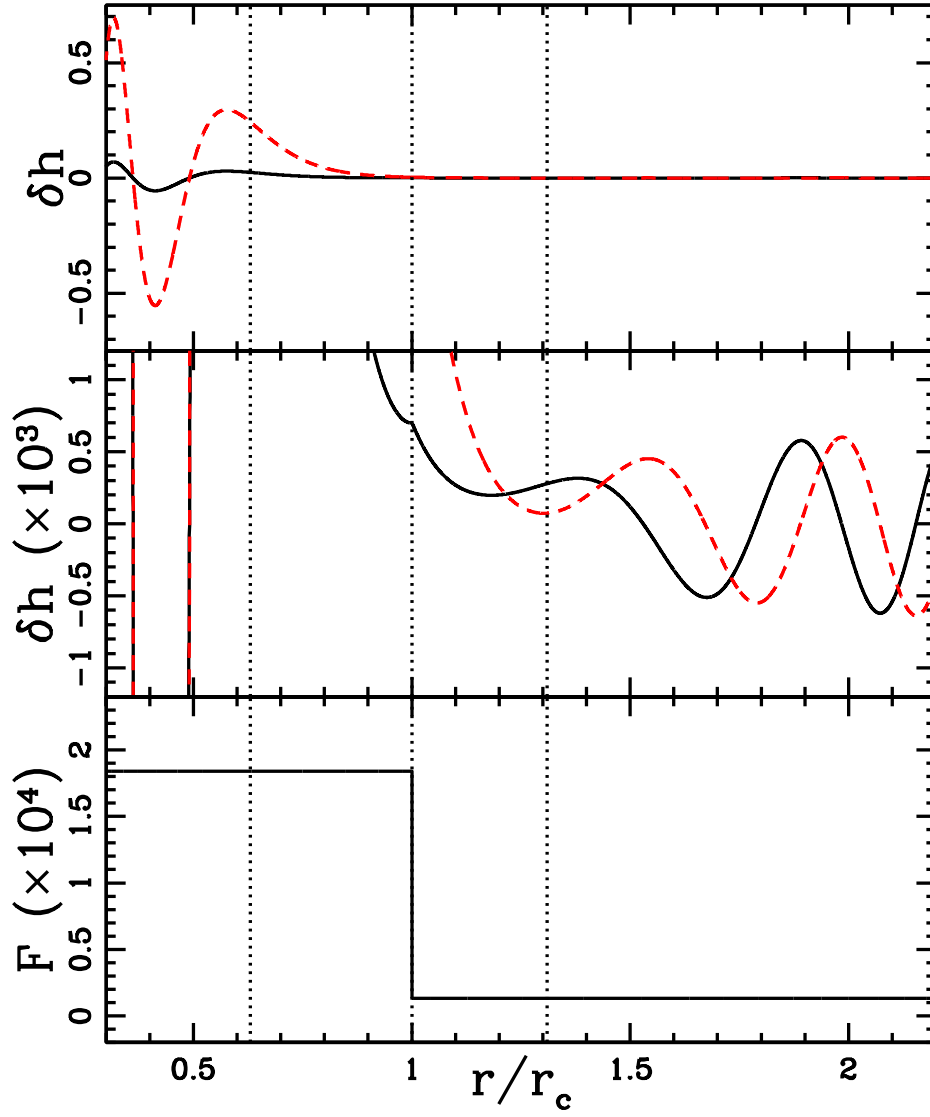
Figure 2.6: Numerical calculation of wave reflection and transmission across corotation for a Keplerian disk with $\nu = 0.033$ and $\beta = 0.1$. The top and middle panel show the enthalpy perturbation δh, with the solid lines depicting the real components and the dashed lines the imaginary components. Note that there is a discontinuity in the derivative of δh at the corotation resonance, resulting in an absorption of flux at the corotation. The bottom panel shows the angular momentum flux carried by the wave [see eq. (67)]. Note that $F(r)$ is conserved away from corotation and the discontinuity in F at $r = r_c$ results from wave absorption. The Lindblad and corotation resonances are indicated by three vertical dotted lines.

such that

$$\delta h' = \left(ik + \frac{S'}{2S} - \frac{k'}{2k} \right) \delta h, \tag{2.85}$$

where ' specifies derivatives with respect to r. At some inner radius $r_{\mathrm{in}} \ll r_{\mathrm{IL}}$, the solution takes the form of equation (71). The reflection coefficient can be obtained from

$$|\mathcal{R}| = \left| \frac{\left[\left(\frac{S'}{2S} - \frac{k'}{2k} \right) - ik \right] \delta h - \delta h'}{\left[\left(\frac{S'}{2S} - \frac{k'}{2k} \right) + ik \right] \delta h - \delta h'} \right|_{r_{\mathrm{in}}} \tag{2.86}$$

while the transmission is

$$|\mathcal{T}| = \left| \frac{2k}{\left[\left(\frac{S'}{2S} - \frac{k'}{2k} \right) + ik \right] \delta h - \delta h'} \right|_{r_{\mathrm{in}}} |\delta h|_{r_{\mathrm{out}}} . \tag{2.87}$$

Because of the singularity at corotation, we include a small positive $\omega_i = \mathrm{Im}(\omega)$ for the frequency so that singularity can be avoided. Figure 2.6 depicts an example calculation for a Keplerian disk with $\beta = 0.1$ and $p = 2$ (so that $\nu = 0.033$).

Figure 2.7 shows our numerical result compared with the calculation from the WKB analysis. There is qualitative agreement between these results. In particular, both the numerical and WKB results show that wave absorption at corotation plays the dominant role in determining $|\mathcal{R}|$, and wave transmission is unimportant even for small (but nonzero) ν.

However, the WKB solution matches the numerical result closely only for $|\nu| \ll 1$, indicating that our WKB analysis can be improved. For the Keplerian disk considered here, the variation in ν was achieved by changing the background density index p. The WKB results shown in Figs. 2.5-2.6 assume that the quantities Θ_{IIa} and Θ_{IIb} are not effected by changing ν. However p plays a non-negligible role in determining the effective wave number away from the corotation and Lindblad resonances. Indeed, in obtaining equation (2.22) or (2.36) from (2.15), we have neglected several terms that are negligible near r_c or
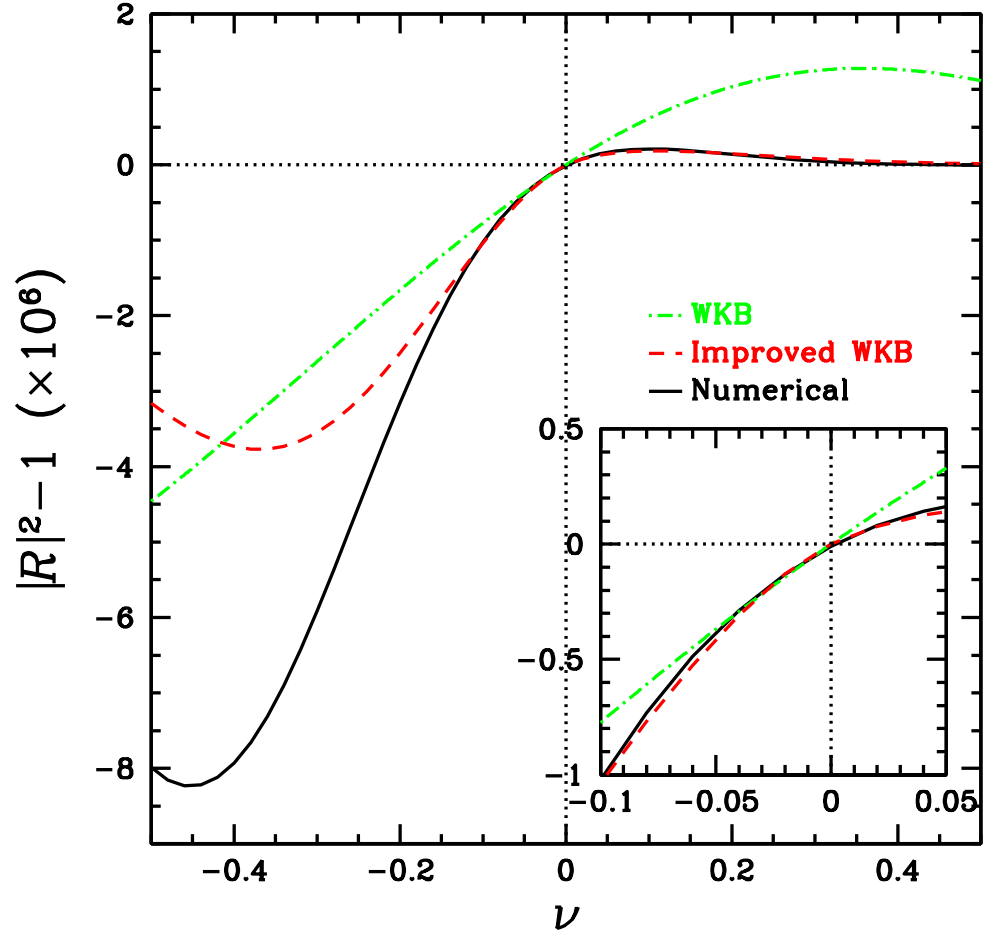
Figure 2.7: The reflection coefficient as a function of ν calculated using the WKB, improved WKB, and numerical methods for a scale free Keplerian disk with sound speed $c = 0.05\Omega r$.

$r_{\text{IL/OL}}$, but nevertheless important away from these resonances. Noting that our connection formulae [equations (32)-(35) and (42)-(43) involve the asymptotic expansions of local solutions around the resonances, we can improve our WKB results by adopting the following ansatz: we modify the integrands in Θ_{IIa} and Θ_{IIb} to include these dropped terms,

$$\Theta = \int \sqrt{-k_{\text{eff}}^2} \, dr, \tag{2.88}$$

$$k_{\text{eff}}^2 = -\frac{D}{c^2} - \frac{m^2}{r^2} - \frac{p^2 - 1}{4r^2} - D^{1/2}\left(\frac{d}{dr}D^{-1/2}\right)\frac{1-p}{2}. \tag{2.89}$$

Note that in the expression above, we have left out the singular term ($\propto \tilde{\omega}^{-1}$) at corotation and the dominant double singular term ($\propto D^{-2}$) at the Linblad resonances since they have already been accounted for by the connection formulae in sections 3. As shown in Fig. 2.6, the improved WKB result matches the numerical solution for a much larger range of ν. The increased values of Θ_{IIa} and Θ_{IIb} for larger $|p|$ act to suppress super-reflection, and drive reflection coefficient toward $|\mathcal{R}| = 1$.

2.7 Global Overstable Modes

As mentioned in Section 1, global disk instabilities are often related to the super-reflection at the corotation barrier. To illustrate this, we consider a simple boundary condition

$$\delta h(r_{\text{in}}) = 0 \tag{2.90}$$

at the inner radius of the disk, $r_{\text{in}} \ll r_{\text{IL}}$. The outgoing boundary condition at $r > r_{\text{OL}}$ implies that the solution in the region $r < r_{\text{IL}}$ is given by

$$\delta h = \sqrt{S/k} \exp\left(-i \int_{r_{\text{IL}}}^{r} k \, dr + \pi/4\right) + \mathcal{R} \sqrt{S/k} \exp\left(i \int_{r_{\text{IL}}}^{r} k \, dr - \pi/4\right). \tag{2.91}$$

Letting $\mathcal{R} = |\mathcal{R}|e^{i\varphi}$, and applying the boundary condition (2.91) yields the eigenvalue condition:

$$\tan\left(\int_{r_{\text{in}}}^{r_{\text{IL}}} k\,dr - \pi/4 - \varphi/2\right) = -i\left(\frac{|\mathcal{R}| - 1}{|\mathcal{R}| + 1}\right). \tag{2.92}$$

Noting that for complex eigenvalue $\omega = \omega_r + i\omega_i$, the wavenumber k is also complex

$$k = k_r + ik_i = \frac{1}{c}\sqrt{(\tilde{\omega}_r + i\tilde{\omega}_i)^2 - \kappa^2} \simeq \frac{1}{c}\sqrt{\tilde{\omega}_r^2 - \kappa^2} + i\frac{\omega_i\tilde{\omega}_r}{c\sqrt{\tilde{\omega}_r^2 - \kappa^2}}, \tag{2.93}$$

where we have assumed $|\omega_i| \ll |\omega_r|$. $\tilde{\omega}_r = \omega_r - m\Omega$ (< 0 for region I) and thus the real part of the eigenvalue condition gives

$$\int_{r_{\text{in}}}^{r_{\text{IL}}} \frac{1}{c}\sqrt{(\omega_r - m\Omega)^2 - \kappa^2}\,dr - \pi/4 - \varphi/2 = n\pi, \tag{2.94}$$

where n is an integer. The imaginary part of (2.92) gives (assuming $|k_i| \ll |k_r|$)

$$\int_{r_{\text{in}}}^{r_{\text{IL}}} k_i\,dr \simeq -\left(\frac{|\mathcal{R}| - 1}{|\mathcal{R}| + 1}\right), \tag{2.95}$$

from which we find the growth rate

$$\omega_i = \left(\frac{|\mathcal{R}| - 1}{|\mathcal{R}| + 1}\right)\left[\int_{r_{\text{in}}}^{r_{\text{IL}}} |\tilde{\omega}_r|/c\sqrt{\tilde{\omega}_r^2 - \kappa^2}\,dr\right]^{-1}. \tag{2.96}$$

Thus the modes are overstable ($\omega_i > 0$) for $|\mathcal{R}| > 1$, and stable ($\omega_i < 0$) for $|\mathcal{R}| < 1$.

2.8   Conclusion

In this chapter we have derived explicit expressions for the reflection coefficient, transmission coefficient and wave absorption coefficient when a wave is scattered by the corotation barrier in a disk. These expressions include both

the effects of corotation amplifier (which exists regardless of the gradient of the vortensity $\zeta = \kappa^2/\Omega\Sigma$ of the background flow) and wave absorption at the corotation (which depends on $d\zeta/dr$). They demonstrate clearly that the corotation wave absorption plays a dominant role in determining the reflectivity and that the sign of $d\zeta/dr$ determines whether the corotation singularity enhances or diminishes the super-reflectivity. Our result can be understood in terms of the location of the Rossby wave zone relative to the corotation radius. We also carried out numerical calculations of the reflectivity. Our result provides the conditions (in terms of disk thickness, rotation profile and surface density profile) for which super-reflection is achieved and global overstable modes in disks are possible.

In future works we will explore global oscillation modes and their stabilities in a variety of astrophysical contexts, ranging from accreting white dwarfs to accreting black hole systems. The possible overstabilities of these modes are directly linked to the effects studied in this chapter and may provide explanations for some of the quasi-periodic variabilities observed in these systems.

CHAPTER 3

COROTATIONAL INSTABILITY OF INERTIAL-ACOUSTIC MODES IN BLACK HOLE ACCRETION DISKS AND QUASI PERIODIC OSCILLATIONS

3.1 Introduction

3.1.1 Models of Quasi-Periodic X-Ray Oscillations: A Brief Review

Rapid X-ray variabilities from Galactic compact binary systems have been studied for decades (e.g. van del Klis 2006). In recent years, our knowledge of quasi-periodic oscillations (QPOs) in black-hole X-ray binaries has greatly improved (see Remillard & McClintock 2006 for a review), thanks in large part to NASA's *Rossi X-ray Timing Explorer* (Swank 1999). The low-frequency QPOs (about 0.1-50 Hz) are common, observable when the systems are in the hard state and the steep power-law state (also called "very high state"; see Done, Gierlinski & Kubota 2007), and they typically have high amplitudes and high coherence ($Q > 10$), and can vary in frequency on short timescales (minutes). However, it is the weaker, transient High-Frequency QPOs (HFQPOs, 40–450 Hz) that have attracted more attention, since their frequencies do not vary significantly in response to sizable (factors of 3-4) luminosity changes and are comparable to the orbital frequencies at the Innermost Stable Circular Orbit (ISCO) of black holes with mass $M \sim 10M_\odot$. As such, HFQPOs potentially provide a probe to study the effects of strong gravity. HFQPOs are usually observed in the very high

state of the X-ray binaries, and have low amplitudes (0.5 – 2% rms at 2-60 keV) and low coherence ($Q \sim 2 - 10$). Out of the seven black-hole binaries from which HFQPOs have been reported, four show pairs of QPOs (first discovered in GRO J1655-40; Strohmayer 2001) with frequency ratios close to 2 : 3 (300 and 450 Hz in GRO J1655-40, 184 and 276 Hz in XTE J1550-564, 113 and 168 Hz in GRS 1915+105, 165 and 240 Hz in H1743-322; note that GRS 1915+105 also has a second pair of QPOs with f = 41 and 67 Hz).

It is worth noting that QPO (with period of $\sim$ 1 hour) in X-ray emission has recently been detected in the active galaxy RE J1034+396 (Gierlinski et al. 2008). This could be the "supermassive" analog of the HFQPOs detected in black-hole X-ray binaries.

Despite the observational progress, the origin of the HFQPOs remain unclear. A number of possibilities/models have been suggested or studied to various degrees of sophistication. We comment on some of these below:

– Stella, Vietri & Morsink (1999) and others (see Schnittman & Bertschinger 2004, Schnittman 2005) suggested that orbiting hot spots (blobs) in the disk oscillating with epicyclic frequencies may provide variability in the X-ray emission. However the radial positions of such blobs are free parameters, which must be tuned to match the observed QPO frequencies, and it is also not clear that the blobs can survive the differential rotation of the disk.

– Abramowicz & Kluzniak (2001) suggested that HFQPOs involve certain nonlinear resonant phenomenon in the disk (e.g., coupling between the radial and vertical epicyclic oscillations of the disk fluid element; Kluzniak & Abramowicz 2002). This was motivated by the observed stability of the QPO

frequencies and the commensurate frequency ratio. However, so far analysis has been done based only on toy models involving coupled harmonic oscillators (e.g. Rebusco 2004; Horak & Karas 2006) and no fluid dynamical model producing these resonances has been developed (see Abramowicz et al 2007 and Rebusco 2008 for recent reviews). Petri (2008) considered the resonant oscillation of a test mass in the presence of a spiral density wave, but the origin of the wave is unclear.

– Acoustic oscillation modes in pressure-supported accretion tori have been suggested as a possible source of the observed QPOs (Rezzolla et al. 2003; Lee, Abramowicz & Kluziniak 2004; see also Blaes, Arras & Fragile 2006; Schnittman & Rezzolla 2006, Blaes et al 2007, Sramkova et al 2007). In this model, the commensurate mode frequencies arise from matching the radial wavelength to the size of the torus. Note that the QPO frequencies are determined mainly by the radial boundaries of the torus, which must be tuned to match the observed QPO frequencies. It is also not clear that the accretion flow in the very high state (in which HFQPOs are observed) is well represented by such a torus (e.g. Done et al 2007).

– Li & Narayan (2004) considered the dynamics of the interface between the accretion disk and the magnetosphere of a central compact object (see also Lovelace & Romanova 2007). The interface is generally Rayleigh-Tayor unstable and may also be Kelvin-Helmholtz unstable. While such an interface is clearly relevant to accreting magnetic neutron stars, Li & Narayan suggested that it may also be relevant to accreting black holes and that the strongly unstable interface modes may give rise to QPOs with commensurate frequencies.

– Perhaps the theoretically most appealing is the relativistic diskoseismic

oscillation model, according to which general relativistic (GR) effects produce trapped oscillation modes in the inner region of the disk (Kato & Fukue 1980; Okazaki et al. 1987; Nowak & Wagoner 1991; see Wagoner 1999; Kato 2001 for reviews; see also Tassev & Bertschinger 2007 for the kinematic description of some of these wave modes). A large majority of previous studies have focused on disk g-modes (also called inertial modes or inertial-gravity modes, whose wavefunctions – such as the pressure perturbation, contain nodes in the vertical direction), because the trapping of the g-mode does not require a reflective inner/outer disk boundary. Kato (2003a) and Li, Goodman & Narayan (2003) showed that the g-mode that contains a corotation resonance (where the wave patten frequency equals the rotation rate of the background flow) in the wave zone is heavily damped. Thus the only nonaxisymmetric ($m \neq 0$) g-modes of interest are those trapped around the maximum of $\Omega + \kappa/m$ (where Ω is the rotational frequency, κ is the radial epicyclic frequency and m is the azimuthal mode number; see Fig. 1 below). Unfortunately, the frequencies of such modes, $\omega \simeq m\Omega_{\rm ISCO}$, are too high (by a factor of 2-3) compared to the observed values, given the measured mass and the estimated spin parameter of the black hole (Silbergleit & Wagoner 2007; see also Tassev & Bertschinger 2007). Axisymmetric g-modes ($m = 0$) may still be viable in the respect, and recent studies showed that they can be resonantly excited by global disk deformations through nonlinear effects (Kato 2003a,2008; Ferreira & Ogilvie 2008). Numerical simulations (Arras, Blaes & Turner 2006; Reynolds & Miller 2008), however, indicated that while axisymmetric g-mode oscillations are present in the hydrodynamic disk with no magnetic field, they disappear in the magnetic disk where MHD turbulence develops. Also, Fu & Lai (2008) carried out an analytic study of the effect of magnetic fields on diskoseismic modes and showed that even a weak (sub-

thermal) magnetic field can "destroy" the self-trapping zone of disk g-modes, and this may (at least partly) explain the disappearance of the g-modes in the MHD simulations.

– Tagger and collaborators (Tagger & Pellat 1999; Varniere & Tagger 2002; Tagger & Varniere 2006; see Tagger 2006 for a review) developed the theory of accretion-ejection instability for disks threaded by strong (of order or stronger than equipartition), large-scale poloidal magnetic fields. They showed that such magnetic field provides a strong coupling between spiral density waves and Rossby waves at the corotation, leading to the growth of the waves and energy ejection to disk corona. Tagger & Varniere (2006) suggested that normal modes trapped in the inner region of the disk become strongly unstable by a combination of accretion-ejection instability and an MHD form of the Rossby wave instability (see Lovelace et al. 1999; Li et al. 2000; see section 6 below). The Tagger model has the appealing feature that the instability leads to energy ejection into the disk corona, and thus explains why HFQPOs manifest mainly as the variations of the nonthermal (power-law) radiation from the systems.

3.1.2 Chapter Summary

In this chapter we study the global corotational instability of nonaxisymmetric p-modes (also called inertial-acoustic modes) trapped in the inner-most region of the accretion disk around a black hole. The p-modes do not have vertical structure (i.e., the wavefunctions have no node in the vertical direction). We focus on these modes because their basic wave properties (e.g. propagation diagram) are not affected qualitatively by disk magnetic fields (Fu & Lai 2008)

and they are probably robust under hydromagnetic effects and disk turbulence (see Reynolds & Miller 2008).

The corotational instability of p-modes studied in this chapter relies on the well-known GR effect of test-mass orbit around a black hole: Near the black hole, the radial epicyclic frequency κ reaches a maximum (at $r = 8GM/c^2$ for a Schwarzschild black hole) and goes to zero at the ISCO ($r_{\mathrm{ISCO}} = 6GM/c^2$). This causes non-monotonic behavior in the fluid vortensity, $\zeta = \kappa^2/(2\Sigma\Omega)$ (assuming the surface density Σ is relatively smooth), such that $d\zeta/dr > 0$ for $r < r_{\mathrm{peak}}$ (where r_{peak} is the radius where ζ peaks) and $d\zeta/dr < 0$ for $r > r_{\mathrm{peak}}$. The vortensity gradient $d\zeta/dr$ plays an important role in wave absorption at the corotation resonance (Tsang & Lai 2008a; see also Goldreich & Tremaine 1979 for corotational wave absorption due to external forcing). We show that the p-modes with frequencies such that the corotation radii lie inside the vortensity peak can grow in amplitude due to absorption at the corotation resonance, and that the overstability can be achieved for several modes with frequencies closely commensurate with the azimuthal wavenumber m. Tagger & Varniere (2006) have studied similar modes in disks threaded by strong magnetic fields, but in our analysis magnetic fields play no role.

The trapping of the p-modes requires the existence of a (partially) reflecting boundary at the disk inner edge, close to the ISCO. One may suspect that the rapid radial inflow at the ISCO will diminish any potential instabilities in the inner accretion disk (see Blaes 1987 for the case of thick accreting tori). Our analysis of the wave perturbations in the transonic accretion flow (see section 5) suggests that waves are partially reflected at the sonic point, and global overstable p-modes may still be produced under certain conditions (e.g., when the

surface density of the flow varies on sufficiently small length scale around the sonic point). Even better mode trapping (and therefore larger mode growth) may be achieved when the system is an accretion state such that the inner disk edge does not behave as a zero-torque boundary (see section 7 for discussion and references).

This chapter is organized as follows. After summarizing the basic fluid equations for our problem in section 2, we give a physical discussion of the origin of the corotational instability of disk p-modes in section 3. We present in section 4 our calculations of the growing p-modes with simple reflective inner disk boundary conditions. Section 5 contains our analysis of the effect of the transonic radial inflow at the ISCO on the p-mode growth rate. In section 6, we discuss the role of the Rossby wave instability and show that it is not effective in typical accretion disks under consideration. In section 7 we discuss the application of our results to HFQPOs in black hole X-ray binaries.

3.2   Setup and Basic equations

We consider a geometrically thin disk and adopt cylindrical coordinate system (r, ϕ, z). The flow is assumed to be barotropic, so that the vertically integrated pressure, $P = \int p \, dz$, depends only on the surface density, $\Sigma = \int \rho \, dz$. We use the pseudo-Newtonian potential of Paczynski & Wiita (1980)

$$\Phi = -\frac{GM}{r - r_S},\tag{3.1}$$

with $r_S = 2GM/c^2$ the Schwarzschild radius. The free-particle (Keplerian) orbital and radial epicyclic (angular) frequencies are

$$\Omega_K = \left(\frac{1}{r}\frac{d\Phi}{dr}\right)^{1/2} = \sqrt{\frac{GM}{r}}\frac{1}{r - r_S} \ , \qquad \kappa = \left[\frac{2\Omega_K}{r}\frac{d}{dr}(r^2\Omega_K)\right]^{1/2} = \Omega_K\sqrt{\frac{r - 3r_S}{r - r_S}}. \quad (3.2)$$

The function κ peaks at $r = (2 + \sqrt{3})r_S$ and declines to zero at $r_{\mathrm{ISCO}} = 3r_S$ (while for a Schwarzschild black hole in GR, κ peaks at $r = 4r_S$). The unperturbed flow has velocity $\mathbf{u}_0 = (u_r, r\Omega, 0)$. Since pressure is negligible for thin disks, we have $\Omega \simeq \Omega_K$.

Neglecting the self-gravity of the disk we have the linear perturbation equations:

$$\frac{\partial}{\partial t}\delta\Sigma + \nabla \cdot (\Sigma\,\delta\mathbf{u} + \mathbf{u}_0\,\delta\Sigma) = 0, \quad (3.3)$$

$$\frac{\partial}{\partial t}\delta\mathbf{u} + (\mathbf{u}_0 \cdot \nabla)\delta\mathbf{u} + (\delta\mathbf{u} \cdot \nabla)\mathbf{u}_0 = -\nabla\delta h, \quad (3.4)$$

where $\delta\Sigma$, $\delta\mathbf{u}$ and $\delta h = \delta P/\Sigma$ are the (Eulerian) perturbations of surface density, velocity and enthalpy, respectively. For barotropic flow, δh and $\delta\Sigma$ are related by

$$\delta h = c_s^2\frac{\delta\Sigma}{\Sigma}, \quad (3.5)$$

where c_s is the sound speed, with $c_s^2 = dP/d\Sigma$. We assume all perturbed quantities to be of the form $e^{im\phi - i\omega t}$, where m is a positive integer, and ω is the wave (angular) frequency. The perturbation equations then become

$$-i\tilde{\omega}\frac{\Sigma}{c_s^2}\delta h + \frac{1}{r}\frac{\partial}{\partial r}(\Sigma r\delta u_r) + \frac{im}{r}\Sigma\delta u_\phi + \frac{1}{r}\frac{\partial}{\partial r}(ru_r\delta\Sigma) = 0, \quad (3.6)$$

$$-i\tilde{\omega}\delta u_r - 2\Omega\delta u_\phi + \frac{\partial}{\partial r}(u_r\delta u_r) = -\frac{\partial}{\partial r}\delta h, \quad (3.7)$$

$$-i\tilde{\omega}\delta u_\phi + \frac{\kappa^2}{2\Omega}\delta u_r + \frac{u_r}{r}\frac{\partial}{\partial r}(r\delta u_\phi) = -\frac{im}{r}\delta h, \quad (3.8)$$

where

$$\tilde{\omega} = \omega - m\Omega, \quad (3.9)$$

46

is the wave frequency in the frame corotating with the unperturbed fluid.

Except very near the inner edge of the disk, $r_{\rm in} \simeq r_{\rm ISCO}$, the unperturbed radial velocity is small, $|u_r| \ll r\Omega$. In our calculations of the disk modes, we will neglect u_r and set the last terms on the left-hand sides of equations (3.6)-(3.8) to zero (However, u_r plays an important role in determining the inner boundary condition of the fluid perturbations at $r_{\rm in}$; see section 5). Eliminating the velocity perturbations in favor of the enthalpy, we obtain our master equation

$$\left[\frac{d^2}{dr^2} - \frac{d}{dr}\left(\ln \frac{D}{r\Sigma}\right)\frac{d}{dr} - \frac{2m\Omega}{r\tilde{\omega}}\left(\frac{d}{dr} \ln \frac{\Omega\Sigma}{D}\right) - \frac{m^2}{r^2} - \frac{D}{c_s^2} \right]\delta h = 0, \qquad (3.10)$$

where

$$D = \kappa^2 - \tilde{\omega}^2. \qquad (3.11)$$

For concreteness we assume the surface density to have a the power-law form

$$\Sigma \propto r^{-p}, \qquad (3.12)$$

where p is the density index.

The above equations adequately describe disk p-modes (also called inertial-acoustic modes), which do not have vertical structure. Other disk modes (g-modes and c-modes) involve the vertical degree of freedom [see Kato 2001 for a review; also see Fig. 1 of Fu & Lai (2008) for a quick summary], and their stability properties are studied by Kato (2003a), Li et al. (2003) and Tsang & Lai (2008b).

To determine the global modes of the disk, appropriate boundary conditions must be specified. These are discussed in sections 4 and 5.

3.3 P-modes and Their Growth Due to Corotation Resonance: A Physical Discussion

A WKB analysis of the wave equation (3.10) yields the dispersion relation for the local plane wave $\delta h \propto \exp\left[i \int^r k(s)ds\right]$:

$$k^2 + \frac{D}{c_s^2} + \frac{2m\Omega}{r\tilde{\omega}}\left(\frac{d}{dr}\ln\frac{\Omega\Sigma}{D}\right) \simeq 0. \tag{3.13}$$

Far from the singularity ($\tilde{\omega} = 0$) at the corotation radius r_c, this reduces to the well-known dispersion relation of spiral density wave with no self-gravity (e.g., Shu 1992), $k^2 \simeq -D/c_s^2$, or

$$\tilde{\omega}^2 = \kappa^2 + k^2 c_s^2 . \tag{3.14}$$

Density waves (p-modes) can propagate inside the inner Lindblad resonance radius r_{IL} (defined by $\tilde{\omega} = -\kappa$), and outside the outer Lindblad resonance radius r_{OL} (defined by $\tilde{\omega} = \kappa$), i.e., in the region where $\omega/m < \Omega - \kappa/m$ and $\omega/m > \Omega + \kappa/m$, respectively (see Fig. 1). Between r_{IL} and r_{OL}, waves are evanescent except that a very narrow Rossby wave zone exists around the corotation radius. Indeed, in the vicinity of $\tilde{\omega} = 0$, equation (3.13) reduces to

$$\tilde{\omega} \simeq \frac{2m\Omega}{r(k^2 + \kappa^2/c_s^2)}\left(\frac{d\ln\zeta}{dr}\right)_{r_c}, \tag{3.15}$$

where

$$\zeta = \frac{\kappa^2}{2\Omega\Sigma} \tag{3.16}$$

is the vortensity of the (unperturbed) flow. For $(d\zeta/dr)_{r_c} > 0$, the Rossby wave zone lies between r_c and $r_c + \Delta r_R$, where $\Delta r_R = (2c_s/\kappa)|\nu|$ and $\int_{r_c}^{r_c+\Delta r_R} k\, dr = \pi\nu$, with the number of wavelengths in the Rossby zone given by (Tsang & Lai 2008a)

$$\nu = \left(\frac{c_s}{q\kappa}\frac{d\ln\zeta}{dr}\right)_{r_c} = \frac{c_s}{q\kappa}\left[\frac{d}{dr}\ln\left(\frac{\kappa^2}{\Omega}\right) + \frac{p}{r}\right]_{r_c}, \tag{3.17}$$

where $q \equiv -(d\ln\Omega/d\ln r)_{r_c}$, and the second equality assumes $\Sigma \propto r^{-p}$. For $(d\zeta/dr)_{r_c} < 0$, the Rossby wave zone lies inside r_c, between $r_c - |\Delta r_R|$ and r_c (see Fig. 1). Note that since $\nu \sim c_s/(\kappa r) \sim H/r \ll 1$, no standing Rossby wave can exist in the Rossby zone (see also section 6).

Assuming that there exists a reflecting boundary at the inner disk radius $r_{\rm in} \simeq r_{\rm ISCO}$ (see sections 4.3 and 5), normal modes can be produced, with the waves partially trapped between $r_{\rm in}$ and $r_{\rm IL}$ – these are the p-modes that we will focus on in this chapter. The mode eigen-frequency $\omega = \omega_r + i\omega_i$ is generally complex, with the real part ω_r determined approximately by the Sommerfeld "quantization" condition

$$\int_{r_{\rm in}}^{r_{\rm IL}} \frac{1}{c_s} \sqrt{\tilde{\omega}_r^2 - \kappa^2}\, dr = n\pi + \varphi, \tag{3.18}$$

where $\tilde{\omega}_r = \omega_r - m\Omega$, n is an integer and φ (of order unity) is a phase factor depending on the details of the (inner and outer) boundary conditions. The overstability of the p-mode is directly related to the reflectivity of the corotation barrier between $r_{\rm IL}$ and $r_{\rm OL}$. In the WKB approximation, the imaginary part of the mode frequency is given by (Tsang & Lai 2008a; see also Narayan et al. 1987, who considered shearing-sheet model)

$$\omega_i = \left(\frac{|\mathcal{R}| - 1}{|\mathcal{R}| + 1}\right) \left(\int_{r_{\rm in}}^{r_{\rm IL}} \frac{|\tilde{\omega}_r|}{c_s \sqrt{\tilde{\omega}_r^2 - \kappa^2}}\, dr\right)^{-1}, \tag{3.19}$$

where $\mathcal{R}$ is the reflectivity (see below). Thus the mode becomes overstable ($\omega_i > 0$) for $|\mathcal{R}| > 1$ (termed "super-reflection") and stable ($\omega_i < 0$) for $|\mathcal{R}| < 1$.

Super-reflection in fluid disks arises because the waves inside the corotation radius and those outside carry energy or angular momentum of different signs: Since the wave inside r_c has pattern speed ω_r/m less than the fluid rotation rate
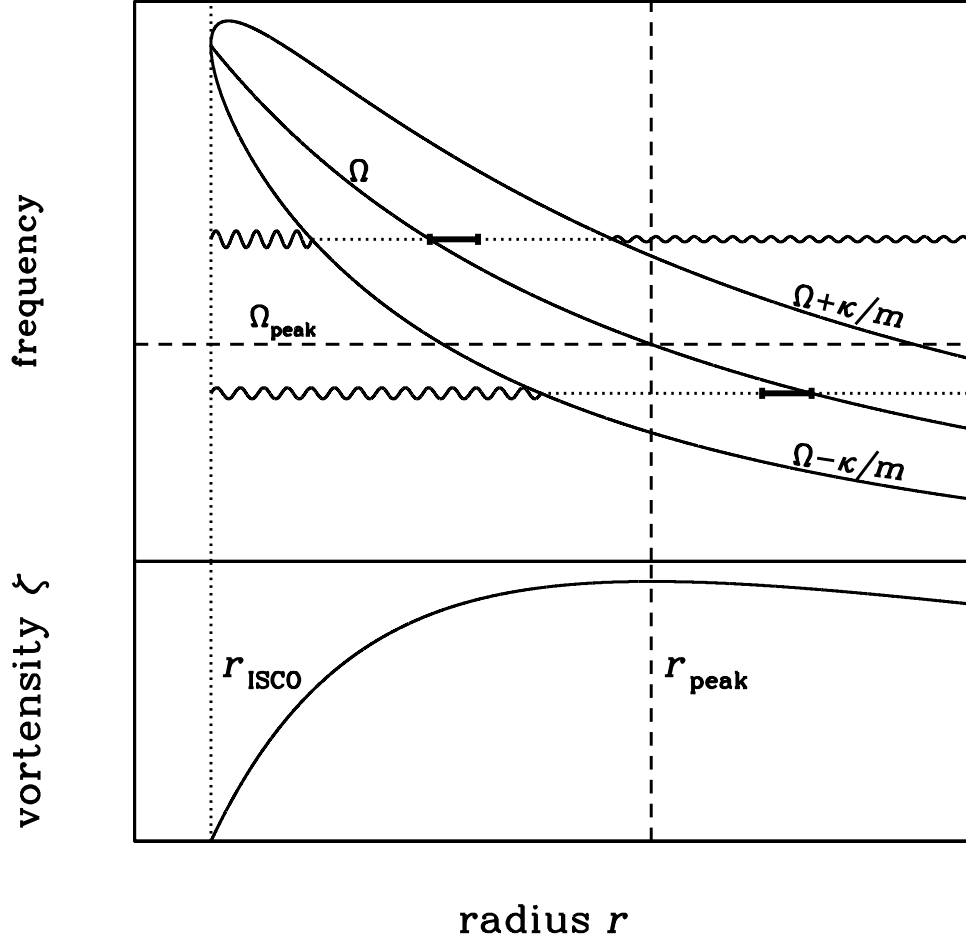
Figure 3.1: Wave propagation diagram for non-axisymmetric p-modes in thin accretion disks around black holes. In the upper panel, the three solid curves depict the disk rotation profile $\Omega(r)$ and $\Omega \pm \kappa/m$ (where κ is the radial epicyclic frequency); note that the three curves join each other at the disk inner radius $r_{\text{in}} = r_{\text{ISCO}}$ (the inner-most circular orbit) since $\kappa(r_{\text{ISCO}}) = 0$. The wavy lines (of height ω/m) indicate the propagation zones for inertial-acoustic waves. Disc p-modes are trapped between r_{in} and the inner Lindblad resonance radius (where $\omega/m = \Omega - \kappa/m$), but can tunnel through the corotation barrier. The lower panel depicts the disk vortensity profile, $\zeta = \kappa^2/(2\Omega\Sigma)$, which has a maximum at the radius r_{peak} (as long as the surface density Σ does not vary too strongly with r). P-modes with $\omega/m > \Omega_{\text{peak}} = \Omega(r_{\text{peak}})$ (the upper wavy line) are overstable due to wave absorption at the corotation resonance radius r_c (where $\omega/m = \Omega$) since $(d\zeta/dr)_{r_c} > 0$. P-modes with $\omega/m < \Omega_{\text{peak}}$ (the lower wavy line) tend to be damped by wave absorption at r_c since $(d\zeta/dr)_{r_c} < 0$. Note that a narrow Rossby wave zone (labeled by thick horizontal bars) exists just outside or inside the corotation radius — the location of this Rossby zone determines the sign of the corotational wave absorption.

$\Omega(r)$, it carries negative energy; outside r_c, we have $\omega_r/m > \Omega(r)$, the wave carries positive energy. Consider an incident wave $\delta h \propto \exp(-i \int^r k \, dr)$, carrying energy of the amount (-1), propagating from small radii toward the corotation barrier [1]. The wave reflected at r_{IL} takes the form $\delta h \propto \mathcal{R} \exp(i \int^r k \, dr)$, and the transmitted wave in the region $r > r_{\mathrm{OL}}$ is $\delta h \propto \mathcal{T} \exp(i \int^r k \, dr)$. Because of the corotation singularity, the wave energy can also be transferred to the background flow and dissipated at the corotation radius. Energy conservation then gives $-1 = (-1)|\mathcal{R}|^2 + |\mathcal{T}|^2 + \mathcal{D}_c$, or

$$|\mathcal{R}|^2 = 1 + |\mathcal{T}|^2 + \mathcal{D}_c, \qquad (3.20)$$

where $\mathcal{D}_c$ is the wave energy dissipated at the corotation.

Tsang & Lai (2008a) derived the analytical expressions (in the WKB approximation) for $\mathcal{T}$, $\mathcal{R}$ and $\mathcal{D}_c$. Two effects determine the reflectivity. (i) The transmitted wave (corresponding to the $|\mathcal{T}|^2$ term) always carries away positive energy and thus increases $|\mathcal{R}|^2$. (ii) Wave absorption at the corotation can have both signs, depending on ν: For $\nu > 0$, the Rossby wave zone lies outside r_c, positive wave energy is dissipated and we have $\mathcal{D}_c > 0$; for $\nu < 0$, the Rossby zone lies inside r_c and we have $\mathcal{D}_c < 0$ (see Fig. 1). Tsang & Lai (2008a) showed explicitly that under most conditions, $|\mathcal{D}_c| \gg |\mathcal{T}|^2$ (except when $\nu \simeq 0$, for which $\mathcal{D}_c \simeq 0$). In the limit of $|\nu| \ll 1$, we have

$$|\mathcal{T}|^2 \simeq \exp(-2\Theta_{\mathrm{II}}), \qquad \mathcal{D}_c \simeq 2\pi\nu \exp(-2\Theta_{\mathrm{IIa}}), \qquad (3.21)$$

where

$$\Theta_{\mathrm{II}} \equiv \int_{r_{\mathrm{IL}}}^{r_{\mathrm{OL}}} \frac{\sqrt{\kappa^2 - \tilde{\omega}_r^2}}{c_s}, \qquad \Theta_{\mathrm{IIa}} \equiv \int_{r_{\mathrm{IL}}}^{r_c} \frac{\sqrt{\kappa^2 - \tilde{\omega}_r^2}}{c_s} \qquad (3.22)$$

[these expressions are valid for $\Theta_{\mathrm{II}}, \Theta_{\mathrm{IIa}} \gg 1$; see Tsang & Lai (2008a) for more general expressions]. Thus super-reflectivity ($|\mathcal{R}|^2 > 1$) and growing modes ($\omega_i >$

---

[1] Note that since the group velocity of the wave has opposite sign as the phase velocity for $r < r_{\mathrm{IL}}$, the wave of the form $\exp(-i \int^r k \, dr)$ (with $k > 0$) is outward propagating.

0) are achieved when

$$\nu > \nu_{\text{crit}} = -\frac{1}{2\pi} \exp(-2\Theta_{\text{IIb}}), \qquad \text{with} \quad \Theta_{\text{IIb}} = \Theta_{\text{II}} - \Theta_{\text{IIa}} = \int_{r_c}^{r_{\text{OL}}} \frac{\sqrt{\kappa^2 - \tilde{\omega}_r^2}}{c_s}. \qquad (3.23)$$

Note that typically $|\nu_{\text{crit}}| \ll 1$; if $|\mathcal{T}|^2$ is neglected compared to $\mathcal{D}_c$, then $\nu_{\text{crit}} = 0$.

As mentioned before, since κ is non-monotonic near the black hole, the vortensity ζ is also non-monotonic, attaining a peak value at $r = r_{\text{peak}}$ before dropping to zero at the ISCO. Therefore, p-modes with frequencies such that the corotation radius r_c lies inside r_{peak} are expected to be overstable by the corotational instability discussed above. In other words, when $\omega_r/m > \Omega_{\text{peak}} \equiv \Omega(r_{\text{peak}})$, the corotation resonance acts to grow the mode. Note that Ω_{peak} depends on the surface density profile as well as the spacetime curvature around the black hole (see Fig. 2). On the other hand, when $\omega_r/m < \Omega_{\text{peak}}$ ($\nu < 0$), the corotational wave absorption acts to damp the mode. However, when ω_r/m is only slightly smaller than Ω_{peak} ($\nu_{\text{crit}} < \nu < 0$) mode growth can still be obtained due to wave leakage beyond the outer Lindblad resonance, though the growth rate will be small (see section 4.4 for examples).

3.4   Calculations of Trapped, Overstable P-modes

To determine the eigenvalues ω_r and ω_i of the trapped modes, we solve equations (3.6)-(3.8) (with $u_r = 0$) or equation (3.10) subjected to appropriate boundary conditions at r_{in} and r_{out}.
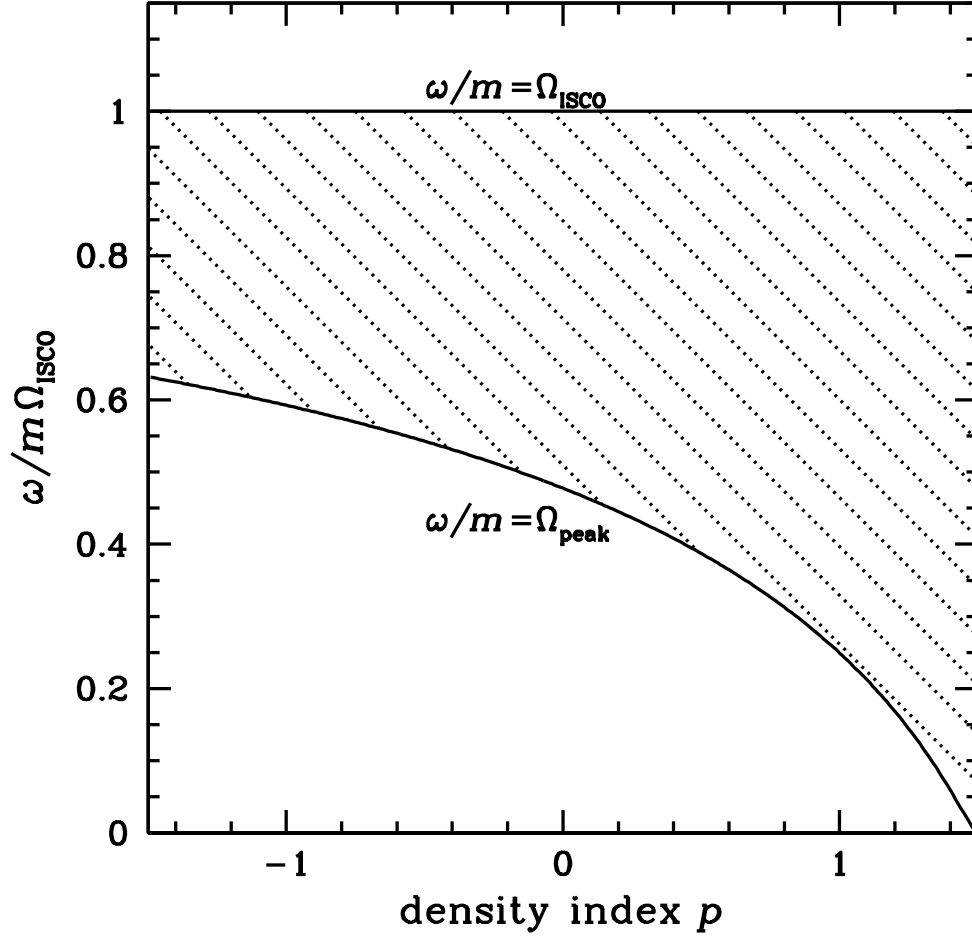
Figure 3.2: Critical mode frequency for corotational instability as a function of the disk surface density index p (with $\Sigma \propto r^{-p}$). Wave absorption at the corotation resonance acts to grow the mode only if the corotation occurs in the region of positive vortensity gradient, i.e., if the mode pattern frequency $\omega/m > \Omega_{\rm peak}$ (see Fig. 1). P-mode trapping also requires $\omega/m < \Omega_{\rm ISCO} = \Omega(r_{\rm ISCO})$. Note that weak mode growth can still occur when ω/m is slightly below $\Omega_{\rm peak}$ due to wave leakage beyond the outer Lindblad resonance radius. See text for detail.

3.4.1 "Landau" Integration Contour

When solving eigenvalue problem using the standard method (e.g. the shooting method as described in Press et al 1998), we encountered a conundrum: For $v > 0$, we could find both a growing mode and a decaying mode, with almost the same ω_r but opposite ω_i. This appears to contradict our discussion in section 3. This conundrum arises because our numerical integration is confined to the real r axis. However, analogous to Landau's analysis of wave damping in a plasma (e.g., Lifshitz & Pitaevskii 1981), care must be taken in defining appropriate contour of integration across the corotation resonance. Indeed, at corotation, equation (3.10) contains a singular term, proportional to

$$\frac{1}{\tilde{\omega}} \propto \frac{1}{r - R_c}, \tag{3.24}$$

where $R_c \equiv r_c - ir_c\omega_i/(q\omega_r)$ is the complex pole, r_c is determined by $\omega_r = m\Omega(r_c)$ and $q = -(d\ln\Omega/d\ln r)_c > 0$.

As discussed in Lin (1955) in the context of hydrodynamical shear flows, to obtain physically relevant solutions of the fluid system, it is necessary that the integration contour lies above the pole. This is the Landau contour. In essence, only by adopting such a Landau contour can one obtain the correct wave absorption (dissipation) at the corotation. For growing modes ($\omega_i > 0$), $\text{Im}(R_c) < 0$, our numerical integration along the real r axis constitutes the correct Landau contour. On the other hand, for decaying modes ($\omega_i < 0$), the real r axis is not the correct Landau contour as $\text{Im}(R_c) > 0$. Instead, to obtain physical solutions for these decaying modes, the integration contour must be deformed so that R_c lies below it (see Fig. 3). As we are primarily interested in over-stable modes in this chapter, it is adequate to integrate along the real r axis in our calculation.
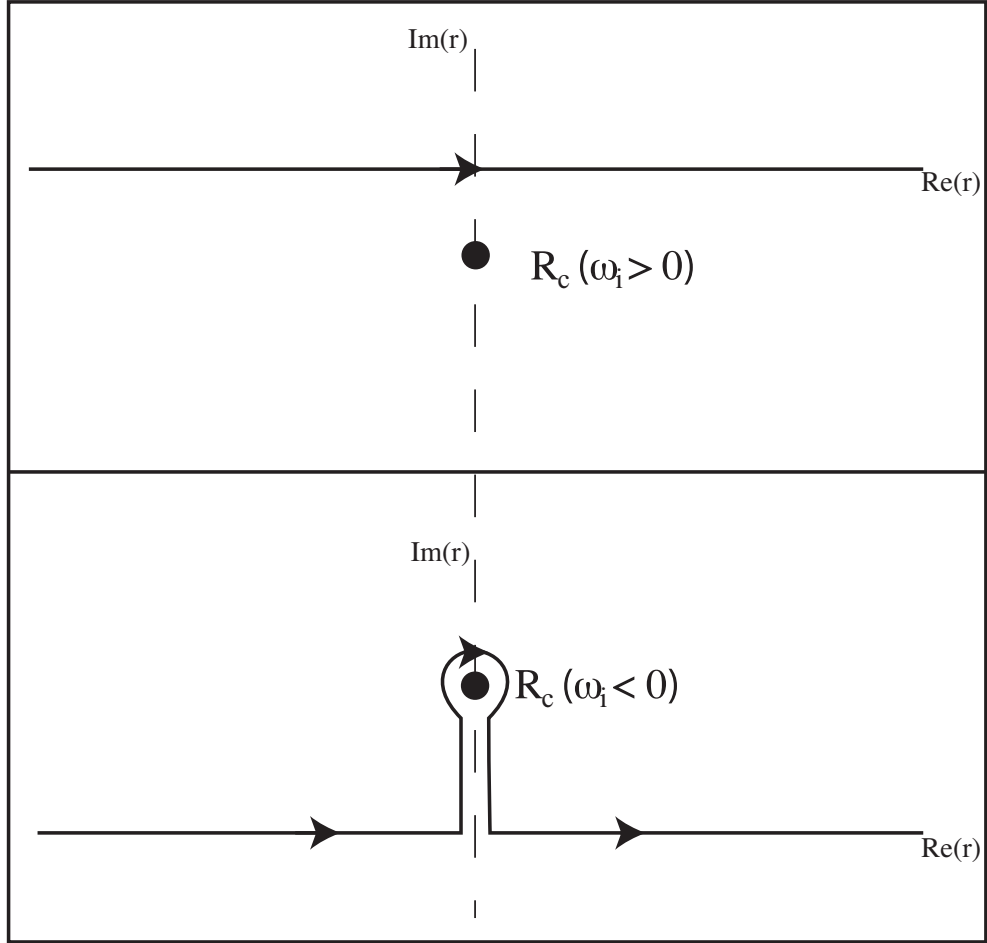
Figure 3.3: "Landau" contour for integration across the corotation resonance. To calculate the growing mode ($\omega_i > 0$), it is adequate to integrate the fluid perturbation equations along the real r axis (upper panel). To obtain the physical solution for the shrinking mode ($\omega_i < 0$), the integration contour must deformed so that the corotational pole R_c lies below the contour.

3.4.2 Outer Boundary Condition

As we are interested in self-excited modes in the inner region of the disk, we adopt the radiative outer boundary condition. Specifically, far from the outer Lindblad resonance ($r > r_{OL}$) we demand that only an outgoing wave exists:

$$\delta h \propto A \exp\left[i \int^r k \, dr\right], \quad \text{with } A = \left(\frac{D}{r\Sigma k}\right)^{1/2},\tag{3.25}$$

where $k = \sqrt{-D/c_s^2}$ (see Tsang & Lai 2008a). This gives the boundary condition at some $r_{out} > r_{OL}$:

$$\delta h'(r_{out}) = \delta h(r_{out})\left(ik + \frac{1}{A}\frac{dA}{dr}\right)_{r_{out}}.\tag{3.26}$$

In practice, we find that $r_{out} \sim 2r_{OL}$ would yield sufficiently accurate results.

3.4.3 Inner Boundary Conditions

To obtain global trapped modes, at least partial wave reflection must occur at r_{in}. To focus on the effect of corotational instability discussed in section 3, in this section we consider two simple inner boundary conditions. We defer our analysis of the effect of radial inflow on the p-modes to section 5.

(i) At the ISCO, the flow plunges into the black hole, we expect a sudden decrease in the surface density of the disk. Thus, it is reasonable to consider the free surface boundary condition, i.e., the Lagrangian pressure perturbation $\Delta P = 0$. Using $\delta u_r = -i\tilde{\omega}\xi_r$ (where ξ_r is the radial Lagrangian displacement), and $\Delta P = \delta P + \xi_r dP/dr$, we have

$$\left(\frac{\Delta P}{\Sigma}\right)_{r_{in}} = \left(\delta h - pc_s^2\frac{i\delta u_r}{r\tilde{\omega}}\right)_{r_{in}} = 0,\tag{3.27}$$

where we have used $dP/dr = (dP/d\Sigma)(d\Sigma/dr) = -pc_s^2\Sigma/r$ for barotropic, power-law disks ($\Sigma \propto r^{-p}$).

(ii) We assume that the radial velocity perturbation vanishes at the inner boundary, i.e., $\delta u_r = 0$. This was adopted by Tagger & Varniere (2006) in their calculations of overstable global modes due to accretion-ejection instability.

Both of these boundary conditions correspond to zero loss of wave energy at the inner boundary: If a wave from large radii impinges toward $r_{\rm in}$, the reflected wave will have the same amplitude. However, the phase shifts due to reflection differ in the two cases, and the resulting mode frequencies ω_r are different. Since the corotational wave amplification depends on ω_r, the mode growth rate ω_i will also be different.

3.4.4 Numerical Results

We solve for the complex eigen-frequency $\omega = \omega_r + i\omega_i$ using the shooting method, with a fifth-order Runge-Kutta integrator (Press et al. 1992). As discussed in section 4.1 we only calculate the growing modes ($\omega_i > 0$). We consider disk models with different surface density profile (characterized by the index p), sound speed c_s, and inner boundary conditions. For a given set of disk parameters and the azimuthal mode wavenumber m, the lowest order (highest frequency) mode has the best chance of being overstable. This is easily understood from our discussion in section 3 (see Fig. 1): a low-frequency wave has to penetrate a wider evanescent barrier for the corotational amplifier to be effective, and when $\omega_r < m\Omega_{\rm peak}$ the corotation resonance acts to damp the mode. For most disk models we have considered, the lowest order mode (of a given m) is
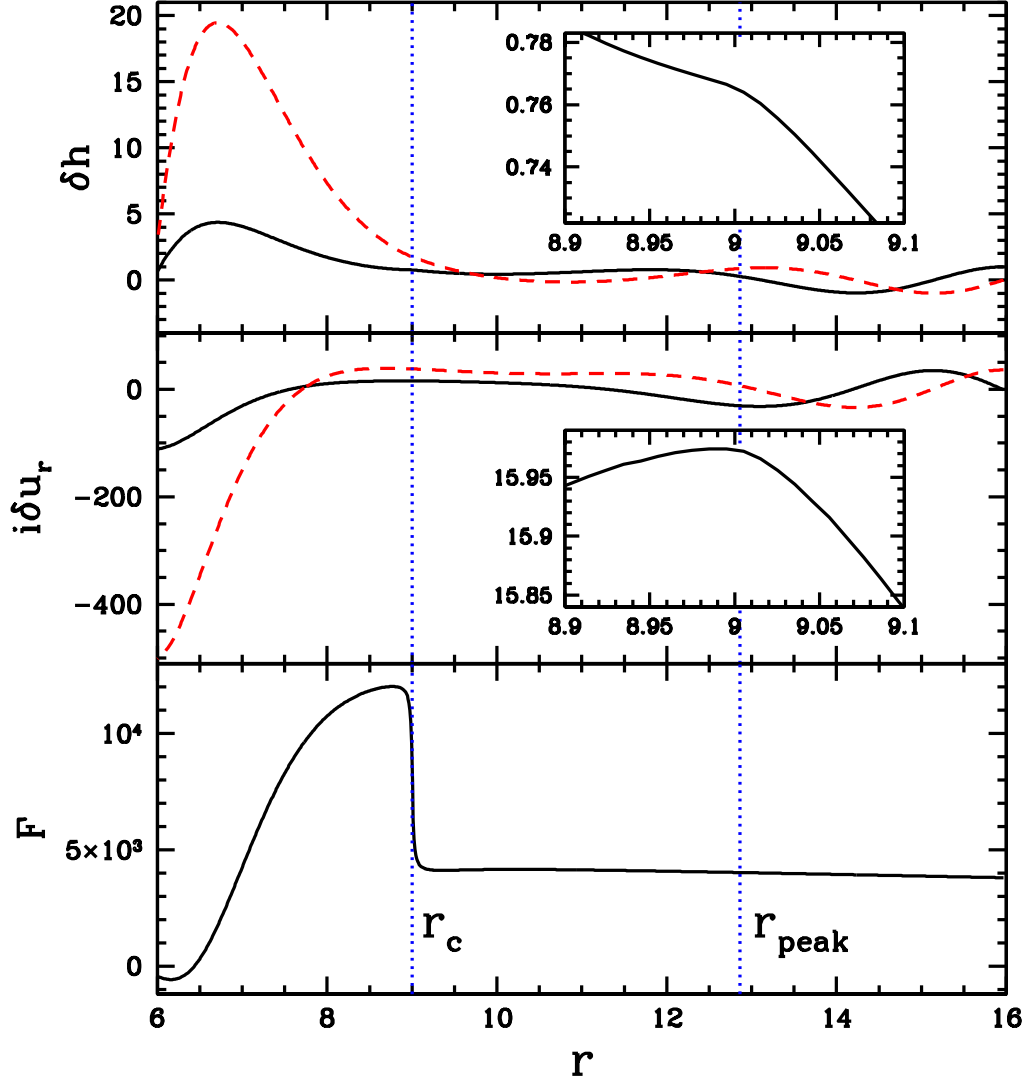
Figure 3.4: Example wavefunction for disk p-modes. The upper and middle panels show δh and $i\delta u_r$ (the solid lines for the real part and dashed lines for the imaginary part), the lower panels show the angular momentum flux, all in arbitrary units [with $\delta h(r_{\text{out}}) = 1$]. The radius r is in units of GM/c^2. The disk sound speed is $c_s = 0.1r\Omega$, and the $m = 2$ modes are obtained using the inner boundary condition $\Delta P(r_{\text{ISCO}}) = 0$. This shows the p-mode for the disk with a density profile $\Sigma \propto r^{-1}$, with the eigenvalues $\omega_r = 0.467m\Omega_{\text{ISCO}}$, $\omega_i/\omega_r = 0.0029$ [where $\Omega_{\text{ISCO}} = \Omega(r_{\text{ISCO}})$. The inserts show the blowups of the real wavefunctions near the corotation radius.
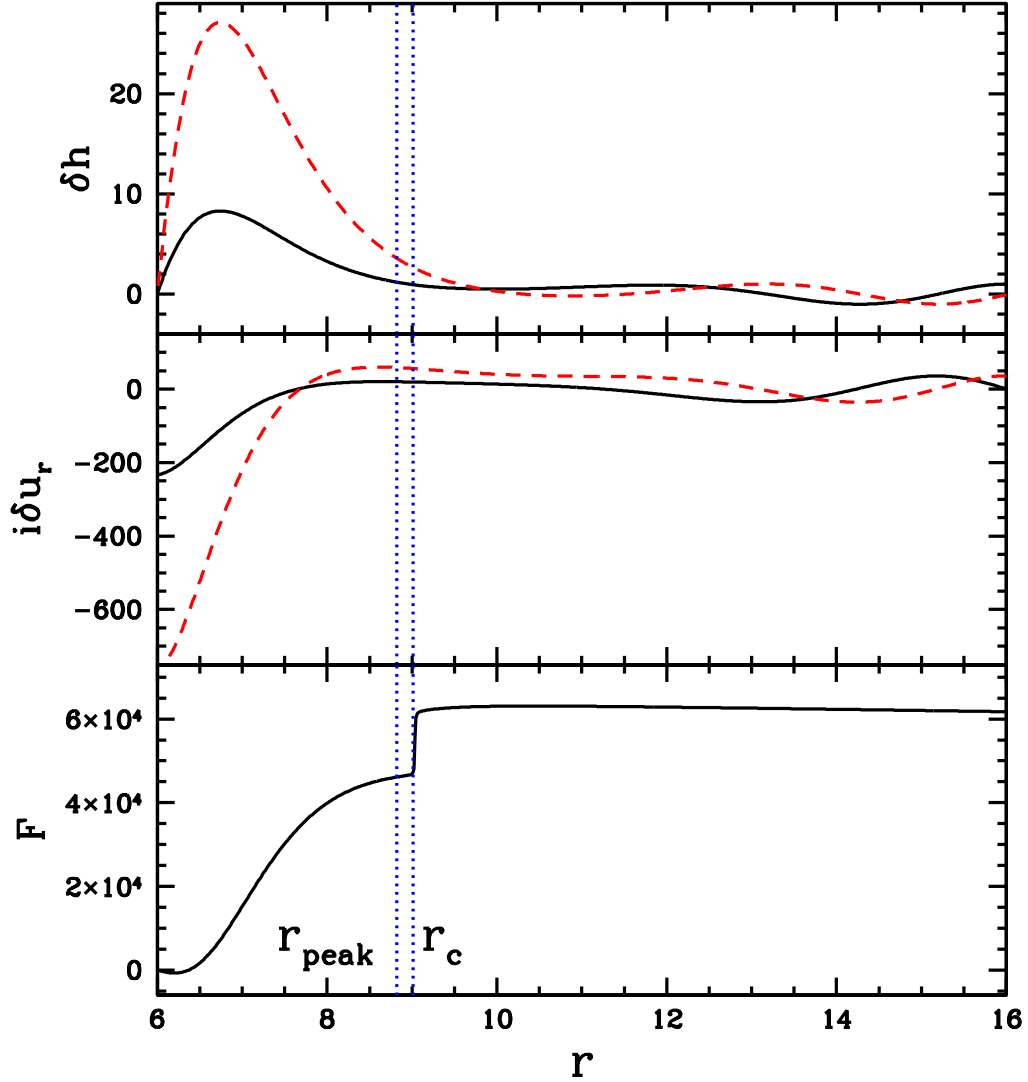
Figure 3.5: Example wavefunction for disk p-modes. The upper and middle panels show δh and $i\delta u_r$ (the solid lines for the real part and dashed lines for the imaginary part), the lower panels show the angular momentum flux, all in arbitrary units [with $\delta h(r_{\mathrm{out}}) = 1$]. The radius r is in units of GM/c^2. The disk sound speed is $c_s = 0.1r\Omega$, and the $m = 2$ modes are obtained using the inner boundary condition $\Delta P(r_{\mathrm{ISCO}}) = 0$. This shows the mode for the disk with constant surface density profile ($p = 0$), with eigenvalues $\omega_r = 0.464m\Omega_{\mathrm{ISCO}}$, $\omega_i/\omega_r = 0.00073$. Note that the model shown in the previous figure has $r_c < r_{\mathrm{peak}}$ (the radius of peak vortensity) and thus $F(r_c+) < F(r_c-)$, while the model shown here has $r_c > r_{\mathrm{peak}}$ and $F(r_c+) > F(r_c-)$. In both models there is a positive flux for $r > r_c$ due to the outward propagating wave.
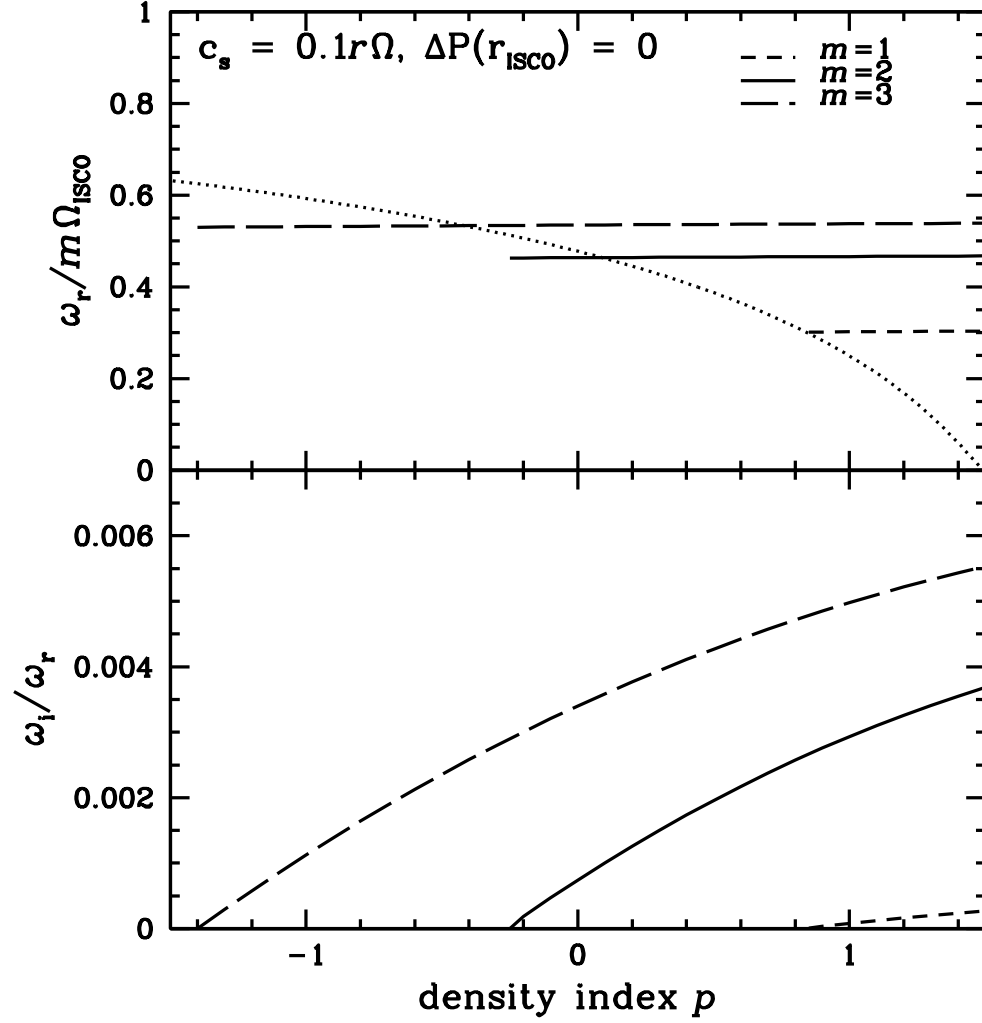
Figure 3.6: The real and imaginary frequencies of disk p-modes (with azimuthal wave numbers $m = 1, 2, 3$) as a function of the surface density index p (where $\Sigma \propto r^{-p}$). The modes are calculated assuming the inner boundary condition $\Delta P(r_{\mathrm{ISCO}}) = 0$ and $c_s = 0.1r\Omega$. The dotted lines denote the lower bound $\omega_r/m = \Omega_{\mathrm{peak}}$ for which the corotational wave absorption acts to enhance mode growth.
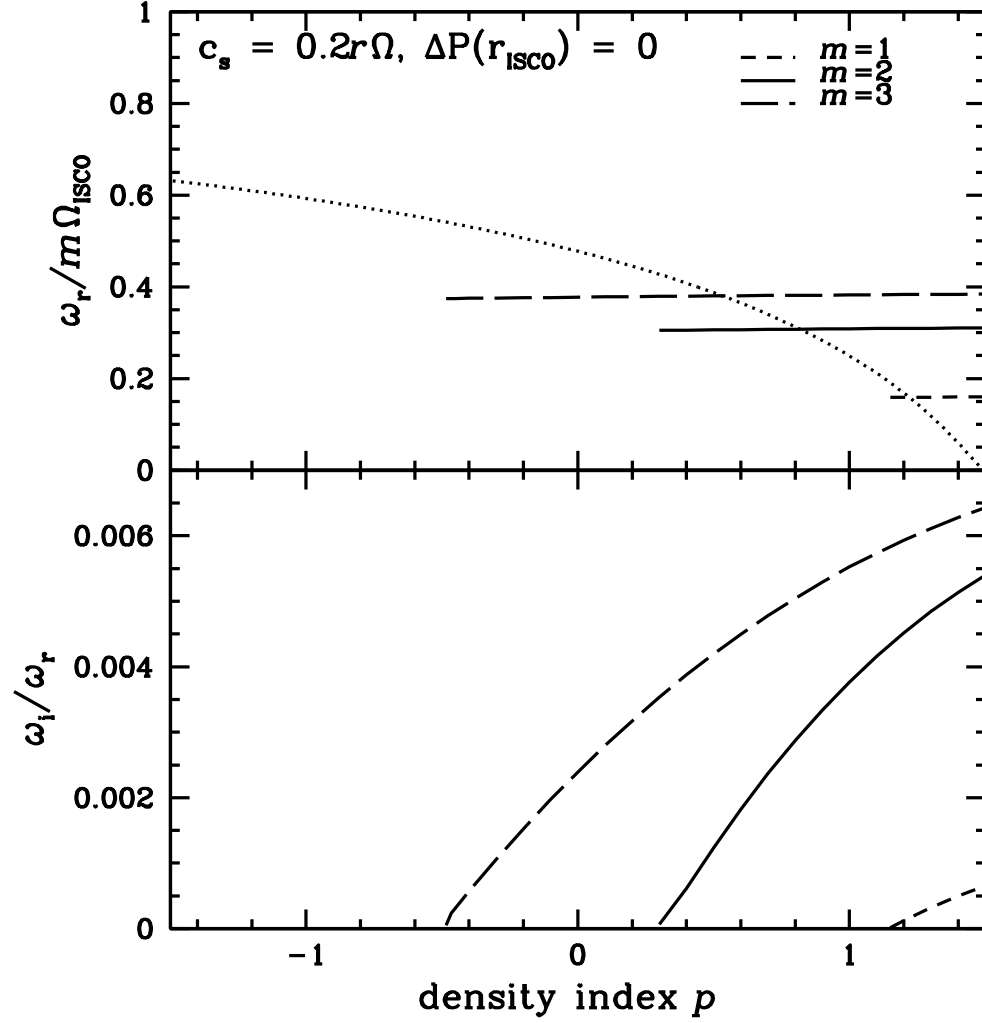
Figure 3.7: The real and imaginary frequencies of disk p-modes (with azimuthal wave numbers $m = 1, 2, 3$) as a function of the surface density index p (where $\Sigma \propto r^{-p}$). The modes are calculated assuming the inner boundary condition $\Delta P(r_{\rm ISCO}) = 0$ and $c_s = 0.2r\Omega$. The dotted lines denote the lower bound $\omega_r/m = \Omega_{\rm peak}$ for which the corotational wave absorption acts to enhance mode growth.
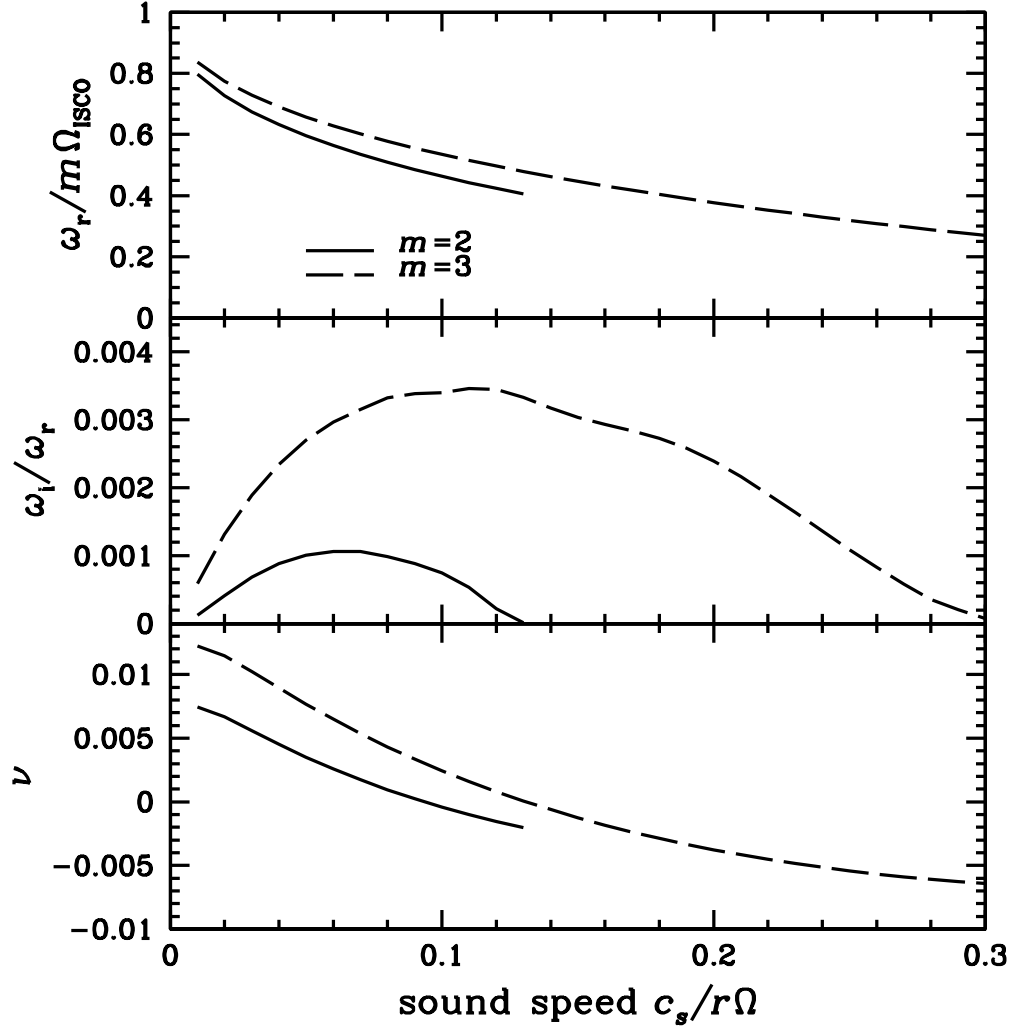
Figure 3.8: The real and imaginary frequencies of disk p-modes (with $m = 2, 3$) as a function of the normalized sound speed $c_s/(r\Omega)$. The disk is assumed to have a constant density profile ($p = 0$), and the inner boundary condition is $\Delta P(r_{\mathrm{ISCO}}) = 0$. The bottom panel shows the ν parameters for the modes.
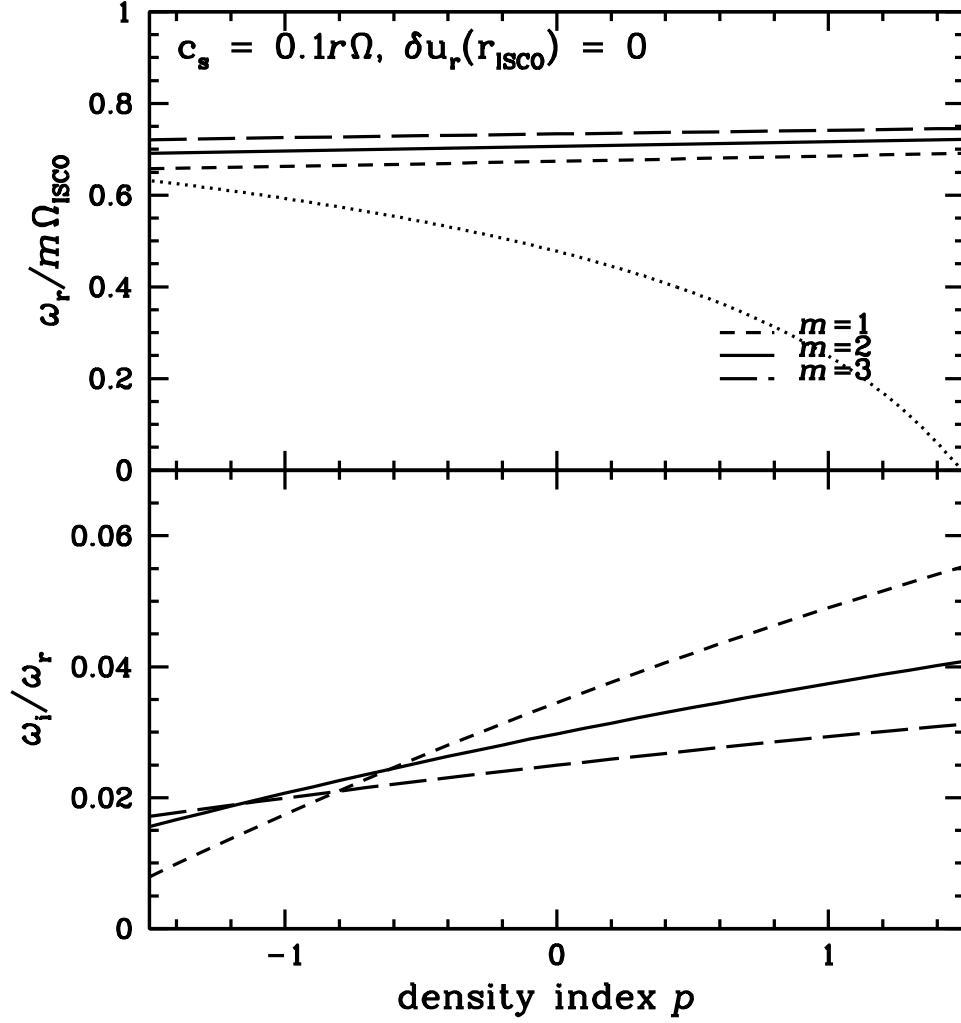
Figure 3.9: The real and imaginary frequencies of disk p-modes (with azimuthal wave numbers $m = 1, 2, 3$) as a function of the surface density index p (where $\Sigma \propto r^{-p}$). The modes are calculated assuming the inner boundary condition $\delta u_r(r_{ISCO}) = 0$, and $c_s = 0.1r\Omega$. The dotted lines denote the lower bound $\omega/m = \Omega_{peak}$ for which the corotational wave absorption acts to enhance mode growth.
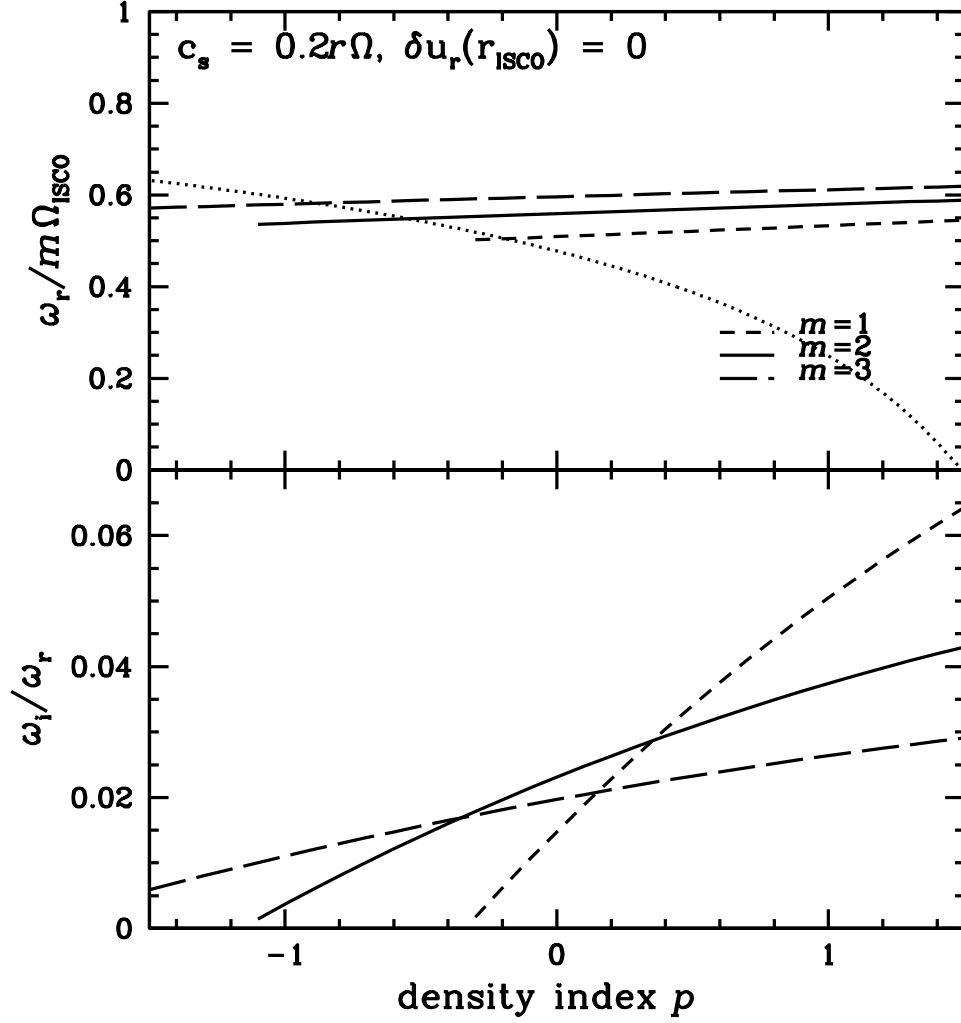
Figure 3.10: The real and imaginary frequencies of disk p-modes (with azimuthal wave numbers $m = 1, 2, 3$) as a function of the surface density index p (where $\Sigma \propto r^{-p}$). The modes are calculated assuming the inner boundary condition $\delta u_r(r_{\mathrm{ISCO}}) = 0$, and $c_s = 0.2r\Omega$. The dotted lines denote the lower bound $\omega/m = \Omega_{\mathrm{peak}}$ for which the corotational wave absorption acts to enhance mode growth.

64

the only mode that has $\omega_i > 0$.

Our numerical results are presented in Figures 3.4–3.10. Figure 4 gives two examples of the eigenfunctions of overstable trapped p-modes, obtained with the inner boundary condition $\Delta P = 0$. In addition to δh and δu_r, we also plot the angular momentum flux carried by the wave across the disk (e.g., Goldreich & Tremaine 1979; Zhang & Lai 2006)

$$F(r) = \pi r^2 \Sigma \, \mathrm{Re}\left(\delta u_r \delta u_\phi^*\right) = \frac{\pi m r \Sigma}{D} \, \mathrm{Im}\left(\delta h \frac{d\delta h^*}{dr}\right), \tag{3.28}$$

where the second equality follows from equations (3.6)-(3.8) (with $u_r = 0$). We see from Fig. 4 that outside the corotation radius (r_c), F is nearly constant since only the outgoing wave exists in this region and the wave action is conserved in the limit of $\omega_i \ll \omega_r$. Inside r_c, the interference between the ingoing and outgoing waves gives rise to the variation of F. At r_{ISCO}, F approaches zero since no wave action is lost through the disk inner boundary when $\Delta P = 0$.[2] Figure 4 also shows a flux jump across the corotation. In the limit of $\omega_i \ll \omega_r$, $d\delta h/dr$, δu_r and δu_ϕ are discontinuous across r_c (although δh is continuous), giving rise to the flux discontinuity (see Tsang & Lai 2008a):

$$F(r_c+) - F(r_c-) = -\frac{2\pi^2 m r \Sigma \nu \kappa}{c_s D}|\delta h|^2\Big|_{r_c}. \tag{3.29}$$

This discontinuity signifies the corotational wave absorption, the sign of which depends on $\nu \propto (d\zeta/dr)_{r_c}$, as discussed in section 3. Thus, the model shown on the left panels of Fig. 4 has $r_c < r_{\mathrm{peak}}$ and $\nu > 0$, and the mode growth is primarily driven by wave absorption at the corotation. The model shown on the right panels of Fig. 4, on the other hand, has $r_c > r_{\mathrm{peak}}$ and $\nu < 0$, thus the corotational wave absorption acts to damp the mode, and the overall growth of

---

[2]Note that equation (3.28) is the time averaged flux and is defined for waves with real ω. Using equation (3.27) and $D\delta u_r = i\tilde{\omega}d\delta h/dr - (2im\Omega/r)\delta h$ (obtained from eqs. [3.7]-[3.8]) it is easy to show that $F(r_{\mathrm{in}}) = 0$ exactly for real ω.

the mode is due to the outgoing wave beyond r_c, and the growth rate is much smaller than the model shown on the left panels.

Figures 5–6 show the frequencies of the fundamental (no node/highest frequency) growing p-modes (with $m = 1, 2, 3$) for various disk parameters, again obtained with the inner boundary condition $\Delta P = 0$. We consider p in the range between -1.5 and 1.5, and c_s up to $0.3r\Omega$. For a given sound speed, the real mode frequency ω_r depends very weakly on p, but the growth rate ω_i increases with p (see Fig. 5) since a larger value of p leads to a larger ν and enhanced wave absorption at the corotation [see equation (3.17)]. In general, as the sound speed increases, the effective wavelength of the mode increases, and ω_r decreases in order "fit in" the trapping zone between $r_{\rm in}$ and $r_{\rm IL}$ (see Fig. 6). The mode growth rates ω_i depends on c_s in a non-monotonic way because of two competing effects: As c_s increases, less attenuation occurs in the evanescent zone, and more wave energy can be absorbed at the corotation and propagate to the outer edge of the disk; these tend to increase ω_i. On the other hand, increasing c_s also leads to smaller ω_r, which shifts the corotation resonance to a larger radius and leads to decreasing ν and ω_i.

Note that the growing modes shown in Fig. 5 extend below the $\omega_r/m = \Omega_{\rm peak}$ boundary due to the propagation of waves beyond the corotation radius, as discussed in section 3 [see eqs. (3.23)]. Such modes (with $\nu_{\rm crit} < \nu < 0$) grow significantly slower than the modes with $\nu > 0$ as the flux is attenuated by the entire barrier between $r_{\rm IL}$ and $r_{\rm OL}$.

For comparison, Figure 7 shows the disk mode frequencies and growth rates when the inner boundary condition $\delta u_r = 0$ is adopted. The different boundary condition leads to a different phase shift φ and higher mode frequency, but the

66

results are similar to those illustrated in Fig. 5. In particular, as p increases, ω_r remains approximately constant while ω_i increases.

3.5 Effect of Radial Inflow on the P-Mode Growth Rate

Our mode calculations presented in section 4 neglect the radial velocity of the accretion flow and assume a loss-less inner disk boundary condition (either $\Delta P = 0$ or $\delta u_r = 0$ at r_{ISCO}). In real disks, the radial inflow velocity u_r is not negligible as r approaches r_{ISCO}, and the flow goes through a transonic point (where $u_r = -c_s$) at a radius very close to r_{ISCO}. We expect that part of the fluid perturbations may be advected into the black hole and the inner disk boundary will not be completely loss-less. Here we study the effect of the transonic flow on the p-mode growth rate.

We note that just as the accretion disk is not laminar but turbulent, the accretion flow around r_{ISCO} is complicated. General relativistic MHD simulations in 3D are only beginning to shed light on the property of the black hole accretion flow (e.g., Beckwith, Hawley & Krolik 2008; Shafee et al. 2008; Noble, Krolik & Hawley 2008), and many uncertainties remain unresolved. Here, to make analytic progress, we adopt a simple viscous transonic flow model, which qualitatively describes the inner accretion flow of the black hole as long as the flow remains geometrically thin (see Afshordi & Paczynski 2003).

3.5.1 Boundary Condition at the Sonic Point

We rewrite equations (3.6)-(3.7) as

$$\frac{u_r}{c_s^2}\delta h' + \delta u_r' = \left[\frac{i\tilde{\omega}}{c_s^2} - u_r\left(c_s^{-1}\right)'\right]\delta h + \frac{u_r'}{u_r}\delta u_r - \frac{im}{r}\delta u_\phi \equiv \mathcal{A}_1, \tag{3.30}$$

$$\delta h' + u_r\,\delta u_r' = (i\tilde{\omega} - u_r')\,\delta u_r + 2\Omega\,\delta u_\phi \equiv \mathcal{A}_2, \tag{3.31}$$

where ′ stands for d/dr and we have used $r\Sigma u_r = $ constant for the background flow. Solving for $\delta h'$ and $\delta u_r'$ we have

$$\delta h' = \frac{\mathcal{A}_2 - \mathcal{A}_1 u_r}{1 - u_r^2/c_s^2}, \tag{3.32}$$

$$\delta u_r' = \frac{\mathcal{A}_1 - (u_r/c_s^2)\mathcal{A}_2}{1 - u_r^2/c_s^2}. \tag{3.33}$$

Clearly, in order for the perturbation to be regular at the sonic point r_s, where $u_r = -c_s$, we require

$$\mathcal{A}_2 + c_s\mathcal{A}_1 = 0 \quad \text{at } r = r_s. \tag{3.34}$$

For definiteness, we characterize the variations of Σ and c_s at the sonic point $r_s \simeq r_{\text{ISCO}}$ by the two length scales:

$$\left(\frac{\Sigma'}{\Sigma}\right)_{r_s} = \frac{1}{L_\Sigma}, \qquad \left(\frac{c_s'}{c_s}\right)_{r_s} = \frac{1}{L_c}. \tag{3.35}$$

From $r\Sigma u_r = $ constant, we also have $u_r' = c_s(r_s^{-1} + L_\Sigma^{-1})$ at $r = r_s$. Then equation (3.34) becomes

$$\left(\frac{i\tilde{\omega}}{c_s} - \frac{2}{L_c}\right)\delta h + \left[i\tilde{\omega} - 2c_s\left(\frac{1}{r} + \frac{1}{L_\Sigma}\right)\right]\delta u_r + \left(2\Omega - \frac{imc_s}{r}\right)\delta u_\phi = 0 \quad \text{at } r = r_s. \tag{3.36}$$

This is the boundary condition for the fluid perturbations at the sonic point.

3.5.2 Properties of the Transonic Flow

Before exploring the effect the radial inflow on the disk modes, we first estimate the length scale for the surface density variation, L_Σ, using the viscous slim disk

model (e.g., Muchotrzeb & Paczynski 1982; Matsumoto et al. 1984; Abramowicz et al. 1988)

The basic steady-state slim disk equations are

$$\dot{M} = -2\pi r \Sigma u_r, \tag{3.37}$$

$$u_r u_r' = -c_s^2 \frac{\Sigma'}{\Sigma} + (\Omega^2 - \Omega_K^2)r, \tag{3.38}$$

$$\dot{M} l_0 = \dot{M} l + 2\pi \nu_{\mathrm{vis}} r^3 \Sigma \Omega', \tag{3.39}$$

where $l = r^2 \Omega$ is the specific angular momentum of the flow, Ω is the actual rotation rate, Ω_K is given by equation (3.2), ν_{vis} is the kinetic viscosity, and l_0 is the eigenvalue that must be solved so that flow pass through the sonic point smoothly. We shall use the α-disk model, so that $\nu_{\mathrm{vis}} = \alpha H c_s$, with $H \simeq c_s/\Omega_K$.

To estimate L_Σ, we assume $l(r) \simeq r^2 \Omega_K(r)$ for $r \gtrsim r_{\mathrm{ISCO}}$ and $l_0 \simeq l_K(r_{\mathrm{ISCO}})$. Equation (3.39) gives

$$u_r(1 - l_0/l) \simeq -3\nu_{\mathrm{vis}}/(2r) = -3\alpha H c_s/(2r), \tag{3.40}$$

valid for $r \gtrsim r_{\mathrm{ISCO}}$. At the radius $r = r_{\mathrm{ISCO}} + \Delta r$, we have $u_r(\Delta r/r_{\mathrm{ISCO}})^2 \simeq -4\alpha H c_s/r_{\mathrm{ISCO}}$. The sonic point ($u_r = -c_s$) is at $\Delta r \simeq 2\sqrt{\alpha H r_{\mathrm{ISCO}}}$, and $u_r = -c_s/2$ at $\Delta r \simeq 2\sqrt{2\alpha H r_{\mathrm{ISCO}}}$. Thus $u_r'(r_s) \sim c_s/L_\Sigma$, with

$$L_\Sigma = \left(\frac{\Sigma}{\Sigma'}\right)_{r_s} \sim 2\sqrt{\alpha H r_s} = 2\sqrt{\alpha\beta}\, r_s, \tag{3.41}$$

where $\beta = c_s/(r\Omega)$. This should be compared to the disk thickness $H = \beta r$: depending on the value of α, both $L_\Sigma < H$ and $L_\Sigma > H$ are possible.

The value and sign of L_c depend on the thermodynamical and radiative properties of the flow, and cannot be estimated in a simple way. It is reasonable to expect $|L_c| \sim r_s$.

3.5.3 Reflectivity at the Sonic Point

We can understand qualitatively the effect of the transonic boundary condition on the p-mode by calculating the reflectivity $\mathcal{R}_s$ of the inner boundary.

Consider a density wave $\delta h \propto \exp(i \int^r k\, dr)$ in the wave zone $r_{\text{in}} = r_s < r < r_{\text{IL}}$, traveling toward the inner disk boundary. [3]. Upon reflection, the wave becomes $\delta h \propto \mathcal{R}_s \exp(-i \int^r k\, dr)$. Including the correct WKB amplitude (see Tsang & Lai 2008a), the wave outside the sonic point can be written as (up to a constant prefactor)

$$\delta h = A \left[\exp\left(i \int_{r_s}^r k\, dr \right) + \mathcal{R}_s \exp\left(-i \int_{r_s}^r k\, dr \right) \right], \qquad (r_s < r < r_{\text{IL}}) \tag{3.42}$$

where

$$k = \frac{(-D)^{1/2}}{c_s}, \quad A = \left(\frac{D}{r \Sigma k} \right)^{1/2}. \tag{3.43}$$

To apply the boundary condition (3.36) to equation (3.42), we neglect u_r in equations (3.6)–(3.8) at $r = r_s + \varepsilon$, with $\varepsilon \ll r_s$ and $r_s \simeq r_{\text{ISCO}}$. Implicit in this procedure is the assumption that the fluid perturbations do not vary significantly between r_s and $r_s + \varepsilon$. We then obtain

$$\mathcal{R}_s = \left. \frac{ik + L_A^{-1} + K - 2m\Omega/(r\tilde{\omega})}{ik - L_A^{-1} - K + 2m\Omega/(r\tilde{\omega})} \right|_{r_s}, \tag{3.44}$$

where

$$L_A^{-1} = \left(\frac{A'}{A} \right)_{r_s}, \tag{3.45}$$

and

$$K = \left. \left(\frac{\tilde{\omega}^2 L_\Sigma}{2c_s^2} \right) \frac{1 - (mc_s/r\tilde{\omega})^2 - i\left[2mc_s\Omega/(r\tilde{\omega}^2) - 2c_s/(\tilde{\omega}L_c) \right]}{1 + (L_\Sigma/r) - i(\tilde{\omega}L_\Sigma/2c_s)} \right|_{r_s}. \tag{3.46}$$

---

[3]Note that since the group velocity of the wave has opposite sign as the phase velocity for $r < r_{\text{IL}}$, the wave of the form $\exp(i \int^r k\, dr)$ (with $k > 0$) is inward propagating.

Figure 3.11: The wave reflectivity at the transonic point of the inner disk as a function of the parameter L_Σ/H, for $r_s/L_c = 0$. The heavier lines are for $c_s = 0.1r\Omega$ and the lighter lines for $c_s = 0.05r\Omega$. The short-dashed, solid and long-dashed lines are for $m = 1, 2, 3$, respectively. The wave frequency is set to be $\omega = 0.7m\Omega(r_s)$.
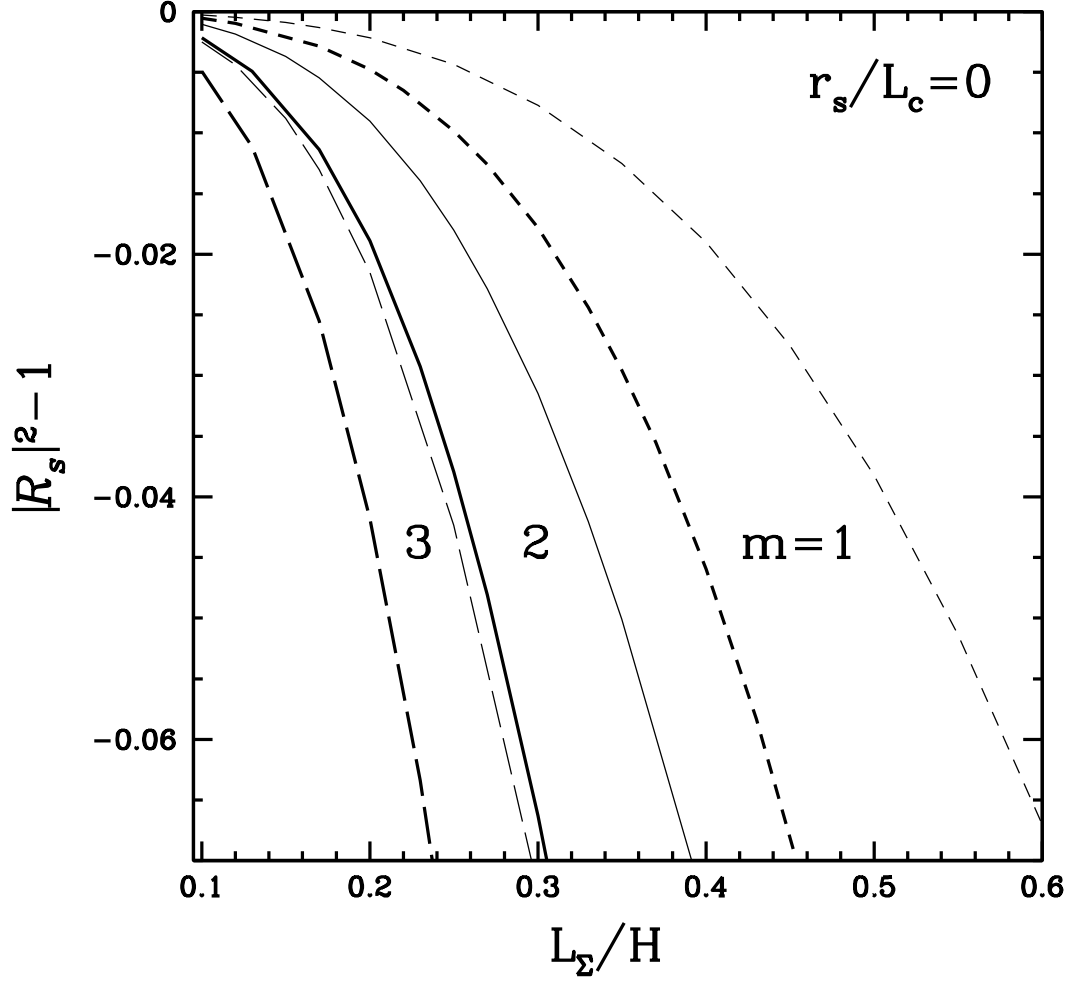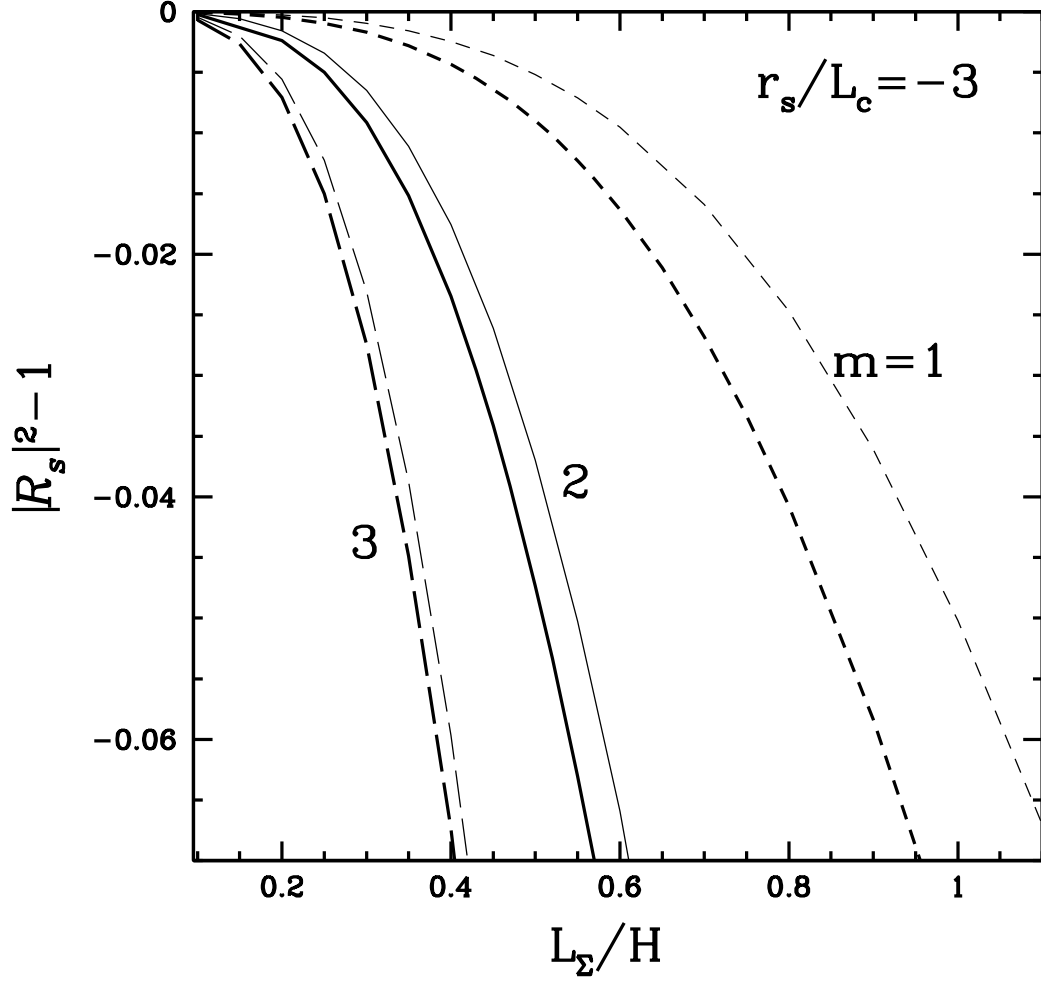
Figure 3.12: The wave reflectivity at the transonic point of the inner disk as a function of the parameter L_Σ/H, for $r_s/L_c = -3$ (the right panel). The heavier lines are for $c_s = 0.1r\Omega$ and the lighter lines for $c_s = 0.05r\Omega$. The short-dashed, solid and long-dashed lines are for $m = 1, 2, 3$, respectively. The wave frequency is set to be $\omega = 0.7m\Omega(r_s)$.

When considering the damping of the p-mode due to the transonic flow, the quantity $|\mathcal{R}_s|^2 - 1$ is the most relevant (see section 5.4 below). Let

$$K = |K| \exp(-i\psi), \tag{3.47}$$

we have

$$|\mathcal{R}_s|^2 - 1 = -\frac{4\, k\, |K| \sin\psi}{(L_A^{-1} + |K| \cos\psi)^2 + (k + |K| \sin\psi)^2}\bigg|_{r_s}. \tag{3.48}$$

Using $\beta = c_s/(r\Omega)$, $\tilde{\omega} = -\hat{\omega} m \Omega_{\mathrm{ISCO}}$ (where $0 < \hat{\omega} < 1$), we find from equation (3.46) that

$$\psi = \tan^{-1}\left(\frac{2\beta}{m\hat{\omega}^2}\frac{1 + r_s\hat{\omega}/L_c}{1 - \beta^2/\hat{\omega}^2}\right) + \tan^{-1}\left(\frac{m\hat{\omega}L_\Sigma}{2\beta r_s}\frac{1}{1 + L_\Sigma/r_s}\right). \tag{3.49}$$

Figures 3.11 and 3.12 shows how the reflectivity depends on various parameters of the disk inner edge. In particular, for small $L_\Sigma/H = L_\Sigma/(\beta r_s)$, i.e., when the surface density of the disk decreases rapidly at the sonic point, $|\mathcal{R}_s|^2$ is only slightly smaller than unity and the wave loss at the inner edge of the disk is small.

3.5.4 Mode Growth Rate in the WKB Approximation

Consider the p-mode trapped between $r_{\mathrm{in}} = r_s \simeq r_{\mathrm{ISCO}}$ and r_{IL}. With the reflectivity at r_{IL} given by $\mathcal{R}$ (see section 3), we can write the wave amplitude for $r < r_{\mathrm{IL}}$ as[4]

$$\delta h \propto \left(\frac{D}{r\Sigma k}\right)^{1/2}\left[\exp\left(-i\int_{r_{\mathrm{IL}}}^{r} k\, dr\right) + \mathcal{R}\exp\left(i\int_{r_{\mathrm{IL}}}^{r} k\, dr\right)\right], \qquad (r_s < r < r_{\mathrm{IL}}) \tag{3.50}$$

---

[4]Note that this definition of $\mathcal{R}$ differs from that in Tsang & Lai (2008a) by a phase factor of $\exp(i\pi/4)$.

On the other hand, with the reflectivity at $r_{\text{in}} = r_s$ given by $\mathcal{R}_s$, the wave can also be expressed as (3.42). For stationary waves we therefore require

$$\exp(2i\Theta) = \mathcal{R}\mathcal{R}_s, \qquad \text{with} \ \ \Theta = \int_{r_{\text{in}}}^{r_{\text{IL}}} k\,dr = \Theta_r + i\Theta_i, \tag{3.51}$$

where Θ_r and Θ_i are real. The real eigen-frequency ω_r is given by

$$\Theta_r = \int_{r_{\text{in}}}^{r_{\text{IL}}} k_r\,dr = \int_{r_{\text{in}}}^{r_{\text{IL}}} \frac{\sqrt{\tilde{\omega}_r^2 - \kappa^2}}{c_s}\,dr = n\pi + \frac{\varphi}{2}, \tag{3.52}$$

where $\mathcal{R}\mathcal{R}_s = |\mathcal{R}\mathcal{R}_s|\exp(i\varphi)$, and n is an integer. The mode growth rate ω_i is determined by $|\mathcal{R}\mathcal{R}_s| = \exp(-2\Theta_i)$, or

$$\tanh\Theta_i = -\left(\frac{|\mathcal{R}\mathcal{R}_s| - 1}{|\mathcal{R}\mathcal{R}_s| + 1}\right). \tag{3.53}$$

For $\Theta_i = \int_{r_{\text{in}}}^{r_{\text{IL}}} k_i\,dr \ll 1$ and $k_i \simeq \omega_i\tilde{\omega}_r/(c_s\sqrt{\tilde{\omega}_r^2 - \kappa^2})$, we obtain

$$\omega_i = \left(\frac{|\mathcal{R}\mathcal{R}_s| - 1}{|\mathcal{R}\mathcal{R}_s| + 1}\right)\left[\int_{r_{\text{in}}}^{r_{\text{IL}}} \frac{|\tilde{\omega}_r|}{c_s\sqrt{\tilde{\omega}_r^2 - \kappa^2}}\,dr\right]^{-1}, \tag{3.54}$$

where we have assumed $\tilde{\omega}_r < 0$. Equation (3.54) is to be compared with (3.19), where perfect reflection at r_{in} is assumed. Clearly, to obtain growing modes we require $|\mathcal{R}\mathcal{R}_s| > 1$. For a given $|\mathcal{R}| > 1$, growing modes are possible only when the loss at the sonic point is sufficiently small (i.e., $|\mathcal{R}_s|$ is sufficiently close to unity).

3.5.5 Numerical Results

We solve equations (3.6)-(3.8) (with $u_r = 0$) subjected to the radiative outer boundary condition (3.26) and the transonic inner boundary condition (3.36).

Figure 3.13 depicts an example of the p-mode wavefunctions. Again, the discontinuity in the angular momentum flux F at r_c signifies wave absorption;
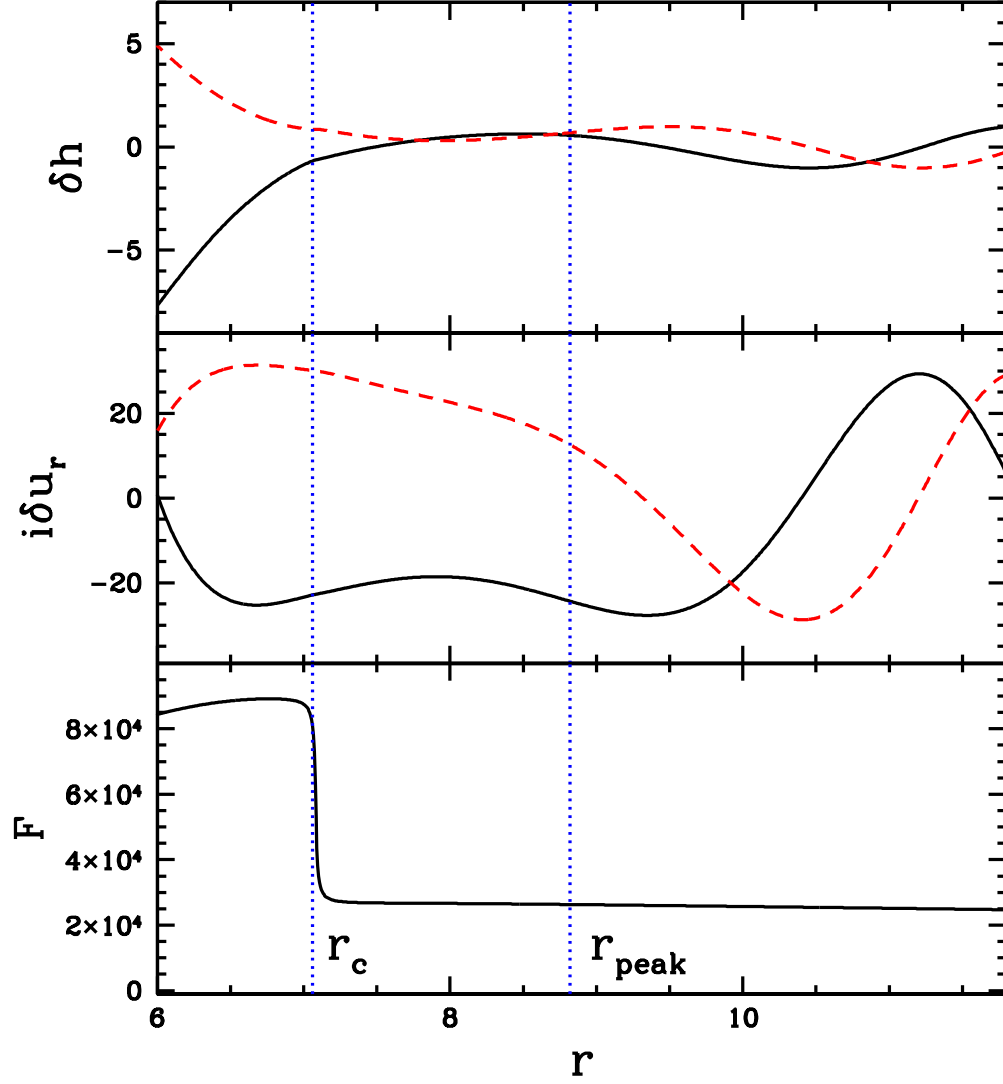
Figure 3.13: Wavefunctions for a disk p-mode. The notations are the same as in Fig. 3.4. The disk has sound speed $c_s = 0.1r\Omega$ and constant density profile ($p = 0$), and the $m = 2$ mode is calculated using the transonic inner boundary condition (3.36) with $L_\Sigma/H = 0.25$ and $L_c = \infty$. The eigenvalues are $\omega_r = 0.725m\Omega_{\text{ISCO}}$ and $\omega_i/\omega_r = 0.00267$.
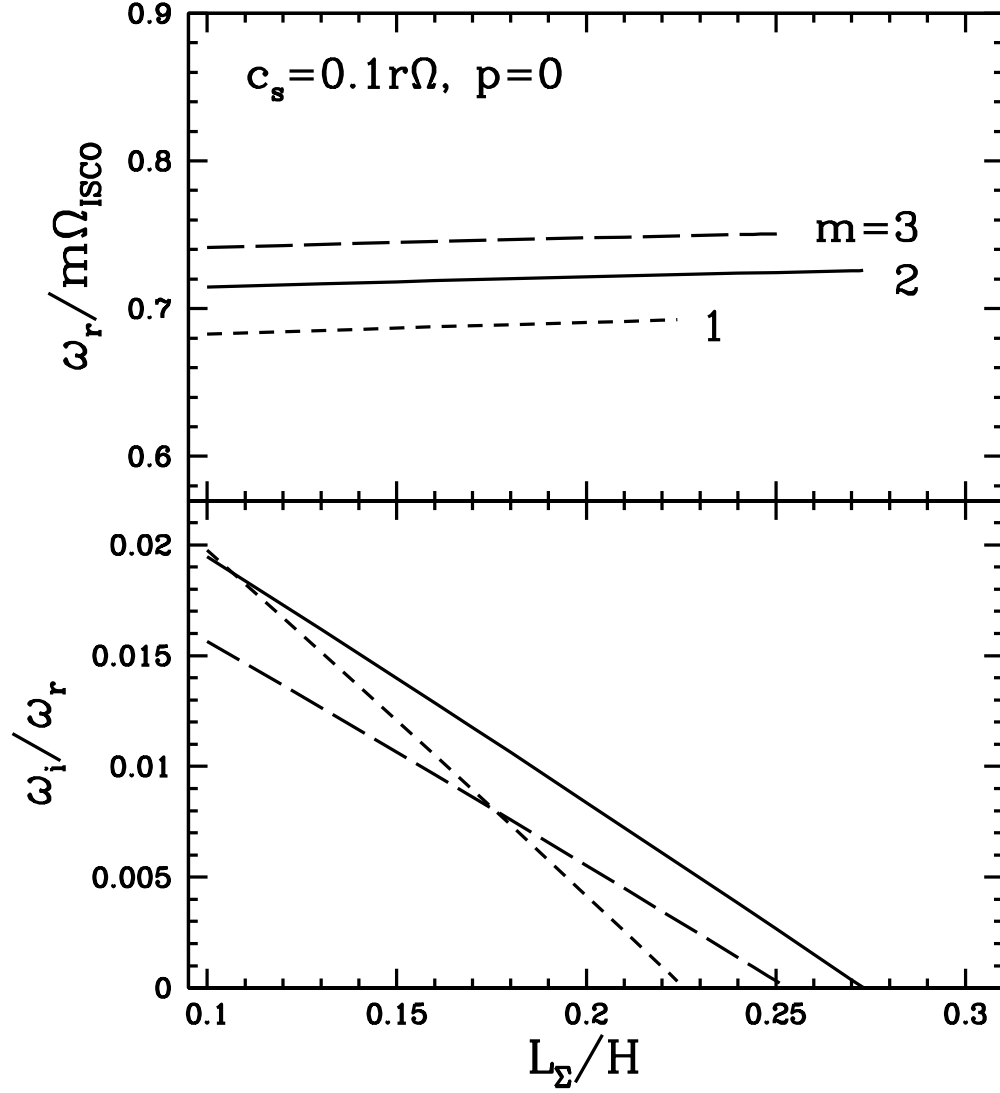
Figure 3.14: The real and imaginary frequencies of disk p-modes (with azimuthal wave numbers $m = 1, 2, 3$) as a function of L_Σ/H [see eq. (3.35)] The modes are calculated using the transonic inner boundary condition (3.36) with $L_c = \infty$. The disk has a constant surface density profile and the sound speed is $c_s = 0.1r\Omega$.
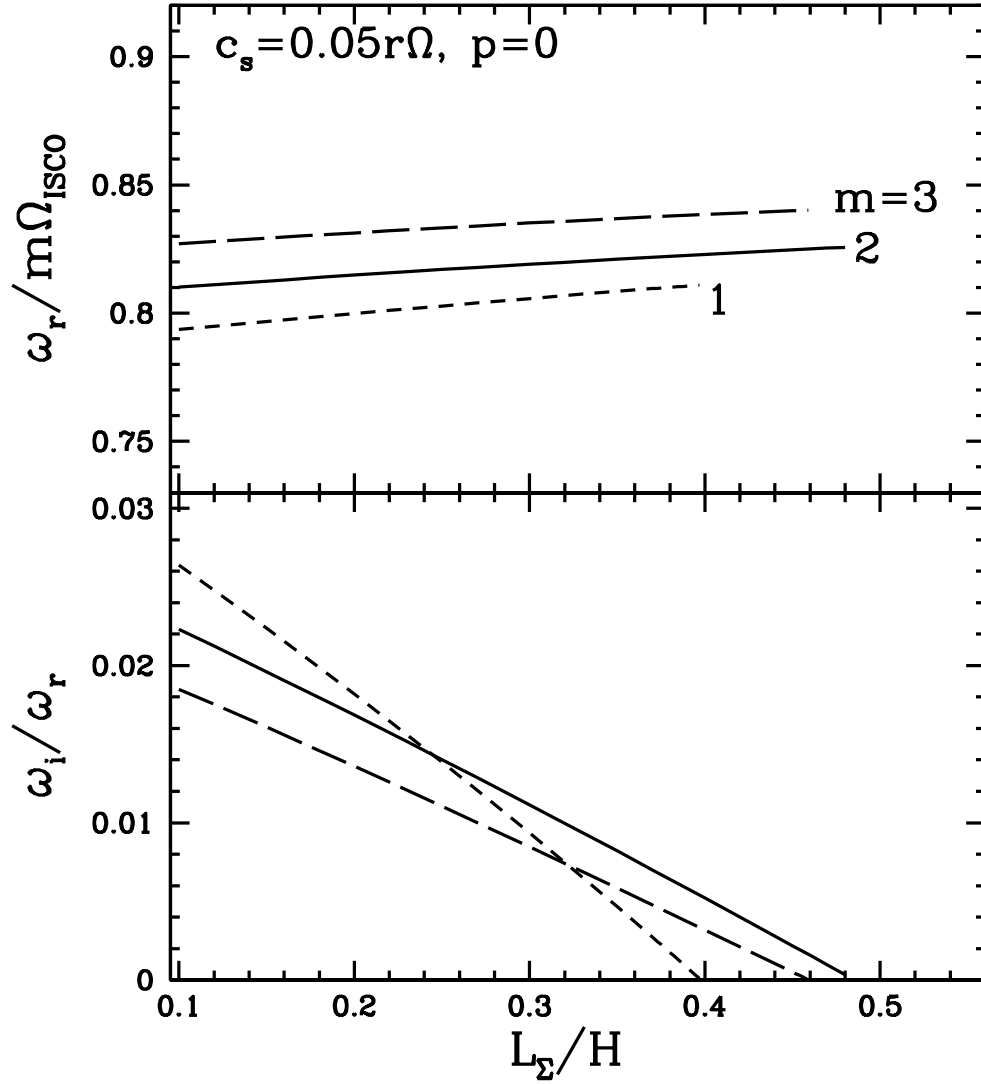
Figure 3.15: The real and imaginary frequencies of disk p-modes (with azimuthal wave numbers $m = 1, 2, 3$) as a function of L_Σ/H [see eq. (3.35)] The modes are calculated using the transonic inner boundary condition (3.36) with $L_c = \infty$. The disk has a constant surface density profile and the sound speed is $0.05r\Omega$ (right panels).
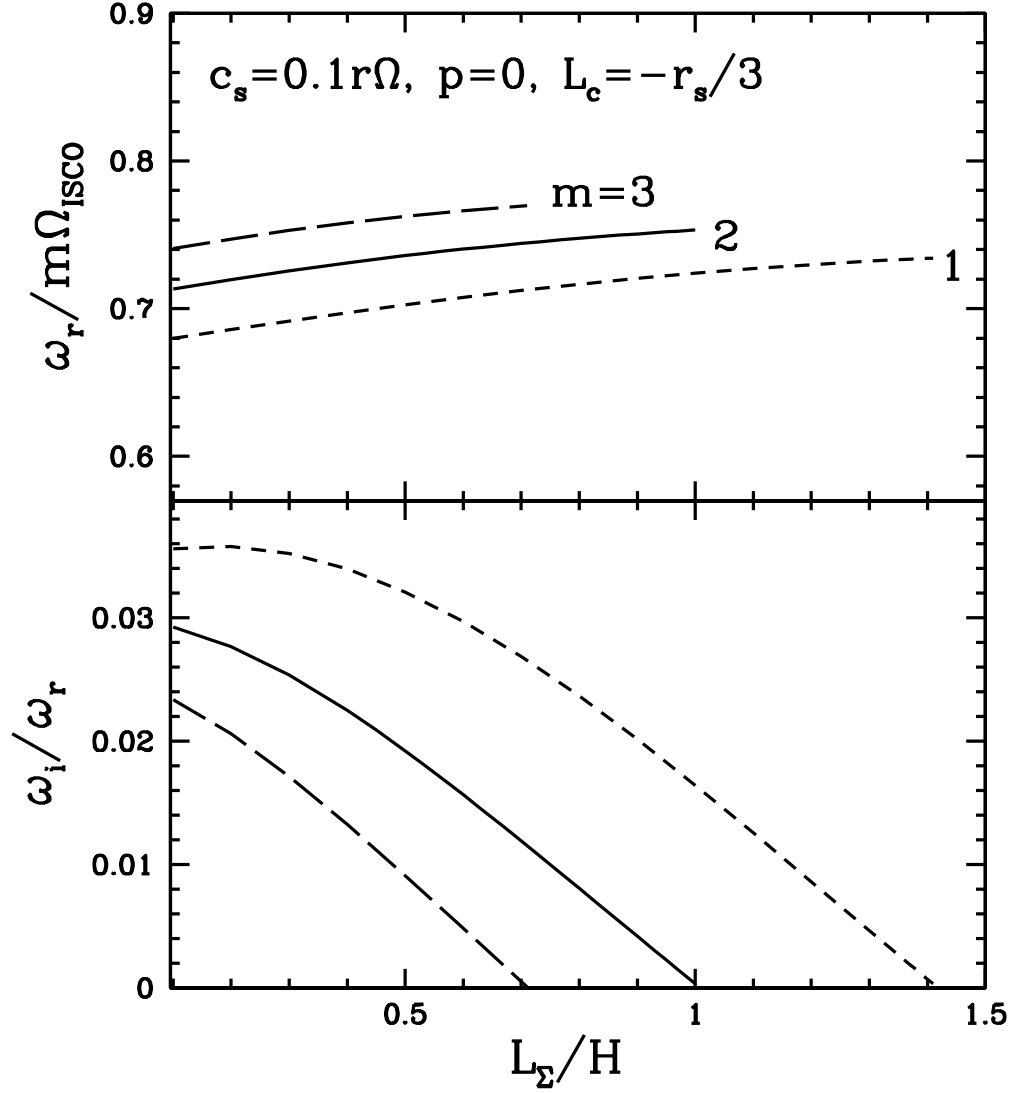
Figure 3.16: The real and imaginary frequencies of disk p-modes (with azimuthal wave numbers $m = 1, 2, 3$). The modes are calculated using the transonic inner boundary condition (3.36). The disk has a constant surface density profile and the sound speed is $c_s = 0.1r\Omega$. This figure shows the cases with $L_c = -r_s/3$ by varying L_Σ/H [see eq. (3.35)].
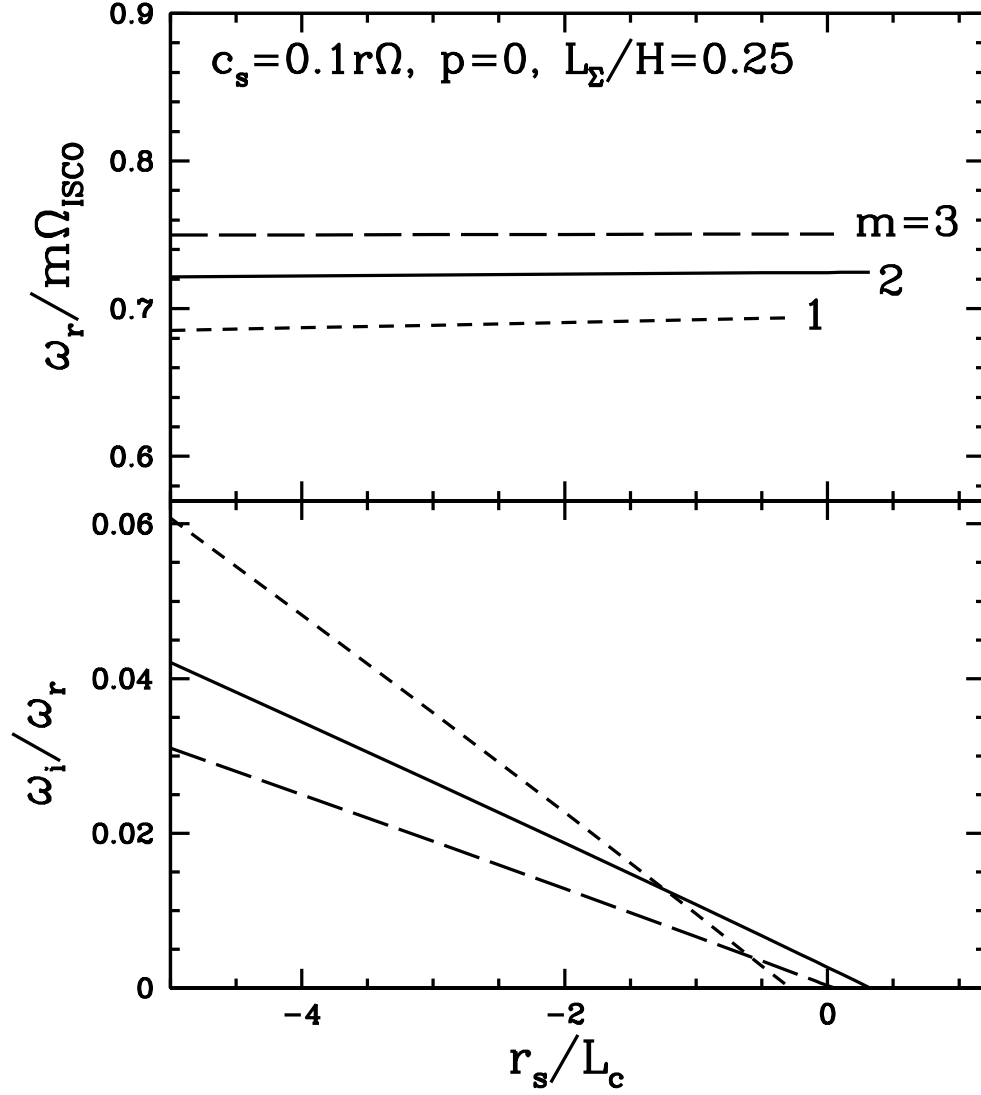
Figure 3.17: The real and imaginary frequencies of disk p-modes (with azimuthal wave numbers $m = 1, 2, 3$). The modes are calculated using the transonic inner boundary condition (3.36). The disk has a constant surface density profile and the sound speed is $c_s = 0.1r\Omega$. This figure shows the cases with $L_\Sigma/H = 0.25$ by varying r_s/L_c [see eq. (3.35)].

since $r_c < r_{\text{peak}}$, this leads to mode growth. Comparing with Figures 3.4 and 3.5, here the angular momentum flux at r_{in} is significantly nonzero, indicating wave loss through the sonic point. Nevertheless, the corotational instability is sufficiently strong to overcome the loss and makes the mode grow.

Figures 3.14-3.17 show the fundamental p-mode frequencies and growth rates as a function of the disk parameters. Consistent with the result of section 5.3 (see Fig. 8), growing modes are obtained for sufficiently small L_Σ. Negative L_c also tends to reduce wave loss at r_s and make the growing modes possible. Such values of L_Σ and L_c are not unreasonable for black hole accretion disks.

It is important to note that while the mode growth rates ω_i depend sensitively on the inner disk parameters, particularly the physical property of the transonic flow near the ISCO, the real mode frequencies ω_r show only weak dependence on the inner disk parameters (e.g., ω_r decreases with increasing sound speed; see Fig. 3.8). Thus we may expect that kHz QPOs appear only in certain accretion states of the black hole, and the frequencies do not vary much as the accretion rate changes.

3.6   The Role of Rossby Wave Instability

Lovelace et al. (1999) (see also Li et al. 2000) have shown that when the vortensity $\zeta = \kappa^2/(2\Omega\Sigma)$ has an extremum at a certain radius (r_{peak}) in the disk[5], it is possible to form normal Rossby modes around r_{peak}. If the trapped Rossby waves can propagate on both sides of the corotation, a standing pattern of waves of

---

[5]Lovelace et al. considered non-barotropic flows, so the "generalized vortensity" depends on the entropy profile of the disk.

opposite energies are formed, making the mode unstable — This is the "Rossby wave instability". Tagger & Varniere (2006) have considered the MHD version of the instability and suggested that it played a role in the diskoseismic modes around black holes (see also Tagger 2006).

We do not find any trapped Rossby modes in our calculation. To clarify the issue in light of works by Lovelace et al. and by Tagger & Varniere, let us consider equation (3.10) and define the effective potential

$$V_{\text{eff}}(r) = \frac{2m\Omega}{r\tilde{\omega}}\left(\frac{d}{dr}\ln\frac{\Omega\Sigma}{D}\right) + \frac{m^2}{r^2} + \frac{D}{c_s^2}. \tag{3.55}$$

The wave equation can be approximated by $(d^2/dr^2 - V_{\text{eff}})\delta h \simeq 0$ (see Tsang & Lai 2008a). We will focus on modes with r_c very close to r_{peak} (i.e., $|r_c - r_{\text{peak}}| \ll r_c$, so that $\omega_r \simeq m\Omega_{\text{peak}}$; see Fig. 1). For $|r - r_{\text{peak}}| \ll r_{\text{peak}}$ in a thin disk (so that m^2/r^2 can be neglected compared to κ^2/c_s^2), the effective potential becomes

$$V_{\text{eff}}(r) \simeq -\frac{2m\Omega}{r\tilde{\omega}}\left(\frac{d}{dr}\ln\zeta\right) + \frac{\kappa^2}{c_s^2} \simeq \frac{2}{qL_\zeta^2}\left(\frac{r - r_{\text{peak}}}{r - R_c}\right) + \frac{\kappa^2}{c_s^2}, \tag{3.56}$$

where in the second equality we have used $R_c = r_c - i(r_c\omega_i/q\omega_r)$, $\Omega \propto r^{-q}$, and defined L_ζ via

$$\frac{d\ln\zeta}{dr} = -\frac{r - r_{\text{peak}}}{L_\zeta^2}, \qquad (\text{for } |r - r_{\text{peak}}| \ll r_{\text{peak}}). \tag{3.57}$$

Consider the case $r_c < r_{\text{peak}}$ and assume $\omega_i \ll \omega_r$. The Rossby wave zone (where $V_{\text{eff}} < 0$) lies between r_c and $r_c + \Delta r_R$, with

$$\Delta r_R \simeq \frac{r_{\text{peak}} - r_c}{(q/2)(L_\zeta/H)^2}, \tag{3.58}$$

where $H \simeq c_s/\kappa$, and we have used $L_\zeta/H \sim r/H \gg 1$. The number of wavelengths in the Rossby zone is

$$\int_{r_c}^{r_c+\Delta r_R} k\,dr = \int_{r_c}^{r_c+\Delta r_R} (-V_{\text{eff}})^{1/2}\,dr \sim \frac{4H(r_{\text{peak}} - r_c)}{qL_\zeta^2} \tag{3.59}$$

Two points should be noted: (i) Since $\int_{r_c}^{r_c+\Delta r_R} k\, dr \ll 1$ for $L_\zeta \sim r_{\mathrm{peak}}$, no stationary wave can form in the Rossby zone; (ii) since the Rossby zone lies only on one side of the corotation radius, even if the mode can be trapped it will not grow by the Rossby wave instability mechanism. Similar result can be obtained for the $r_c > r_{\mathrm{peak}}$ case. We conclude that for the "smooth" vortensity maximum (with length scale $L_\zeta \sim r$; see the lower panel of Fig. 1) considered in this chapter, there is no trapped Rossby mode around r_{peak} and the Rossby wave instability is ineffective.

In the hypothetical situation where the vortensity ζ has a *minimum* at $r = r_{\mathrm{min}}$, equation (3.56) should be replaced by

$$V_{\mathrm{eff}}(r) \simeq -\frac{2}{qL_\zeta^2}\left(\frac{r - r_{\mathrm{min}}}{r - R_c}\right) + \frac{\kappa^2}{c_s^2}, \tag{3.60}$$

where we have used

$$\frac{d \ln \zeta}{dr} = \frac{r - r_{\mathrm{min}}}{L_\zeta^2}, \qquad (\text{for } |r - r_{\mathrm{min}}| \ll r_{\mathrm{min}}). \tag{3.61}$$

In this case, for a mode with $\omega_r = m\Omega(r_{\mathrm{min}})$ (or $r_c = r_{\mathrm{min}}$), we find $V_{\mathrm{eff}}(r_c) \simeq -2/(qL_\zeta^2) + 1/H^2$ (for $\omega_i \ll \omega_r$). When $V_{\mathrm{eff}}(r_c) < 0$, or when

$$L_\zeta < \left(\frac{2}{q}\right)^{1/2} H, \tag{3.62}$$

Rossby waves can propagate on both sides of the corotation, leading to mode growth — this is the Rossby wave instability. Thus, the Rossby wave instability would operate if there existed a "sharp" vortensity *minimum* in the disk (with ζ varying on the lengthscale comparable or less than the disk thickness) — this is not the case for typical black hole accretion disks considered in this chapter.

3.7 Discussion

High-frequency QPOs (HFQPOs) in black-hole X-ray binaries have been studied observationally for more than a decade now and they provide a potentially important tool for studying the strong gravitational fields of black holes (see Remillard & McClintock 2006). Despite much theoretical effort, the physical mechanisms that generate these QPOs remain unclear (see section 1.1 for a brief review of existing theoretical models). Ultimately, numerical simulations of realistic accretion disks around black holes may provide the answer. However, such simulations are still at their early stage of development and have their own limitations (e.g., De Villiers & Hawley 2003; Machida & Matsumoto 2003; Arras et al. 2006; Fragile et al. 2007; Reynolds & Miller 2008; Beckwith et al. 2008; Shafee et al. 2008; Noble et al. 2008), semi-analytical study remains a useful, complementary approach in order to identify the key physics involved.

In this chapter, we have studied the global instability of the non-axisymmetric p-modes in black-hole accretion disks. These modes have frequencies $\omega \sim (0.5 - 0.7)m\Omega_{\mathrm{ISCO}}$ (where m is the azimuthal wave number, Ω_{ISCO} is the disk rotation frequency at the inner-most stable circular orbit), where the pre-factor (0.5-0.7) depends on the inner disk structure. Recent works (Arras et al. 2006; Reynolds & Miller 2008; Fu & Lai 2008) suggested that, unlike other diskoseismic modes (g-modes and c-modes), the p-modes may be robust in the presence of disk magnetic fields and turbulence. Our linear analysis showed that due to GR effects, the p-modes may grow in amplitude due to wave absorptions at the corotation resonance. For a given m, only the lowest-order p-mode has sufficiently high frequency ($\omega > m\Omega_{\mathrm{peak}}$; see Fig. 1) to be driven overstable by the corotational instability, while high-order (lower frequency) modes are

damped by the corotational wave absorption.

The greatest uncertainty of our calculation of the p-mode growth rate concerns the boundary condition at the inner disk edge near the ISCO. In particular, the rapid radial inflow at the ISCO has the tendency to damp the mode (see Blaes 1986). While our analysis in section 5 indicates that this damping does not completely suppress the mode growth under certain disk conditions, it suggests that mode growth may not always be achieved in real black-hole accretion disks. Observationally, it is of interest to note that HFQPOs are observed only when the X-ray binaries are in the steep power-law state, while they do not appear in other spectral states (Remillard & McClintock 2006). In particular, HFQPOs are absent in the thermal (soft-high) state, believed to correspond to geometrically thin disks extending down to the ISCO. It is reasonable to expect that in this state p-modes are damped due to the rapid radial inflow.

Our current understanding of the steep power-law state (also called very high state) of black-hole X-ray binaries is rather limited. A thermal-radiation-emitting disk is suggested by spectral modelings, but it is not clear whether the disk is truncated at the ISCO or slightly larger radius (see Done et al. 2007). The observed power-law radiation component requires a significant corona that Compton up-scatters the disk thermal radiation. It is possible that in the steep power-law state, the inner disk behaves as a more reflective boundary (modeled in section 4) than a transonic flow (modeled in section 5), and thus more robust p-mode growth can be achieved. One possibility is that a significant magnetic field flux can accumulate in the inner disk when the disk accretion rate is sufficiently high (see Bisnovtyi-Kogan & Lovelace 2007; Rothstein & Lovelace 2008 and references therein). Such a magnetic field may also enhance the corotational

instability and induce variability in the power-law radiation flux (see Tagger & Varniere 2006).

Although the p-mode growth rates depend sensitively on a number of (uncertain) disk parameters (particularly those related to the inner disk boundary), the mode frequencies are more robust (see Figs. 5-7, 10-11). More precisely, the real mode frequency can be written as $\omega_r = \bar{\omega} m \Omega_{\mathrm{ISCO}}$, where $\bar{\omega} < 1$ depends weakly on m and has only modest dependence on disk parameters (e.g. sound speed). This implies a commensurate frequency ratio as observed in HFQPOs (note that in some of our models, the $m = 2, 3$ modes have the largest growth rates; see Fig. 5). The fact that $\bar{\omega} < 1$ would also make the numerical values of the p-mode frequencies more compatible with the measurements of the QPO frequencies and black hole masses.

We note that our calculations in this work are done with a pseudo-Newtonian potential. For direct comparison with observations a fully general relativistic calculation[6] is needed including a careful treatment of the corotation singularity. Including the effect of black hole spin would likely increase the value of ω by modifying r_{ISCO} and Ω_{ISCO}, while $\bar{\omega}$ will likely remain similar to the non-spinning case discussed above. We plan to study these effects in future work.

---

[6]Previous work on relativistic diskoseismic g-modes has been done by Perez et al. (1992) and Silbergleit & Wagoner (2008) while the c-mode was studied by Silbergleit et al. (2001). Axisymmetric p-modes were studied using a general relativistic formalism by Ortega-Rodriguez et al. (2002), but these do not include the effect of the corotation singularity.

CHAPTER 4

COROTATIONAL ABSORPTION OF DISKOSEISMIC C-MODES IN

BLACK HOLE ACCRETION DISKS

4.1   Introduction

Diskoseismic oscillations of accretion disks around relativistic objects have been studied for over two decades (e.g., Kato & Fukue 1980; Okazaki et al. 1987; Nowak & Wagoner 1991, see Wagoner 1999, Kato 2001 for reviews), and have been used as models for the time variability and quasi-periodic oscillations (QPOs) in X-ray emissions from black-hole X-ray binaries.

The c-modes (or so-called corrugation waves) were first proposed to explain low-frequency variabilities as their oscillation frequencies are lower than the associated g-modes and p-modes (see section 3). Kato (1983) and Okazaki & Kato (1985) showed the existence of one-armed ($m = 1$), low-frequency modes in nearly Keplerian (Newtonian) disks, while later work (Kato 1989; Silbergleit et al. 2001) demonstrated the presence of low-frequency c-modes in relativistic accretion disks, particularly the one-armed corrugation waves with a single node ($n = 1$; see section 3 below) in the vertical direction, which oscillate at (approximately) the Lense-Thirring precession frequency evaluated at the outer edge of the trapping region.

In the previous chapter, we studied the global corotational instability of non-axisymmetric p-modes ($n = 0$) in black hole accretion disks. The mode is trapped inside the corotation resonance radius r_c (where the wave pattern rotation speed ω/m equals the disk rotation rate Ω) and carries a negative energy.

We showed that when the mode frequency ω is sufficiently high, positive wave energy is absorbed at the corotation resonance, leading to the growth of mode amplitude. The mode growth is further enhanced by wave transmission beyond the corotation barrier. Non-axisymmetric g-modes, on the other hand, may contain a corotation resonance in the wave zone. Kato (2003) and Li, Goodman & Narayan (2003) showed that such g-modes are heavily damped as the wave propagate through the corotation resonance (see also Zhang & Lai 2006).

Diskoseismic c-modes are trapped in the inner most regions of black hole accretion disks. Although their primary wave zones are separated from the corotation resonance, the wave can tunnel through the evanescent barrier and propagate again around the corotation. In this chapter we calculate the analytic damping rate of c-modes due to wave absorption at the corotation resonance. In section 2 we briefly review the basic properties of perturbations in a thin isothermal disk, and present the basic working perturbation equations. In section 3 we discuss the propagation regions associated with various diskoseismic modes, while in section 4 we demonstrate the effect of the corotation resonance on wave propagation. In section 5 the effect of the corotation on the c-mode is studied and the c-mode damping rates are calculated for different disk parameters. Section 6 contains our conclusion.

4.2   Basic Setup and Equations

Consider a thin isothermal disk with the unperturbed velocity $\mathbf{u}_o = (0, r\Omega, 0)$ in the cylindrical coordinates. The vertical density profile is given by (for small

$z \ll r$)

$$\rho_o(r, z) = \frac{\Sigma(r)}{\sqrt{2\pi}H} \exp\left(-z^2/2H^2\right). \tag{4.1}$$

Here $\Sigma(r)$ is the (vertically integrated) surface density and $H = c_s/\Omega_\perp$ is the vertical scale height, where $\Omega_\perp$ is the vertical oscillation frequency and c_s is the isothermal sound.

Perturbing the mass and momentum conservation equations gives

$$\frac{\partial}{\partial t}\delta\rho + \nabla \cdot (\rho_o\delta\mathbf{u} + \mathbf{u}_o\delta\rho) = 0, \tag{4.2}$$

$$\frac{\partial}{\partial t}\delta\mathbf{u} + (\mathbf{u}_o \cdot \nabla)\delta\mathbf{u} + (\delta\mathbf{u} \cdot \nabla)\mathbf{u}_o = -\nabla\delta h, \tag{4.3}$$

with the enthalpy perturbation $\delta h \equiv \delta P/\rho = c_s^2\delta\rho/\rho$, where we assume that the perturbations are also isothermal. Assuming perturbations of the form $\delta P, \delta\mathbf{u}, \delta\rho \propto \exp(im\phi - i\omega t)$, we have

$$-i\tilde{\omega}\frac{\rho_o}{c_s^2}\delta h + \frac{1}{r}\frac{\partial}{\partial r}(r\rho_o\delta u_r) + \frac{im}{r}\rho_o\delta u_\phi + \frac{\partial}{\partial z}(\rho\delta u_z) = 0 \tag{4.4}$$

$$-i\tilde{\omega}\delta u_r - 2\Omega\delta u_\phi = -\frac{\partial}{\partial r}\delta h \tag{4.5}$$

$$-i\tilde{\omega}\delta u_\phi + \frac{\kappa^2}{2\Omega}\delta u_r = -\frac{im}{r}\delta h \tag{4.6}$$

$$-i\tilde{\omega}\delta u_z = -\frac{\partial}{\partial z}\delta h \tag{4.7}$$

where $\tilde{\omega} = \omega - m\Omega$. Following Okazaki et al. (1987), we assume a z-dependence of the perturbations such that $\delta h, \delta u_r, \delta u_\phi \propto H_n(z/H)$ where $H_n(z/H)$ is the Hermite polynomial of order n. Then equation (4.4) reduces to

$$-i\tilde{\omega}\frac{\rho_o}{c_s^2}\delta h + \frac{1}{r}\frac{\partial}{\partial r}(r\rho_o\delta u_r) + \frac{im}{r}\rho_o\delta u_\phi - \frac{n\rho_o}{i\tilde{\omega}}\delta h = 0 \tag{4.8}$$

Neglecting terms proportional to $dH/dr \sim O(1/r)$, and eliminating the velocity perturbations δu_r and δu_ϕ from equations (4.5), (4.6) and (4.8), we obtain (see eq. [29] in Zhang & Lai [2006])

$$\frac{d^2}{dr^2}\delta h - \left(\frac{d}{dr}\ln\frac{D}{r\Sigma}\right)\frac{d}{dr}\delta h + \left[\frac{2m\Omega}{r\tilde{\omega}}\frac{d}{dr}\ln\frac{D}{\Omega\Sigma} - \frac{m^2}{r^2} - \frac{D(\tilde{\omega}^2 - n\Omega_\perp^2)}{c_s^2\tilde{\omega}^2}\right]\delta h = 0, \tag{4.9}$$

where $D = \kappa^2 - \tilde{\omega}^2$. This is our basic working equation.

The approach above is Newtonian. More rigorous fully relativistic deriva-tions of the dispersion relation have been given by Ipser (1994, 1996), Perez et al. (1997), and Silbergleit et al. (2001). Some aspects of the general relativis-tic effects can be incorporated into our analysis by using the Paczynski-Witta psuedo-Newtonian potential, which gives $\kappa < \Omega = \Omega_\perp$. For our purposes of esti-mating the c-mode damping rates, it suffices to employ equation (4.9) but with the relevant fully general relativistic frequencies (e.g., Aliev & Gal'tsov 1981; Okazaki et al. 1987)

$$\Omega = \frac{1}{r^{3/2} + a},\tag{4.10}$$

$$\Omega_\perp = \Omega\left(1 - \frac{4a}{r^{3/2}} + \frac{3a^2}{r^2}\right)^{1/2},\tag{4.11}$$

$$\kappa = \Omega\left(1 - \frac{6}{r} + \frac{8a}{r^{3/2}} - \frac{3a^2}{r^2}\right)^{1/2},,\tag{4.12}$$

where the frequencies are in units of c^3/GM, r in units of GM/c^2, and a is the spin parameter of the black hole.

4.3   Propagation Diagram and C-Modes

There are three possible critical resonant points in the disk: the Lindblad reso-nances (LRs) where $D = 0$, the vertical resonances (VR) where $\tilde{\omega}^2 = n\Omega_\perp^2$, and the corotation resonance (CR) where $\tilde{\omega} = 0$. Far from these critical points, the WKB dispersion relation [for $\delta h \propto \exp(i \int k\, dr)$] takes the form (Okazaki et al. 1987)

$$c_s^2 k^2 = \frac{(\kappa^2 - \tilde{\omega}^2)(n\Omega_\perp^2 - \tilde{\omega}^2)}{\tilde{\omega}^2}.\tag{4.13}$$

The modes with $n = 0$ have no vertical structure, and are referred to as p-modes – their stability properties are studied in Lai & Tsang (2008). We focus on the
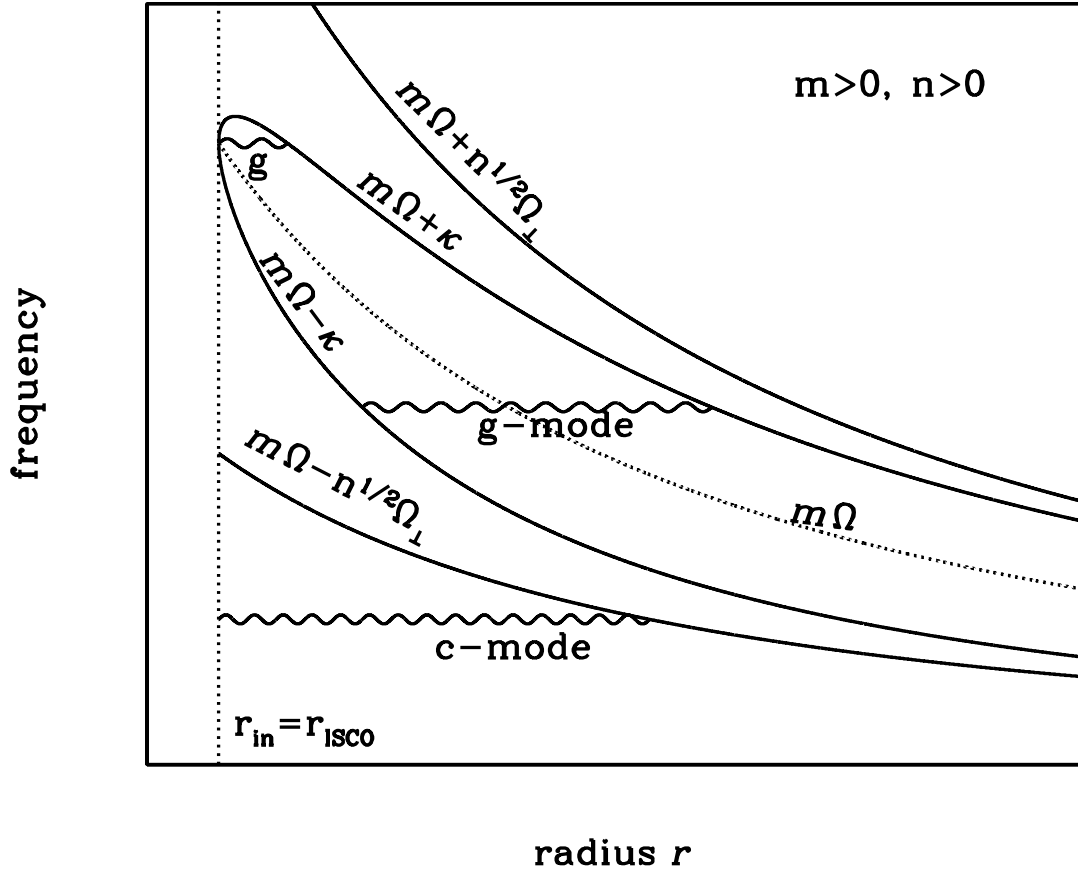
Figure 4.1: The propagation diagram for non-axisymmetric g-modes and c-modes. Note that the curves $m\Omega - \kappa$ and $m\Omega + \kappa$ meet at $r = r_{\mathrm{ISCO}}$ since $\kappa(r_{\mathrm{ISCO}}) = 0$ due to general relativistic effects. The g-modes are trapped between the inner Lindblad resonance (where $\omega = m\Omega - \kappa$) and the outer Lindblad resonance (where $\omega = m\Omega + \kappa$), or around the peak of the $m\Omega + \kappa$ curve.

modes with $n \geq 1$ and $m \geq 1$ in this chapter. Wave propagation is allowed in regions where $\tilde{\omega}^2 < \kappa^2 < n\Omega_\perp^2$ or $\tilde{\omega}^2 > n\Omega_\perp^2 > \kappa^2$ (note that $\kappa < \Omega_\perp$ in GR). The former defines the g-mode propagation zone: the mode is trapped in the region where $m\Omega - \kappa < \omega < m\Omega + \kappa$; the latter leads to c-modes, for which the wave zone is specified by $\omega < m\Omega - \sqrt{n}\Omega_\perp$ (see Fig. 1). Clearly, the c-modes exist only when $m\Omega - \sqrt{n}\Omega_\perp > 0$ and wave reflection occurs at $r = r_{in} = r_{ISCO}$, the radius of the Inner-most Stable Circular Orbit. For Newtonian disks, since $\Omega_\perp = \kappa = \Omega$ the c-modes can only exist if $m > \sqrt{n}$; for relativistic disks, however, $\Omega > \Omega_\perp$ (for spinning black holes), we can obtain modes for $m = \sqrt{n}$ that may have very low frequencies. The "fundamental" c-mode, with $m = n = 1$ is of particular interest (Kato 1990), since it corresponds to the Lense-Thirring precession of the inner, tilted disk. Note that for extremely low mode frequencies, the terms of order $1/r$ previously ignored may become important, and care must be taken to obtain the real eigenfrequencies for trapped modes. Here we ignore these complications and refer to Silbergleit et al. (2001) for a more thorough relativistic analysis.

4.4   Wave Absorption at the Corotation Resonance

The Lindblad resonances ($D = 0$) are apparent singularities of the master equation (4.9) [this can be seen easily by writing (4.9) as two coupled first-order differential equations], and no wave absorption occurs at the Lindblad resonances (e.g., Goldreich & Tremaine 1979; Li et al. 2003; Zhang & Lai 2006). The vertical resonances (where $\tilde{\omega}^2 = n\Omega_\perp^2$) act purely as turning points, and no wave absorption occurs there either. However, the corotation resonance must be treated more carefully (Kato 2003; Li et al. 2003; Zhang & Lai 2006).

Here we follow the analysis of Zhang & Lai (2006). Near the corotation ($r = r_c$, where $\omega = m\Omega$), equation (4.9) can be written as

$$\frac{d^2}{dr^2}\delta h - \frac{D(\tilde{\omega}^2 - n\Omega_\perp^2)}{c_s^2\tilde{\omega}^2}\delta h \simeq 0, \tag{4.14}$$

since for a thin disk the sound speed $c_s \ll r\Omega$ and the last term in (4.9) dominates the other terms. Defining $x \equiv (r - r_c)/r_c$ and expanding (4.14) around $x = 0$, we have

$$\frac{d^2}{dx^2}\delta h + \frac{C}{(x + i\epsilon)^2}\delta h = 0, \tag{4.15}$$

where

$$C \equiv \frac{n}{m^2}\left(\frac{\kappa\Omega_\perp}{c_s d\Omega/dr}\right)^2_{r_c} \gg 1. \tag{4.16}$$

In equation (4.15), we have inserted a small imaginary part $i\epsilon$ (with $\epsilon > 0$) in $1/x^2$ because we consider the response of the disk to a slowly growing perturbation.

The two independent solutions to equation (4.15) are

$$\delta h_\pm = z^{1/2}z^{\pm i\nu} = z^{1/2}e^{\pm i\nu \ln z} \tag{4.17}$$

where $\nu = \sqrt{C - \frac{1}{4}} \gg 1$ and $z = x + i\epsilon$. The solution $z^{1/2}z^{i\nu}$ has a local wavenumber $k = d(\nu \ln z)/dr = \nu/(r_c x)$, with the group velocity $v_g = d\omega/dk = -\tilde{\omega}/k = -qr_c x^2\omega/\nu < 0$ (where we have assumed $\Omega \propto r^{-q}$, with $q > 0$), thus it represents waves propagating toward small r. Similarly, the solution $z^{1/2}z^{-i\nu}$ has $v_g > 0$ and represents waves propagating toward large r.

As shown in Zhang & Lai (2006), waves with $n \geq 1$ can propagate into the corotation region and be absorbed there. Consider an incident wave propagating from the $x < 0$ (or $r < r_c$) region toward $x = 0$, with the amplitude (up to a constant factor)

$$\delta h(x < 0) = z^{1/2}e^{-i\nu \ln z} = ie^{\pi\nu}(-x)^{1/2}e^{-i\nu \ln(-x)}, \qquad \text{(incident wave)}. \tag{4.18}$$

92

The transmitted wave is simply

$$\delta h(x > 0) = x^{1/2} e^{-iv \ln x}, \qquad \text{(transmitted wave)}, \qquad (4.19)$$

and there is no reflection. Thus the amplitude of the transmitted wave is de-creased by a factor of $e^{-\pi v}$ (Zhang & Lai 2006). Similarly, a wave incident from the $r > r_c$ region toward r_c encounters the same attenuation. Since $v \gg 1$ for thin disks, We readily conclude that all waves incident upon the corotation will be absorbed (Kato 2003; Li et al. 2003; see Zhang & Lai 2006 and Lai & Zhang 2008 for applications of this result to the problem of wave excitation by external forces).

4.5   Corotational Damping of C-modes

The result of section 4 shows that waves propagating through the corotation are heavily damped. Since g-modes trapped between the inner and outer Lindblad resonances must cross the corotation, they are damped very quickly by coro-tation absorption, as shown by Kato (2003) and Li et al. (2003). Only higher frequency g-modes which are trapped around the peak of $m\Omega + \kappa$ (see Fig. 1) can avoid such corotational damping; these modes have frequencies $\omega \simeq m\Omega(r_{\text{ISCO}})$.

In this section we calculate the damping rate of the c-mode. The damping mechanism is illustrated in Fig. 2, where we also plot the effective potential:

$$V_{\text{eff}}(r) = \frac{D(\tilde{\omega}^2 - n\Omega_{\perp}^2)}{c_s^2 \tilde{\omega}^2} + \frac{m^2}{r^2} + \frac{2m\Omega}{r\tilde{\omega}} \left(\frac{d}{dr} \ln \frac{\Omega\Sigma}{D} \right). \qquad (4.20)$$

Based on the result of section 4, we will adopt the approximation that waves transmitted through the barrier between the inner vertical resonance (IVR) and

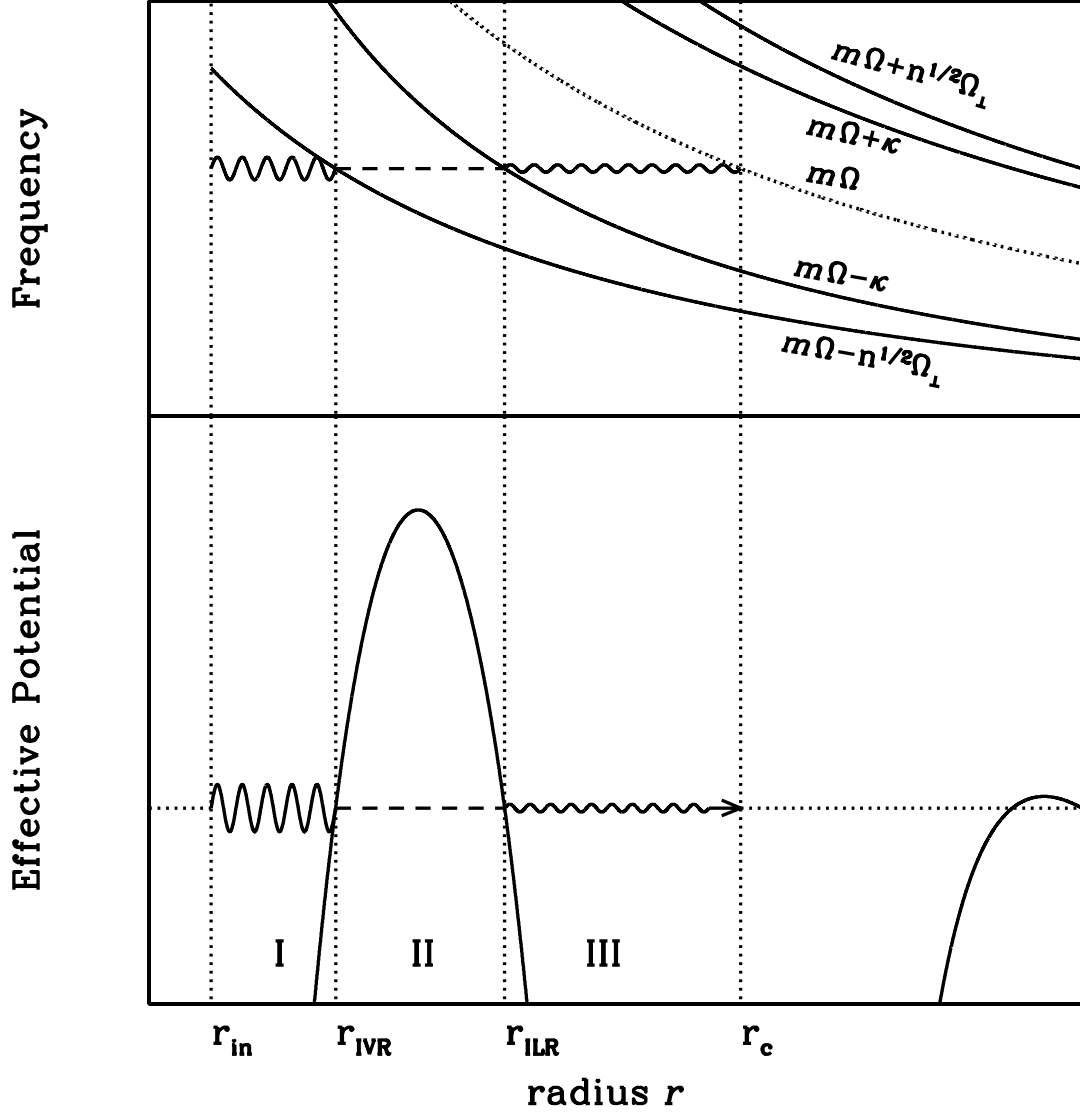Figure 4.2: The wave propagation diagram (upper panel) and effective potential (lower panel) for c-modes. The modes are trapped in region I (between $r_{in} = r_{ISCO}$ and the inner vertical resonance r_{IVR}), but can tunnel through an evanescent barrier (region II, between the IVR and the inner Lindblad resonance r_{ILR}) and propagate into the corotation (r_c), where they are absorbed.

the inner Lindblad resonance (ILR) are absorbed at the corotation. We will also assume that the inner disk boundary is completely reflective (see section 6).

4.5.1 Reflection Coefficient

We first calculate the reflection coefficient $\mathcal{R}$ when a wave in region I (see Fig. 2) propagates outward and is reflected back at the IVR.

From the dispersion relation (4.13), the group velocity of the wave is given by

$$v_g \equiv \frac{d\omega}{dk} = \frac{kc_s^2}{\tilde{\omega}\left[1 - (\kappa/\tilde{\omega})^2(n\Omega_\perp^2/\tilde{\omega}^2)\right]}. \tag{4.21}$$

The relative sign of v_g and the phase velocity $v_p = \omega/k$ is important. In region III ($r_{\mathrm{ILR}} < r < r_c$), v_g and v_p have the same sign, thus waves propagating outwards correspond to $k > 0$. In region I ($r < r_{\mathrm{IVR}}$), v_g and v_p have opposite signs, so that waves propagating outwards have $k < 0$ and waves propagating inwards have $k > 0$.

As shown in the previous section we can, to good approximation, assume that waves propagating into the corotation are completely damped. Thus, only an outward-propagating wave exists in region III (see Fig. 2), with the wave amplitude (up to a constant prefactor) given by

$$\delta h = A \exp\left(i \int_{r_{\mathrm{ILR}}}^{r} k\, dr + \frac{\pi}{4}\right), \tag{4.22}$$

where $k > 0$ is given by equation (4.13) and and $A \equiv \sqrt{D/rk\Sigma}$ is the WKB amplitude. The connection formulae for the ILR (Tsang & Lai 2008) are

$$\delta h_1 \sim \begin{cases} \frac{1}{2}A \exp\left(-\int_r^{r_{\mathrm{ILR}}} |k|\, dr\right) & \text{for } r \ll r_{\mathrm{ILR}} \\ A \cos\left(\int_{r_{\mathrm{ILR}}}^{r} k\, dr + \pi/4\right) & \text{for } r \gg r_{\mathrm{ILR}} \end{cases} \tag{4.23}$$

$$\delta h_2 \sim \begin{cases} A \exp\left(\int_r^{r_{\mathrm{ILR}}} |k|\, dr\right) & \text{for } r \ll r_{\mathrm{ILR}} \\ A \sin\left(\int_{r_{\mathrm{ILR}}}^r k\, dr + \pi/4\right) & \text{for } r \gg r_{\mathrm{ILR}} . \end{cases} \tag{4.24}$$

These then give for the evanescent zone (region II in Fig. 2):

$$\begin{aligned} \delta h &\simeq \frac{A}{2} \exp\left(-\int_r^{r_{\mathrm{ILR}}} |k|\, dr\right) + iA \exp\left(\int_r^{r_{\mathrm{ILR}}} |k|dr\right) \\ &= \frac{A}{2} \exp(-\Theta_{\mathrm{II}}) \exp\left(\int_{r_{\mathrm{IVR}}}^r |k|dr\right) + iA \exp(+\Theta_{\mathrm{II}}) \exp\left(-\int_{r_{\mathrm{IVR}}}^r |k|dr\right) \end{aligned} \tag{4.25}$$

where

$$\Theta_{\mathrm{II}} = \int_{r_{\mathrm{IVR}}}^{r_{\mathrm{ILR}}} |k|\, dr. \tag{4.26}$$

The connection formulae at the IVR can be similarly derived; they are [1]

$$\delta h_1 \sim \begin{cases} \frac{1}{2}A \exp\left(-\int_{r_{\mathrm{IVR}}}^r |k|\, dr\right) & \text{for } r \gg r_{\mathrm{IVR}} \\ A \sin\left(\int_r^{r_{\mathrm{IVR}}} k\, dr + \pi/4\right) & \text{for } r \ll r_{\mathrm{IVR}} \end{cases} \tag{4.27}$$

$$\delta h_2 \sim \begin{cases} A \exp\left(\int_{r_{\mathrm{IVR}}}^r |k|\, dr\right) & \text{for } r \gg r_{\mathrm{IVR}} \\ A \cos\left(\int_r^{r_{\mathrm{IVR}}} k\, dr + \pi/4\right) & \text{for } r \ll r_{\mathrm{IVR}} \end{cases} \tag{4.28}$$

(Abramowitz & Stegun 1964). Thus, we find that for $r < r_{\mathrm{IVR}}$ (region I in Fig. 2),

$$\delta h \simeq \frac{A}{2} e^{-\Theta_{\mathrm{II}}} \cos\left(\int_r^{r_{\mathrm{IVR}}} k\, dr + \frac{\pi}{4}\right) + i2A e^{\Theta_{\mathrm{II}}} \sin\left(\int_r^{r_{\mathrm{IVR}}} k\, dr + \frac{\pi}{4}\right) . \tag{4.29}$$

Expressing this in terms of traveling waves and defining $y = \int_{r_{\mathrm{IVR}}}^r k dr - \pi/4$, we have

$$\delta h \simeq iA \left[e^{-iy}\left(e^{+\Theta_{\mathrm{II}}} + \frac{1}{4}e^{-\Theta_{\mathrm{II}}}\right) - e^{+iy}\left(e^{\Theta_{\mathrm{II}}} - \frac{1}{4}e^{-\Theta_{\mathrm{II}}}\right) \right], \tag{4.30}$$

where the first term ($\propto e^{-iy}$) corresponds to the incident (outgoing) wave and the second term ($\propto e^{iy}$) the inward going wave reflected from the IVR. Thus the

---

[1]Note that around the IVR, the differential equation is matched by the Airy functions, rather than by the Airy function derivatives as in the case of the ILR.

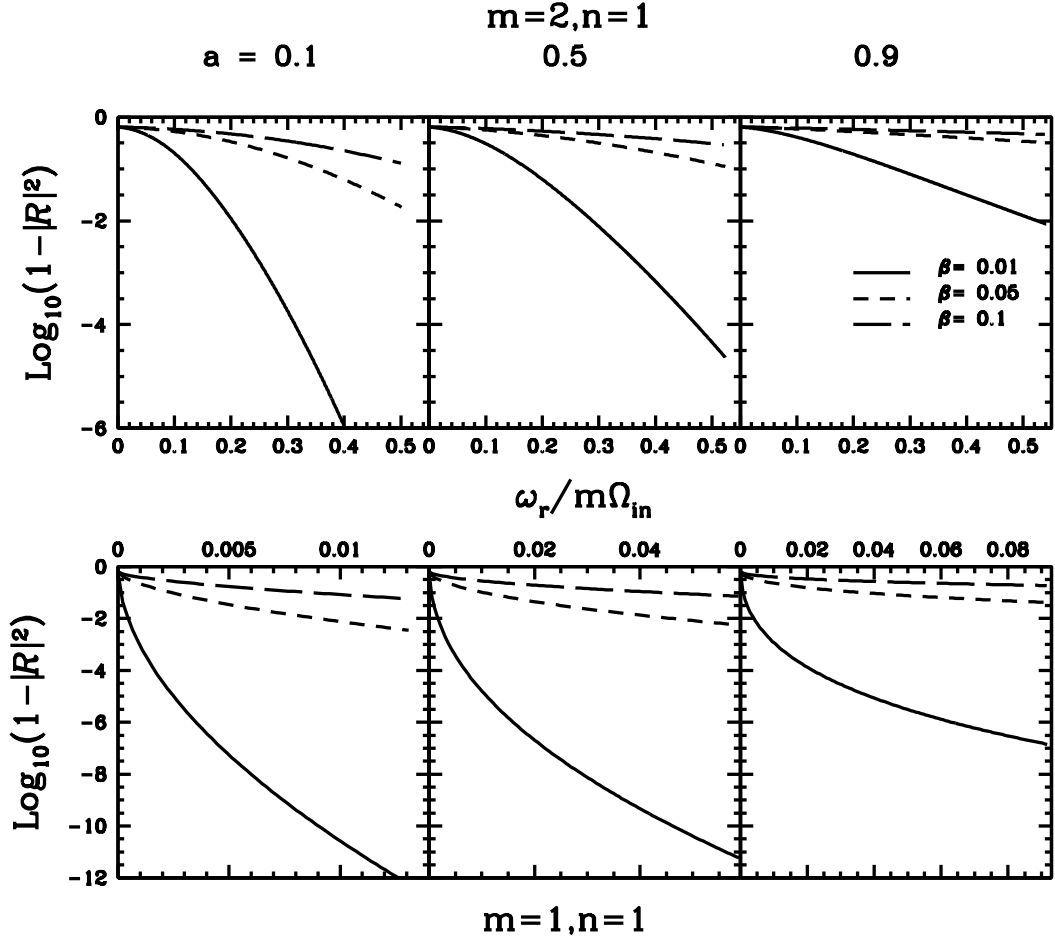Figure 4.3: The reflection coefficient, $\mathcal{R}$, of waves incident upon the inner vertical resonance (IVR), as a function of the (real) wave frequency ω_r (in units of $m\Omega_{in}$, where Ω_{in} is the disk rotation rate at $r = r_{in}$), for various black hole spin parameters (a) and sound speeds $c_s = \beta r\Omega_{in}$. The upper panels are for $m = 2$, $n = 1$ and the lower panels for $m = n = 1$.

reflection coefficient is

$$\mathcal{R} = -\frac{e^{\Theta_{II}} - \frac{1}{4}e^{-\Theta_{II}}}{e^{\Theta_{II}} + \frac{1}{4}e^{-\Theta_{II}}}, \tag{4.31}$$

and the transmission coefficient (through region II) is

$$\mathcal{T} = \frac{i}{e^{\Theta_{II}} + \frac{1}{4}e^{-\Theta_{II}}}. \tag{4.32}$$

We can clearly see that $|\mathcal{R}|^2 < 1$.

4.5.2   Trapped C-modes and their Damping Rates

Assuming a reflective boundary exists at $r = r_{\text{in}} < r_{\text{IVR}}$, we can develop trapped c-modes in the inner disk, between r_{in} and the IVR. To illustrate this we consider a simple boundary condition at $r = r_{\text{in}}$:

$$\delta h(r_{\text{in}}) = 0. \tag{4.33}$$

From section 5.1, the wave in region I can be written as

$$\delta h = A \exp(-iy) + \mathcal{R}A \exp(iy), \qquad \text{with } y = \int_{r_{\text{IVR}}}^{r} k \, dr - \pi/4. \tag{4.34}$$

where $k = k_r + ik_i$ is complex. Applying the boundary condition (4.33) to equation (4.34) yields the eigenvalue condition:

$$\exp(2i\Theta) = -i|\mathcal{R}|, \quad \text{with } \Theta = \int_{r_{\text{in}}}^{r_{\text{IVR}}} k \, dr = \Theta_r + i\Theta_i, \tag{4.35}$$

where Θ_r and Θ_i are real. The real eigen frequency ω_r is given by

$$\Theta_r = \int_{r_{\text{in}}}^{r_{\text{IVR}}} k_r \, dr = \int_{r_{\text{in}}}^{r_{\text{IVR}}} \frac{\sqrt{(\kappa^2 - \tilde{\omega}_r^2)(n\Omega_\perp^2 - \tilde{\omega}_r^2)}}{c_s|\tilde{\omega}_r|} \, dr = \mu\pi + \frac{3\pi}{4}, \tag{4.36}$$

where $\mu = 0, 1, 2, \cdots$ is an integer and $\tilde{\omega}_r = \omega_r - m\Omega < 0$ in the trapping region between r_{in} and r_{IVR}. The imaginary part of the frequency ω_i is determined by $|\mathcal{R}| = \exp(-2\Theta_i)$, or

$$\tanh \Theta_i = -\left(\frac{|\mathcal{R}| - 1}{|\mathcal{R}| + 1}\right). \tag{4.37}$$

Note that $\Theta_i = \int_{r_{\text{in}}}^{r_{\text{IVR}}} k_i \, dr \ll 1$ and

$$k_i = \omega_i \frac{dk}{d\omega}\bigg|_{\omega_r} = \frac{\omega_i \tilde{\omega}_r}{k_r c_s^2}\left(1 - \frac{n\kappa^2 \Omega_\perp^2}{\tilde{\omega}_r^4}\right). \tag{4.38}$$

We then obtain

$$\omega_i \simeq -\frac{1}{4}\exp(-2\Theta_{\text{II}})\left[\int_{r_{\text{in}}}^{r_{\text{IVR}}} \frac{|\tilde{\omega}_r|^2}{\sqrt{(\kappa^2 - \tilde{\omega}^2)(n\Omega_\perp^2 - \tilde{\omega}^2)}}\left(1 - \frac{n\kappa^2 \Omega_\perp^2}{\tilde{\omega}_r^4}\right)\frac{dr}{c_s}\right]^{-1}. \tag{4.39}$$

Note that in the trapping region (between r_{in} and r_{IVR}), $n\kappa^2 \Omega_\perp^2/\tilde{\omega}^4 < 1$. Thus the mode is always damped ($\omega_i < 0$).

4.5.3   Numerical Results

Figure 3 depicts the reflection coefficients for waves impinging upon the inner vertical resonance (IVR) from $r < r_{\text{IVR}}$ as a function of the wave frequency. We consider both the $m = 2$, $n = 1$ and the $m = 1$, $n = 1$ modes. The real frequency ranges from 0 to $(m\Omega - \sqrt{n}\Omega_\perp)|_{r_{\text{in}}}$. Waves with higher frequencies are "protected" by a larger potential barrier in the evanescent zone (larger Θ_{II}) and have $|\mathcal{R}|^2$ closer to unity.

Figures 4-5 show the real and imaginary c-mode frequencies, computed using the WKB expressions derived in section 5.2. Waves with higher frequencies have smaller damping rate $|\omega_i|$, consistent with the reflectivity results shown in Fig. 3. The damping rate is also smaller for cooler (smaller β) disks. For the

Figure 4.4: The real and imaginary frequencies for the primary trapped c-mode with the $\delta h(r_{\rm in}) = 0$ boundary condition and $r_{\rm in} = r_{\rm ISCO}$ for various sound speeds versus the black hole spin parameter.
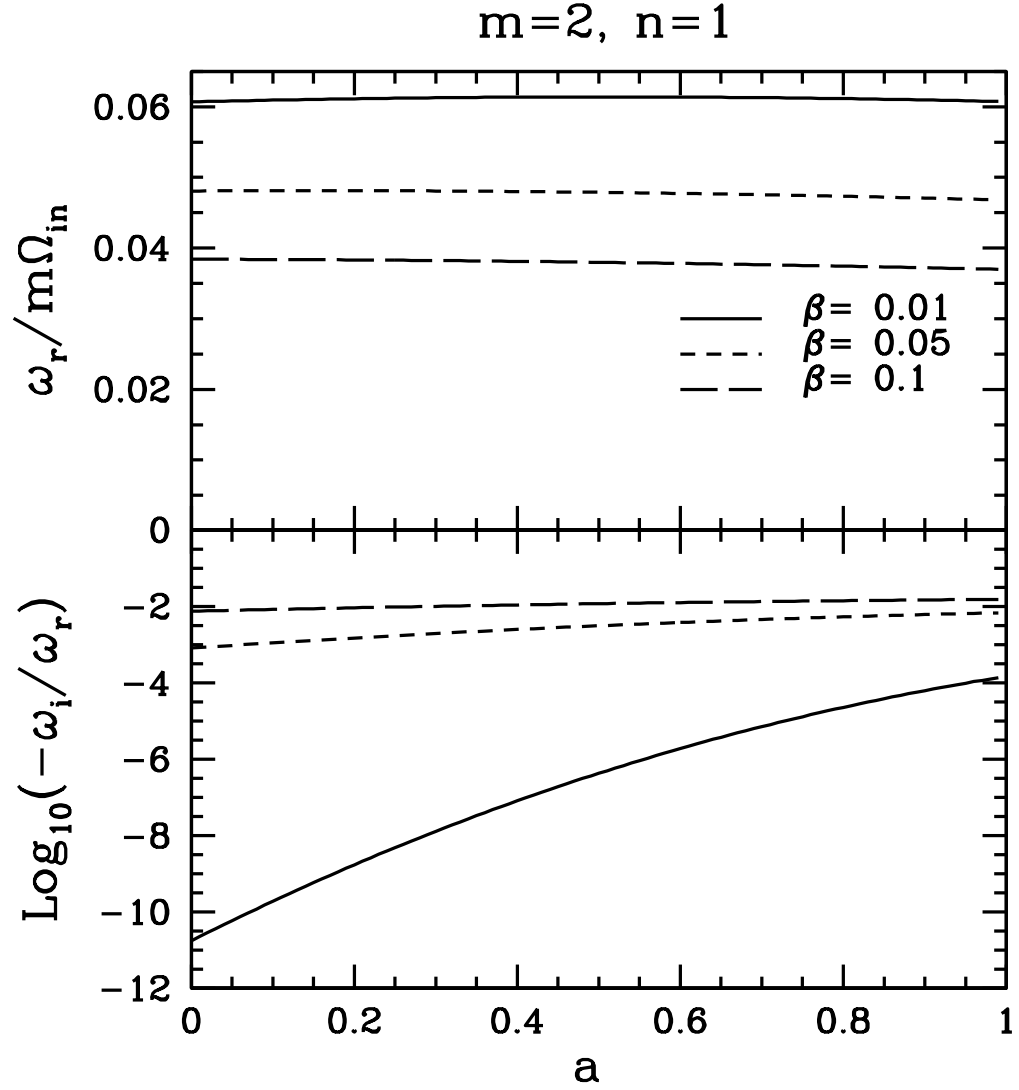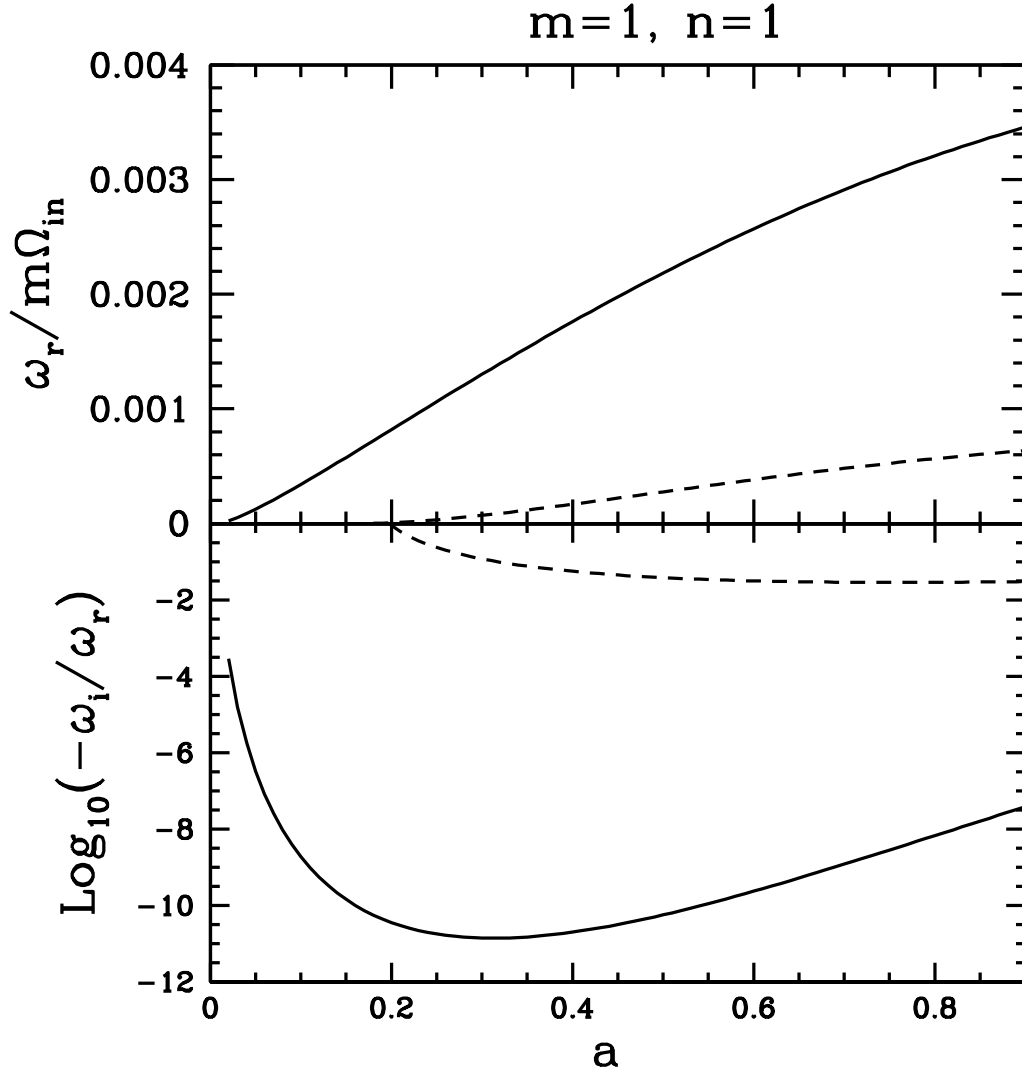
Figure 4.5: The real and imaginary frequencies for the primary trapped c-mode with the $\delta h(r_{in}) = 0$ boundary condition and $r_{in} = r_{ISCO}$ for various sound speeds versus the black hole spin parameter. The legend is the same as figure 4.4. Note that there is no mode for the one-armed corrugation wave for sound speed $c_s = 0.1 r\Omega_{in}$.

$m > n$ case (e.g. Fig. 4, left panel), the dimensionless damping rate $|\omega_i|/m\Omega_{in}$ increases with increasing a (while $\omega_r/m\Omega_{in}$ remans approximately constant), because the width of the region between r_{IVR} and r_{ILR} is smaller for larger a. For the $m = n = 1$ case (Fig. 4, right panel) the range of possible c-mode frequencies is bounded from above by the Lense-Thirring precession frequency at the inner boundary. Thus $\omega_r \to 0$ when $a \to 0$. This leads to larger $|\omega_i/\omega_r|$ for small a since the potential barrier in the evanescent zone decreases with decreasing $\omega_r/m\Omega_{in}$. Note that although we use the relativistic frequencies (4.10)-(4.12) our calculations not fully relativistic, and the real frequencies calculated shown in Fig. 4, particularly for the $m = n = 1$ mode with large black hole spin parameter a, are correct only in orders of magnitude [Fully relativistic calculation of the real frequencies of these trapped modes was done by Silbergleit et al. (2001).] Also note that adopting different inner disk boundary conditions would lead to different real mode eigenfrequencies than presented in Fig. 4.

Finally, we note that equation (4.39) is valid only when there is no loss of wave energy at the inner disk boundary r_{in}. In the presence of the rapid radial inflow at the ISCO, we would expect additional mode damping due to the leakage of waves into the plunging region of the disk (see Lai & Tsang 2008 for a study of such leakage for p-modes). Alternatively, a sufficiently strong excitation mechanism is needed to overcome the corotational damping and make the c-modes grow.

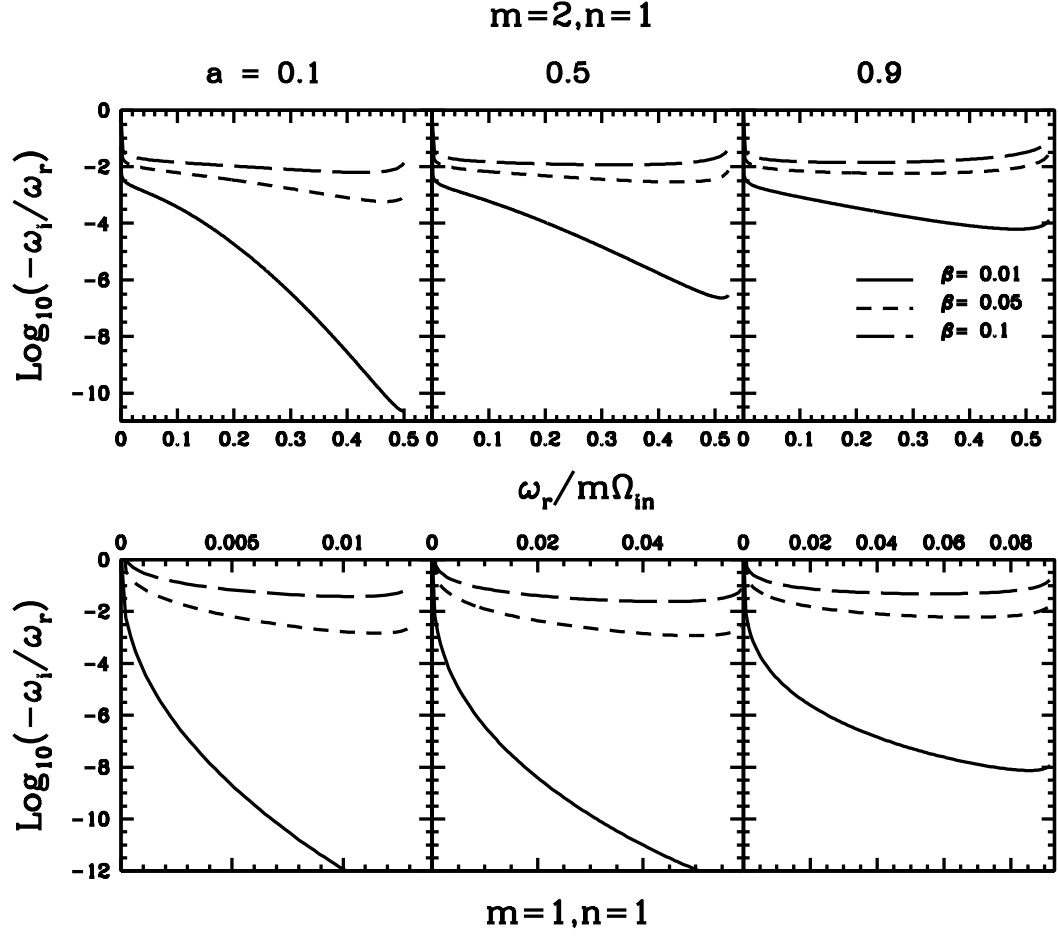Figure 4.6: The damping rate $|\omega_i|$ for various sound speeds and black hole spin parameters for c-modes with purely reflective boundary conditions at r_{in} as a function of the real mode frequencies ω_r. The upper panels show the results for the $m = 2, n = 1$ modes and the lower panels show the $m = n = 1$ modes. The sound speeds are taken to be constant, $c_s = \beta r \Omega_{in}$.

4.6 Conclusion

In this chapter, we have shown that diskoseismic c-modes suffer corotational damping due to wave absorption at the corotation resonance. These modes are trapped between the inner disk edge and the inner vertical resonance (where $\omega - m\Omega = -\sqrt{n}\Omega_\perp$, with $m, n \geq 1$), but can tunnel through the evanescent zone and leak out to the corotation zone where wave absorption occurs. The mode damping rates are generally much smaller than the mode frequencies, and depend sensitively on the disk sound speed and the black hole spin parameters.

With this chapter, we now have in hand a complete picture of how the corotation resonance affects various diskoseismic modes in black-hole accretion disks, at least in the linear regime: Non-axisymmetric g-modes are heavily damped at the corotation resonance (Kato 2003; Li et al. 2003), while p-modes (inertial-acoustic modes) can be overstable due to the corotational wave absorption (see Lai & Tsang 2008 and references therein). The corotational damping rates of c-modes are much smaller than those of g-modes.

Diskoseismic c-modes have been invoked to explain low-frequency variabilities in black-hole X-ray binaries (van der Klis 2006; Remillard & McClintock 2006). Fu & Lai (2008) showed that the basic properties of c-modes are largely unaffected by the disk magnetic fields and thus these modes are be present in real disks. The results presented in this chapter show that in order for the c-modes to be observable, a sufficiently strong excitation mechanism is needed to overcome the corotational damping.

CHAPTER 5

INTERFACE MODES AND THEIR INSTABILITIES IN ACCRETION DISK
BOUNDARY LAYERS

5.1   Introduction

Quasi-periodic variabilities have been observed in the timing data of various
types of accreting objects. Several types of quasi-periodic oscillations (QPOs)
are observed in X-ray binaries with accreting black holes (BHs) or neutron stars
(NSs) (e.g., Remillard & McClintock 2006; Van der Klis 2006). Oscillations are
also seen in the outbursts of accreting white dwarf (WD) systems (e.g., Patterson
1981; see Warner 2004 for a review).

In accreting NS and BH X-ray binaries the observed QPO frequencies (40 −
450 Hz for the high-frequency QPOs in the BH systems and $\gtrsim$ 300 Hz for kHz
QPOs in the NS systems) imply a source close to the central compact object
where the Keplerian orbital frequencies are high. Since the BH systems lack a
hard surface where oscillations may occur, it is likely that the source of the vari-
ability is in the inner regions of the disc itself or in some interface regions be-
tween the disc and the plunging flow. Gilfanov et al (2003), however, found that,
based on spectral analysis of the disc emission components, the quasi-periodic
variability in Low Mass NS X-ray Binary systems are most likely caused by vari-
ations in the disc boundary layer, rather than the disc itself.

In Cataclysmic Variables (CVs) the Dwarf Nova Oscillations (DNOs) seen
during during outbursts have frequencies roughly corresponding to the Keple-
rian rotation rate at the WD surface (e.g., Patterson, 1981; Warner, 2004; Knigge

et al, 1998), which imply an origin at or near the inner disk boundary.

Several models involving accretion disk boundary dynamics have been proposed in different contexts. Popham (1999) studied the effect of a non-axysymmetric bulge at the optically thick to optically thin transition radius as a model for DNOs. Piro & Bildsten (2004) examined the surface wave oscillations that would occur within the thin equatorial belt around a non-magnetized WD formed by the accretion spreading layer, while Warner & Woudt (2002) considered accretion onto a slipping belt. In the context of accreting magnetic (neutron) stars, Arons & Lea (1976) and Elsner & Lamb (1977) considered the interchange instability at the magnetosphere boundary. Spruit & Taam (1990) and Spruit, Stehle & Papaloizou (1995) investigated the stability of thin rotating magnetized discs. Of particular relevance to the present chapter is the work of Li & Narayan (2004), who examined a simplified cylindrical model of the Rayleigh-Taylor and Kelvin-Helmholtz instabilities at the boundary between a magnetosphere and an incompressible rotating flow. There have also been a number of numerical simulations of the interface at the magnetosphere-disc boundary (see Romanova et al., 2008 and Kulkarni & Romanova, 2008 and references therein).

In this chapter we study global non-axisymmetric oscillation modes confined near inner boundary of the accretion disc (interface modes). We consider two simple models. The first model involves the magnetosphere-disc boundary similar to the model of Li & Narayan (2004): we consider an uniformly rotating incompressible magnetosphere with low gas density (where magnetic pressure dominates), which truncates a thin barotropic accretion disc (where gas pressure dominates). This situation may arise from magnetic field build up due

to accretion (e.g., Bisnovatyi-Kogan & Ruzmaikin, 1974, 1976; Igumenshchev et al., 2003; Rothstein & Lovelace, 2008) or by the magnetosphere of a central (neutron) star. Unlike Li & Narayan (2004), who restricted their model to incompressible fluid, our discs are compressible and we show that because of the differential rotation of the disc, finite disc sound speed plays an important role in the development of the instability of the interface modes.

In our second model we examine the interface modes for accretion onto a non-magnetic stellar surface. Though the structure of the boundary layer is non-trivial and may affect boundary modes (see, e.g., Carroll et al., 1985; Collins et al., 2000), we consider the instabilities for a thin disc truncated by a sharp transition to a dense uniformly rotating stellar atmosphere. This simplified model may provide insight for modes with characteristic radial length scale much greater than the radial length scale of the boundary layer.

In Section 2 we describe the basic setup for the magnetospheric boundary model, and in Section 3 we discuss the resulting interface mode instabilities. We describe the star-disc boundary and analyze its possible instabilities in Section 4. We then conclude in Section 5 with a discussion of possible applications of our findings.

5.2   Magnetosphere-Disc Setup

We begin by considering a simplified model of the magnetosphere-disc boundary similar to the one considered by Li & Narayan (2004). The magnetic field is assumed to be negligible in the disc region ($r > r_{\rm in}$), while the magnetosphere region ($r < r_{\rm in}$) is assumed to be incompressible and have low density compared

to the disc region, with purely vertical magnetic field. Unlike Li & Narayan (2004), who assumed infinite sound speed in the disc, our disc has sound speed c_s much less than the disk rotation speed $r\Omega$.

In terms of the vertically integrated density (Σ), pressure (P), magnetic field (**B**) and fluid velocity (**u**) the ideal MHD equations are:

$$\frac{\partial \Sigma}{\partial t} + \nabla \cdot (\Sigma \mathbf{u}) = 0 \tag{5.1}$$

$$\frac{\partial \mathbf{u}}{\partial t} + (\mathbf{u} \cdot \nabla)\mathbf{u} = -\frac{1}{\Sigma}\nabla\Pi - \nabla\Phi + \frac{1}{\Sigma}\mathbf{T} \tag{5.2}$$

$$\frac{\partial \mathbf{B}}{\partial t} = \nabla \times (\mathbf{u} \times \mathbf{B}). \tag{5.3}$$

where $\Pi \equiv P + B^2/8\pi$ is the total pressure, $\mathbf{T} = \frac{1}{4\pi}(\mathbf{B} \cdot \nabla)\mathbf{B}$ is the magnetic tension, and Φ is the gravitational potential due to the central object (e.g. Fu & Lai, 2008). Using cylindrical coordinates (r, ϕ, z), we consider the case where the magnetic field is purely poloidal and $\mathbf{B} = B_z\hat{z}$ in the disc plane, which gives $\mathbf{T} = 0$. We assume an axisymmetric background flow with fluid velocity $\mathbf{u} = r\Omega(r)\hat{\phi}$. The unperturbed flow satisfies the condition

$$g_{\text{eff}} \equiv -\frac{1}{\Sigma}\frac{d\Pi}{dr} = \frac{d\Phi}{dr} - \Omega^2 r\,. \tag{5.4}$$

The linearized equations of (5.1) and (5.2) with perturbations of the form $e^{im\phi - i\omega t}$ (assuming no vertical dependence) take the form:

$$-i\tilde{\omega}\delta\Sigma + \frac{1}{r}\frac{\partial}{\partial r}(\Sigma r \delta u_r) + \frac{im\Sigma}{r}\delta u_\phi = 0\,, \tag{5.5}$$

$$-i\tilde{\omega}\delta u_r - 2\Omega\delta u_\phi = -g_{\text{eff}}\frac{\delta\Sigma}{\Sigma} - \frac{1}{\Sigma}\frac{\partial}{\partial r}\delta\Pi\,, \tag{5.6}$$

$$-i\tilde{\omega}\delta u_\phi + \frac{\kappa^2}{2\Omega}\delta u_r = -\frac{im}{\Sigma r}\delta\Pi\,, \tag{5.7}$$

where $\tilde{\omega} = \omega - m\Omega$ is the Doppler shifted frequency, $\kappa = \left[\frac{2\Omega}{r}\frac{d}{dr}(r^2\Omega)\right]^{1/2}$ is the radial epicyclic frequency, and $\delta\Sigma$, $\delta\Pi$ and $\delta\mathbf{u}$ are the Eulerian perturbations of

the fluid variables. Additionally, assuming a barotropic flow we have

$$\delta\Sigma = \frac{1}{c_s^2}\delta P = \frac{1}{c_s^2}(\delta\Pi - \frac{1}{4\pi}\mathbf{B} \cdot \delta\mathbf{B}) \, . \tag{5.8}$$

with the sound speed $c_s \equiv (dP/d\Sigma)^{1/2}$.

5.2.1 The Magnetosphere

In the inner, magnetically dominated region ($r < r_{\rm in}$), we assume the flow to be incompressible, and have uniform rotation ($\Omega = \Omega_- = $ const) and uniform surface density ($\Sigma = \Sigma_- = $ const). Equations (5.5) - (5.7) then reduce to

$$\frac{1}{r}\frac{\partial}{\partial r}(\Sigma r \delta u_r) + \frac{im\Sigma}{r}\delta u_\phi = 0 \tag{5.9}$$

$$-i\tilde{\omega}\delta u_r - 2\Omega\delta u_\phi = -\frac{1}{\Sigma}\frac{\partial}{\partial r}\delta\Pi \tag{5.10}$$

$$-i\tilde{\omega}\delta u_\phi + \frac{\kappa^2}{2\Omega}\delta u_r = -\frac{im}{\Sigma r}\delta\Pi, \tag{5.11}$$

As in Li & Narayan (2004) we define $W \equiv r\delta u_r$ and find $\delta u_\phi = (i/m)dW/dr$ and

$$\frac{1}{r}\frac{d}{dr}\left(r\frac{dW}{dr}\right) - \frac{m^2}{r^2}\left[1 - \frac{r}{m\tilde{\omega}}\frac{d}{dr}\left(\frac{\kappa^2}{2\Omega}\right)\right]W = 0 \, . \tag{5.12}$$

For uniform rotation, $\kappa = 2\Omega$, equation (5.12) has the solution $W \propto r^{\pm m}$. Since $r < r_{\rm in}$, we take the positive sign to be the physical solution so that the perturbation falls off away from the interface. Thus the exact solution for the $r < r_{\rm in}$ region is

$$\delta u_r = \delta u_r(r_{\rm in})\left(\frac{r}{r_{\rm in}}\right)^{m-1} \, . \tag{5.13}$$

5.2.2 The Disc

In the disc ($r > r_{\rm in}$), we take the magnetic field to be small, such that $P \gg B^2/(8\pi)$, and the angular velocity of the unperturbed flow to be nearly Keplerian, such
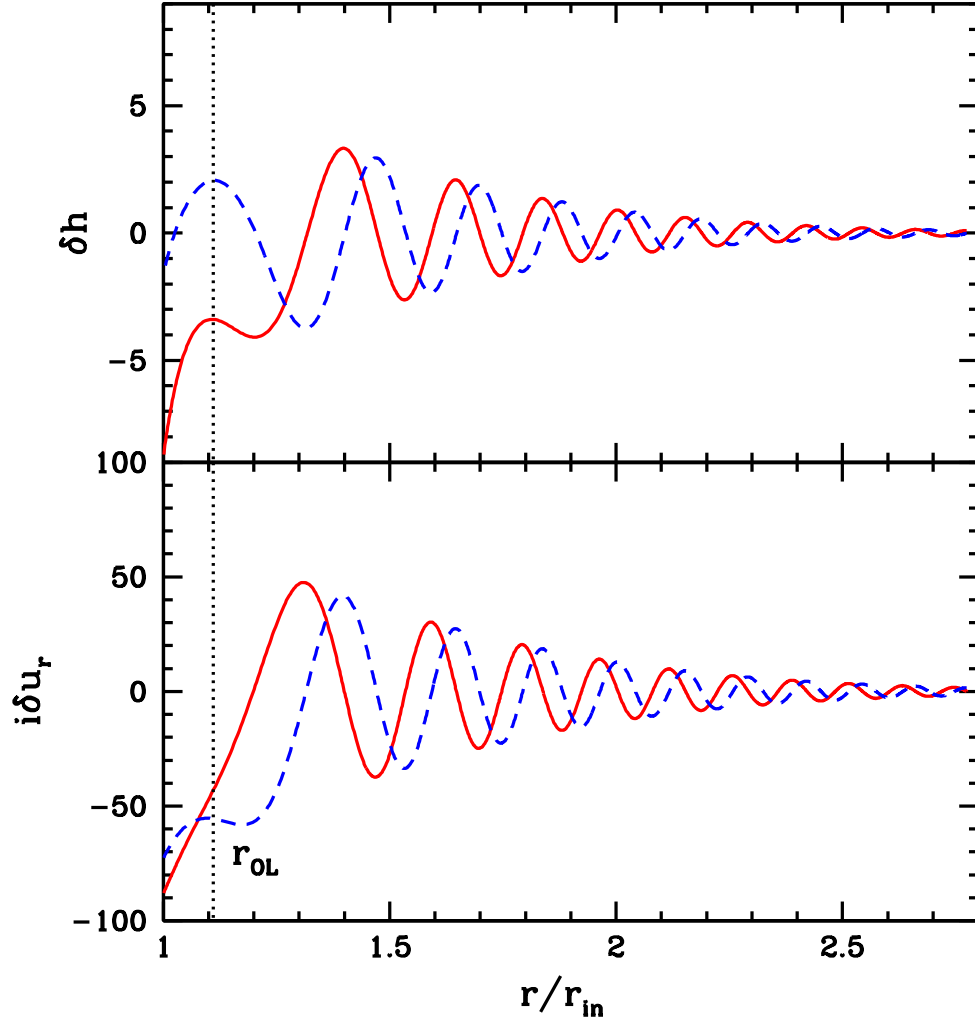
Figure 5.1: The wavefunctions for the interface mode for $m = 4$, $c_s = 0.1r\Omega$, $\Sigma_-/\Sigma_+ = 1/99$ and $\Omega_-/\Omega_{in} = 1$, with the mode frequency $\omega/\Omega_{in} = 4.275 + 0.1914i$, where $\Omega_{in} \equiv \Omega(r_{in+}) \simeq \Omega_k(r_{in})$. The real components are shown in solid lines, while the imaginary components are dashed lines. Note that for the interface modes only the outer Lindblad resonance (r_{OL}, denoted by the dotted line) exists outside r_{in}

that $\Omega(r) \approx \Omega_k(r) \equiv \sqrt{\frac{1}{r}\frac{d\Phi}{dr}}$. Rewriting equations (5.5) - (5.7) we have

$$-i\tilde{\omega}\frac{\Sigma}{c_s^2}\delta h + \frac{1}{r}\frac{\partial}{\partial r}(\Sigma r \delta u_r) + \frac{im\Sigma}{r}\delta u_\phi \quad = \quad 0 \,, \tag{5.14}$$

$$-i\tilde{\omega}\delta u_r - 2\Omega\delta u_\phi \quad = \quad -\frac{\partial}{\partial r}\delta h \,, \tag{5.15}$$

$$-i\tilde{\omega}\delta u_\phi + \frac{\kappa^2}{2\Omega}\delta u_r \quad = \quad -\frac{im}{r}\delta h \,, \tag{5.16}$$

where

$$\delta h \equiv c_s^2\frac{\delta\Sigma}{\Sigma} = \frac{\delta P}{\Sigma} \tag{5.17}$$

is the enthalpy perturbation. Eliminating the velocity perturbations in favor of the enthalpy, we obtain the second order ODE for the enthalpy perturbation in the disc,

$$\left[\frac{d^2}{dr^2} - \frac{d}{dr}\left(\ln\frac{D}{r\Sigma}\right)\frac{d}{dr} - \frac{2m\Omega}{r\tilde{\omega}}\left(\frac{d}{dr}\ln\frac{\Omega\Sigma}{D}\right) - \frac{m^2}{r^2} - \frac{D}{c_s^2}\right]\delta h = 0 \,. \tag{5.18}$$

where $D \equiv \kappa^2 - \tilde{\omega}^2$. For concreteness we will assume a power-law disc surface density profile $\Sigma \propto r^{-p}$.

5.2.3   Matching Conditions Across the Interface

The matching conditions across the interface at r_{in} between the magnetosphere and the disc region are given by demanding the continuity of the Lagrangian displacement in the radial direction $\xi_r = i\delta u_r/\tilde{\omega}$, and the total Lagrangian pressure perturbation $\Delta\Pi = \delta\Pi + \xi_r\frac{d\Pi}{dr}$ across the boundary. The former gives

$$\frac{i\delta u_{r+}}{\tilde{\omega}_+} = \frac{i\delta u_{r-}}{\tilde{\omega}_-} \,, \tag{5.19}$$

where the subscript "±" implifes that the quantities are evaluated at $r = r_{in\pm}$.
The total Lagrangian pressure perturbation for $r = r_{in-}$ is given by

$$
\begin{aligned}
\Delta\Pi_- &= \Sigma_- \left[\left(\frac{i\kappa^2}{2m\Omega} + \frac{i}{r\tilde\omega} \frac{d\Pi}{dr} \right) W + \frac{ir\tilde\omega}{m^2} \frac{dW}{dr} \right]_{r_{in-}} \\
&= \Sigma_- \left[\frac{2r\Omega\tilde\omega}{m} - g_{eff-} + \frac{r\tilde\omega^2}{m} \right] \frac{i\delta u_r}{\tilde\omega} \bigg|_{r_{in-}}.
\end{aligned}
\tag{5.20}
$$

In the disc region, we have

$$
\begin{aligned}
\Delta\Pi_+ &= \Delta P_+ = \Sigma_+ \left(\delta h + \frac{i\delta u_r}{\tilde\omega} \frac{1}{\Sigma} \frac{dP}{dr} \right)_{r_{in+}} \\
&= \Sigma_+ \left(\frac{\tilde\omega\delta h}{i\delta u_r} - \frac{pc_s^2}{r} \right) \frac{i\delta u_r}{\tilde\omega_+} \bigg|_{r_{in+}}.
\end{aligned}
\tag{5.21}
$$

The condition $\Delta\Pi_+ = \Delta\Pi_-$ then gives

$$
\Sigma_+ \left(\frac{\tilde\omega\delta h}{i\delta u_r} - \frac{pc_s^2}{r} \right)_{r_{in+}} = \Sigma_- \left(\frac{2r\Omega\tilde\omega}{m} - g_{eff} + \frac{r\tilde\omega^2}{m} \right)_{r_{in-}}.
\tag{5.22}
$$

5.3   Interface Modes at the Magnetosphere-Disc Boundary

Perturbations mainly confined to the magnetosphere-disc interface can become
unstable due to Rayleigh-Taylor or Kelvin Helmholtz instability. In order to cal-
culate the growth rates, we must solve the eigenvalue problem given by equa-
tion (5.18) with an outgoing wave boundary condition at some outer radius, and
equation (5.22) at the interface radius r_{in}.

5.3.1   Numerical Solution

We adopt the radiative outer boundary condition in the outer wave zone of the
disc, such that far from the outer Lindblad resonance radius r_{OL} (where $\omega - m\Omega = $

Figure 5.2: Real and imaginary frequencies for interface modes for various *m* as a function of the disc sound speed c_s for $\Sigma_-/\Sigma_+ = 0$. The solid lines show the eigenfrequencies for $m = 5$ modes, the dash-dotted lines for $m = 4$, the long-dashed lines for $m = 3$, the short-dashed lines for $m = 2$, and the dotted lines for $m = 1$.
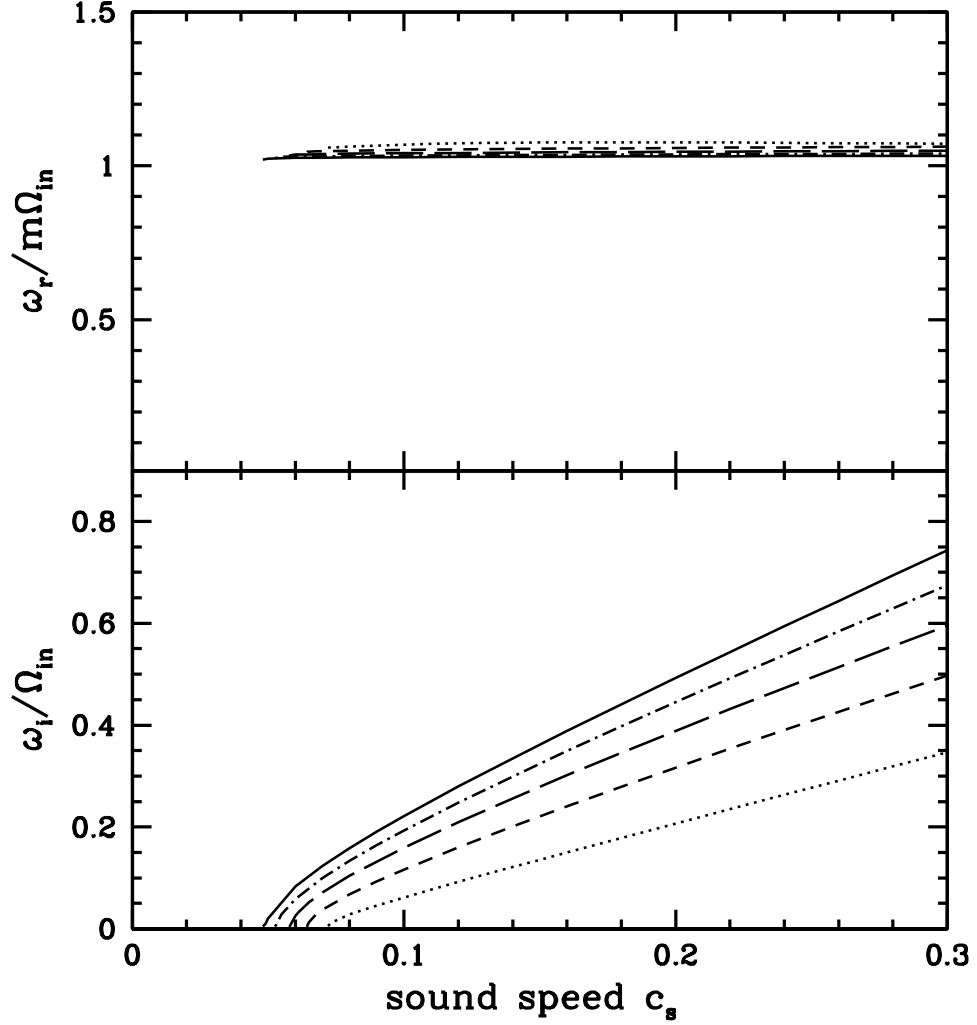
Figure 5.3: Real and imaginary frequencies for interface modes for various m as a function of sound speed c_s for $\Sigma_-/\Sigma_+ = 1/9$, with $\Omega_-/\Omega_{in} = 1$, where $\Omega_{in} \equiv \Omega_k(r_{in})$. The solid lines show the eigenfrequencies for $m = 5$ modes, the dash-dotted lines for $m = 4$, the long-dashed lines for $m = 3$, the short-dashed lines for $m = 2$, and the dotted lines for $m = 1$.
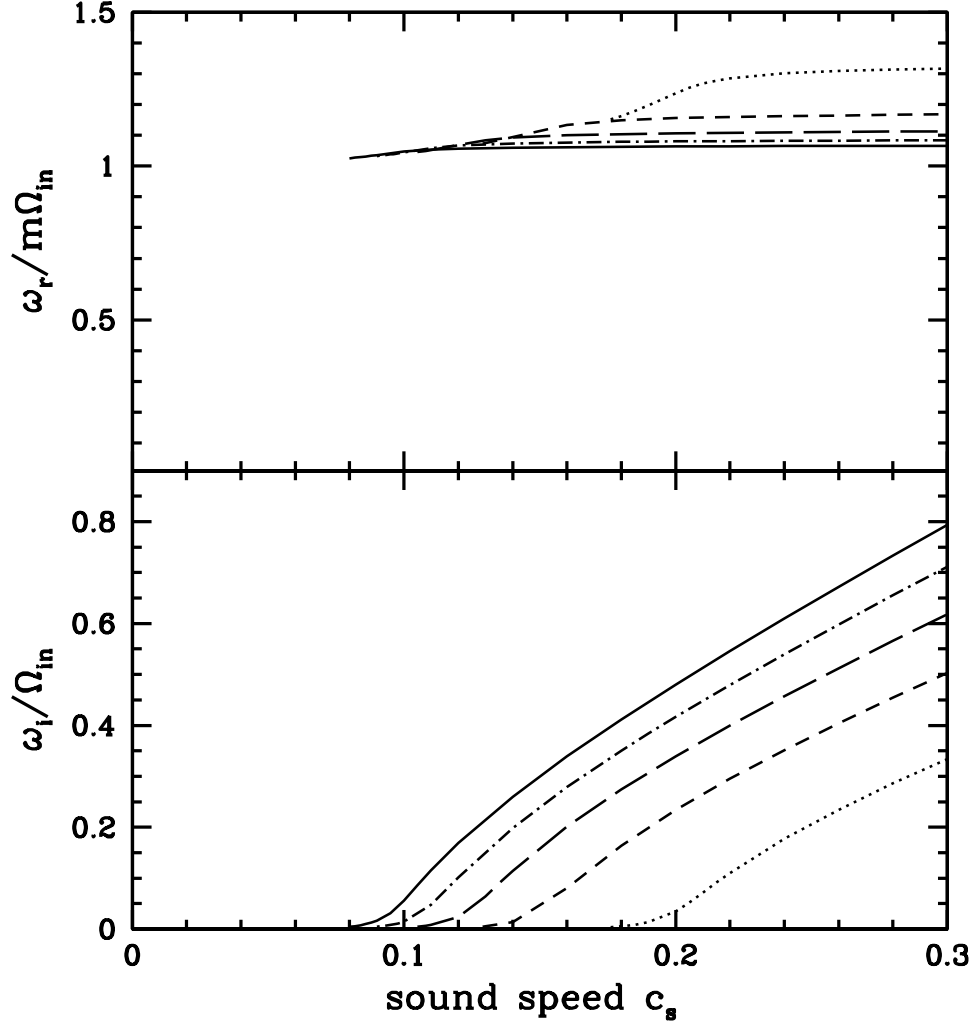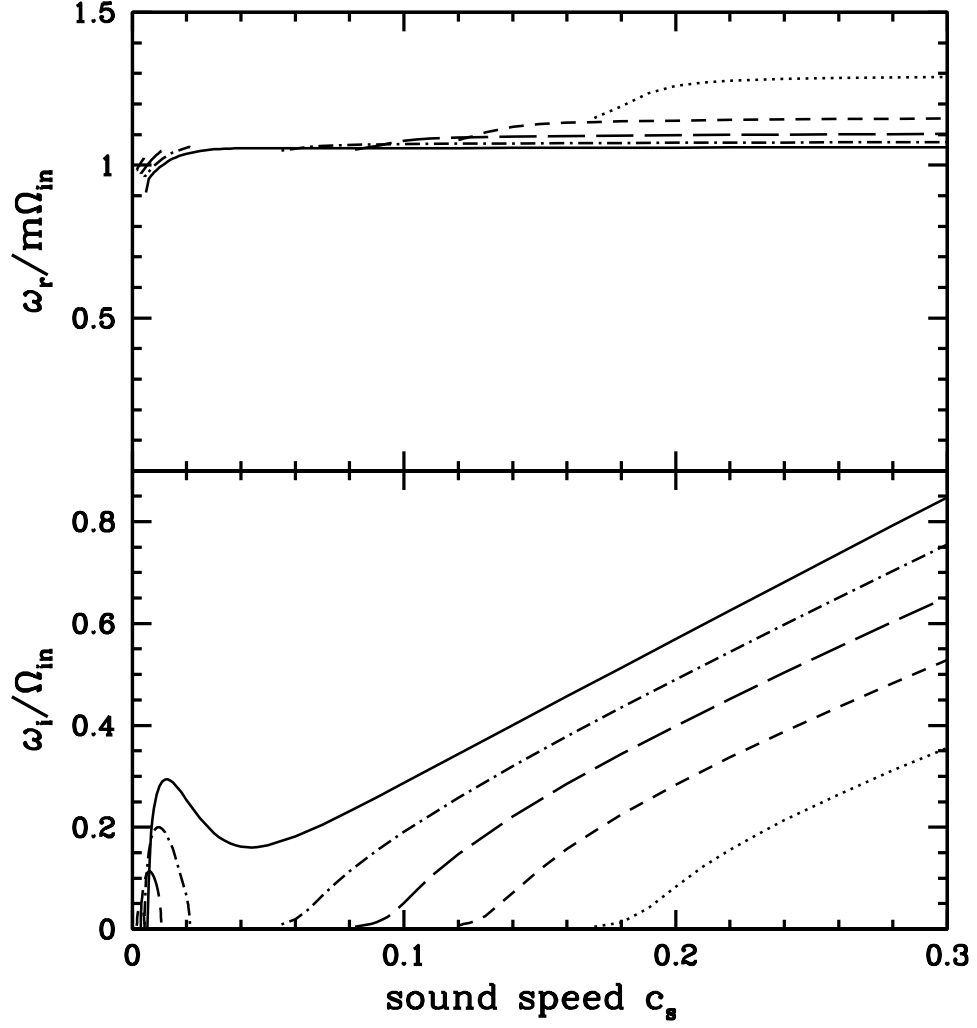
Figure 5.4: Real and imaginary frequencies for interface modes for various m as a function of sound speed c_s for $\Sigma_-/\Sigma_+ = 1/99$ with $\Omega_-/\Omega_{in} = 0.5$. The solid lines show the eigenfrequencies for $m = 5$ modes, the dash-dotted lines for $m = 4$, the long-dashed lines for $m = 3$, the short-dashed lines for $m = 2$, and the dotted lines for $m = 1$.

Figure 5.5: Real and imaginary frequencies for interface modes for various m (denoted as in Figure 2) as a function of sound speed c_s for $\Sigma_-/\Sigma_+ = 1/9$ with $\Omega_-/\Omega_{in} = 0.5$. The solid lines show the eigenfrequencies for $m = 5$ modes, the dash-dotted lines for $m = 4$, the long-dashed lines for $m = 3$, the short-dashed lines for $m = 2$, and the dotted lines for $m = 1$.
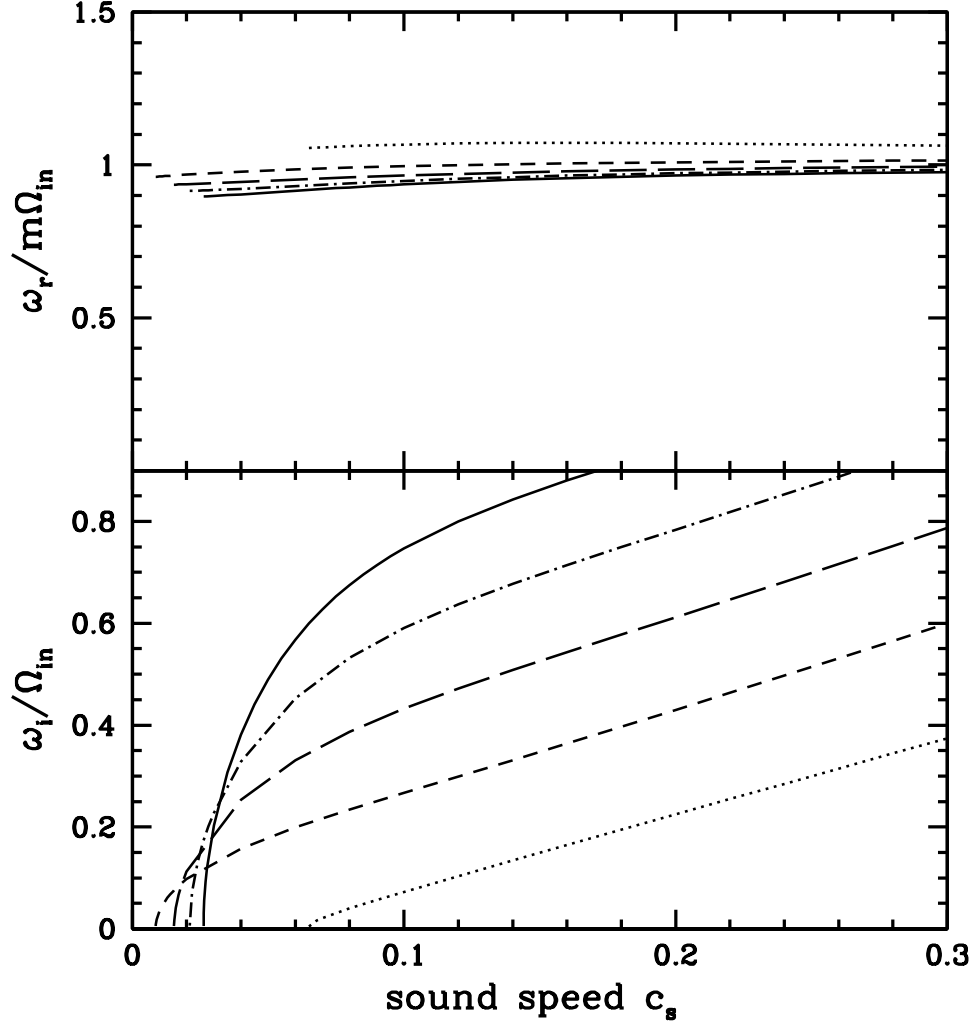
116

κ) we have the solution of the form:

$$\delta h \propto A \exp\left[i \int^{r} k \, dr\right],$$ (5.23)

with $A = (D/r\Sigma k)^{1/2}$ and $k = (-D/c_s^2)^{1/2}$ (see Tsang & Lai 2008, Lai & Tsang, 2008). This gives the boundary condition at $r = r_{\text{out}} > r_{\text{OL}}$:

$$\delta h'(r_{\text{out}}) = \delta h(r_{\text{out}}) \left(ik + \frac{1}{A}\frac{dA}{dr}\right)_{r_{\text{out}}}.$$ (5.24)

We adopt (5.22) as the inner boundary condition for the disc and solve the eigen-value problem using a standard shooting method (Press et al 1998). For the numerical solutions below, the density profile of the disk was assumed to be $\Sigma \sim r^{-3/2}$ so that corotation absorption plays no role in determining the mode stability (Tsang & Lai 2008). An example wavefunction for an interface mode is shown in Figure 1, for typical disc parameters.

The numerical eigenvalues are shown in Figure 2 and Figure 3 for various disc and magnetosphere parameters, for $m = 1, 2, \ldots, 5$.

5.3.2 Discussion of Numerical Results

Figure 2 shows the complex eigenvalues as a function of sound speed c_s, for density contrasts corresponding to $\Sigma_- = 0$ and $\Sigma_- = \frac{1}{9}\Sigma_+$, with magnetosphere ro-tation rate equal to the Kepler frequency at the interface [$\Omega_- = \Omega(r_{\text{in}+}) \simeq \Omega_k(r_{\text{in}})$]. For this case we see that there exists a cutoff in the disc sound speed below which no growing interface modes are found. This arises from the stabilizing effect of the background differential rotation, and can be understood as follows.

Setting $\Sigma_- = 0$ and rewriting (5.22) in terms of the radial velocity perturba-

tion δu_r, we have:

$$\zeta_+ \tilde{\omega} + \frac{\tilde{\omega}^2}{m\Sigma_+ \delta u_r} \frac{d}{dr}(\Sigma_+ r \delta u_r) + g_{\text{eff}+}\left(\frac{r\tilde{\omega}^2}{mc_s^2} - \frac{m}{r}\right) = 0 \tag{5.25}$$

where $g_{\text{eff}+} = pc_s^2/r$ [see Eq. (5.4)] and $\zeta \equiv \kappa^2/(2\Omega)$ is the vorticity, and where all quantities are evaluated at the interface $r_{\text{in}+}$. For the wave frequencies of interest, the waves are evanescent in the region of the disk just outside the interface. Let $\tilde{k} \equiv -\delta u_r'/\delta u_r > 0$. Equation (5.25) can be solved in terms of $\tilde{k}$, giving

$$\tilde{\omega} = \frac{m\zeta}{2\gamma} \pm i \sqrt{\frac{g_{\text{eff}+}m^2}{r\gamma} - \frac{m^2\zeta^2}{4\gamma^2}} \tag{5.26}$$

where $\gamma \equiv \tilde{k}r - 1$. The terms inside the square root correspond to the mode growth due to Rayleigh-Taylor instability and the suppression due to vorticity, respectively. With $g_{\text{eff}+} = pc^2/r$ we find the critical sound speed

$$c_{\text{crit}} \approx \sqrt{\frac{\zeta^2 r^2}{4p\gamma}}, \tag{5.27}$$

above which the perturbations will be unstable.

Figure 3 shows cases where the inner region is uniformly rotating at an angular frequency of one half the Kepler frequency at the interface [$\Omega_- = 0.5\Omega(r_{\text{in}+})$]. When $\Sigma_- > 0$ this leads to the development of the Kelvin-Helmholtz instability, and both this and the Rayleigh-Taylor instability play a role in the mode growth. In the Appendix we derive the expression for the plane-parallel Rayleigh-Taylor and Kelvin-Helmholtz instabilities for a compressible upper region (with density ρ_+ and horizontal velocity u_+), and incompressible lower region (with density ρ_- and horizontal velocity u_-). For $\rho_- \ll \rho_+$ we have $\omega \approx ku_+ \pm i\omega_i$ where k is the horizontal wavenumber and

$$\omega_i = \sqrt{k\tilde{k}(u_+ - u_-)^2\left(\frac{\rho_-}{\rho_+}\right) + g\tilde{k}} \equiv \sqrt{\omega_{\text{KH}}^2 + \omega_{\text{RT}}^2}. \tag{5.28}$$

118

Here $\tilde{k} \approx \frac{1}{2H_z}\left[\sqrt{1 + H_z^2 k^2} - 1\right]$, g is the acceleration due to gravity in the vertical direction, and H_z is the vertical scale height in the upper region. The Kelvin-Helmholtz term is approximately

$$\omega_{\mathrm{KH}}^2 \approx k\tilde{k}(u_+ - u_-)^2 \left(\frac{\rho_-}{\rho_+}\right). \tag{5.29}$$

For $kH_z \gg 1$ this reduces to the incompressible limit with $\omega_{\mathrm{KH}}^2 \approx k^2(u_+ - u_-)^2 \rho_-/\rho_+$. For $kH_z \ll 1$ we have $\omega_{\mathrm{KH}}^2 \approx (H_z k)k^2(u_+ - u_-)^2 \rho_-/\rho_+$, a factor of $H_z k$ smaller than the incompressible result.

For the rotating system under consideration, the imaginary part of the mode frequency can be written schematically as [cf. equation (5.28)]

$$\omega_i \approx \sqrt{\omega_{\mathrm{KH}}^2 + \omega_{\mathrm{RT}}^2 + \omega_{\mathrm{vort}}^2}. \tag{5.30}$$

We also have $H_z \sim c_s^2/g_{\mathrm{eff}} \sim r$ and $k \sim m/r$ so $kH_z \sim m$. Thus $\omega_{\mathrm{KH}}^2 \sim (\Delta\Omega)^2 \Sigma_-/\Sigma_+$, and ω_{KH}^2 depends weakly on sound speed. On the other hand, from equation (5.26) we see that the vorticity suppresses mode growth through the term $\omega_{\mathrm{vort}}^2 = -m^2 \zeta^2/(4\gamma^2)$. For sufficiently small c_s, equation (5.18) indicates $\delta h \propto e^{-\kappa r/c_s}$, i.e. $\tilde{k} \sim \kappa/c_s$. Therefore the vorticity term scales with sound speed as $\omega_{\mathrm{vort}}^2 \sim -m^2 c_s^2/r^2$, and can be dominated by the Kelvin-Helmholtz term for small enough sound speed. In the left panel of Figure 3, the mode growth ($\omega_i > 0$) for small c_s is mainly driven by the Kelvin-Helmholtz instability. For $m \geq 5$ the sound speed ranges where ω_{RT}^2 and ω_{KH}^2 dominate over ω_{vort}^2 overlap, and hence the critical sound speed in equation (5.27) is not relevant. For larger values of Σ_- these regions can overlap for all m.
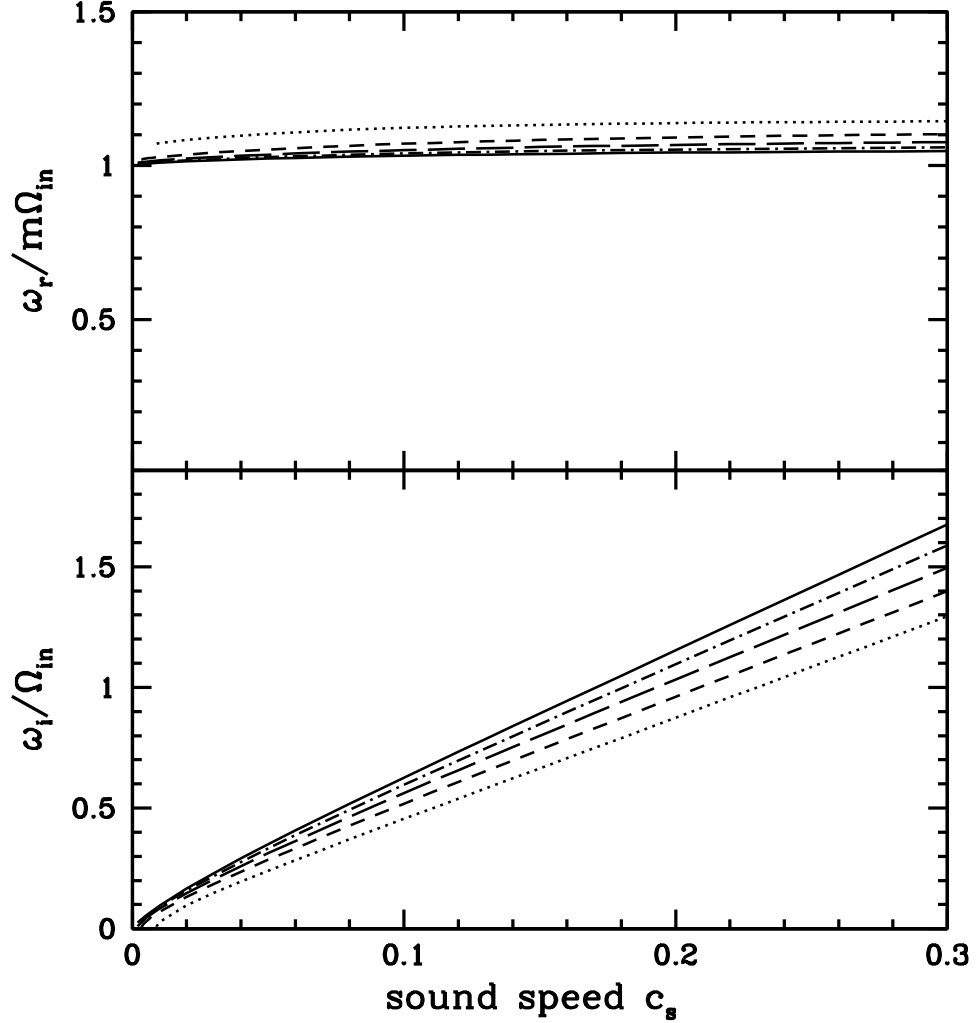
Figure 5.6: Real and imaginary frequencies for interface modes for various m as a function of sound speed c_s with $r_{in} = r_{ISCO}$ for the pseudo-newtonian GR potential. There is no sound speed cutoff for unstable modes as the vorticity is zero at the interface. $\Sigma_- = 0$. The solid lines show the eigenfrequencies for $m = 5$ modes, the dash-dotted lines for $m = 4$, the long-dashed lines for $m = 3$, the short-dashed lines for $m = 2$, and the dotted lines for $m = 1$.
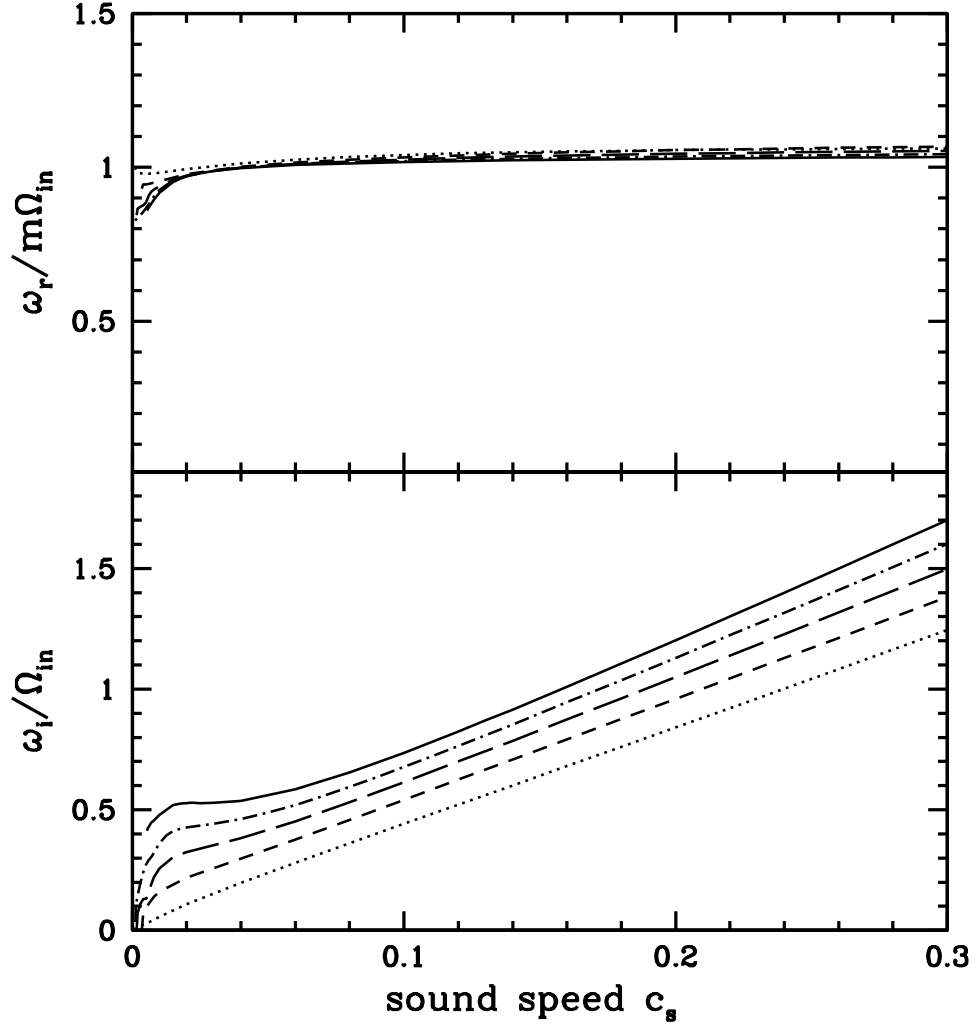
Figure 5.7: Real and imaginary frequencies for interface modes for various m (denoted as in Figure 2) as a function of sound speed c_s with $r_{in} = r_{ISCO}$ for the pseudo-newtonian GR potential. There is no sound speed cutoff for unstable modes as the vorticity is zero at the interface. $\Sigma_- = \frac{1}{99}\Sigma_+$, and $\Omega_- = 0.5\Omega_{in}$. The solid lines show the eigenfrequencies for $m = 5$ modes, the dash-dotted lines for $m = 4$, the long-dashed lines for $m = 3$, the short-dashed lines for $m = 2$, and the dotted lines for $m = 1$.

5.3.3 Effect of a Relativistic Potential

While in Section 3.2 and other sections of the chapter we focus on Newtonian discs, it is of interest to consider how general relativity may modify our results. The effect of general relativity can be approximated by using the pseudo-Newtonian Paczynski & Wiita (1980) potential:

$$\Phi = -\frac{GM}{r - r_S},\tag{5.31}$$

with $r_S = 2GM/c^2$ the Schwarzschild radius. This gives the Keplerian orbital frequency (Ω_k) and epicyclic frequency (κ) as:

$$\Omega_k = \left(\frac{1}{r}\frac{d\Phi}{dr}\right)^{1/2} = \sqrt{\frac{GM}{r}}\frac{1}{r - r_S}\,, \qquad \kappa = \left[\frac{2\Omega_k}{r}\frac{d}{dr}(r^2\Omega_k)\right]^{1/2} = \Omega_k\sqrt{\frac{r - 3r_S}{r - r_S}}.\tag{5.32}$$

with $\kappa \to 0$ at $r_{ISCO} = 3r_S = 6GM/c^2$.

For $r_{in} \gg r_{ISCO}$ the interface modes are the same as for the Newtonian case. However, as $r_{in} \to r_{ISCO}$ the suppression effect of ω_{vort}^2 [see Eq. (5.26)] is reduced as the vorticity goes to zero at r_{ISCO}, so that for $r_{in} = r_{ISCO}$ there is no cutoff sound speed (see Figures 2-3) for interface mode instability. This is illustrated in Figure 4. Thus if the magnetosphere boundary is at r_{ISCO}, the interface modes will always be present and highly unstable for any sound speed.

5.3.4 P-modes with Magnetosphere Boundary

The boundary condition given by equation (5.22) also provides an inner reflection boundary for disc p-modes, which were studied in detail in Lai & Tsang (2008). These modes have wavefunctions primarily "trapped" in the wave region between the disc boundary r_{in} and the inner Lindblad resonance radius,
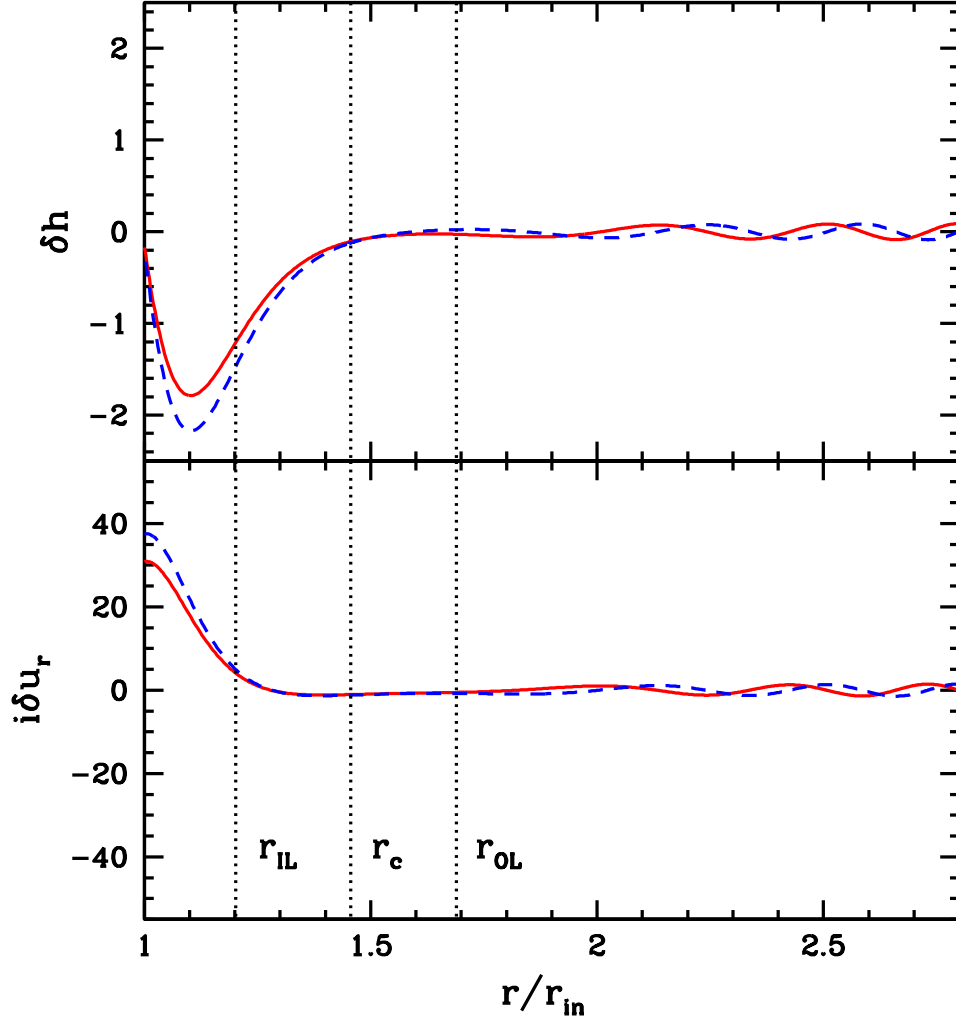
Figure 5.8: The p-mode wavefunctions for $m = 4$, $c_s = 0.1r\Omega$, $\Sigma_-/\Sigma_+ = 1/99$, $\Omega_-/\Omega_+ = 1$ with $\omega/\Omega_{in} = 1.914 + 0.000127i$. The real components are shown in solid lines, while the imaginary components are dashed lines. For p-modes the inner and outer Lindblad resonances and the corotation resonance are outside r_{in}, denoted by the dotted lines. The solid lines show the eigenfrequencies for $m = 5$ modes, the dash-dotted lines for $m = 4$, the long-dashed lines for $m = 3$, and the short-dashed lines for $m = 2$.

r_{ILR}, where $\omega - m\Omega = -\kappa$. Figure 5 depicts an example of the p-mode wave function for the same disc model as in Figure 1. The growth rates of these p-modes are determined primarily by the outgoing flux at the outer boundary and the effect of the corotation resonance, as discussed in Lai & Tsang (2008). In Figure 6 the eigenfrequencies are shown for p-modes in a disc with the density profile $\Sigma \propto r^{-p}$, where $p = 3/2$ so that wave absorption at the corotation resonance is inactive (since in this case the vortensity $\kappa^2/(2\Omega\Sigma)$ is constant). For the density profile $p < 3/2$, the corotation absorption tends to damp the mode, while for $p > 3/2$ the corotation absorption enhances it.

5.4 Interface Modes at the Star-Disc Boundary

5.4.1 Star-Disc Boundary Condition

In the case of accretion on to a non-magnetic star, our model consists of a dense uniformly rotating compressible stellar atmosphere truncating the accretion disc. This model ignores the structure of the boundary layer. However the qualitative properties of the dynamics should be captured for modes with characteristic radial length scale much greater than the radial scale of the boundary layer.

Several studies of CVs (e.g. by examining the rotationally broadened line emissions from the stellar surface) have shown that the stellar rotation rates are significantly below the breakup rotation rate (see Warner, 2004), and we limit our examinations to systems with $|\Omega_-| \leq 0.5\Omega(r_{\mathrm{in+}})$. As in the case of the disc, we consider only the effect of perturbations on a cylindrical equatorial
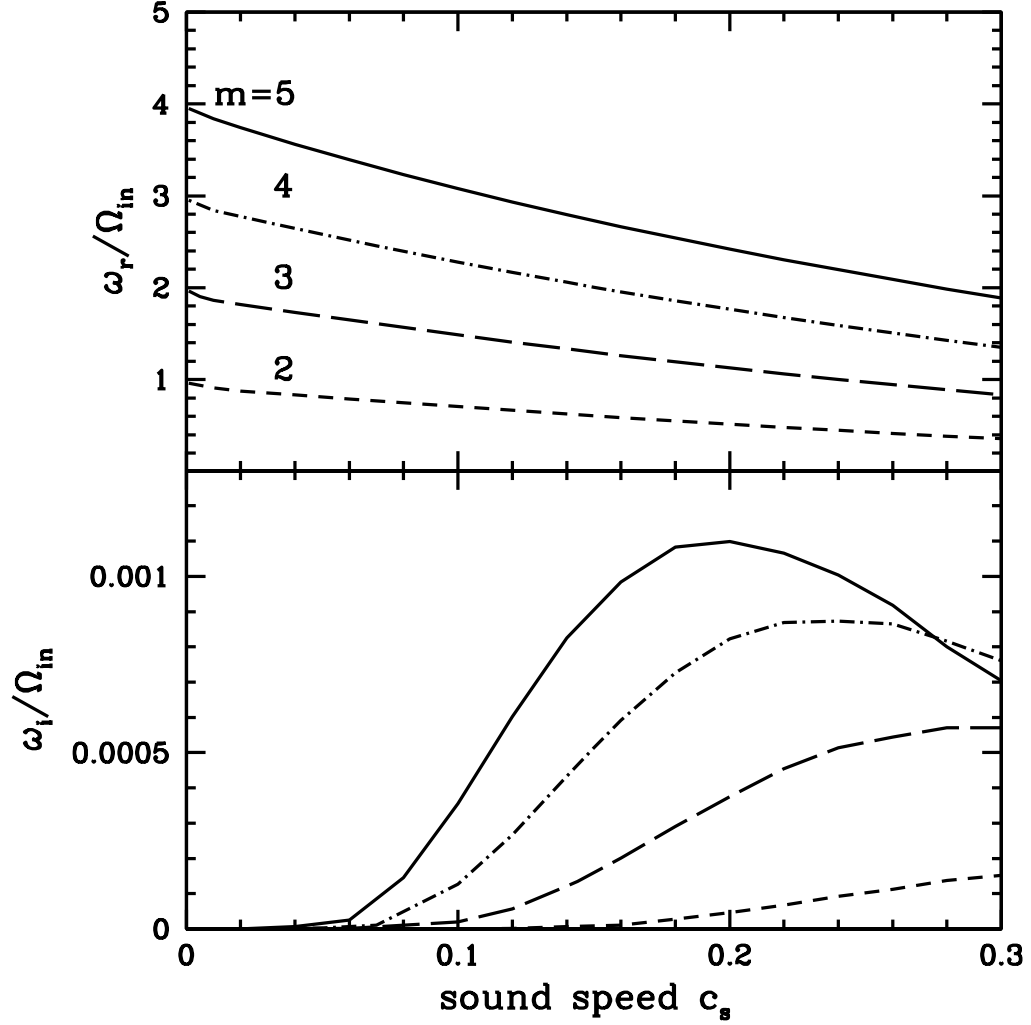
Figure 5.9: Real and imaginary frequencies for p-modes for the magnetosphere boundary condition with $\Sigma_- = (1/99)\Sigma_+$ and $\Omega_- = 0.5\Omega_{in}$. For $\Sigma_- \ll \Sigma_+$ the p-mode frequencies have very little dependence on Ω_-. Here the disc surface density profile is chosen to be $\Sigma \propto r^{-3/2}$, so that the corotation absorption is inactive and mode growth is purely due to propagation outward at r_{out}.

surface of the stellar atmosphere (i.e., we are considering a "cylindrical" star). In this region equation (5.18) also describes the enthalpy perturbations within the stellar atmosphere. Inside the atmosphere, we assume a small constant density scale height, $-\Sigma/\Sigma' \equiv H_\Sigma \ll r$. Equation (5.18) then becomes

$$\delta h'' - \frac{1}{H_\Sigma}\delta h' - \left(\frac{2m\Omega}{r\tilde{\omega}H_\Sigma} + \frac{D}{c_s^2}\right)\delta h \approx 0. \tag{5.33}$$

For $H_\Sigma \ll r$ and $H_\Sigma \ll c_s/\Omega$, this has the solution

$$\delta h \propto \exp[(r - r_{\text{in}})/H_\Sigma]. \tag{5.34}$$

The Lagrangian pressure perturbation at the stellar surface is then

$$\begin{aligned}
\Delta P_- &= \Sigma_- \left[\frac{\tilde{\omega}\delta h}{i\delta u_r} - r(\Omega_k^2 - \Omega^2)\right]_{r_{\text{in}-}} \frac{i\delta u_r}{\tilde{\omega}} \\
&= \left[\frac{\kappa^2 - \tilde{\omega}^2}{\frac{2\Omega m}{r\tilde{\omega}} - \frac{1}{H_\Sigma}} - r(\Omega_k^2 - \Omega^2)\right]_{r_{\text{in}-}} \Sigma_- \frac{i\delta u_r}{\tilde{\omega}}.
\end{aligned} \tag{5.35}$$

Once again matching the Lagrangian displacement and pressure perturbation at the interface gives the boundary condition for the interface modes for the star-disc boundary case:

$$\Sigma_+ \left[\frac{\tilde{\omega}\delta h}{i\delta u_r} - \frac{pc_s^2}{r}\right]_{r_{\text{in}+}} = \Sigma_- \left[\frac{\kappa^2 - \tilde{\omega}^2}{\frac{2\Omega m}{r\tilde{\omega}} - \frac{1}{H_\Sigma}} + r(\Omega^2 - \Omega_k^2)\right]_{r_{\text{in}-}}. \tag{5.36}$$

5.4.2 Numerical Results

We repeat the numerical procedure of Section 3 using the radiative outer boundary condition [equation (5.24)] and using equation (5.36) as the inner disc boundary condition. A sample wavefunction for the star-disc interface mode is shown in Figure 7. For typical mode frequencies the region just outside the boundary is an evanescent zone; wave propagation becomes possible only beyond the outer Lindblad resonance (r_{OL}). Figure 8 shows the eigenfrequencies

for the lowest order modes with $m = 1, 2, \ldots, 5$ as a function of disc sound speed, for representative parameters $H_\Sigma = 0.01 r_{in}$, $\Sigma_- = 10\Sigma_+$ and $\Omega_- = 0.1\Omega_+$. Figure 9 shows the dependence of the mode eigenfrequencies on the density (Σ_-), rotation rate (Ω_-), and scale height (H_Σ) of the star. We see that both the real mode frequency ω_r and the growth rate ω_i do not depend strongly on these parameters.

5.4.3   Discussion of Numerical Results

When the disc is truncated by the star's surface, the effective gravity acts to stabilize the perturbations (since $\Sigma_- > \Sigma_+$), as does the vorticity. Thus compared to the interface mode in the magnetosphere-disc case (Sections 3.1 – 3.2), the mode growth rates here are much smaller and are primarily driven by wave propagation through the corotation, beyond the outer Lindblad resonance. In the left panels of Figure 8 the eigenfrequencies are shown for typical parameters [$\Sigma_- = 10\Sigma_+(r_{in})$, $\Omega_- = 0.1\Omega(r_{in+})$, $H_\Sigma = 0.01 r_{in}$], and disc density index $p = 3/2$, so that the corotation absorption plays no role. For other density indices, wave absorption at the corotation can act to either damp or grow the interface modes (Tsang & Lai 2008; Lai & Tsang 2008). For example, in the Shakura-Sunyaev α-disc model the disc solution for the outer disc solution (with free-free opacity and gas pressure dominating) has the surface density $\Sigma \propto r^{-3/4}$, hence the modes would be stabilized by absorption at the corotation resonance. However, for models where the disc has density index $p > 3/2$ at corotation, the corotational absorption acts to enhance mode growth, as shown in the right panels of Figure 8.
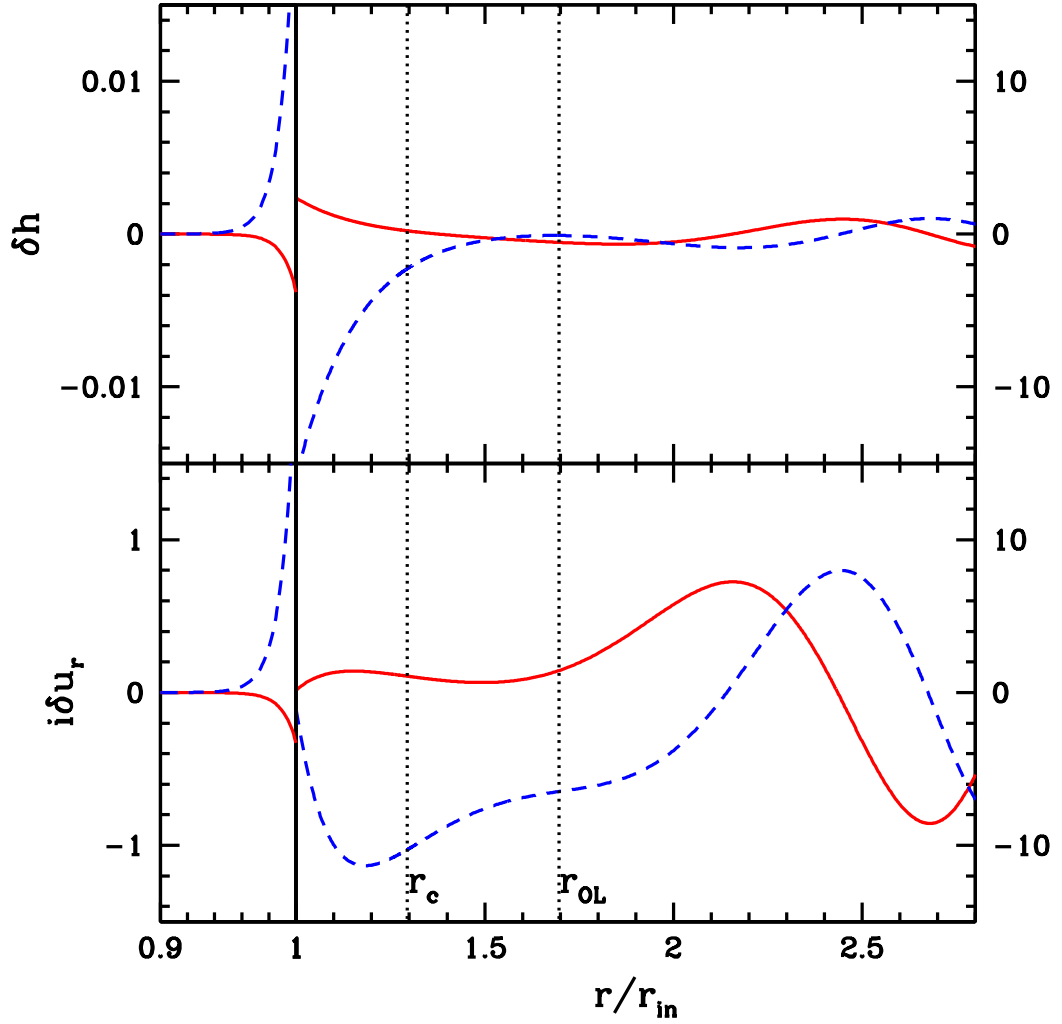
Figure 5.10: An example wavefunction for a disc/non-magnetized star interface with $m = 2$, $\Sigma_- = 10\Sigma_+$, $\Omega_- = 0.1\Omega_{in}$ and $H_\Sigma = 0.01r_{in}$ with the eigenfrequency $\omega/\Omega_{in} = 1.378 + 0.0030i$. The left side ($r < r_{in}$) of the plot denotes the perturbation eigenfunctions inside the star, while the right side shows the disc perturbations. The vertical dotted lines denote the corotation resonance radius (r_c) and the outer Lindblad resonance radius (r_{OL}).
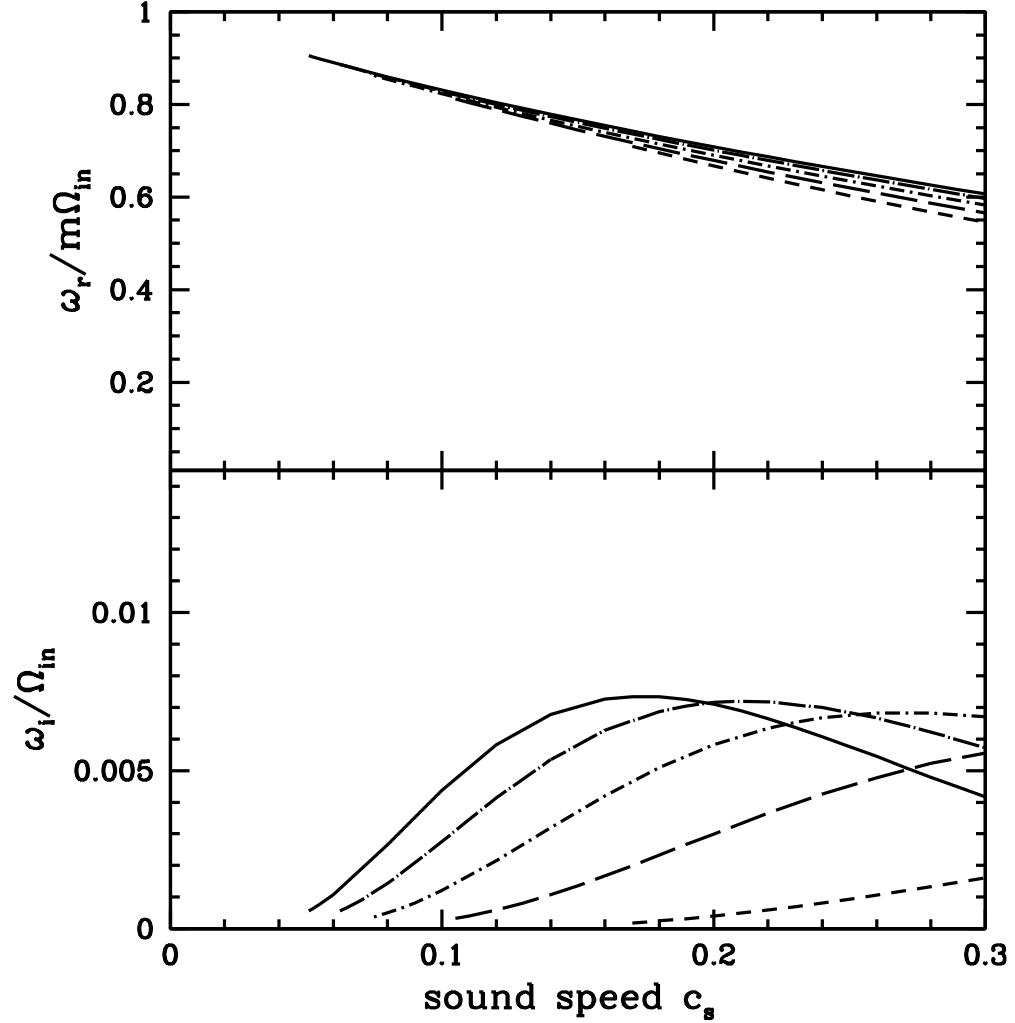
Figure 5.11: Interface modes for the star/disc boundary for $H_\Sigma = 0.01 r_{in}$, $\Sigma_- = 10\Sigma_+$, $\Omega_- = 0.1\Omega_{in}$, as a function of sound speed, for $m = 1\ldots 5$. The vertically integrated surface density of the disc is given by $\Sigma_+ \propto r^{-p}$ with $p = 3/2$, so that corotation absorption plays no role. The solid line shows the eigenfrequencies for $m = 5$ modes; the dashed and dotted line, $m = 4$; long dashed line, $m = 3$; short dashed line, $m = 2$; and dotted line $m = 1$.
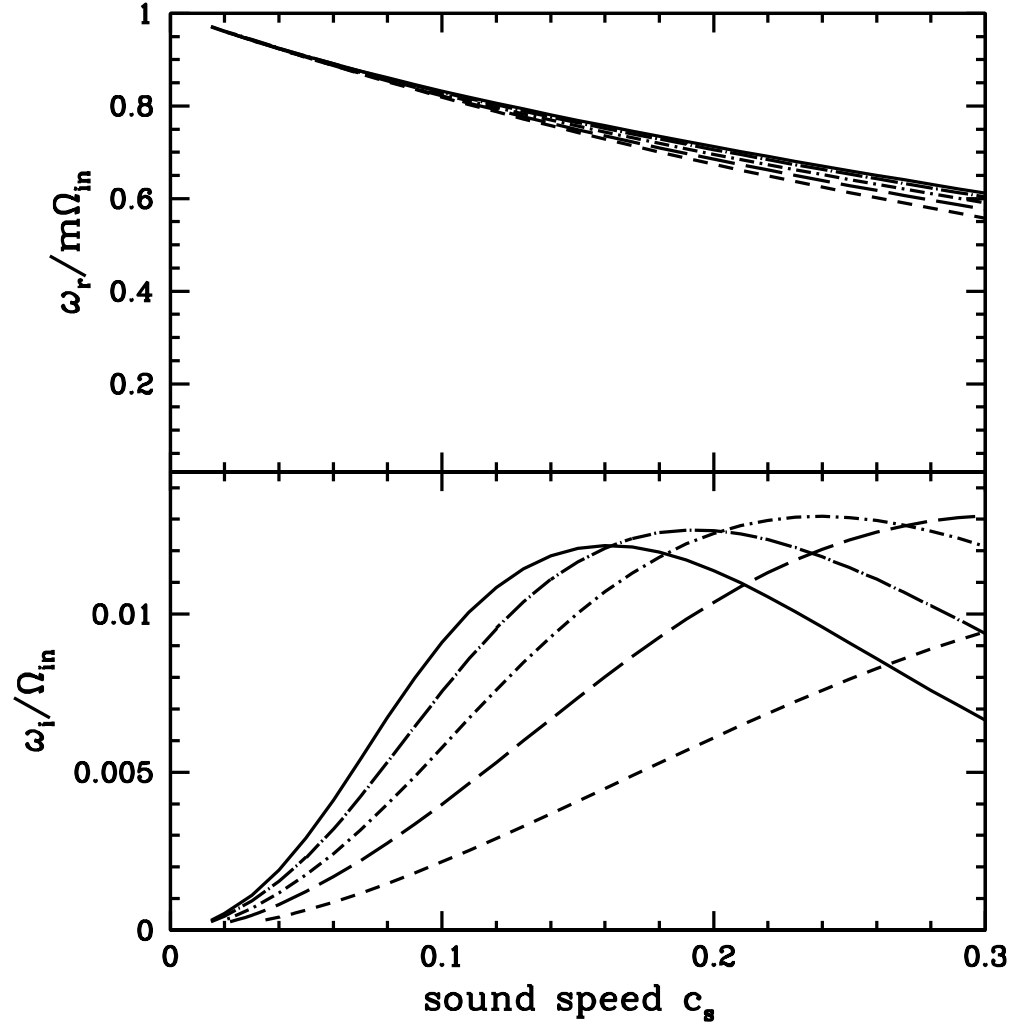
Figure 5.12: Interface modes for the star/disc boundary for $H_\Sigma = 0.01 r_{\rm in}$, $\Sigma_- = 10\Sigma_+$, $\Omega_- = 0.1\Omega_{\rm in}$, as a function of sound speed, for $m = 1 \ldots 5$. The vertically integrated surface density of the disc is given by $p = 2$ for the right panels, so that corotation absorption acts to enhance the mode growth. The solid line shows the eigenfrequencies for $m = 5$ modes; the dashed and dotted line, $m = 4$; long dashed line, $m = 3$; short dashed line, $m = 2$; and dotted line $m = 1$.

labelfig5.12

The mode eigenfrequencies have very little dependence on the properties of the stellar atmosphere ($\Sigma_-, \Omega_-, H_\Sigma$), as shown in Figure 9. The mode frequencies instead primarily depend on the disc sound speed, which in turn depends on the accretion rate. Observations of CVs indicate that DNOs are usually only detected in high $\dot{M}$ states, with the oscillation period decreasing with increasing luminosity (Warner 2004). The downward trend of the $\omega_r/m\Omega_{in}$ as a function of c_s in Figure 8 would appear to contradict the observed period-luminosity anti-correlation. But note that in our model, the interface mode frequency depends on the sound speed at the inner-most disc region and boundary layer, and it will be necessary to model the thermodynamic and radiative properties of the boundary layer in order to compare with observation directly. Also, the oscillations of the type considered here would yield periods shorter than the surface Keplerian period, except for the $m = 1$ mode. Though higher-m modes would be more difficult to observe due to the averaging out of the luminosity variation, most observed DNOs, even those with 1:2:3 harmonic structure (Warner & Woudt, 2005) occur with period roughly at or greater than the corresponding surface Keplerian period. These long-period oscillations cannot be explained by the model considered here.

5.5   Conclusions

We have studied the non-radial oscillation modes at the interface between an accretion disc and a magnetosphere or stellar surface. Although the models explored in this chapter are perhaps too simplified compared to realistic situations, they offer some insight into the behavior of the interface modes in various astrophysical contexts.
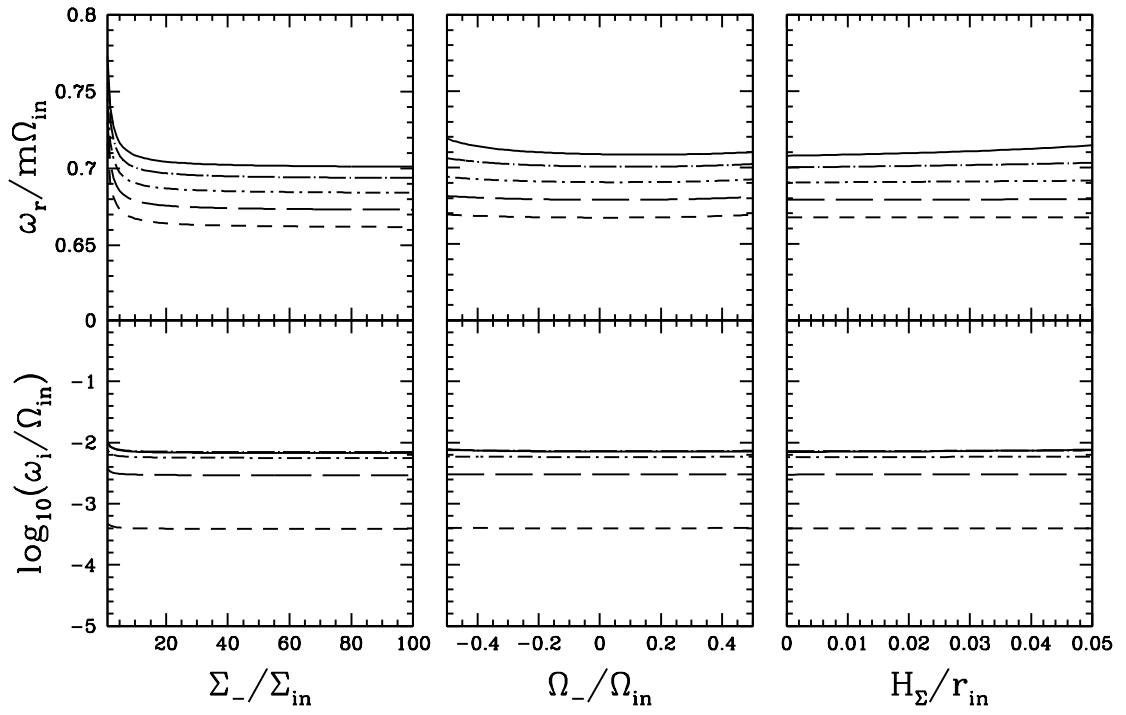
Figure 5.13: Eigenfrequencies for disc-star interface modes as a function of star density (Σ_-), rotation rate (Ω_-), and characteristic scale height ($\Sigma_-/\Sigma'_- = H_\Sigma$). The canonical values for various parameters are: $c_s = 0.2 r_{in}\Omega_{in}$, $\Omega_- = 0.1\Omega_{in}$, $H_\Sigma = 0.01 r_{in}$ and $\Sigma_- = 10\Sigma_+$.

Our study of the interface modes at the magnetosphere-disc boundary extended the work by Li & Narayan (2004), who considered incompressible disc flow (and therefore could not treat real discs). The model can have very strongly unstable modes due to Rayleigh-Taylor and Kelvin-Helmholtz instabilities. In systems where the magnetosphere has developed from advection of frozen magnetic flux, the magnetosphere is expected to be roughly rotating with at the Keplerian rate. Since there is no shear at the interface, only the Rayleigh-Taylor instability may occur. However the disc vorticty (due to differential rotation) acts to suppress the instability, leading to a cutoff below a critical sound speed. Thus a sufficiently hot disc is required to generate unstable low-m modes. For magnetospheres rotating with the central star, shearing is expected between the magnetosphere and disc, and the Kelvin-Helmholtz instability becomes active. This can help to drive the instability for low-m modes to overcome the vorticity in low sound-speed discs. In discs that terminate near the ISCO in a general relativistic potential, the vorticity approaches zero at the inner disc radius, and unstable interface modes can be found for any sound speed.

We can expect a strong dependence of the interface mode growth rates on the sound speed, and thus accretion rate, while the real frequencies of these oscillations remain close to $(1 - 1.3)m\Omega_{in}$, and do not depend strongly on the sound speed. It is worth noting that the same boundary condition that gives rise to the interface modes also gives rise to intertial-acoustic modes (or p-modes) in the disc.

Although higher-m interface modes are more unstable in our model, these are less likely to be observed due to the averaging out of the luminosity variation over the observable emitting region. In addition, if the effect of viscous

133

damping is considered (e.g., Wang & Robertson 1985), small wavelength or high-*m*, perturbations are suppressed.

These results are for perturbations with no vertical structure, and are applicable mainly to the midplane of accretion discs interacting with a magnetosphere. Global 3D numerical studies of Rayleigh-Taylor instability induced accretion onto magnetized stars have been performed by Romanova, Kulkarni & Lovelace (2008) and Kulkarni & Romanova (2008), and show such small *m* instabilities in the disk midplane. The low-*m* oscillations at the magnetosphere-disc interface may be relevent to the high-frequency QPOs observed in some NS and BH X-ray binary systems (Li & Narayan, 2004; see Section 1 of Lai & Tsang for a critical review of various theoretical models), although to obtain the correct QPO frequencies for the BH systems, the disc inner radius must lie outside the inner-most stable circular orbit.

For the star-disc boundary model considered in in this chapter, the interface mode growth rates are much smaller than for the magnetospheric case, since the effective gravity now acts to stabilize the system, and the Rayleigh-Taylor instability is inactive. The modes discussed here are unstable due primarily to propagation through the corotation. With sufficiently steep disc density profile ($\Sigma \propto r^{-p}$ with $p > 3/2$), corotation absorption can also help to drive these modes, as studed previously by Tsang & Lai (2008) and Lai & Tsang (2008). Such modes may be responsible for the high-frequency (of order the Keplerian frequency at the stellar surface) dwarf nova oscillations observed in CVs, although oscillations with longer periods would require a different explanation.

CHAPTER 6

RAYTRACING IN THE KERR METRIC

6.1 Introduction

In previous chapters we developed models for the growth rate of density wave perturbations in accretion disks near compact objects. However, the mapping of density perturbation to observable is non-trivial for several reasons, including, the unknown structure of the upscattering corona or advection dominated accretion flow (ADAF) necessary for converting thermal photons emitted by the disk into observed X-rays, as well as the effect of the space-time curvature of the compact object itself on the emitted photons. In this chapter we study the latter effect by performing relativistic raytracing in the Kerr metric.

Many papers have been written discussing the treatment of X-ray emissions from accretion discs around black holes. Emission from the high velocity matter in theses discs will be distorted by the high gravity regime surrounding the black hole, resulting in changes in the observed energy (doppler shifting and gravitational redshifting), time delay, and light path. Many of these effects were first calculated by Cunningham (1975), who used a transfer function approach in calculating the effects of relativity, allowing the resulting observed spectrum to be found by a convolution of the local emission spectrum and the relativistic transfer function.

One of the main thrusts of research has been the study of sharp disc emissions resulting from flourescence lines from X-rays incident on the disc, such as the $6.4 keV\ FeK\alpha$ line. The advantage of considering such sharp emissions is

that the relativistic effects may be seen more clearly, as the intrinsic disc emission mechanisms are not well understood. Iwasawa et al showed in 1996 that the observation of the MCG 6-30-15 line exhibited a broadening of the red wing and a disapearnce of the blue wing of the typical double horned curve. This is taken by several authors to indicate an emission from the inner $6M$ radius of the black hole region, which can not be supported by a Schwarzschild geometry, and thus perhaps providing us with a probe of the geometry around a rotating black hole.

If the X-rays incident on the accretion disc are from a flaring region in the disc corona, different regions will emit the flouresence lines at different arrival times. Thus the observed spectra will vary over time, due to the light crossing time, and light bending effects. Such "reverberation" effects have been studied by Reynold et al. (1998).

Iron line emissions have been studied extensively, as ASCA observations of Seyfert I galaxies exhibit reprocessed x-ray emissions, specifically broadened iron line emissions that may be explained by the effect of strong gravity. In particular several papers (Dabrowski et al 1997, Dovciak et al 2004 etc) have analysed observations of MCG-6-30-15(Tanaka et al 1995), a particlarly bright source, using disc-line models to determine the local spacetime structure.

Similar methods are used to study QPOs with emission in the X-ray regime. Schnittman and Bertschinger (2004) study the emission of a hot spots in a background daccretion discs. We utilize raytracing methods to construct a tool for generating observables for emissions around black holes.

6.2 Geodesic Raytracing

In order to calculate various spectrum and light curve properties we must first construct a simulated image of the black hole and accretion disc in the observer's frame. In this frame the image is broken down into individual pixels of equal solid angle, and each corresponding to a single ray emitted by the accretion disc. At the observer each pixel can be indexed by the impact parameters α($\perp$ to the spin axis projection), and β ($\parallel$ to the spin axisprojection).

Solving for the geodesics, each of these rays can be backtraced to their source, allowing us to construct a complete image of the disc as seen by a distant observer.

The contravariant components of photon momenta in a kerr metric can be given in Boyer Linquist coordinates, assuming $G = c = M_{BH} = 1$ (e.g. MIsner, Thorne & Wheeler, 1973)

$$\left(\frac{dt}{d\lambda}\right) = \rho^{-2}\left[\frac{r^2 + a^2}{\Delta}[E(r^2 + a^2) - L_z] - a(aE\sin^2\theta - L_z)\right] \tag{6.1}$$

$$\left(\frac{dr}{d\lambda}\right) = \rho^{-2}[(E(r^2 + a^2) - L_z a)^2 - \Delta((L_z - aE)^2 + Q)]^{1/2} \tag{6.2}$$

$$\left(\frac{d\theta}{d\lambda}\right) = \rho^{-2}[Q - \cos^2\theta(L_z^2\csc^2\theta - E^2a^2)]^{1/2} \tag{6.3}$$

$$\left(\frac{d\phi}{d\lambda}\right) = \rho^{-2}\left[-aE + L_z\csc^2\theta + \frac{a}{\Delta}(E(r^2 + a^2) - L_z a)\right] \tag{6.4}$$

where a is the black hole spin, λ is the affine parameter, and $\Delta = r^2 - 2r + a^2$. E, the photon energy, L_z the angular momentum, and Q, Carter's constant, are constants of motion.

This form allows the use of simple Runge-Kutte routines to integrate out the photon paths, and are used by many authors as a comprimise between code complexity and computational speed. Care must be taken at the turning points

of the u and μ variables to ensure proper integration.

Utilizing elliptical integrals, and hence greater code complexity, Cunningham and Bardeen (1973) outline a quicker method of calculating the photon trajectories using a Hamilton-Jacobi method. Here we follow a related procedure. Rearranging and switching variables from the affine parameter to a "Mino parameter" (see e.g. Drasco & Hughes, 2004) $\lambda' : \frac{d\lambda}{d\lambda'} = \rho^{-2}E$ we get the following coupled first order ODEs for the coordinates as a function of mino-parameter,

$$\left(\frac{dt}{d\lambda'}\right) = T(r,\theta) = \left[\frac{(r^2+a^2)^2}{\Delta} - a^2\sin^2\theta\right] + al\left[1 - \frac{r^2+a^2}{\Delta}\right] \tag{6.5}$$

$$\left(\frac{dr}{d\lambda'}\right)^2 = R(r) = (r^2+a^2-la)^2 - (r^2-2r+a^2)[(l-a)^2+q^2] \tag{6.6}$$

$$\left(\frac{d\theta}{d\lambda'}\right)^2 = \Theta(\theta) = q^2 - l^2\cot^2\theta + a^2\cos^2\theta \tag{6.7}$$

$$\left(\frac{d\phi}{d\lambda'}\right) = \Phi(r,\theta) = l\csc^2\theta + a\left(\frac{r^2+a^2}{\Delta}-1\right) - \frac{a^2l}{\Delta}. \tag{6.8}$$

where $l = L_z/E$, $q^2 = Q/E^2$. The constants of motion l and q^2 are related to the impact parameters (α,β) by $l = -\alpha\sqrt{1-\mu_o^2}$ and $q^2 = \beta^2 + \mu_o^2(\alpha^2-a^2)$.

We can solve these ODE's in an semi-analytic fashion using the Jacobi elliptic functions and elliptic integrals. We first solve for the two independant variables, $r(\lambda')$ and $\theta(\lambda')$

6.2.1 The R equation

The roots of the equation

$$R(r) = (r^2+a^2-al)^2 - (r^2-2r+a^2)[(l-a)^2+q^2] = 0 \tag{6.9}$$

can be expressed (Cadez et al., 2003) as

$$r_1 = \frac{1}{2}B + \frac{1}{2}\sqrt{-A + 2D - 4C/B} \tag{6.10}$$

$$r_2 = \frac{1}{2}B + \frac{1}{2}\sqrt{-A + 2D - 4C/B} \tag{6.11}$$

$$r_3 = -\frac{1}{2}B + \frac{1}{2}\sqrt{-A + 2D + 4C/B} \tag{6.12}$$

$$r_4 = -\frac{1}{2}B + \frac{1}{2}\sqrt{-A + 2D + 4C/B} \tag{6.13}$$

where

$$C = (a-l)^2 + q^2 \tag{6.14}$$

$$D = \frac{2}{3}(q^2 + l^2 - a^2) \tag{6.15}$$

$$E = \frac{9}{4}D^2 - 12a^2q^2 \tag{6.16}$$

$$F = -\frac{27}{4}D^3 - 108a^2q^2D + 108C^2 \tag{6.17}$$

$$B = \sqrt{A+D} \tag{6.18}$$

with

$$A = \frac{1}{3}\left(\frac{F + \sqrt{F^2 - 4E^3}}{2}\right)^{1/3} + \frac{1}{3}\left(\frac{F - \sqrt{F^2 - 4E^3}}{2}\right)^{1/3} \tag{6.19}$$

For numerical evaluation this is better expressed (if $F^2 \geq 4E^3$)

$$A = \frac{1}{3}\left(\frac{F + \sqrt{F^2 - 4E^3}}{2}\right)^{1/3} + \frac{E}{3}\left(\frac{2}{F + \sqrt{F^2 - 4E^3}}\right)^{1/3} \tag{6.20}$$

and if $F < 4E^3$ we take the principal value of

$$A = \frac{2}{3}\sqrt{E}\cos[\frac{cos^{-1}(F/2E^{3/2})}{3}] \tag{6.21}$$

139

Allowing us to rewrite the differential equation for $dr/d\lambda'$ as

$$\frac{dr}{d\lambda'} = \sqrt{R(r)} \tag{6.22}$$

$$= -\sqrt{(r-r_1)(r-r_2)(r-r_4)(r-r_3)} \tag{6.23}$$

$$\Delta\lambda' = -\int_{r_o}^{r} \frac{dr}{\sqrt{(r-r_1)(r-r_2)(r-r_4)(r-r_3)}} \tag{6.24}$$

$$= \frac{2}{\sqrt{(r_2-r_4)(r_1-r_3)}} F\left(\sin^{-1}\sqrt{\frac{(r-r_1)(r_2-r_4)}{(r-r_2)(r_1-r_4)}}, \sqrt{\frac{(r_1-r_4)(r_2-r_3)}{(r_2-r_4)(r_1-r_3)}}\right)\Bigg|_r^{\infty} \tag{6.25}$$

$$= \frac{2}{\sqrt{(r_2-r_4)(r_1-r_3)}} \mathrm{sn}^{-1}\left(\sqrt{\frac{(r-r_1)(r_2-r_4)}{(r-r_2)(r_1-r_4)}}, \sqrt{\frac{(r_1-r_4)(r_2-r_3)}{(r_2-r_4)(r_1-r_3)}}\right)\Bigg|_r^{\infty} \tag{6.26}$$

where sn is the Jacobi elliptic function and F is the Jacobi elliptic integral of the first kind. [1]

With the negative value of the momentum corresponding to backtraced photon decreasing in r. Solving for $r(\Delta\lambda')$ we get

$$r(\Delta\lambda') = \frac{r_1(r_2-r_4) - r_2(r_1-r_4)\,\mathrm{sn}^2(u,\kappa_r)}{(r_2-r_4) - (r_1-r_4)\,\mathrm{sn}^2(u,\kappa_r)} \tag{6.27}$$

where

$$\kappa_r = \sqrt{\frac{(r_1-r_4)(r_2-r_3)}{(r_2-r_4)(r_1-r_3)}} \tag{6.28}$$

$$u = \frac{\sqrt{r_2-r_4)(r_1-r_3)}\,\Delta\lambda'}{2} - u_\infty \tag{6.29}$$

$$u_\infty = \mathrm{sn}^{-1}\left(\sqrt{\frac{r_2-r_4}{r_1-r_4}}, \kappa_r\right) \tag{6.30}$$

even for complex values of r_n.

To calculate the value of $\Delta\lambda'(r)$ we must carefully consider any turning points that may be encountered in r. If any root r_n is a positive real value greater than

---

[1]We calculate the Jacobi elliptic functions and elliptic integrals utilizing standard recurrence relations modified to work with values on part of the complex plane, combined with the Landen's transforms to change the complex arguments (see Appendix D)

the horizon radius then the photon may have a turning point in r. If no turning point is encountered before the emission point then the value of $\Delta\lambda'(r)$ is given by

$$\Delta\lambda'(r) = \frac{2}{\sqrt{(r_2 - r_4)(r_1 - r_3)}}\left[F\left(\sin^{-1}\psi_\infty, \kappa_r\right) - F\left(\sin^{-1}\psi(r), \kappa_r\right)\right] \tag{6.31}$$

where $\psi(r) = \sqrt{\frac{(r-r_1)(r_2-r_4)}{(r-r_2)(r_1-r_4)}}$ and $\psi_\infty = \psi(r)|_{r\to\infty} = \sqrt{\frac{(r_2-r_4)}{(r_1-r_4)}}$.

If a photon turning point is encountered by the backtrace before reaching the emission point (ie $\Delta\lambda' > \Delta\lambda'(r_{turn})$) then the corresponding value of $\Delta\lambda'$ is given by

$$\Delta\lambda'(r) = \frac{2}{\sqrt{(r_2 - r_4)(r_1 - r_3)}}\left[F\left(\sin^{-1}\psi(r), \kappa_r\right)\Big|_{r_{turn}}^{\infty} + F\left(\sin^{-1}\psi(r), \kappa_r\right)\Big|_{r_{turn}}^{r_{em}}\right] \tag{6.32}$$

As the change in sign corresponds to the change in the sign of the photon momenta at the turning point.

6.2.2 The Θ equation

Examining the θ equation we perform the substitution $z = \cos^2\theta$ such that

$$\frac{d\theta}{d\lambda'} = \pm\sqrt{\frac{-a^2 z^2 - z[q^2 + l^2 - a^2] + q^2}{1 - z}} \tag{6.33}$$

$$= \pm\sqrt{\frac{a^2(z_+ - z)(z - z_-)}{1 - z}} \tag{6.34}$$

where $z_\pm = -\frac{q^2 + l^2 - a^2}{2a^2} \pm \sqrt{\frac{(q^2 + l^2 - a^2)^2}{4a^4} + \frac{q^2}{a^2}}$ If we take $\chi : z = z_+ \cos^2\chi$ we have

$$\frac{d\chi}{d\theta} = \pm\sqrt{\frac{1 - z}{(z_+ - z)}} \tag{6.35}$$

which gives

$$\frac{d\chi}{d\lambda'} = \frac{d\chi}{d\theta}\frac{d\theta}{d\lambda'} = \sqrt{a^2(z - z_-)} \tag{6.36}$$

$$= \sqrt{a^2(z_+ \cos^2\chi - z_-)} \tag{6.37}$$

141

which gives the integral

$$\lambda'(\chi) - \lambda'(\chi_o) = \int_{\chi_o}^{\chi} \frac{d\chi}{\sqrt{a^2(z_+ \cos^2\chi - z_-)}} \tag{6.38}$$

$$= \frac{1}{a\sqrt{z_+ - z_-}} \left[F\left(\chi, \sqrt{\frac{z_+}{z_+ - z_-}}\right) - F\left(\chi_o, \sqrt{\frac{z_+}{z_+ - z_-}}\right) \right] \tag{6.39}$$

where $F(\psi, k)$ is the elliptic integral of the first kind. (In Abramowitz and Stegun notation this is $F = F(\psi|m)$, where $m = k^2$.)

Inverting this equation and solving for θ we finally obtain:

$$\theta(\lambda') = \cos^{-1}\left(\sqrt{z_+}\, cn(a\sqrt{z_+ - z_-}\lambda' + u_{\theta_o}, \kappa_\theta)\right) \tag{6.40}$$

where

$$u_{\theta_o} = \text{sgn}(\beta)\, cn^{-1}(\cos(\theta_o)/\sqrt{z_+}, \kappa_\theta) \tag{6.41}$$

$$\kappa_\theta = \sqrt{\frac{z_+}{z_+ - z_-}} \tag{6.42}$$

and $cn(u, \kappa)$ is the Jacobi elliptic function which has inverse $cn^{-1}(u, \kappa) = F(\cos^{-1}(u), \kappa)$.

In order to calculate the mino-parameter corresponding to a particular value of θ we see

$$\Delta\lambda'(\theta) = \frac{1}{a\sqrt{z_+ - z_-}} \left[F\left(\chi, \sqrt{\frac{z_+}{z_+ - z_-}}\right) - F\left(\chi_o, \sqrt{\frac{z_+}{z_+ - z_-}}\right) \right] \tag{6.43}$$

where

$$\chi = \cos^{-1}\left(\frac{\cos\theta}{\sqrt{z_+}}\right) \tag{6.44}$$

$$\chi_o = \text{sgn}(\beta)\cos^{-1}\left(\frac{\cos\theta_o}{\sqrt{z_+}}\right) \tag{6.45}$$

thus we can solve for λ' corresponding to intersection of the ray with simple fixed θ_{em} disc configurations. The flat disc model of $\theta_{em} = \pi/2$ is of particular interest.

6.2.3   The Φ Equation

The $\phi(\lambda')$ differential equation is more complicated than the equations for the first two spatial coordinates, however the differential equation can be solved by breaking the integration into two parts, integration over θ and integration over r.

First rewriting the $\Phi(r, \theta)$ equation we see

$$\frac{d\phi}{d\lambda'} = \frac{l}{1 - \cos^2 \theta} + a\frac{2r + la}{r^2 - 2r + a^2} \tag{6.46}$$

Integrating the first term we see

$$\Delta\phi_1 = \int_{\lambda'_o}^{\lambda'_{em}} \frac{l d\lambda'}{1 - \cos^2 \theta} \tag{6.47}$$

$$= \int_{\lambda'_o}^{\lambda'_{em}} \frac{l d\lambda'}{1 - z_+ \operatorname{cn}^2(a\sqrt{z_+ - z_-}\lambda' + u_{\theta_o}, k_\theta)} \tag{6.48}$$

$$= \int_{\lambda'_o}^{\lambda'_{em}} \frac{l d\lambda'}{1 - z_+(1 - \operatorname{sn}^2)} \tag{6.49}$$

$$= \frac{l}{(1 - z_+)} \int_{\lambda'_o}^{\lambda'_{em}} \frac{d\lambda'}{1 + \frac{z_+}{1 - z_+} \operatorname{sn}^2} \tag{6.50}$$

$$= \frac{l/a}{(1 - z_+)\sqrt{z_+ - z_-}} \int_{u_o}^{u_{em}} \frac{du}{1 + \frac{z_+}{1 - z_+} \operatorname{sn}^2(u, k_\theta)} \tag{6.51}$$

$$= \frac{l/a}{(1 - z_+)\sqrt{z_+ - z_-}} \Pi\left(\chi, \frac{z_+}{1 - z_+}, \kappa_\theta\right)\Big|_{\chi_o}^{\chi_{em}} \tag{6.52}$$

where $u = a\sqrt{z_+ - z_-}\lambda' + u_o$, $\chi = \operatorname{am}(u, \kappa_\theta)$ is the Jacobi amplitude of u, and $\Pi(\psi, n, \kappa)$ is the elliptic integral of the third kind. All these values are real, and there is no difficulty in evaluating $\Pi(\psi, n, \kappa)$ through the standard recurrence relations.

The second term proves slightly more complicated:

$$\Delta\phi_2 \quad = \quad a \int_{\lambda'_o}^{\lambda'_{em}} \frac{(2r + la)d\lambda'}{r^2 - 2r + a^2} \tag{6.53}$$

$$= \quad a \int_{\infty}^{r_{em}} \frac{2r + la}{(r - r_+)(r - r_-)} \frac{d\lambda'}{dr} dr \tag{6.54}$$

$$= \quad a\left(\frac{2r_+ + al}{r_+ - r_-}\right) \int_{r_{em}}^{\infty} \frac{1}{(r - r_+)} \frac{dr}{\sqrt{(r - r_1)(r - r_2)(r - r_3)(r - r_4)}}$$

$$-a\left(\frac{2r_- + al}{r_+ - r_-}\right) \int_{r_{em}}^{\infty} \frac{1}{(r - r_-)} \frac{dr}{\sqrt{(r - r_1)(r - r_2)(r - r_3)(r - r_4)}} \tag{6.55}$$

$$= \quad a\left[\frac{2r_2 + al}{r_2^2 - 2r_2 + a^2}\right]\Delta\lambda' + \frac{2a}{\sqrt{(r_1 - r_3)(r_2 - r_4)}}\left(\frac{r_1 - r_2}{r_+ - r_-}\right)$$

$$\times\left[\frac{2r_- + al}{(r_1 - r_-)(r_2 - r_-)}\Pi_- - \frac{2r_+ + al}{(r_1 - r_+)(r_2 - r_+)}\Pi_+\right]_{r_{em}}^{\infty} \tag{6.56}$$

where

$$r_\pm \quad = \quad 1 \pm \sqrt{1 - a^2} \tag{6.57}$$

$$\Pi_\pm \quad = \quad \Pi(\psi(r), n_\pm, \kappa_r) \tag{6.58}$$

$$n_\pm \quad = \quad \psi^2(r)\Big|_{r=r_\pm}. \tag{6.59}$$

Thus we have

$$\Delta\phi(\Delta\lambda') = \Delta\phi_1 + \Delta\phi_2 \tag{6.60}$$

Note that when a turning point is encountered in r, the $\Delta\phi_2$ must be evaluated with the appropriate sign change as for $\Delta\lambda'(r)$.

In general the parameters of the elliptical integrals of the third kind will be complex. This limits evaluation of $\Delta\phi_2$ using recurrence relations to a particular domain of complex parameter space. Evaluations outside of this domain can be performed using numerical quadrature.

144

6.2.4   The T Equation

The solution to the time coordinate is the most complicated of the four Boyer-Linquist coordinates.Simplifying the $T(r, \theta)$ equation we have:

$$\frac{dt}{d\lambda'} = -a^2 \sin^2 \theta + \frac{(r^2 + a^2)^2 + 2alr}{r^2 - 2r + a^2} \tag{6.61}$$

The first term can be integrated in a relatively straightforward fashion as:

$$\Delta t_1 = \int a^2 (1 + \cos^2 \theta) d\lambda' \tag{6.62}$$

$$= a^2 \Delta\lambda' - \int a^2 z_+ \operatorname{cn}^2(u_\theta, \kappa_\theta)) \frac{du_\theta}{a \sqrt{z_+ - z_-}} \tag{6.63}$$

$$= a^2 \Delta\lambda' - \frac{a z_+}{\sqrt{z_+ - z_-}} \frac{1}{\kappa_\theta^2} \left[\mathrm{E}(\mathrm{am}(u_\theta), \kappa_\theta) - (1 - \kappa_\theta^2)u_\theta \right]_{u_o}^{u_{em}} \tag{6.64}$$

$$= a^2 \left[a + \frac{z_+(1 - \kappa_\theta^2)}{\kappa_\theta^2} \right] \Delta\lambda' - \frac{a z_+}{\kappa_\theta^2 \sqrt{z_+ - z_-}} \mathrm{E}(\chi, \kappa_\theta) \Big|_{\chi_o}^{\chi_{em}} \tag{6.65}$$

For the second term,Δt_2, the analytic solution can be determined as a very long combination of elliptical integrals of the first, second and third kinds as well as the Jacobi elliptic functions.

However, the values of observer time elapsed for the intervals between photon emission and observation at infinity are necessarily divergent. Though one could simply evaluate Δt_2 only up to a large arbitrary value of r, it is better to instead subtract off the same infinite constant for each ray, as our interest is limited to the elapsed observer time difference between different rays ,by considering the Kerr time.

Remembering that the time in Kerr-coordinates is given by a transformation:

$$dt_{Kerr} = dt_{BL} + \left(\frac{r^2 + a^2}{r^2 - 2r + a^2} \right) dr \tag{6.66}$$

145

we can then subtract off the same constant for each ray by taking

$$\Delta t' \quad = \quad \Delta t_{Kerr} - \int_{r_{em}}^{r_{bitrary}} \frac{r^2 + a^2}{r^2 - 2r + a^2} dr \tag{6.67}$$

$$= \quad \Delta t_{BL} + \int_{\infty}^{r_{em}} \frac{r^2 + a^2}{r^2 - 2r + a^2} dr - \int_{r_{em}}^{r_{bitrary}} \frac{r^2 + a^2}{r^2 - 2r + a^2} dr \tag{6.68}$$

$$= \quad \Delta t_1 + \Delta t_2 - \int_{r_{bitrary}}^{\infty} \frac{r^2 + a^2}{r^2 - 2r + a^2} dr \tag{6.69}$$

$$= \quad \Delta t_1 + \int_{r_{em}}^{r_{bitrary}} \frac{(r^2 + a^2)^2 + 2alr}{r^2 - 2r + a^2} \frac{dr}{\sqrt{R(r)}}$$

$$+ \int_{r_{bitrary}}^{\infty} \left[\frac{(r^2 + a^2)^2 + 2alr}{r^2 - 2r + a^2} \frac{1}{\sqrt{R(r)}} - \frac{r^2 + a^2}{r^2 - 2r + a^2} \right] dr. \tag{6.70}$$

where $r_{bitrary}$ is some r beyond the disc range.

These integrations are best performed with numerical quadrature as evaluation of the elliptic integrals and Jacobi elliptic functions prove less efficient than the numerical integration. In addition the $1/\sqrt{R(r)}$ term makes it difficult to remove the divergent components of the analytic solution so it may be evaluated numerically.

6.3   Calculation of Observables

We know that along each ray I_ν/ν^3 is lorentz invariant, and the redshift is defined as $g = \nu_{obs}/\nu_{em}$. Hence we have $I_{\nu_{obs}} = g^3 I_{\nu_{em}}$ along a particular ray.

However including lensing/magnification effects we see that over a ray bundle of area dS

$$I_{\nu_{obs}} = g^3 I_{\nu_{em}} \left| \frac{dS_\perp}{dS_{obs}} \right| \tag{6.71}$$

where $dS_\perp$ is the area element perpendicular to the ray bundle at the emission point, in the local disc frame.

Covariantly the redshift can be given as:

$$g = \frac{p_{obs\mu}U_{obs}{}^\mu}{p_{em\nu}U_{em}^\nu} = -\frac{1}{p_{em\nu}U_{em}^\nu} \tag{6.72}$$

for a distant stationary observer, where U_{em} is the four velocity of the disc material.

The most important observable to be calculated for each pixel is the observed flux. We have

$$F_{\nu_{obs}} = \int \frac{dF_{\nu_{obs}}}{d\Omega} d\Omega \tag{6.73}$$

$$= \int I_{\nu_{obs}} d\Omega \tag{6.74}$$

$$= \frac{1}{D^2} \int g^3 I_{\nu_{em}} \left| \frac{dS_\perp}{dS_{obs}} \right| D^2 d\Omega \tag{6.75}$$

$$= \frac{1}{D^2} \int g^3 I_{\nu_{em}} \left| \frac{dS_\perp}{dS_{obs}} \right| dS_{obs} \tag{6.76}$$

where $dS_\perp$ can be expressed covariantly as:

$$dS_\perp = -\frac{U_{em}^\gamma p_{em}^\delta dS_{\gamma\delta}}{U_{em}^\nu p_{em\nu}} \tag{6.77}$$

with $dS_{\gamma\delta}$, the area tensor, given by

$$\frac{dS_{\gamma\delta}}{dS_{obs}} = \frac{dx^\mu}{d\alpha} \frac{dx^\nu}{d\beta} \varepsilon_{\gamma\delta\mu\nu} \tag{6.78}$$

and ε is the levi-civita tensor.

Thus we have

$$F_{\nu_{obs}} = \frac{1}{D^2} \iint g^3 I_{\nu_{em}} \left| -\frac{U_{em}^\gamma p_{em}^\delta}{U_{em}^\epsilon p_{em\,\epsilon}} \frac{dx^\mu}{d\alpha} \frac{dx^\nu}{d\beta} \varepsilon_{\gamma\delta\mu\nu} \right| d\alpha d\beta \tag{6.79}$$
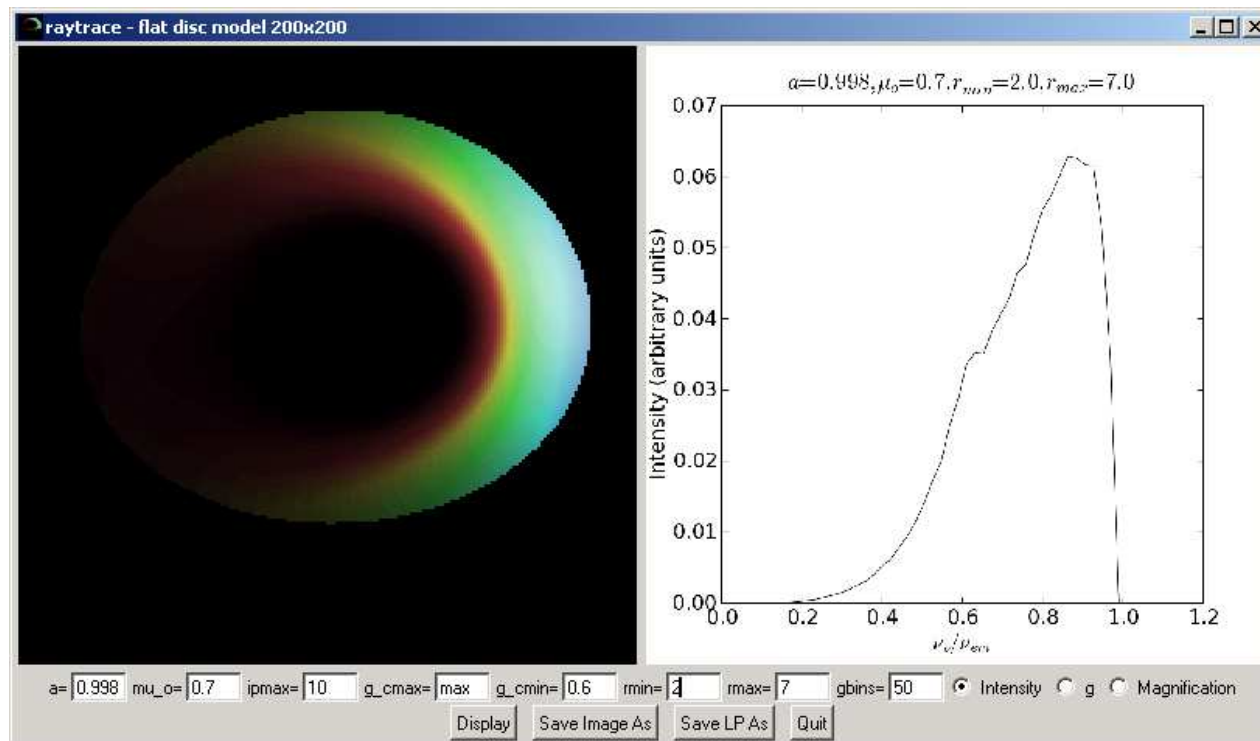
147

Figure 6.1: A simple example of a 200x200 pixel image and line profile generated by the raytracer interface.
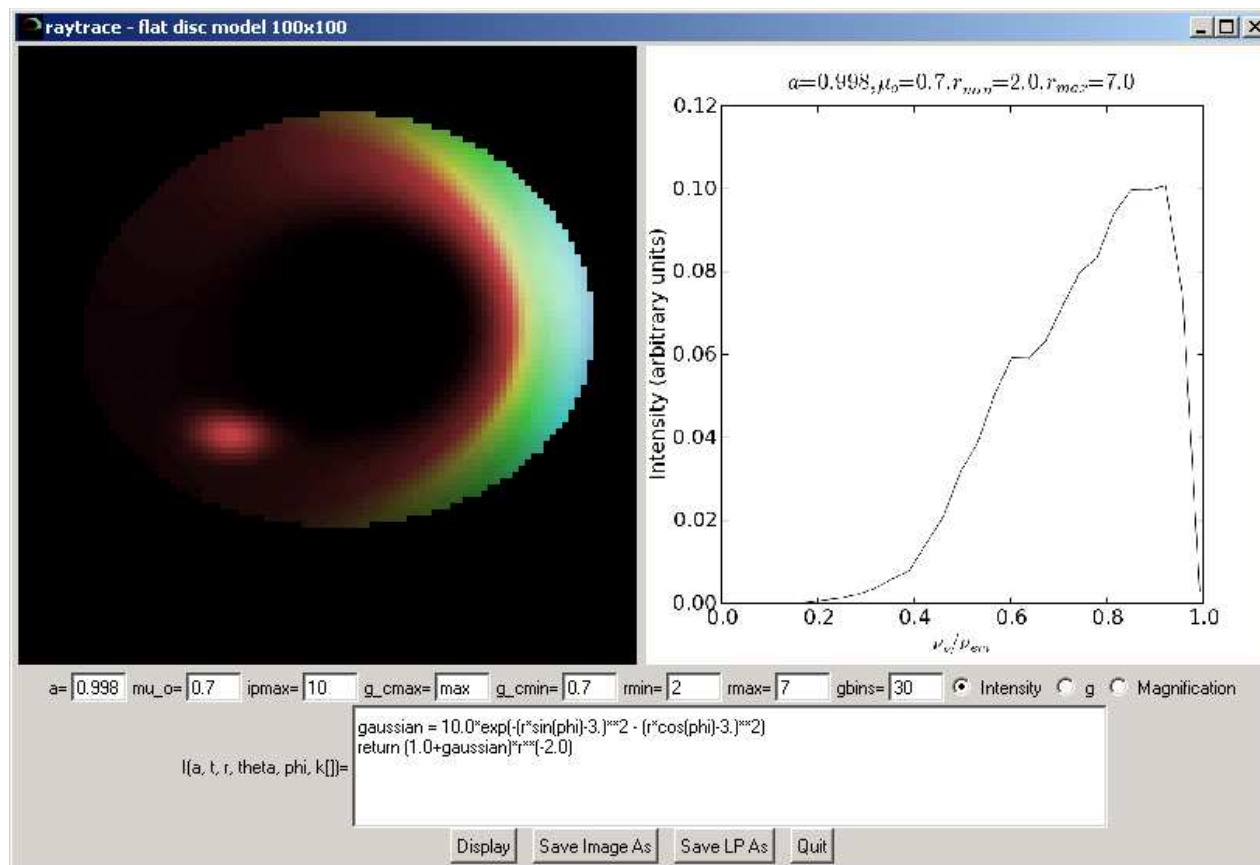
Figure 6.2: A simple example of a 100x100 pixel image and line profile generated by the raytracer interface for a disk with a hotspot in the user defined emitted intensity.

6.3.1 Line Profiles

Line profile calculation is usually done using either of two methods, tracing forwards from the emission point or backwards from the observer. In the former case a ray tracing routine is used to trace forward a calculated emission from a given point. If an emission angle is traced forward and reaches the observer at infinity (observer angle θ_{obs}), the impact paramter, redshift, and observed intensity etc are stored. In the back-tracing case the geodesics with for each set of impact parameters ($\alpha, beta$) are traced forward until intersection with the disc or horizon

In the Schwarzschild case (Fabian et al 1989) the ray tracing is reduced to a simple analytic calculation with

$$g = \left(1 - \frac{3M}{r_s}\right)^{1/2} \left\{1 + \frac{\cos\beta}{[r_s(1 + \tan^2\xi)/M - 2]^{1/2}}\right\}^{-1} \tag{6.80}$$

where β is the angle between the disc plane and the plane of the photon trajectory, and $\xi + \pi/2$ is the angle between the direction of photon emission and the black hole-observer axis.

A double horned shape is common to most of these relativistic disc line profiles, due to the doppler shifting from either side of the spinning discs. The transverse doppler shift, and the gravitational redshift cause the assymetry between the two peaks, lowering the red peak, but broadening the red wing. The inner radius does not seem to effect the profile much, except in the red tail, whereas shifting the outer radius of the disc causes a widening (more extreme doppler shifting from either side of a larger keplarian disc) of the double horned shape, however a hard blue edge is maintained. The effect of the inclination angle is most apparent, with the lowering of inclination angle the effects of the

transverse Doppler and gravitational dominate with the mean photon energy tending towards the red, and the line shape becoming single peaked for very low inclination angle (or large r_o).

Several authors (Laor 1991, Kojima 1991, Dabrowski et al 1997, Fanton et al 1997) have explored a similar case for the Kerr black hole. More recent calculations by Beckwith and Done (2004) and Dovciak, Karas and Yaqoob (2004) have introduced new computational techniques to calculate the line profiles in strong gravity. For the most part their calculations develop and refine the calculations done previously, comparing their models to those produced by the XSPEC packages "diskline" and "laor".

The raytracer interface depicted in Figure 6.1 is used for generating line profiles and disk images. Figure 6.2 shows a disk image and line-profile based on a user-defined functional input for the disk emission profile showing a hotspot. It was developed using a Tcl/Tk & Python interface to the semi-analytic raytrace engine described above. Here the line profiles are calculated by summing the specific intensities into a number of redshift bins over all pixels.

Higher resolution disk images are shown in Figure 6.3, while Figure 6.4 demonstrates sample line profile calculations for 1000x1000 pixel images of a maximally spinning black hole with simple r^{-2} emission profile.
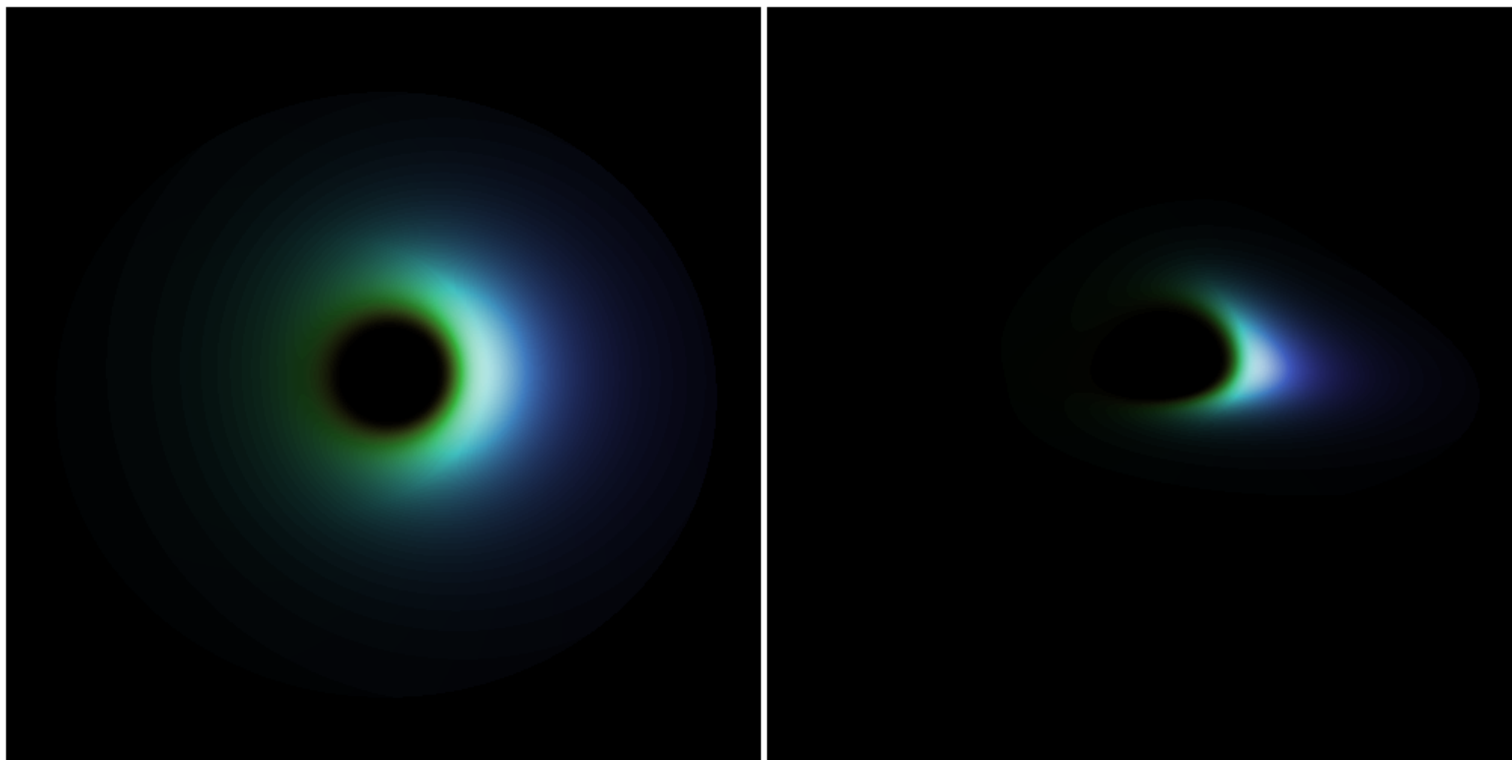
Figure 6.3: Example 500x500 pixel disk images for emission law $\propto r^{-2}$ for inclination angle 30° (left), 70° (right)
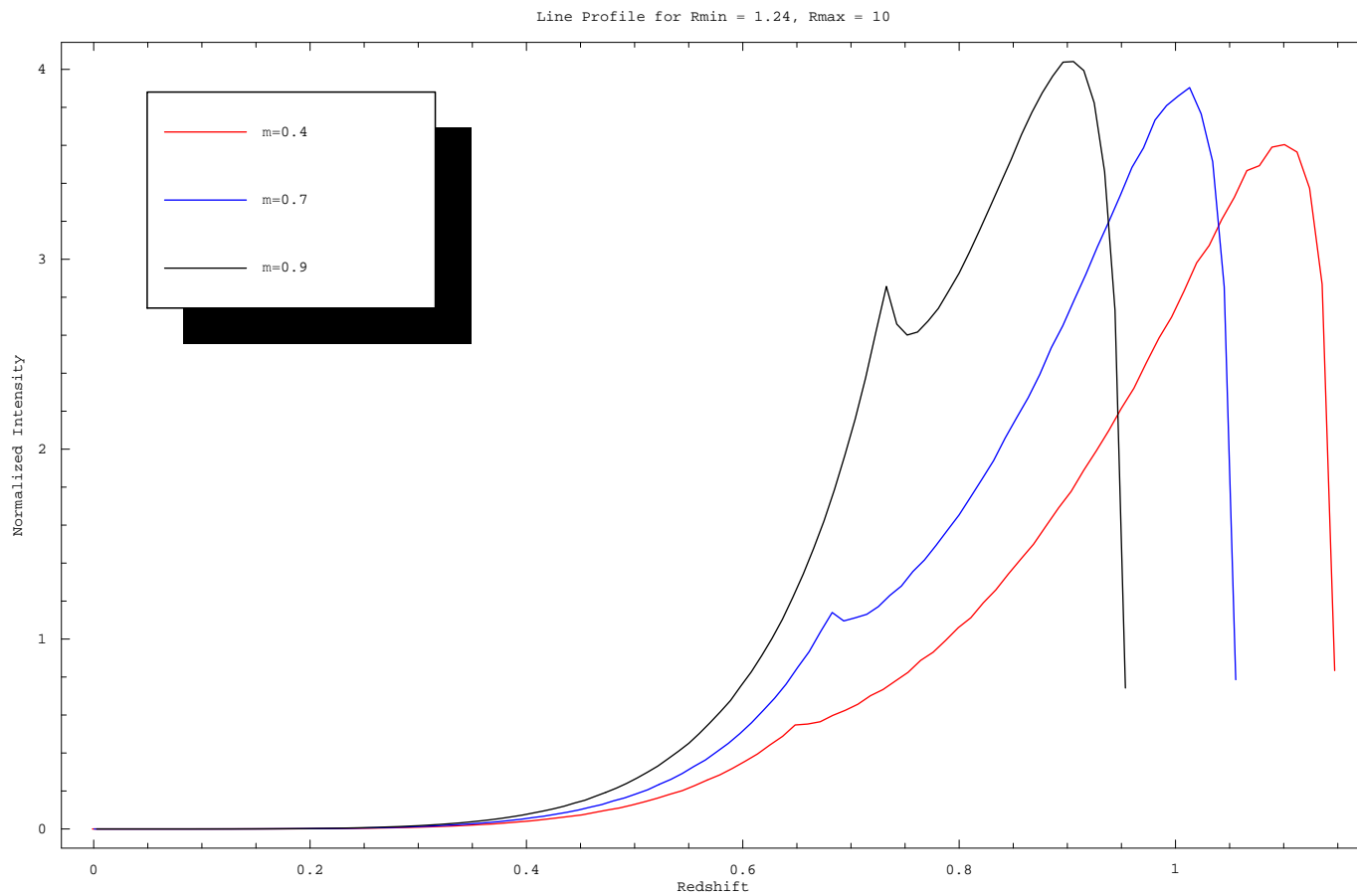
Figure 6.4: Example line profiles for emission law $\propto r^{-2}$ for various inclination angles on disk with outer radius $10M$ and inner radius at the ISCO for a maximally spinning black hole.

6.3.2 Polarization

Another observable of such emissions that can be measured is the polarization. First discussed by Connors, Piran and Stark (1980), the space-time geometry is found to play an important role in determining the polarization features of isotropic disc emission near black holes. In particular, for an isotropic electron scattering emission, there is found to be a dependance on photon energy and the degree and angle of polarization. These result from the tendancy for photons of a certain energy to emerge mostly from a certain radius and thus suffer related polarization effects.

More recent work by Chen and Eardley (1991) examine the polarization properties of line emissions from an accretion disc around a Schwarzschild black hole and show that the red wing is always more polarized than the blue wing as the emission angle in the emitting frame is larger for the receding (red) part of the disc than it is for the approaching (blue) part of the disc.the polarization angle was also found to decrease with observed frequency. Chen and Eardley propose to take these two polarization effects as a signature of relativistic line emission in strong gravity. Ogura Ohuo and Kojima (2000) extend this work to the maximal Kerr case, and find that the polarization effects change signficantly with higher spin and r_{ISCO} closer to the black hole.
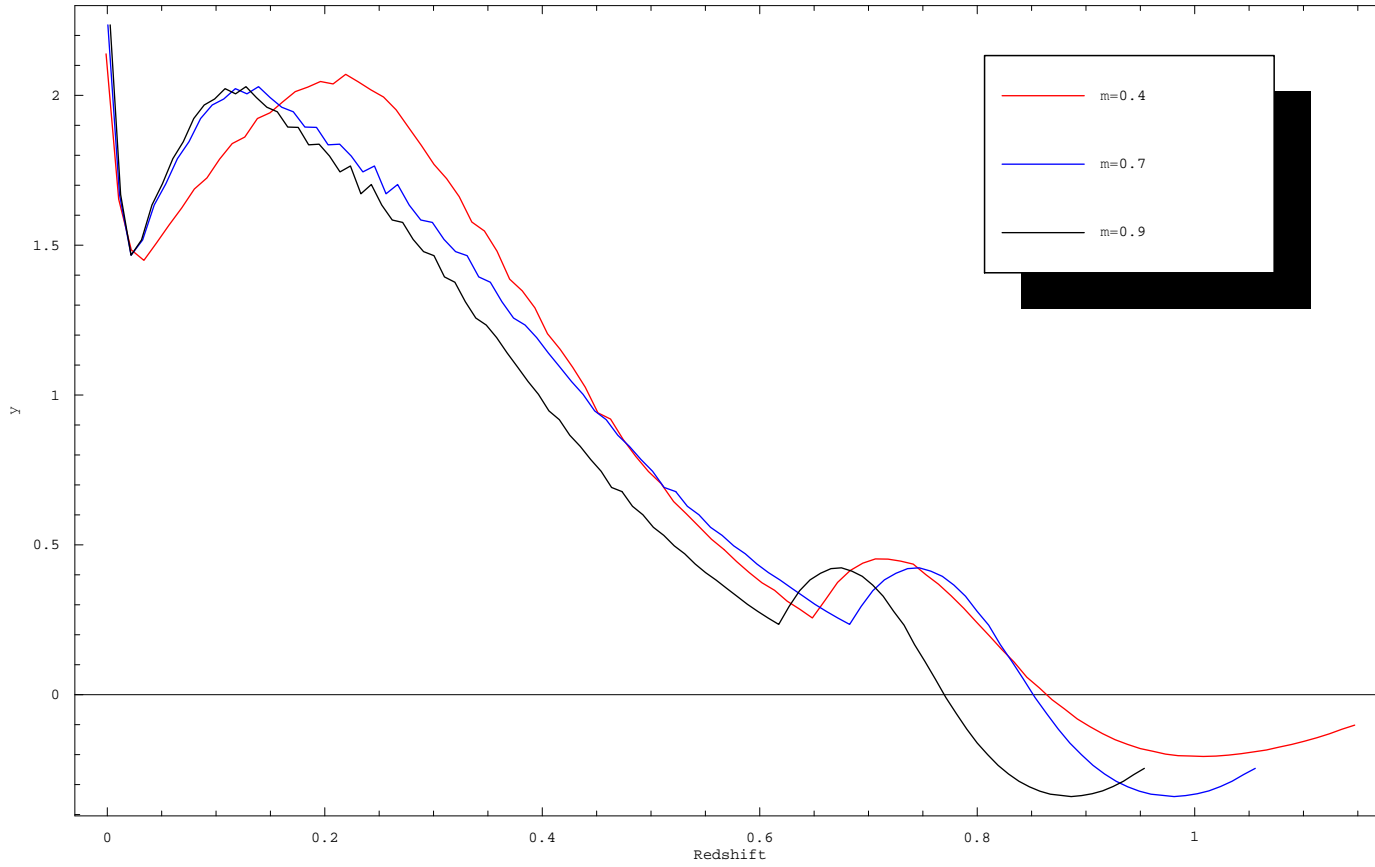
Figure 6.5: Example polarization angle ψ as a function of redshift g for various inclination angles for a disk around a maximally rotating black hole. The emission law is assumed to be $\propto r^{-2}$ with the disk extending to $r = 10M$.

The polarization state for a given photon can be calculated using the raytracing procedure by considering the Penrose-Walker constant.

$$
\begin{aligned}
\kappa_{PW} &= \kappa_r - \iota\kappa_i \\
&= (\epsilon - \iota\xi)(r - \iota a \sin\theta)
\end{aligned}
$$

where f^μ is the polarization vector, (defined with $k \cdot f = 0$ and $f \cdot f = 1$, and depending on the disc properties) and

$$
\begin{aligned}
\epsilon &= (k^t f^r - k^r - f^t) + a\sin^2\theta(k^r f^\phi - k^\phi f^r) \\
\xi &= [(r^2 + a^2)(k^\phi f^\theta - f^\phi k^\theta) - a(k^t f^\theta - -k^\theta f^t)]\sin\theta
\end{aligned}
$$

We can define this polarization four vector for an electron scattering disc by taking the polarization 3-vector in the local (rotating) frame, $f'^i = \{-k'^{(\phi')}, 0, k'^{(r')}\}$ (perpendicular to the wave-vector, but parallel to the disc surface) and changing it to a spacelike 4-vector,

$$
f'^\mu = \{0, -k'^{(\phi')}, 0, k'^{(r')}\}
$$

where $k'^{(\mu')}$ is the wave-vector in the local rotating frame.

In order to obtain the polarization vector in the non-rotating frame we must use the transformation described by Connors Piran and Stark, as

$$
f^\mu_{nr} = f^\mu - \frac{f^t k^\mu}{k^t}
$$

where f^μ is $f'^{(\mu')}$ vector lorentz tranformed to the observer's frame. We then use f^μ_{nr} and k^μ to calculate κ_{PW}.

For electron scattering (no circular polarization) we are concerned with the linear polarization at inifinity,

$$X_\infty \;=\; Q_\infty/I_\infty = \delta(S\kappa_i - T\kappa_r)/(S^2 + T^2)$$

$$Y_\infty \;=\; U_\infty/I_\infty = \delta(-S\kappa_r - T\kappa_i)/(S^2 + T^2)$$

where δ is the degree of polarization (lorentz invariant), and

$$S \;=\; \lambda/\sin\theta_{obs} - a\sin\theta_{obs}$$

$$T \;=\; sgn(k^\theta)_\infty \sqrt{q^2 - \lambda^2 \cot\theta_{obs} + a^2 \cos^2\theta_{obs}}$$

With the wave vector determined, and a disc model assumed, the degree of the redshift g, degree of polarization δ, polarization angle $\psi = \frac{1}{2}\tan^{-1} Y_\infty/X_\infty$, and Intensity $I_\infty(\alpha,\beta) = g^3 I_e m(r_e m)$ can be determined and output for each pixel.

Example polarization vs redshift plots are shown in Figure 6.5 for various inclination angles.

6.3.3   Appearance of Disc Perturbations

Lastly we provide an example of the observed intensity variation due to a disk perturbation such as those described in Chapter 3. Though the perturbations calculated in Chapter 3 were for a pseudo-Newtonian potential, we nevertheless utilize the full raytracing engine in the Kerr metric to demonstrate its efficacy.[2]

Here we utilize the emissivity law estimated by Falanga et al. (2007) and take the intensity variation disk emitted Intensity I_{em} to be given by

$$I_{em} \propto \Sigma^{15/4} r^{-13/8} \tag{6.81}$$

---

[2]The general setup for perturbations of a thin disk in a Kerr spacetime is discussed briefly in Appendix E.
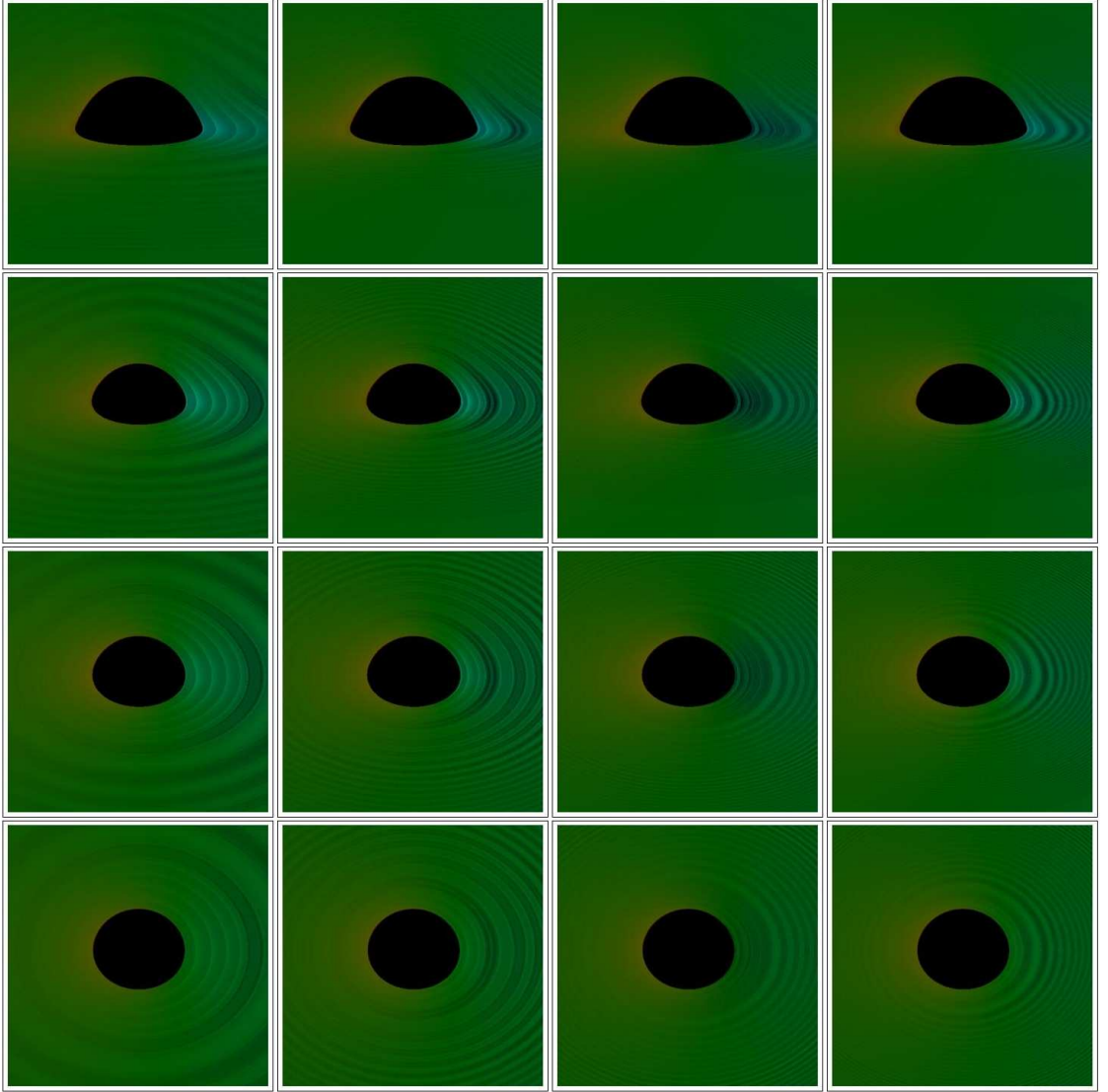
Figure 6.6: False color images of the observed perturbed disk emissions, with (left to right) $m = 1, 2, 3, 4$, and (top to bottom) $\cos i = 0.2, 0.4, 0.6, 0.8$.

From Chapter 2 we have for barotropic flow $\delta h = c_s^2 \delta\Sigma/\Sigma$ and our assumed surface density profile $\Sigma \propto r^{-p}$ our perturbed disk emission will then be

$$\delta I_{\rm em} \propto \frac{15}{4} c_s^2 \delta h \, r^{-\frac{30p+13}{8}}. \tag{6.82}$$

The complex value of δh allows for us to calculate a complex local emission intensity $\tilde{I}_{\nu_{\rm em}}$. This in turn allows us to write from equation (6.79)

$$\tilde{F}_{\nu_{obs}} = \frac{1}{D^2} \iint g^3 \tilde{I}_{\nu_{em}} \exp[i\omega_r \Delta t'(\alpha,\beta) - i\omega_r t] \left| -\frac{U_{em}^\gamma p_{em}^\delta}{U_{em}^\epsilon p_{em\,\epsilon}} \frac{dx^\mu}{d\alpha} \frac{dx^\nu}{d\beta} \varepsilon_{\gamma\delta\mu\nu} \right| d\alpha d\beta \tag{6.83}$$

where the perturbation has eigenfrequency $\omega_r + i\omega_i$, and $\Delta t'(\alpha,\beta)$ is the time delay of each pixel given by equation (6.70).

We can then Fourier transform equation (6.83) to get the power spectrum due to the disk perturbations.

$$\mathcal{F}[\tilde{F}_{\nu_{obs}}] = \left[\frac{1}{D^2} \iint g^3 \tilde{I}_{\nu_{em}} \exp[i\omega_r \Delta t'(\alpha,\beta)] \left| -\frac{U_{em}^\gamma p_{em}^\delta}{U_{em}^\epsilon p_{em\,\epsilon}} \frac{dx^\mu}{d\alpha} \frac{dx^\nu}{d\beta} \varepsilon_{\gamma\delta\mu\nu} \right| d\alpha d\beta \right] \delta(\omega - \omega_r) \tag{6.84}$$

6.4 Conclusions

We have developed a tool for relativistic raytracing in the Kerr metric that allows us to calculate several observables useful for the analysis of disk emissions, including line profiles, disk images, polarization and time dependent emissions from disk perturbations. While the use of the general Kerr metric is not strictly necessary for examining the emissions due to the pertrubations discussed in earlier chapters, future work will include fully relativistic disk perturbations (see Appendix E) for which these techniques will be necessary.

APPENDIX A

STOKES PHENOMENON AND THE MATCHING CONDITION ACROSS THE COROTATION SINGULARITY

As we saw in section 2.3.2 the perturbation equation near the corotation resonance can be solved in terms of the Whittaker function. However in order to provide the matching conditions we must carefully consider the effect of the Stokes Phenomenon on the asymptotic expansions.

Stokes phenomenon causes the functional form of the asymptotic expansion of an entire function to be different at different points in the complex plane. The general asymptotic solution of the Whittaker equation for $|z| \gg 1$ can be written as a linear combination of two functions

$$P(z) = e^{z/2}z^{-\nu}, \qquad Q(z) = e^{-z/2}z^{\nu}, \tag{A.1}$$

i.e., $AP(z) + BQ(z)$. However, because of the Stokes phenomenon, the coefficients A and B can change when crossing the Stokes lines. For Whittaker functions, the Stokes lines are the positive real axis (where P is dominant and Q is subdominant) and negative real axis (where Q is dominant and P is sub-dominant).

Consider specific solution to the Whittaker equation, with the asymptotic expansion ($|z| \gg 1$) given by

$$F(z) \to AP(z) + BQ(z), \qquad (\text{for} \quad \arg(z) = 0) \tag{A.2}$$

on the real axis. Our goal is to derive the expansion coefficients of $F(z)$ on the negative real axis ($\arg(z) = \pi$). To achieve this, we use the general results obtained by Heading (1962):

(1) "The coefficient of the subdominant term after crossing the Stokes line = the coefficient of the subdominant term before crossing the Stokes line + $T_n\times$ the coefficient of the dominant term on the Stokes line."

(2) "The coefficient of the subdominant term on the Stokes line = the coefficient of the subdominant term before the Stokes line $+\frac{1}{2}T_n\times$ the coefficient of the dominant term on the Stokes line."

Here T_n is the Stokes multiplier for crossing the Stokes line $\arg(z) = n\pi$ in the direction of increasing $\arg(z)$ given by [1]

$$T_n = \frac{2\pi i e^{-2\pi i n s\nu}}{\Gamma(s\nu)\Gamma(1 + s\nu)} \tag{A.3}$$

where $s = (-1)^n$. Note that since the pole of equation (2.39) lies below the real axis, $\arg(z)$ increases as we we move along the contour from z positive and real ($\arg(z) = 0$) to z negative and real ($\arg(z) = \pi$).

Since equation (A.2) is given on one of the Stokes line, we first determine $F(z)$ in the region $-\pi < \arg(z) < 0$:

$$F(z) \sim AP(z) + \left(B - \frac{1}{2}T_0 A\right) Q(z), \qquad (\text{for } -\pi < \arg(z) < 0). \tag{A.4}$$

Then in region $0 < \arg(z) < \pi$ we have

$$F(z) \sim AP(z) + \left(B + \frac{1}{2}T_0 A\right) Q(z), \qquad (\text{for } 0 < \arg(z) < \pi). \tag{A.5}$$

Thus on the negative real axis, we obtain

$$F(z) \sim \left[A + \frac{1}{2}T_1\left(B + \frac{1}{2}T_0 A\right)\right] P(z) + \left(B + \frac{1}{2}T_0 A\right) Q(z), \qquad (\text{for } \arg(z) = \pi). \tag{A.6}$$

---

[1]Note that a typo in equation (18) of Heading (1962) has been corrected here.

The connection formulae for the two independent Whittaker functions for $|z| \gg 1$ are

$$\psi_- = W_{\nu,1/2}(z) \sim \begin{cases} Q(z) & \arg(z) = 0 \\ Q(z) + \frac{1}{2}T_1 P(z) & \arg(z) = \pi \end{cases} \tag{A.7}$$

$$\psi_+ = e^{-i\pi\nu} W_{-\nu,1/2}(z e^{-i\pi}) + \frac{1}{2} T_0 W_{\nu,1/2}(z). \sim \begin{cases} P(z) & \arg(z) = 0 \\ \frac{1}{2}T_0 Q(z) + \left(1 + \frac{1}{4}T_0 T_1\right) P(z) & \arg(z) = \pi, \end{cases} \tag{A.8}$$

where $P(z)$ and $Q(z)$ have the asymptotic behavior

$$P(z) = e^{+z/2 - \nu \log(z)} \sim \begin{cases} \exp\left(\int_{r_c}^{r} \tilde{k}\, dr\right) & \text{for } r \gg r_c \\ e^{-i\pi\nu} \exp\left(-\int_{r}^{r_c} \tilde{k}\, dr\right) & \text{for } r \ll r_c \,. \end{cases} \tag{A.9}$$

$$Q(z) = e^{-z/2 + \nu \log(z)} \sim \begin{cases} \exp\left(-\int_{r_c}^{r} \tilde{k}\, dr\right) & \text{for } r \gg r_c \\ e^{i\pi\nu} \exp\left(\int_{r}^{r_c} \tilde{k}\, dr\right) & \text{for } r \ll r_c \,. \end{cases} \tag{A.10}$$

for $|z| \gg 1$, since in this limit $|z| \gg \log|z|$.

APPENDIX B

RESONANCE TUNNELING

To help understand the effect of wave absorption at the corotation singularity we consider the following toy problem. For a 1-D quantum mechanical potential of the form

$$V(x) = \frac{C}{x},$$ (B.1)

we have the time-independent wave equation

$$\left(\frac{1}{2} \frac{d^2}{dx^2} + E - \frac{C}{x + i\epsilon} \right) \psi = 0,$$ (B.2)

where we have set the Planck constant and particle mass to unity. In equation (B.2), a small imaginary part $i\epsilon$ is added to x, to account for the physical requirement of a growing incoming perturbation. The sign of ϵ must be the same as the sign of C, so as to give us the correct physical behavior. For concreteness we will assume $C > 0$ (and thus $\epsilon > 0$), though the same calculation can be performed for $C < 0$ ($\epsilon < 0$) with similar results.

Let $y = 2ik(x + i\epsilon)$, where $k = \sqrt{2E}$, we have

$$\frac{d^2\psi}{dy^2} + \left(-\frac{1}{4} + \frac{\nu}{y} \right) \psi = 0, \qquad \text{with } \nu = iC/k, ,$$ (B.3)

which we recognize as the Whittaker differential equation. With $C > 0$, y lies in the domain $\pi/2 \leq \arg(y) \leq 3\pi/2$. Using the same procedure as discussed in Appendix A, we obtain the connection formulae for the general solution of equation (B.3) as

$$\psi \rightarrow \begin{cases} AP(z) + BQ(z) & \text{for } \arg(z) = \pi/2 \\ (A + T_1B)P(z) + BQ(z) & \text{for } \arg(z) = 3\pi/2. \end{cases}$$ (B.4)

Consider a wave propagating from $x = -\infty$ and impinging on the potential. The transmitted wave at $x > 0$ has the form

$$\psi_+ \to e^{y/2} y^{-\nu} = e^{ikx - i(C/k)\ln|2kx| + \pi C/2k} \qquad \text{for } x \gg 1/k. \qquad \text{(B.5)}$$

The corresponding wave solution in the $x < 0$ region has the asymptotic form

$$\psi_+ \to e^{y/2} y^{-\nu} = e^{ikx - i(C/k)\ln|2kx| + 3\pi C/2k} \qquad \text{for } x \ll -1/k. \qquad \text{(B.6)}$$

This gives

$$|\mathcal{R}| = 0, \qquad |\mathcal{T}| = e^{-\pi C/k} \qquad \text{(B.7)}$$

for a wave incident from $x < 0$.

Now consider a wave incident from the $x > 0$ region towards small x. The transmitted wave is given by

$$\psi_- \to e^{-y/2} y^{+\nu} = e^{-ikx + i(C/k)\ln|2kx| - 3\pi C/2k} \qquad \text{for } x \ll -1/k. \qquad \text{(B.8)}$$

Connecting to the $x > 0$ region, we have

$$\psi_- \to e^{-y/2} y^{+\nu} - T_1 e^{y/2} y^{-\nu} = e^{-ikx + i(C/k)\ln|2kx| - \pi C/2k} - T_1 e^{ikx - i(C/k)\ln|2kx| + \pi C/2k} \qquad \text{for } x \gg 1/k.$$
$$\text{(B.9)}$$

This gives the reflection and transmission coefficients

$$\begin{aligned}
|\mathcal{R}| &= e^{\pi C/k} |T_1| \\
&= \frac{2\pi e^{-\pi C/k}}{|\Gamma(-iC/k)\Gamma(1 - iC/k)|} = 2e^{-\pi C/k} \sinh(\pi C/k) = 1 - e^{-2\pi C/k}, \qquad \text{(B.10)} \\
|\mathcal{T}| &= e^{-\pi C/k}, \qquad\qquad\qquad\qquad\qquad\qquad\qquad\qquad\qquad\qquad\qquad\quad \text{(B.11)}
\end{aligned}$$

for a wave incident from the positive side of the singularity [a similar result was obtained by Budden (1979) in the context of wave propagation in cold plasma].

We can define the wave absorption coefficient at the singularity as

$$\mathcal{D} = 1 - |\mathcal{T}|^2 - |\mathcal{R}|^2 \qquad \text{(B.12)}$$

For the forward moving incident wave (+) and the backwards moving incident wave (−), we have

$$\mathcal{D}_+ = 1 - e^{-2\pi C/k}, \qquad \mathcal{D}_- = e^{-2\pi C/k}\left(1 - e^{-2\pi C/k}\right). \tag{B.13}$$

APPENDIX C

PLANE PARALLEL FLOW WITH A COMPRESSIBLE UPPER LAYER

Consider a system consisting of two fluids in the gravitational field $\mathbf{g} = -g\hat{\mathbf{z}}$. The upper fluid ($z > 0$) has density $\rho = \rho_+ e^{-z/H_z}$ (with $H_z = c_s^2/g$, where c_s is the sound speed) and horizontal velocity u_+ along the x-axis; the lower fluid ($z < 0$) is incompressible with density ρ_- and horizontal velocity u_-.

The linear perturbation equations for the upper fluid are

$$\frac{\partial}{\partial t}\delta\rho + \nabla \cdot (\rho\delta\mathbf{u} + \mathbf{u}\delta\rho) = 0 \tag{C.1}$$

$$\frac{\partial}{\partial t}\delta\mathbf{u} + (\mathbf{u} \cdot \nabla)\delta\mathbf{u} + (\delta\mathbf{u} \cdot \nabla)\mathbf{u}_o = -\nabla\delta h \tag{C.2}$$

where $\delta h = \delta P/\rho$. For perturbations of the form $e^{ikx - i\omega t}$, these become

$$-i\tilde{\omega}\delta\rho + ik\rho\delta u_x + \frac{\partial}{\partial z}(\rho\delta u_z) = 0, \tag{C.3}$$

$$i\tilde{\omega}\delta u_z = \frac{\partial}{\partial z}\delta h, \tag{C.4}$$

$$i\tilde{\omega}\delta u_x = ik\delta h, \tag{C.5}$$

where $\tilde{\omega} = \omega - ku$ with $u = u_+$. Assuming the perturbation is isothermal, so that $\delta P = c_s^2\delta\rho$ we obtain

$$\delta h''(z) - \frac{1}{H_z}\delta h'(z) - (k^2 - \tilde{\omega}^2/c^2)\delta h(z) = 0. \tag{C.6}$$

The two independent solutions of equation (C.6)

$$\delta h \propto \exp\left[\frac{z}{2H_z}\left(1 \pm \sqrt{1 + 4H_z^2 k_z^2}\right)\right] \tag{C.7}$$

where $k_z^2 = (k^2 - \tilde{\omega}^2/c^2)$. Obviously, the physically relevant solution is

$\delta h \propto \exp(-\tilde{k}z)$, with $\tilde{k} = (\sqrt{1 + 4H_z^2 k_z^2} - 1)/2H_z$.

This gives, by equation (C.4) the Eulerian pressure perturbation for the upper region:

$$\delta P_+ = -\frac{i\tilde{\omega}_+ \rho_+}{\tilde{k}}\delta u_{z+}. \tag{C.8}$$

For the lower region the fluid is an incompressible potential flow with $\delta \mathbf{u} = \nabla \delta \psi$ with $\delta \psi$ satisifying $\nabla^2 \delta \psi = 0$. For $z < 0$, the appropriate solution is

$$\delta \psi \propto \exp(kz). \tag{C.9}$$

This gives $\nabla(i\omega\delta\psi + \delta P_-/\rho_-) = 0$ which gives for the Eulerian pressure perturbation in the lower region ($z < 0$):

$$\delta P_- = \frac{i\rho\tilde{\omega}}{k}\delta u_{z-}. \tag{C.10}$$

Matching the Lagrangian displacement and Lagrangian pressure perturbation across the boundary between the upper and lower regions we get

$$\frac{\tilde{\omega}_+^2 \rho_+}{\tilde{k}} + \rho_+ g = -\frac{\tilde{\omega}_-^2}{k} + \rho_- g, \tag{C.11}$$

which can be written as the quadratic:

$$\omega^2 - \left[\frac{\rho_+\frac{k}{\tilde{k}}2ku_+ + \rho_- 2ku_-}{\rho_+\frac{k}{\tilde{k}} + \rho_-}\right]\omega + \frac{\rho_+\frac{k}{\tilde{k}}k^2u_+^2 + \rho_- k^2 u_-^2}{\rho_+\frac{k}{\tilde{k}} + \rho_-} + g\frac{\rho_+ - \rho_-}{\rho_+\frac{k}{\tilde{k}} + \rho_-}. \tag{C.12}$$

where $\tilde{k}$ has a non trivial dependence on ω. This has a solution

$$\omega = \frac{k(\tilde{\rho}_+ u_+ + \rho_- u_-)}{\tilde{\rho}_+ + \rho_-} \pm \sqrt{-\frac{k^2(u_+ - u_-)\tilde{\rho}_+ \rho_-}{(\tilde{\rho}_+ + \rho_-)^2} - \frac{kg(\rho_+ - \rho_-)}{\tilde{\rho}_+ + \rho_-}} \tag{C.13}$$

where $\tilde{\rho}_+ = \rho_+ k/\tilde{k}$.

APPENDIX D

NUMERICAL METHODS FOR JACOBI ELLIPTIC FUNCTIONS AND INTEGRALS

D.1   Evaluating $\text{sn}(z, k)$

D.1.1   4 real roots

In the case of 4 real roots the evaluation of $\text{sn}(u, k)$ becomes a straightforward application of the Press et al. (1998) routines following Bulirsch (1965) (computation by the succesive applications of Gauss' transformation).

D.1.2   4 complex roots

Form of the $R(4)$ quartic gives us roots that, if all complex, yield a purely real modulus k. Using the complex argument relation given in Byrd & Friedman(1971),

$$\text{sn}(u \pm iv, k) = \frac{\text{sn}(u, k)\text{dn}(v, k') \pm i\text{cn}(u, k)\text{dn}(u, k)\text{sn}(v, k')\text{cn}(v, k')}{1 - \text{sn}^2(v, k')\text{dn}^2(u, k)} \tag{D.1}$$

we can thus evaluate sn using the routines provided in NR. Similar transformations are also available for cn and dn.

$$\text{cn}(u \pm iv, k) = \frac{\text{cn}(u, k)\text{cn}(v, k') \mp i\text{sn}(u, k)\text{dn}(u, k)\text{sn}(v, k')\text{dn}(v, k')}{1 - \text{sn}^2(v, k')\text{dn}^2(u, k)} \tag{D.2}$$

$$\text{dn}(u \pm iv, k) = \frac{\text{dn}(u, k)\text{cn}(v, k')\text{dn}(v, k') \mp ik^2\text{sn}(u, k)\text{cn}(u, k)\text{sn}(v, k')\text{dn}(v, k')}{1 - \text{sn}^2(v, k')\text{dn}^2(u, k)} \tag{D.3}$$

D.1.3   2 real, 2 complex roots

In the case of r_1 r_2 real, and r_3 r_4 complex, we have

$$k^2 = \frac{4B^2 - (\sqrt{-A + 2D + 4C/B} - i\sqrt{-A + 2D - 4C/B})^2}{4B^2 - (\sqrt{-A + 2D + 4C/B} + i\sqrt{-A + 2D - 4C/B})^2} \tag{D.4}$$

which is complex in general, but with $|k^2| = 1$.

Examining Landen's Transformation (see Byrd) we have

$$sn[(1 + k')u, k_1] = (1 + k')sn(u, k)cd(u, k) \tag{D.5}$$

where

$$cd(u, k) = \frac{cn(u, k)}{dn(u, k)} \tag{D.6}$$

$$k_1 = (1 - k')/(1 + k') \tag{D.7}$$

$$\tag{D.8}$$

and $k' = \sqrt{1 - k^2}$ is the complementary modulus.

Taking $k' = i\kappa$ and noting that $|k_1| = |(1 - i\kappa)/(1 + i\kappa)| = 1$ we see that

$$sn[z, \sqrt{m}] = (1 + i\kappa)sn\left(\frac{z}{1 + i\kappa}, \sqrt{1 + \kappa^2}\right)cd\left(\frac{z}{1 + i\kappa}, \sqrt{1 + \kappa^2}\right) \tag{D.9}$$

if $|m| = 1$ and

$$\kappa = -\frac{1}{\xi} + \sqrt{\frac{1}{\xi} + 1} \tag{D.10}$$

$$\xi = -\frac{Re(m)}{Im(m)} + \sqrt{\left(\frac{Re(m)}{Im(m)}\right)^2 + 1} \tag{D.11}$$

In evaluating the elliptic functions for the complex argument z the modulus $i\kappa$

occurs and the imaginary modulus transformations can be used in these cases.

$$\operatorname{sn}(u, ik) \;=\; \frac{1}{\sqrt{1+k^2}} \frac{\operatorname{sn}(u\sqrt{1+k^2}, k/\sqrt{1+k^2})}{\operatorname{dn}(u\sqrt{1+k^2}, k/\sqrt{1+k^2})} \tag{D.12}$$

$$\operatorname{cn}(u, ik) \;=\; \frac{\operatorname{cn}(u\sqrt{1+k^2}, k/\sqrt{1+k^2})}{\operatorname{dn}(u\sqrt{1+k^2}, k/\sqrt{1+k^2})} \tag{D.13}$$

$$\operatorname{dn}(u, ik) \;=\; \frac{1}{\operatorname{dn}(u\sqrt{1+k^2}, k/\sqrt{1+k^2})} \tag{D.14}$$

$$F(\phi, ik) \;=\; \frac{1}{\sqrt{1+k^2}} F(\beta, k/\sqrt{1+k^2}) \tag{D.15}$$

where $\beta = \sin^{-1}\left[\frac{\sqrt{1+k^2}}{\sqrt{1+k^2 \sin^2 \phi}} \sin\phi \right]$.

D.2 Evaluating u_∞

Evaluating the elliptic integral as $r \to \infty$ we obtain the "initial" condition

$$u_\infty = \operatorname{sn}^{-1}\left(\sqrt{\frac{r_2 - r_3}{r_1 - r_3}}, k \right) \tag{D.16}$$

Again we must be careful in evaluating this for different cases involving real and complex roots.

D.2.1 r_n all real and r_n all complex

For r_n all real, we can simply evaluate the expression using the routine for $F(u, k)$ from Press et al. (1998) as

$$\operatorname{sn}^{-1}(u, k) = F(\sin^{-1} u, k) \tag{D.17}$$

For the all complex case the the modulus k is still purely real, but the argument u is not in general. However we can simply utilize the relation:

$$F(u + iv, k) = F(\lambda, k) + iF(\mu, k') \tag{D.18}$$

where

$$k' = \sqrt{1 - k^2} \qquad (D.19)$$

and $\cot^2 \lambda$ is the positive root of the quadratic

$$x^2 - [\cot^2 u + k^2 \sinh^2 v \csc^2 \phi - (1 - k^2)]x - (1 - k^2)\cot^2 u = 0 \qquad (D.20)$$

and

$$k^2 \tan^2 \mu = \tan^2 u \cot^2 \lambda - 1 \qquad (D.21)$$

D.2.2   2 methods for 2 complex roots and 2 real roots

For complex values of the modulus a general algorithm is provided for evaluating elliptic integrals of the first kind by Morita (1999), as a modificiation to the algorithm provided by Carlson (1979) (this algorithm is used in by Press et al., 1998). This modification allows evaluation of complex modulus $(-\pi < Arg(k) \leq \pi)$ for only real values of the argument u. However, simple extension using the complex argument relation above can be performed to calculate results for generally complex argements and modulus.

However, noting that the modulus k must have $|k| = 1$ for the mixed roots case, we can also use Landen's transformation to achieve the same result.

$$F(\phi, k_1) = (1 + k')F(\theta, k) \qquad (D.22)$$

where we choose k' such that

$$k' = i\kappa \qquad (D.23)$$

$$k_1 = \frac{1 - i\kappa}{1 + i\kappa} \qquad (D.24)$$

$$k = \sqrt{1 + \kappa^2} \qquad (D.25)$$

and θ is given by the equation

$$k_1 \sin \phi = \sin(2\theta - \phi) \tag{D.26}$$

Using Morita's algorithm we require a modification that slightly increases the cost of the Carlson Recursion forumlas, and an implementation of the algorithms that ensures that all arithmetic is done in a complex fashion.

The use of the Landen transformation requires the evaluation of 2 complex arcsin functions, and the use of Carlsons's original algorithm. The two different procedures are roughly equivalent in terms of computational speed, and Morita's algorithm is used when the domain in question is appropriate.

APPENDIX E

2D FLUID DISKS IN THE KERR METRIC USING THE COWLING APPROXIMATION

We begin with the metric from Novikov and Thorne (1973) (and from Perez et al 1997):

$$ds^2 = -\frac{r^2\Delta^*}{A^*}dt^2 + \frac{A^*}{r^2}\left(d\phi - \frac{2ar}{A^*}dt\right)^2 + \frac{r^2}{\Delta^*}dr^2 + dz^2 \qquad (E.1)$$

with $\Delta^* \equiv r^2 - 2r + a^2$ and $A^* = r^4 + r^2a^2 + 2ra^2$ in units of $G = c = M_{BH} = 1$.

From Ipser and Lindblom (1992), we can integrate their equations (8) and (9) in the vertical direction, and carry through the calculation with the vertically integrated quantities $\Sigma = \int \rho dz$ and $P = \int p dz$. Defining $\delta\hat{V} \equiv \delta P/\Sigma\beta\tilde{\omega}$, we have

$$D_\mu[(-g_{tt}g_{\phi\phi} + g_{t\phi}^2)^{1/2}(\Sigma + P)H^{\mu\nu}D_\nu\delta\hat{V}] + (-g_{tt}g_{\phi\phi} + g_{t\phi}^2)^{1/2}\beta\tilde{\omega}\hat{\Phi}\delta\hat{V} = 0 \qquad (E.2)$$

where

$$\beta = dt/d\tau = \frac{r^{3/2} + a}{r^{3/4}(r^{3/2} - 3r^{1/2} + 2a)^{1/2}} \qquad (E.3)$$

converts between coordinate time and proper time of the fluid element (in this case assuming free particle motion). We find from the metric that $-g_{tt}g_{\phi\phi} + g_{t\phi}^2 = \Delta^*$.

Taking $\delta\hat{V} = \delta\hat{V}(r)$ with no vertical structure, and a $p = p(\rho)$ barotropic disk we have the simplified forms for equations (21), (31), and (40)-(42) from Ipser and Lindblom become (since $A_\mu = 0$), (we also assume that $\Sigma \gg P$)

$$\frac{\Lambda}{\beta^2\tilde{\omega}^2} \equiv (\beta^2\tilde{\omega}^2 - 2\Omega^a\chi_a) \simeq \beta^2(\tilde{\omega} - \kappa^2) = -\beta^2 D \qquad (E.4)$$

where $\chi^a = \epsilon^{abcd}u_b\nabla_c u_d$ is the vorticity, and $u^a = \beta(t^a + \Omega\phi^a)$ is the fluid 4-velocity, and we've used equation (2.16) of Perez et al, where the approximation is exact

assuming a flat disk, and the fluid flowing in free-particle circular orbits. Here we are also taking $\Omega = \frac{1}{r^{3/2}+a}$ and $\kappa = \Omega\left(1 - \frac{6}{r} + \frac{8a}{r^{3/2}} - \frac{3a^2}{r^2}\right)^{1/2}$ to be the free particle values. The angular velocity 4-vector is defined in IL as $\Omega^a = \frac{1}{2}\beta\epsilon^{abcd}u_b(\nabla_c t_d + \Omega\nabla_c\phi_d)$ which is $\{0,0,0,r^{-3/2}\}$ for disks with fluid undergoing geodesic orbits.

$$\hat{\Phi} = \frac{\Sigma\beta\tilde{\omega}}{c^2} + H^\mu D_\mu P - \frac{1}{\sqrt{\Delta^*}} D_\mu[\sqrt{\Delta^*}\Sigma H^\mu] - \frac{1}{\sqrt{\Delta^*}} D_\mu\left[\frac{\sqrt{\Delta^*}}{\beta^2\tilde{\omega}^2}\Sigma H^{\mu\nu}D_\nu\beta\tilde{\omega}\right] - \frac{\Lambda\Sigma}{\Delta^*\tilde{\omega}\beta^3}(m+\beta\tilde{\omega}u_\phi)^2$$

(E.5)

with

$$H^{\mu\nu} = \frac{\Lambda}{\beta^2\tilde{\omega}^2}\left[\beta^2\tilde{\omega}^2 g^{\mu\nu} - 2\chi^\mu\Omega^\nu\right] \tag{E.6}$$

$$H^{rr} = -g^{rr}\frac{\beta^2\tilde{\omega}^2}{\beta^2 D} \tag{E.7}$$

$$H^{zz} = 1 \tag{E.8}$$

$$H^{rz} = 0 = H^{zr} \tag{E.9}$$

and

$$H^\mu = \frac{\Lambda}{\beta^2\tilde{\omega}^2}\frac{2}{\sqrt{\Delta^*}\beta^3\tilde{\omega}^2}(m + \beta\tilde{\omega}u_\phi)\epsilon^{\mu\nu}(\beta^2\tilde{\omega}^2\Omega_\nu) \tag{E.10}$$

$$H^r = -\frac{2(m + \beta\tilde{\omega}u_\phi)\Omega^z/\beta}{\sqrt{\Delta^*}\beta^2 D} \tag{E.11}$$

Rewriting equation (2)

$$\delta\hat{V}'' + \frac{d}{dr}\ln\left[\frac{r\Sigma\Upsilon^2\beta^2\tilde{\omega}^2}{\beta^2 D}\right]\delta\hat{V}' - \frac{\beta^2 D}{\Sigma\Upsilon^2\beta\tilde{\omega}}\hat{\Phi}\delta\hat{V} = 0 \tag{E.12}$$

where $\Upsilon^2 \equiv g^{rr} = \Delta^*/r^2$ as defined in Perez et al. And we've used the co-variant derivative in the $r - z$ surface perpendicular to the killing vectors, $D_r f^r = \Upsilon\partial_r[\Upsilon^{-1}f^r]$

Evaulating the last coefficient of $\delta \hat{V}$ we have

$$
\begin{aligned}
\frac{\beta^2 D}{\Sigma \Upsilon^2 \beta \tilde{\omega}} \hat{\Phi} \quad = \quad & \frac{\beta^2 D}{\Upsilon^2 c^2} + \frac{m^{*2}}{\beta^2 \Upsilon^4 r^2} + \frac{2\Omega^z/\beta}{r\beta\tilde{\omega}} \frac{m^*}{\Upsilon^3} \frac{d}{dr} \ln\left[\frac{\Sigma \Upsilon^2 \Omega^z/\beta}{\beta^2 D}\right] \\
& + \frac{2\Omega^z/\beta}{r\beta\tilde{\omega}} \frac{d}{dr}\left(\frac{m^*}{\Upsilon^3}\right) - \frac{(\beta\tilde{\omega})''}{\beta\tilde{\omega}} - \frac{(\beta\tilde{\omega})'}{\beta\tilde{\omega}} \frac{d}{dr}\left[\frac{r\Upsilon^2\Sigma}{\beta^2 D}\right] \quad \text{(E.13)}
\end{aligned}
$$

where $m^* = m + \beta\tilde{\omega}u_\phi$, with $u_\phi = (a^2 - 2ar^{1/2} + r^2)\Omega\beta$.

Converting to the enthalpy $\delta h = \delta \hat{V} \beta \omega = \delta P/\Sigma$ we then have

$$
\frac{d^2}{dr^2}\delta h + \frac{d}{dr}\ln\left[\frac{r\Sigma\Upsilon^2}{\beta^2 D}\right]\frac{d}{dr}\delta h - \frac{\beta^2 D}{\Sigma \Upsilon^2 \beta \tilde{\omega}}\hat{\Phi}\delta h - \frac{(\beta\tilde{\omega})''}{\beta\tilde{\omega}}\delta h - \frac{(\beta\tilde{\omega})'}{\beta\tilde{\omega}}\frac{d}{dr}\left[\frac{r\Upsilon^2\Sigma}{\beta^2 D}\right]\delta h = 0 \quad \text{(E.14)}
$$

which gives

$$
\begin{aligned}
0 = \quad & \frac{d^2}{dr^2}\delta h + \frac{d}{dr}\ln\left[\frac{r\Sigma\Upsilon^2}{\beta^2 D}\right]\frac{d}{dr}\delta h \\
& - \left(\frac{\beta^2 D}{\Upsilon^2 c^2} + \frac{m^{*2}}{\beta^2\Upsilon^4 r^2} + \frac{2m^*\Omega^z/\beta}{\Upsilon^3 r\beta\tilde{\omega}}\frac{d}{dr}\ln\left[\frac{\Sigma m^*\Omega^z/\beta}{\Upsilon\beta^2 D}\right]\right)\delta h \quad \text{(E.15)}
\end{aligned}
$$

In the Newtonian limit $\beta = 1 = \Upsilon$ and $m^* = m$ which gives us

$$
0 = \frac{d^2}{dr^2}\delta h + \frac{d}{dr}\ln\left[\frac{r\Sigma}{D}\right]\frac{d}{dr}\delta h - \left(\frac{D}{c^2} + \frac{m^2}{r^2} + \frac{2m\Omega^z}{r\tilde{\omega}}\frac{d}{dr}\ln\left[\frac{\Sigma\Omega^z}{D}\right]\right)\delta h \quad \text{(E.16)}
$$

BIBLIOGRAPHY

[1] Abramowitz, M, Stegun, I.A. 1964, Handbook of Mathematical Functions (Dover: New York)

[2] Abramowicz, M.A., Czerny, B., Lasota, J. P., Szuszkiewicz, E. 1988, ApJ, 332, 646

[3] Abramowicz, M.A., Kluzniak, W. 2001, A&A, 374, L19

[4] Abramowicz, M.A. et al 2007, Rev. Mexicana Astron. Astrofsica, 27, 8

[5] Afshordi, N., Paczynski, B. 2003, ApJ, 592, 354

[6] Agol, E. 1997, Ph.D thesis, Univ. California, Santa Barbara

[7] Aliev, A.N., Gal'tsov, D.V. 1981, General Relativity and Gravitation, 13, 899

[8] Arons, J. & Lea, S. M., 1976, ApJ, 207, 914

[9] Arras, P., Blaes, O.M. & Turner, N. J., 2006, ApJ, 645, L65

[10] Balbus, S.A., Hawley, J.F. 1998, Rev. Mod. Phys., 70, 1.

[11] Beckwith and Done, 2004 MNRAS 352, 353

[12] Beckwith, K., Hawley, J.F., Krolik, J.H. 2008, MNRAS, in press (arXiv:0801.2974)

[13] Bisnovatyi-Kogan, G. S. & Ruzmaikin, A. A., 1974, Ap&SS, 28, 45

[14] Bisnovatyi-Kogan, G. S. & Rusmaikin, A. A., 1976, Ap&SS, 42, 401

[15] Blaes, O.M. 1987, MNRAS, 227, 975

[16] Blaes, O.M., Arras, P., Fragile, P.C. 2006, MNRAS, 369, 1235

[17] Blaes, O.M., Sramkova, E., Abramowicz, M. A., Kluzniak, W., Torkelsson, U., ApJ, 665, 642

[18] Bisnovatyi-Kogan, G.S., Lovelace, R.V.E. 2007, ApJ, 667, L167

[19] Budden, K.G., Phil. Trans. R. Soc. Lond. A, 1979, 290, 405

[20] Bulirsch, R. 1965, Numerische Mathematik, 7, 78

[21] Byrd, P.F.; Friedman, M.D. Handbook of Elliptic Integrals for Engineers and Scientists, 1971 Sprinter-Verlag, Berlin.

[22] Cadez et al, 2003 A&A 403, 29

[23] Cadez, Fanton, Calvani, 1998 New A 3, 647

[24] Carlson, B.C., 1979, Numerische Mathematik, 33, 1

[25] Carroll, B. W., Cabot, W., McDermott, P. N., Savedoff, M. P. & Van Horn, H. M., 1985, ApJ, 296, 529

[26] Chen and Eardley, 1991 ApJ 382, 125

[27] Collins, T. J. B., Helfer, H. L. & Van Horn, H. M., 2000, ApJ, 534, 944

[28] Connors, Piran and Stark, 1980 ApJ 235, 224

[29] Cunningham, and Bardeen, 1973 ApJ 183, 237

[30] Dabrowski et al, 1997 MNRAS 288, L11

[31] De Villiers, J.-P., Hawley, J.F. 2003, ApJ, 592, 1060

[32] Dickenson, R.E., 1968, J. Atmos. Sci., 25, 984

[33] Done, C., Gierlinski, M., Kubota, A. 2007, Astron. Astrophys. Review, 15, 1

[34] Dovciak, Karas and Yaqoob, 2004 astro-ph/0403541

[35] Drasco and Hughes, 2004 Phys Rev D 69

[36] Elsner, R. & Lamb, F. K., 1976, Nature 262, 356

[37] Elsner, R. & Lamb, F. K., 1977, ApJ, 215, 897

[38] Fabian, Rees, Stella and White, 1989 MNRAS 238, 729

[39] Falanga, M., Melia, F., Tagger, M., Goldwurm, A. & Belanger, G., ApJ, 662, L15

[40] Fanton et al, 1997 PASJ 49, 159

[41] Ferreira, B. T. & Ogilvie, G. I., 2008, astro-ph/08031671

[42] Fragile, P.C., Blaes, O., Anninos, P., Salmonson, J.D. 2007, ApJ, 668, 417

[43] Fu, W., Lai, D. 2008, ApJ, in press (arXiv:0806.1938)

[44] Fukumura and Tsurata, 2004 astro-ph/0405337

[45] Gierlinski, M., Middleton, M., Ward, M., Done, C. 2008, Nature, 455, 369

[46] Ghosh, P. & Lamb, F. K., 1978, ApJ, 223, L83

[47] Ghosh, P. & Lamb, F. K., 1979, ApJ, 232, 259

[48] Gilfanov, M., Revnivtsev, M. & Molkov, S., 2003, A&A, 410, 217

[49] Goldreich, P. 1988, in "Origin, structure and evolution of galaxies" (Proceedings of the Guo Shoujing Summer School of Astrophysics, Tunxi, China), ed. L.Z. Fang (World Scientific: Singapore), p. 127

[50] Goldreich, P., Lynden-Bell, D. 1965, MNRAS, 130, 125

[51] Goldreich, P., Goodman, J., Narayan, R. 1986, MNRAS, 221, 339

[52] Goldreich, P., Tremaine, S. 1979, ApJ, 233, 857

[53] Goodman, J., Evans, N. 1999, MNRAS, 309, 599

[54] Heading, J. 1962, J. Lond. Math. Soc., 37, 195

[55] Horak, J., Karas, V., 2006, A&A, 451, 377

[56] Igumenshchev, I. V., Narayan, R. & Abramowicz, M. A., 2003, ApJ, 592, 1042

[57] Ipser, J.R., 1994, ApJ, 435, 767

[58] Ipser, J.R., 1996, ApJ, 458, 508

[59] Ipser, J.R. & Lindblom, L., 1992, ApJ, 389, 392

[60] Iwasawa, et al, 1996 MNRAS 282, 1038

[61] Julian, W.H., Toomre, A. 1966, ApJ, 146, 810

[62] Kato, S. 1983, PASJ, 35, 249

[63] Kato, S., 1990, PASJ, 42, 99

[64] Kato, S., 2001, PASJ, 53, 1

[65] Kato, S., 2003a, PASJ, 55, 257

[66] Kato, S., 2003b, PASJ, 55, 801

[67] Kato, S., 2008, PASJ, 60, 111

[68] Kato, S. & Fukue, J., 1980, PASJ, 32, 377

[69] Kluzniak, W. & Abramowicz, M. A., 2002, astro-ph/0203314

[70] Knigge, C., Drake, N., Long, K. S., Wade, R. A., Horne, K. & Baptista, R., 1998, ApJ, 499, 29

[71] Kojima, 1991, MNRAS 250, 629

[72] Krolick and Hawley, 2002 ApJ 573, 754

[73] Kulkarni, A.K. & Romanova, M.M., 2008, MNRAS, 386, 673

[74] Lai, D. & Tsang, D., 2008, MNRAS, in press

[75] Lai, D., Zhang, H. 2008, ApJ, 683, 949

[76] Lee, W. H., Abramowicz, M. A. & Kluziniak, W., 2004, ApJ, 603, L93

[77] Li, H., Finn, J.M., Lovelace, R.V.E., Colgate, S.A. 2000, ApJ, 533, 1023

[78] Li, L., Goodman, J., Narayan, R., 2003, ApJ, 593, 980

[79] Li, L., Narayan, R., 2004, ApJ, 601, 414

[80] Lin, C.C., Lau, Y.Y. 1975, SIAM J. Appl. Math., 29, 352

[81] Lifshitz, E.M., Pitaevskii, L.P. 1981, Physical Kinetics (Pergamon Press: Oxford)

[82] Lin, C.C. 1995, The Theory of Hydrodynamic Stability (Cambridge Univ. Press), Chap. 8

[83] Loar, 1991 ApJ 376, 90

[84] Loar, Netzer and Piran, 1990 MNRAS 242, 560

[85] Lovelace, R.V.E., Li, H., Colgate, S.A., Nelson, A.F. 1999, ApJ, 513, 805

[86] Lovelace, R.V.E., Romanova, M.M., 2007, ApJ, 670, L13

[87] Lynden-Bell, D., Kalnajs, A.J. 1972, MNRAS, 157, 1

[88] Machida, M., Matsumoto, R., 2003, ApJ, 585, 429

[89] Machida, M., Matsumoto, R., 2008, PASJ, 60, 613

[90] Mark, J.W.K. 1976, ApJ, 205, 363

[91] Matsumoto, R., Kato, S., Fukue, J., Okazaki, A. T., 1984, PASJ, 36, 71

[92] Misner, C.W., Thorne, K.S. & Wheeler, J.A., 1973, Gravitation, (Freeman, San Francisco)

[93] Morita, T. 1999 Numerische Mathematik 82, 677

[94] Muchotrzeb, B., Paczynski, B. 1982, Acta Astron., 32, 1

[95] Narayan, R., Goldreich, P., Goodman, J. 1987, MNRAS, 228, 1

[96] Noble, S.C., Krolik, J.H., Hawley, J.F. 2008, ApJ, submitted (arXiv:0808.3140)

[97] Novikov I. D. & Thorne K. S. 1973, in Black Holes, eds. C. DeWitt and B. S. DeWitt (New York: Gordon and Breach Publishers), p. 343

[98] Nowak, M. A. & Wagoner, R. V., 1991, ApJ, 378, 656

[99] Nowak, M. A. & Wagoner, R. V., 1992, ApJ, 393, 697

[100] Ogura, Ohuo and Kojima, 2000 PASJ 52

[101] Okazaki, A.T. & Kato, S., 1985, PASJ, 37, 683

[102] Okazaki, A. T., Kato, S. & Fukue, J., 1987, PASJ, 39, 457

[103] Ortega-Rodriguez, M., Silbergleit, A. S. & Wagoner, R. V., 2002, ApJ, 567, 1043

[104] Ortega-Rodriguez, M., Silbergleit, A. S. & Wagoner, R. V., 2006, astro-ph/0611101

[105] Ortega-Rodriguez, M. & Wagoner, R. V., 2007, ApJ, 668, 1158

[106] Paczynski, B., Wiita, P.J. 1980, A&A, 88, 23

[107] Papaloizou, J.C.B., Lin, D.N.C. 1995, ARAA, 33 505

[108] Papaloizou, J.C.B., Pringle, J.E. 1984, MNRAS, 208, 721

[109] Papaloizou, J.C.B., Pringle, J.E. 1987, MNRAS, 225, 267

[110] Patterson, J., 1981 ApJS, 45, 517

[111] Pedlosky, J. 1987, Geophysical Fluid Dynamics. Springer-Verlag, Berlin

[112] Perez, C.A., Silbergleit, A.S., Wagoner, R.V., & Lehr, D.E., 1997, ApJ, 476, 589

[113] Petri, J. 2008, Astrophys. Space Science, in press (arXiv:0809.3115)

[114] Piro, A. L. & Bildsten, L., 2004, ApJ, 616, L155

[115] Popham R., 1999, MNRAS, 308, 979

[116] Press, W.H., Teukolsky, S.A., Vetterling, W.T. & Flannery, B.P., 1998, Numerical Recipes (Cambridge Univ. Press)

[117] Rauch and Blandford, 1994 ApJ 421, 46

[118] Rebusco, P., 2004, PASJ, 56, 553

[119] Rebusco, P., 2008, astro-ph/08013658

[120] Remillard, R. A. & McClintock, J. E., 2006, ARAA, Vol. 44, pp. 49-92

[121] Reynolds et al, 1999 ApJ 514, 164

[122] Reynolds, C. S. & Miller, M. C., 2008, astro-ph/08052950

[123] Rezzolla, L., Yoshida, S'i., Maccarone & Zanotti, O., 2003, MNRAS, 344, L37-L41

[124] Romanova, M. M., Kulkarni, A.K. & Lovelace, R.V.E, 2008, ApJ, 673, L171

[125] Rothstein, D.M., Lovelace, R.V.E. 2008, ApJ, 677, 1221

[126] Shafee, R., et al. 2008, ApJL, submitted (arXiv:0808.2860)

[127] Silbergleit, A. S., Wagoner, R. V. & Ortega-Rodriguez, M., 2001, ApJ, 548, 335

[128] Silbergleit, A. S. & Wagoner, R. V., 2008, ApJ, 680, 1319

[129] Schnittman, J.D. 2005, ApJ, 621, 940

[130] Schnittman, J.D., Bertschinger, E. 2004, ApJ, 606, 1098

[131] Schnittman, J.D., Rezzolla, L. 2006, ApJ, 637, L113

[132] Shu, F.H. 1992, The Physics of Astrophysics II: Gas Dynamics (University Science Books), Chap. 12

[133] Shu, F.H., Laughlin, G., Lizano, S., Galli, D., 2000, ApJ, 535, 190

[134] Spruit, H. C. & Taam, R. E., 1990, A&A, 229, 475

[135] Sramkova, E., Torkelsson, U., Abramowicz, M. A., 2007, A&A, 467, 641

[136] Stella, L., Vietri, M., Morskink, S.M. 1999, ApJ, 524, L63

[137] Strohmayer, T.E. 2001, ApJ, 552, L49

[138] Swank, J. 1999, Nucl. Phys. B, Proc. Suppl., 69, 12 (astro-ph/9802188)

[139] Tagger, M. 2006, arXiv:astro-ph/0612175

[140] Tagger, M. 2006, in the proceedings of the VI Microquasar Workshop "Microquasars and beyond", ed. T. Belloni (arXiv:astro-ph/0612175)

[141] Tagger, M., Pellat, R. 1999, A&A, 349, 1003

[142] Tagger, M., 2001 A&A, 380, 750

[143] Tagger, M., Varniere, P. 2006, ApJ, 652, 1457

[144] Tanaka, H., Takeuchi, T., Ward, W.R. 2002, ApJ, 565, 1257

[145] Tassev, S.V., Bertschinger, E. 2007, ApJ, submitted (arXiv:0711.0065)

[146] Titarchuk, L., 2002, ApJ, 578, L71

[147] Titarchuk, L., 2003, ApJ, 591, 354

[148] Tsang, D. & Lai, D., 2008a, MNRAS, 387, 446

[149] Tsang, D. & Lai, D., 2008b, MNRAS, in press

[150] Tsang, D. & Lai, D., 2008c, MNRAS, submitted

[151] Varniere, P., Tagger, M. 2002, A&A, 394, 329

[152] van der Klis, M. 2006, in Compact Stellar X-ray Sources, ed. W.H.G. Lewin and M. van der Klis (Cambridge Univ. Press) (astro-ph/0410551)

[153] Wagoner, R. V., 1999, Phys. Rep., 311, 259

[154] Warner, B., 2004, PASP, 116, 115

[155] Warner, B. & Woudt, P. A., 2002, MNRAS, 335, 84

[156] Warner, B. & Woudt, P.A., 2005, The Astrophysics of Cataclysmic Variables and Related Objects, Proceedings of ASP Conference Vol. 330. Edited by J.-M. Hameury and J.-P. Lasota. San Francisco: Astronomical Society of the Pacific, 2005., p.227 (arXiv:astro-ph/0409287)

[157] Weaver and Yaqoob, 1998 ApJ 502, L139

[158] Zhang, H., Lai, D., MNRAS, 2006, 368, 917